

SPECKLE PHENOMENA
IN ACTIVE ELECTRO-OPTICAL APPLICATIONS

by

Derek J. Burrell

Copyright © Derek J. Burrell 2023

A Dissertation Submitted to the Faculty of the
WYANT COLLEGE OF OPTICAL SCIENCES

In Partial Fulfillment of the Requirements
For the Degree of

DOCTOR OF PHILOSOPHY
WITH A MAJOR IN OPTICAL SCIENCES

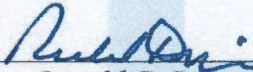
In the Graduate College

THE UNIVERSITY OF ARIZONA

2023

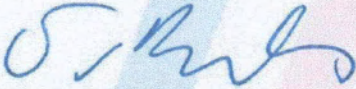
THE UNIVERSITY OF ARIZONA
GRADUATE COLLEGE

As members of the Dissertation Committee, we certify that we have read the dissertation prepared by **Derek James Burrell**, titled ***Speckle Phenomena in Active Electro-Optical Applications*** and recommend that it be accepted as fulfilling the dissertation requirement for the Degree of Doctor of Philosophy.



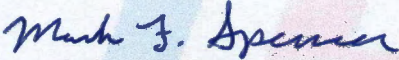
Professor Ronald G. Driggers

Date: 11 Aug 23



Professor David Brady

Date: 11 Aug 23




Professor Mark F. Spencer

Date: 11 Aug 23

Final approval and acceptance of this dissertation is contingent upon the candidate's submission of the final copies of the dissertation to the Graduate College.

I hereby certify that I have read this dissertation prepared under my direction and recommend that it be accepted as fulfilling the dissertation requirement.



Professor Ronald G. Driggers
Dissertation Committee Co-Chair
Wyant College of Optical Sciences

Date: 11 Aug 23

STATEMENT BY AUTHOR

This dissertation has been submitted in partial fulfillment of requirements for an advanced degree at the University of Arizona and is deposited in the University Library to be made available to borrowers under rules of the Library.

Brief quotations from this dissertation are allowable without special permission, provided that accurate acknowledgment of source is made. Requests for permission for extended quotation from or reproduction of this manuscript in whole or in part may be granted by the head of the major department or the Dean of the Graduate College when in his or her judgment the proposed use of the material is in the interests of scholarship. In all other instances, however, permission must be obtained from the author.

This material is based in part upon high-performance computing (HPC) resources supported by the University of Arizona's Technology and Research Initiative Fund (TRIF), University Information Technology Services (UITS), and Office for Research, Innovation, and Impact (RII) and maintained by the Research Technologies Department of UITS.

In reference to IEEE copyrighted material which is used with permission in this dissertation, the IEEE does not endorse any of the University of Arizona's products or services. Internal or personal use of this material is permitted. If interested in reprinting/republishing IEEE copyrighted material for advertising or promotional purposes or for creating new collective works for resale or redistribution, please go to http://www.ieee.org/publications_standards/publications/rights/rights_link.html to learn how to obtain a License from RightsLink.

The views expressed are those of the author and do not necessarily reflect the official policy or position of the Department of the Air Force, the Department of Defense, or the U.S. government.

SIGNED: Derek J. Burrell

ACKNOWLEDGMENTS

Among many other key players, I am grateful beyond measure to the handful of mentors that have gotten me to this point. Chris Middlebrook was the first to take a chance on me as an undergrad at Michigan Tech and convince me that graduate studies were in the cards. Mark Spencer reinforced those beliefs while offering consistency and continuity through all stages of my academic career. Peyman Mirtaheri provided critical inspiration to stay the course when I was at a turning point as an OsloMet exchange student. Ron Driggers proved that success is possible without sacrificing compassion for others or passion for one's own hobbies. Dave Brady was gracious to serve on my committee and share his unique career perspective.

I was fortunate to experience grad school in three distinct phases across three respected institutions, and I wish to thank labmates and colleagues from each. At the University of Central Florida College of Optics and Photonics (CREOL): Bruce Berry, Steve Butrimas, Weiyu Chen, Justin Cook, Matt Cooper, Oles Fylypiv, Heath Gemar, Glenn Goranson, Rob Grimming, Jen Hewitt, C. Kyle Renshaw and Robert Short; at the Air Force Research Laboratory, Directed Energy Directorate (AFRL/RD): Melissa Beason, Max Cubillos, Mason Fitzsimmons, Josh Garretson, Sam Horst, Matt Kernetz, Austin McDaniel, Kelsey Miller, Carrie Noren, Denis Oesch, Cameron Padilla, Greg Pitz, Josh Reding, Stephen Shock, Naresh Tako, Noah Van Zandt, Jeremy Vorenberg and Quincy Zawadzky; and at the University of Arizona Wyant College of Optical Sciences (OSC): Amit Ashok, Col Cavanaugh, Emily Chau, Josh Follansbee, B. Roy Frieden, Michael Hart, Emory Jenkins, Shane Jordan, Patrick Leslie, Will Reynolds and Lindsey Wiley. I'd also like to acknowledge close collaborators scattered among various other affiliations: Wesley Barnes, Jeff Beck, Jeremy Bos, Terry Brennan, Allison Enterline, Orges Furxhi, Szymon Gladysz, Jerry Holst, Matt Kalensky, Andrei Koch, Sze Wah Lee, Eric Mitchell, Cameron Radosevich, Caleb Thomas and Abbie Watnik. Without their interactions I would not have gotten nearly this far in science, let alone in life. And without the efforts of hardworking administrative staff everywhere I could never have graduated.

I extend my gratitude to the Science, Mathematics and Research for Transformation (SMART) Scholarship-for-Service Program, the international society for optics and photonics (SPIE), the Society for Imaging Science and Technology (IS&T), the Directed Energy Professional Society (DEPS), and VIAVI Solutions, Inc., for supporting my graduate research in the form of scholarships and grants.

Special thanks to all my family, all my friends, and all my pets who always lent me the support I needed (whether I knew I needed it or not). And thanks to anyone who ever took the time to play music with me—you were my sanity and my therapy.

DEDICATION

*To Mom and Dad for setting me up,
and to Daniela for keeping me going.*

TABLE OF CONTENTS

LIST OF FIGURES	9
LIST OF TABLES	15
ABSTRACT	16
CHAPTER 1 Introduction	18
CHAPTER 2 Wave-Optics Simulation of Dynamic Speckle: I. In a Pupil Plane	23
2.1 Background	23
2.2 Analytical Irradiance Correlation Coefficient	26
2.2.1 Propagation From the Object Plane to the Pupil Plane	28
2.2.2 Four Different Modes of Extended-Object Motion	31
2.2.3 Analytical Exploration	38
2.3 Numerical Irradiance Correlation Coefficient	38
2.3.1 Simulating Propagation From the Object Plane to the Pupil Plane	41
2.3.2 Simulating Four Different Modes of Extended-Object Motion .	42
2.3.3 Numerical Exploration	45
2.4 Analytical and Numerical Results	46
CHAPTER 3 Wave-Optics Simulation of Dynamic Speckle: II. In an Image Plane	53
3.1 Background	53
3.2 Analytical Irradiance Correlation Coefficient	56
3.2.1 Propagation From the Object Plane to the Image Plane	58
3.2.2 Four Different Modes of Extended-Object Motion	62
3.2.3 Analytical Exploration	71
3.3 Numerical Irradiance Correlation Coefficient	71
3.3.1 Simulating Propagation From the Object Plane to the Image Plane	73
3.3.2 Simulating Four Different Modes of Extended-Object Motion .	75
3.3.3 Numerical Exploration	78
3.4 Analytical and Numerical Results	78

TABLE OF CONTENTS – *Continued*

CHAPTER 4	Active-Tracking Scaling Laws Using the Noise-Equivalent Angle	
	Due to Speckle	86
4.1	Background	86
4.2	Theoretical Analysis	88
	4.2.1 Well-Resolved Objects	90
	4.2.2 Unresolved Objects	95
	4.2.3 Scaling Laws	98
4.3	Numerical Simulation	99
4.4	Results and Discussion	101
CHAPTER 5	Open-Loop Wavefront Sensing in the Presence of Speckle and	
	Weak Scintillation Over Horizontal Paths	112
5.1	Background	112
5.2	Background and Theory	114
	5.2.1 Wavefront Error	115
	5.2.2 Speckle Contrast	117
	5.2.3 Kolmogorov Turbulence	120
	5.2.4 Irradiance Skewness	123
	5.2.5 Dynamic Range	125
5.3	Modeling and Simulation	126
	5.3.1 Simulation Setup	126
	5.3.2 Simulation Methods	127
5.4	Results and Discussion	130
CHAPTER 6	Closed-Loop Adaptive Optics in the Presence of Speckle and	
	Weak Scintillation Over Horizontal Paths	137
6.1	Background	137
6.2	Background and Theory	142
	6.2.1 Kolmogorov Turbulence	143
	6.2.2 Digital Controls	145
	6.2.3 Beacon Characteristics	147
	6.2.4 Performance Metrics	149
6.3	Modeling and Simulation	151
6.4	Results and Discussion	153
	6.4.1 Partially Correlated Speckle	154
	6.4.2 Fully Uncorrelated Speckle	156
CHAPTER 7	System-Level Noise Performance of Coherent Imaging Systems	164
7.1	Background	164
7.2	Noise Theory	165

TABLE OF CONTENTS – *Continued*

7.2.1	Conventional Noise Sources	166
7.2.2	Coherent Noise Sources	168
7.2.3	Coupled Noise Effects	173
7.3	Modeling and Simulation	178
7.4	Results and Discussion	182
CHAPTER 8	Conclusion	185
APPENDIX A	Target Pose Estimation from Dual-Plane Speckle Return	190
A.1	Background	190
A.2	Theory	192
A.3	Methods	193
A.4	Results and Discussion	195
APPENDIX B	Laser Speckle Mitigation Through Substandard Compressive Sensing	196
B.1	Background	196
B.2	Methods	197
B.3	Results and Discussion	198
APPENDIX C	Efficiently Calculating Extended Isoplanatic Angles Over Horizontal Paths	201
C.1	Background	201
C.2	Analysis	201
C.3	Results and Discussion	203
APPENDIX D	Fast Statistical Testing of Scintillated, Speckled Irradiance	205
D.1	Motivation and Background	205
D.2	Test Methods	206
D.3	Results and Discussion	206
APPENDIX E	Wave-Optics Sampling Constraints in the Presence of Speckle and Anisoplanatism	209
E.1	Background	209
E.2	Procedure	210
E.2.1	Physical Constraints	210
E.2.2	Numerical Constraints	213
E.3	Results and Discussion	217
REFERENCES	221

LIST OF FIGURES

2.1	Free-space propagation from an optically rough extended object in the object plane to an observation screen in the pupil plane.	29
2.2	Analytical exploration of the trade space in terms of the four different modes of extended-object motion.	39
2.3	Example irradiance and phase datasets from the wave-optics simulations	40
2.4	Illustration of the free-space system simulated in the wave-optics simulations. Here, we use an optically rough three-bar object (for illustrative purposes).	41
2.5	Numerical exploration in terms of the average RMSE versus the number of Monte-Carlo trials.	45
2.6	Analytical and numerical results for in-plane translation, given (a) square, (b) circular, and (c) Gaussian scattering spots.	48
2.7	Analytical and numerical results for out-of-plane translation, given (a) square, (b) circular, and (c) Gaussian scattering spots.	49
2.8	Analytical and numerical results for in-plane rotation, given (a) square, (b) circular, and (c) Gaussian scattering spots.	50
2.9	Analytical and numerical results for out-of-plane rotation, given (a) square, (b) circular, and (c) Gaussian scattering spots.	51
2.10	An example annular mask for radial isolation of the irradiance datasets (a) without speckle and (b) with speckle.	52
3.1	Free-space propagation from an optically rough extended object in the object plane to a limiting aperture in the pupil plane followed by another free-space propagation to an observation screen in the image plane.	59
3.2	Analytical exploration of the trade space in terms of the four different modes of extended-object motion.	72
3.3	Example irradiance and phase datasets from the wave-optics simulations	74
3.4	Illustration of the imaging system simulated in the wave-optics simulations. Here, we use an optically rough three-bar object (for illustrative purposes).	75
3.5	Numerical exploration in terms of the average RMSE versus the number of Monte-Carlo trials.	79
3.6	Analytical and numerical results for in-plane translation, given (a) square, (b) circular, and (c) Gaussian limiting apertures.	81

LIST OF FIGURES – *Continued*

3.7	Analytical and numerical results for out-of-plane translation, given (a) square, (b) circular, and (c) Gaussian limiting apertures.	82
3.8	Analytical and numerical results for in-plane rotation, given (a) square, (b) circular, and (c) Gaussian limiting apertures.	83
3.9	Analytical and numerical results for out-of-plane rotation, given (a) square, (b) circular, and (c) Gaussian limiting apertures.	84
3.10	An example annular mask for radial isolation of the irradiance datasets (a) without speckle and (b) with speckle.	85
4.1	Black-box imaging geometry with a rough-surface object in the object plane forming a speckled image in the image plane.	91
4.2	Semi-log plot of phase-slope PDF defined in Eq. (4.23); blue shading indicates 99.7% of the area under this curve yielding a realistic range of phase slopes.	97
4.3	Example windowed image for numerical centroid estimation; results from uniform coherent illumination of a circular object such that crosshairs would be perfectly centered on the image if not for the presence of speckle noise.	100
4.4	Normalized NEA as a function of object Fresnel number for uniform (a) circular [cf. Eqs. (4.18), (4.26) & (4.28)] and (b) square [cf. Eqs. (4.22), (4.27) & (4.29)] object–aperture pairings under coherent illumination.	102
4.5	Comparison of Strehl ratios as a function of object Fresnel number for uniform (a) circular [cf. Eqs. (4.28) & (4.30)] and (b) square [cf. Eqs. (4.29) & (4.30)] object–aperture pairings.	103
4.6	Visualization of overlap-integral computation for a circular rough-surface object; limits are shown for $0 < v < 1$	107
4.7	Visualization of overlap-integral computation for a square rough-surface object; limits are shown for $0 < \{v_x, v_y\} < 1$	111
5.1	Example overview of combined phase aberrations due to rough-surface scattering and weak scintillation, both (top row) without and (bottom row) with intraframe speckle averaging.	114
5.2	Theoretical expectation of RMS wavefront error calculated from Eq. (5.9) for various subaperture–object Fresnel numbers and levels of intraframe averaging with (a) $\mu_I = 75\%$, (b) $\mu_I = 50\%$, (c) $\mu_I = 25\%$, and (d) $\mu_I = 0\%$	121

LIST OF FIGURES – *Continued*

5.3	Irradiance histograms with lognormal and exponential fits after propagation through weak scintillation of (a) one speckle subframe and (b) eight subframes averaged together. Note a decrease in skewness from (a) to (b).	124
5.4	Skewness calculated from wave-optics simulation data according to Eq. (5.29) for various levels of intraframe averaging and turbulence strengths (including vacuum).	126
5.5	Object motion required to achieve various levels of subframe decorrelation based on the parameterization specified in Table 5.1 when the mode of object motion is (a) out-of-plane rotation and (b) in-plane translation.	129
5.6	RMS wavefront error from subaperture to subaperture after propagating beacons of various sizes through vacuum and averaging together various numbers of subframes at (a) 25%, (b) 50%, (c) 75% and (d) 100% decorrelation.	131
5.7	Irradiance skewness over the full aperture after propagating beacons of various sizes through vacuum and averaging together various numbers of subframes at (a) 25%, (b) 50%, (c) 75% and (d) 100% decorrelation.	132
5.8	RMS wavefront aberration from subaperture to subaperture after propagating beacons of various sizes through weak scintillation and averaging together various numbers of subframes at (a) 25%, (b) 50%, (c) 75% and (d) 100% decorrelation. Vertical dashed and dash-dotted reference lines delineate fully aberrated and piston-removed isoplanatic patch size, respectively.	133
5.9	Irradiance skewness over the full aperture after propagating beacons of various sizes through weak scintillation and averaging together various numbers of subframes at (a) 25%, (b) 50%, (c) 75% and (d) 100% decorrelation. Vertical dashed and dash-dotted reference lines delineate fully aberrated and piston-removed isoplanatic patch sizes, respectively.	134
5.10	RMS wavefront error/aberration from subaperture to subaperture after propagating beacons of various sizes through (a) vacuum and (b) weak scintillation and averaging together various numbers of subframes with fully mutually uncorrelated speckle realizations; compare with Figs. 5.6d and 5.8d, respectively. Vertical dashed and dash-dotted reference lines delineate fully aberrated and piston-removed isoplanatic patch size, respectively.	135

LIST OF FIGURES – *Continued*

5.11	Irradiance skewness over the full aperture after propagating beacons of various sizes through weak scintillation and averaging together various numbers of subframes with fully mutually uncorrelated speckle realizations; compare with Figs. 5.7d and 5.9d, respectively. Vertical dashed and dash-dotted reference lines delineate fully aberrated and piston-removed isoplanatic patch size, respectively.	136
6.1	Block diagram of a nominal phase-compensation system operating in a null-seeking control loop using a leaky-integrator control law. Here, the matrices \mathbf{K} , \mathbf{G} and \mathbf{H} represent, respectively, the leaky-integrator controller, a continuous-face-sheet DM, and an SHWFS in the Fried geometry; the vectors \mathbf{R} , \mathbf{E} , \mathbf{U} , \mathbf{D} and \mathbf{Y} refer to, respectively, the reference input, the error signal, the control signal, the input disturbance (i.e., aberrated beacon) and the phase-compensated output. Note that the SHWFS and DM sense and correct for the phase aberrations induced by atmospheric turbulence using the compensation offered by the integrator in this multiple-input, multiple-output control loop (hence the use of matrices).	138
6.2	Example overview of combined phase aberrations due to rough-surface scattering and weak turbulence, both (top row) without and (bottom row) with intraframe speckle averaging.	139
6.3	Illustration of anisoplanatism giving rise to distinct PSFs over the image of an extended object.	140
6.4	Bode magnitude plots of closed-loop sensitivity functions corresponding to servos implementing leaky-integrator control at various sample rates, relative to the Greenwood frequency.	148
6.5	Exploration of the subaperture–object Fresnel number (n_{obj}). In general, n_{obj} provides us with a gauge for the average number of speckles across the width of our receiving aperture. As the object size increases from (a) to (c), we see that n_{obj} increases and the total number of received speckles increases from (b) to (d).	152
6.6	Time-domain nPIB results with $f_{\text{eff}} = 40f_G$ and (a) no speckle averaging, as well as 32-subframe averaging at (b) 25% decorrelation, (c) 50% decorrelation, (d) 75% decorrelation and (e) 100% decorrelation of speckle between consecutive subframes.	158
6.7	Time-domain S_{pk} results with $f_{\text{eff}} = 40f_G$ and (a) no speckle averaging, as well as 32-subframe averaging at (b) 25% decorrelation, (c) 50% decorrelation, (d) 75% decorrelation and (e) 100% decorrelation of speckle between consecutive subframes.	159

LIST OF FIGURES – *Continued*

6.8	Steady-state nPIB results with $f_{\text{eff}} = 40f_G$ and various degrees of subframe averaging at (a) 25% decorrelation, (b) 50% decorrelation, (c) 75% decorrelation and (d) 100% decorrelation of speckle between consecutive subframes.	160
6.9	Steady-state S_{pk} results with $f_{\text{eff}} = 40f_G$ and various degrees of subframe averaging at (a) 25% decorrelation, (b) 50% decorrelation, (c) 75% decorrelation and (d) 100% decorrelation of speckle between consecutive subframes.	161
6.10	Time-domain nPIB results with $f_{\text{eff}} = 40f_G$ and (a) no speckle averaging, (b) 2-subframe averaging, (c) 4-subframe averaging, (d) 8-subframe averaging, (e) 16-subframe averaging and (f) 32-subframe averaging for fully uncorrelated speckle between consecutive subframes.	162
6.11	Steady-state nPIB results comparing $f_{\text{eff}} = 40f_G$, $20f_G$ and $10f_G$ for various degrees of speckle averaging with fully uncorrelated speckle between consecutive subframes at (a) $n_{\text{obj}} = 1/20$, (b) $n_{\text{obj}} = 1/10$, (c) $n_{\text{obj}} = 1/5$, (d) $n_{\text{obj}} = 2/5$, (e) $n_{\text{obj}} = 4/5$ and (f) $n_{\text{obj}} = 8/5$	163
7.1	Scale factor describing additional coherent noise due to scintillation when speckle noise is already present [cf. Eq. (7.27)].	178
7.2	Amplitude mask of four-bar target for use in numerical simulations.	179
7.3	Amplitudes of (a) circular pupil and (b) complex-valued ASF; (c) pristine coherent image of four-bar target (not drawn to scale).	180
7.4	Four-bar target image after adding simulated (a) photon shot noise, (b) dark shot noise and (c) read noise.	180
7.5	(a) Underlying phase function of rough-surface target; resulting speckle patterns in the (b) pupil and (c) image planes (not drawn to scale).	181
7.6	Final image of four-bar target including all conventional noise terms in addition to (a) speckle, (b) scintillation and (c) combined speckle and scintillation.	182
7.7	Comparison of theoretical and numerical effective noise as a function of variable read noise with other conventional noise and either (a) speckle or (b) scintillation fixed; vertical lines show fixed values for reference.	183
7.8	Comparison of theoretical and numerical effective noise as a function of variable read noise with other conventional and coherent (speckle and scintillation combined) noise fixed; vertical lines show fixed values for reference.	184

LIST OF FIGURES – *Continued*

A.1	Illustrative schematic of active target illumination with dual-plane monitoring of speckle return.	191
A.2	example	194
B.1	Monte Carlo performance metrics versus average count (N_{avg}) and number of measurements (m).	199
B.2	Irradiance maps of (a) diffraction-limited, (b) speckle-limited and (c) CS-averaged image.	200
C.1	(a) Fully aberrated, piston-removed & piston/tip/tilt-removed isoplanatic angles versus aperture diameter ($\lambda = 1 \mu\text{m}$, $Z = 1.15 \text{ km}$, $C_n^2 = 2.05 \times 10^{-14} \text{ m}^{-2/3}$); (b) qualitative wave-optics simulation results ($D = 30 \text{ cm}$).	204
D.1	Irradiance histogram with lognormal and exponential fits after propagation through weak turbulence with (a) one frame of speckle and (b) eight frames averaged together. Note a decrease in skewness from (a) to (b).	207
D.2	(a) Residuals between actual phase and wavefront reconstruction; (b) skewness in irradiance as a function of uncorrelated averages. Dashed vertical lines indicate the transition from exponential to lognormal GOF outcomes.	208
E.1	Normalized histograms of (a) amplitude, (b) phase and (c) irradiance data representing the Monte Carlo average of 100 independently simulated speckle fields.	214
E.2	Speckle contrast as a function of samples across the object.	217
E.3	Root-mean-square error between numerical and analytical irradiance correlation coefficient as a function of samples per pupil-plane speckle.	218
E.4	Root-mean-square error between numerical and analytical irradiance correlation coefficient as a function of samples per image-plane speckle.	218

LIST OF TABLES

2.1	Closed-form expressions for in-plane translation.	33
2.2	Closed-form expressions for out-of-plane translation.	35
2.3	Closed-form expressions for in-plane rotation.	36
2.4	Closed-form expressions for out-of-plane rotation.	37
2.5	Parameters of interest in the wave-optics simulations.	42
3.1	Closed-form expressions for in-plane translation.	64
3.2	Closed-form expressions for out-of-plane translation.	67
3.3	Closed-form expressions for in-plane rotation.	68
3.4	Closed-form expressions for out-of-plane rotation.	69
3.5	Parameters of interest in the wave-optics simulations.	76
4.1	Sample wave-optics simulation parameters used to validate scaling laws in the well-resolved limit.	101
5.1	Physical and numerical parameters used in wave-optics simulations of open-loop wavefront sensing.	128
6.1	Physical and numerical parameters used in wave-optics simulations of closed-loop wavefront sensing with partially correlated frame-to-frame speckle.	154
6.2	Physical and numerical parameters used in wave-optics simulations of closed-loop wavefront sensing with uncorrelated frame-to-frame speckle.	155
7.1	Speckle-reduction factors used in calculations of absolute coherent noise.	171
7.2	Scintillation-reduction factors in calculations of absolute coherent noise.	173
C.1	Definitions of constants appearing in calculation of piston-removed anisoplanatic error.	202
C.2	Definitions of constants appearing in calculation of piston/tip/tilt-removed anisoplanatic error.	203
E.1	Summary of simulation inputs and physical/numerical derived quantities.	219

ABSTRACT

Active electro-optical systems benefit from stronger signal returns than their passive counterparts by providing scalable illumination power in otherwise limited ambient light. From an imaging standpoint this means higher signal-to-noise ratios for tracking purposes, leading to higher probabilities of detection, classification, recognition and identification of potentially distant objects. By creating an artificial beacon, active illumination also enables wavefront sensing where there is no natural beacon available to act as a reference source. In either application, however, actively illuminating an object of opportunity gives rise to a unique form of multiplicative noise known as speckle. A speckle pattern exhibits spatial variations in both amplitude and phase that result from diffuse scattering off an optically rough surface. Image quality suffers greatly from the presence of fully developed speckle, as the noise in such an image is on the order of the signal level itself. In the case of wavefront sensing, speckle contaminates measurements such that phase aberrations from the object become indistinguishable from those in the atmosphere. Mitigating speckle generally involves increasing the number of degrees of freedom in a speckle field, whether by manipulating coherence or polarization or system dynamics. The latter option allows access to a rich trade space for studying speckle mitigation on a wave-optics simulation basis. With that in mind, this work begins by exploring how different modes of object motion translate to varying degrees of speckle decorrelation in both the pupil and image planes of an optical system. Next, it derives scaling laws that describe the positional uncertainty associated with speckle to quantify active tracking performance. Adapting these scaling laws to the geometry of a Shack–Hartmann wavefront sensor then gives an indication of its open-loop performance limitations, while applying decorrelation theory extends the analysis to cover partially correlated frame-to-frame speckle. Finally, closing the loop on an adaptive-optics control

system gauges the ability to compensate for atmospheric turbulence with both mitigated and unmitigated speckle noise. An additional chapter offers a system-level treatment of radiometric noise performance that includes both speckle and scintillation, and each of these theoretical contributions is validated through high-fidelity wave-optics simulations with strong agreement.

CHAPTER 1

Introduction

Electro-optical (EO) systems are conventionally defined as those operating in the 0.4–3 μm wavelength regime, which covers the visible, near infrared (NIR) and shortwave infrared (SWIR) bands where radiation tends to be more reflective than emissive. By contrast, forward-looking infrared (FLIR) and imaging infrared (I^2R) systems conventionally refer to operation in the midwave infrared (MWIR) and longwave infrared (LWIR) bands where the radiation is mostly emissive [1]. In low-light environments where natural illumination is insufficient to provide an acceptable signal-to-noise ratio (SNR), active imaging with a controlled light source becomes favorable to passive imaging under natural light. Furthermore, wavefront sensing with natural light sources is generally realizable only in astronomical applications where a natural guide star can serve as a reference for ground-to-space geometries. In terrestrial settings, and especially over horizontal rather than slant paths, we rely on focused laser light to provide such information. Because development and scaling of modern active sources is mostly concerned with the visible through SWIR bands, our interests are in EO rather than FLIR/ I^2R systems. A major drawback in all active EO systems, however, is that the use of coherent light creates opportunities for interference effects such as speckle—arising from scattering off a reflective and optically rough surface—and scintillation—arising from propagation through a turbulent medium such as the atmosphere. These irradiance fluctuations manifest as multiplicative noise that undermines imaging, tracking and wavefront sensing performance alike. Considering these predicaments, this dissertation is dedicated to characterizing and mitigating speckle effects in active EO systems.

The two-part paper comprising Chs. 2 and 3 demonstrates the use of wave-optics simulations to model the effects of dynamic speckle. In Part I, we formulate closed-form expressions for the analytical irradiance correlation coefficient in the pupil

plane of an optical system. These expressions are for square, circular, and Gaussian scattering spots and four different modes of extended-object motion, including in-plane and out-of-plane translation and rotation. In Part II, we formulate closed-form expressions for the analytical irradiance correlation coefficient in the image plane of an optical system. These expressions are for square, circular, and Gaussian limiting apertures and four different modes of extended-object motion, including in-plane and out-of-plane translation and rotation. Using a phase-screen approach, we then simulate the equivalent scattering from an optically rough extended object, where we assume that the surface heights are uniformly distributed and delta correlated from grid point to grid point. For comparison to the analytical irradiance correlation coefficient, we also calculate the numerical irradiance correlation coefficient from the dynamic speckle after propagation from the simulated object plane to the simulated pupil and image planes. Overall, the analytical and numerical results definitely demonstrate that, relative to theory, the dynamic speckle in the simulated pupil plane is properly correlated from one frame to the next. Such validated wave-optics simulations provide the framework needed to model more sophisticated setups and obtain accurate results for system-level studies.

It is well known to system engineers that speckle imposes a limitation on active-tracking performance, but scaling laws that quantify this limitation do not currently exist in the peer-reviewed literature. Additionally, existing models lack validation through either simulation or experimentation. With these points in mind, Ch. 4 formulates closed-form expressions that accurately predict the noise-equivalent angle due to speckle. The analysis separately treats both well-resolved and unresolved cases for circular and square apertures. When compared with the numerical results from wave-optics simulations, the analytical results show excellent agreement to a track-error limitation of $(1/3)\lambda/D$, where λ/D is the aperture diffraction angle. As a result, this paper creates validated scaling laws for system engineers that need to account for active-tracking performance.

Shack–Hartmann wavefront sensors are well-established tools for characterizing phase aberrations present in an optical field. The performance of such devices is op-

timized when provided a cooperative point-source beacon at range. If the beacon is instead a noncooperative extended source, the speckle that arises from rough-surface scattering introduces errors into the measurements. In distributed-volume turbulence over horizontal paths, beacon anisoplanatism acts as another source of error due to path averaging. Both types of error grow in severity with growing beacon size. Operating in the weak-turbulence regime where Shack–Hartmann wavefront sensors offer robust performance and using in-plane translation of the beacon to accomplish speckle diversity, we show in Ch. 5 that speckle averaging helps to reduce isoplanatic measurement error but is rendered ineffective for highly anisoplanatic beacons. Understanding these system limitations is critical for performing effective wavefront sensing in horizontal propagation scenarios with noncooperative beacons.

Phase compensation via adaptive optics (AO) is a well-established means of overcoming atmospheric aberrations, but the closed-loop performance of an AO system becomes compromised with the use of an extended beacon. In Ch. 6 we model extended beacons of various sizes using plane-wave illumination of square objects, allowing for partial correlation of frame-to-frame speckle along with the possibility of beacon anisoplanatism as objects grow in size. We then model horizontal-path propagation with Kolmogorov turbulence and frozen flow through wave-optics simulations. Finally, we model a closed-loop phase-compensation system comprised of a Shack–Hartmann wavefront sensor in the Fried geometry, a least-squares phase reconstructor, a continuous-face-sheet deformable mirror, and a leaky-integrator control law. We characterize the severity of speckle and anisoplanatism using the object Fresnel number and object angular extent relative to isoplanatic angle, respectively, and gauge closed-loop performance by the normalized power in the bucket and peak Strehl ratio. Overall results show that while speckle averaging can be an effective strategy for mitigating noise associated with extended beacons, beacon anisoplanatism steadily diminishes and eventually overwhelms any performance gains with a sufficiently large beacon over a horizontal path.

In Ch. 7 we provide an in-depth analysis of noise considerations in coherent imaging, accounting for speckle and scintillation in addition to “conventional” im-

age noise. Specifically, we formulate closed-form expressions for total effective noise in the presence of speckle only, scintillation only (for weak-to-moderate turbulence conditions), and speckle combined with scintillation. We find analytically that photon shot noise is uncorrelated with both speckle and scintillation, despite their shared dependence on the mean signal. Furthermore, unmitigated coherent noise tends to dominate performance limitations due to a squared mean-signal dependence. Strong coupling occurs between speckle and scintillation when both are present, and we characterize this behavior by fitting a scale factor capable of generating variances in closed form. We verify each of these claims through a series of wave-optics simulations, and we see strong agreement in general between numerical results and theoretical predictions. Our findings allow us to confidently gauge signal-to-noise ratio (SNR) expectations when active illumination produces coherent noise.

The appendices at the end of this dissertation provide supplemental information related to the primary subject matter. Appendix A explores the potential for measuring size, distance, and tilt orientation of a simplified object from its returned speckle patterns in the pupil and image planes of a generalized imaging system. Our results show that such measurements are possible to within a 10% error bound. This work was prompted by reviewer comments inquiring about the potential for applying Chs. 2 and 3 to metrology. Appendix B demonstrates an alternative method of alleviating of speckle effects by iteratively reconstructing a single image using compressive sensing. At suboptimal sample rates, reconstructions decorrelate to allow for speckle averaging. Results indicate a potential reduction in speckle contrast by up to 30%. Appendix C presents closed-form expressions for low-order-aberration-removed, aperture-averaged anisoplanatic error across horizontal paths. These solutions are not only computationally inexpensive but easily invertible to numerically calculate extended isoplanatic angles in a given propagation scenario. Appendix D proposes statistical metrics to quickly evaluate speckle's influence on atmospheric wavefront sensing. Integrating over multiple pupil-plane speckle realizations, we find that the skewness in irradiance is ideally ~ 1 . Appendix E characterizes proper sampling of laser speckle in wave-optics simulations, with an emphasis on active im-

agers and wavefront sensors in outdoor environments. We expose tradeoffs between sampling conditions in multiple planes of interest, namely the object, pupil and image planes of an optical system. The goal of our analysis is to develop an optimized numerical tradespace that models the underlying physics of speckle and turbulence with high fidelity. We pay particular attention to the problem of sufficiently sampling an object without subjecting it to anisoplanatism. As a way of overcoming such challenges, we propose and test an optimization routine that defines acceptable simulation parameters based on user-defined physical parameters. Successful implementation of this approach streamlines the design process for applications that involve active tracking and coherent imaging through turbulence.

CHAPTER 2

Wave-Optics Simulation of Dynamic Speckle: I. In a Pupil Plane[†]

2.1 Background

Speckle plays a pivotal role in directed-energy applications. One cannot actively illuminate a distant object without also introducing speckle. Thus, directed-energy applications like long-range imaging [3, 4, 5, 6, 7], tracking [8, 9], wavefront sensing [10, 11], phase compensation [12, 13], and synthetic-aperture ladar [14, 15] depend on the presence of speckle to achieve their desired outcomes. Whenever possible, however, these applications also look to mitigate the effects of speckle in order to achieve the best possible performance.

Optically rough extended objects (i.e., where the surface roughness is on the order of the wavelength of light) diffusely scatter an incident laser beam to produce a speckled irradiance pattern. The associated speckles, in practice, appear as bright regions of constructive interference. Here, the average size of the speckles is roughly equal to a coherence cell from the scattering spot [16]. These speckles unfortunately act as a noise term that limit performance in the aforementioned directed-energy applications. What is more, different modes of extended-object motion serve to perpetuate this noise term on a frame-by-frame basis, due to the effects of dynamic speckle.

Speckle mitigation, in turn, has been an active area of research since the emergence of the laser itself [17]. For example, researchers often perform speckle averaging to mitigate the effects of dynamic speckle. To quantify the benefits of speckle

[†]This material was published previously as [2] in *Applied Optics* with coauthors M. F. Spencer, N. R. Van Zandt, and R. G. Driggers (<https://doi.org/10.1364/AO.427963>) © 2021 Optica Publishing Group. Users may use, reuse, and build upon the article, or use the article for text or data mining, so long as such uses are for non-commercial purposes and appropriate attribution is maintained. All other rights are reserved.

averaging, one can make use of the signal-to-noise ratio (SNR). In practice, the SNR is inversely proportional to the contrast ratio, C , such that

$$C = \frac{\sigma_I}{\bar{I}}, \quad (2.1)$$

where σ_I is the standard deviation of the speckled irradiance pattern and \bar{I} is the mean [17]. A fully developed speckled irradiance pattern (resulting from fully polarized/coherent light) follows a negative-exponential probability density function (PDF). In turn, C goes to unity [18]. Accumulating K patterns, as a result, decreases C to $1/\sqrt{K}$ as the PDF becomes more Gaussian like in accordance with the central-limit theorem. This last statement is only true if the individual speckled irradiance patterns are uncorrelated on a frame-by-frame basis [19]. From a systems-engineering perspective, it is therefore of great interest to accurately define when speckle decorrelation occurs, especially in the presence of dynamic speckle.

Given a fully developed speckle pattern, the real and imaginary parts of the underlying complex-optical field conform to a complex-circular Gaussian joint PDF [20]. Because of this inherent randomness, there are no deterministic solutions for the size of the speckles and thus for the speckle decorrelation. A general approach to this problem is to derive a correlation function that accounts for the lowest-order statistics of the complex-optical field at two different points in space [21]. Normalizing this function to its peak value yields an analytical irradiance correlation coefficient equal to one for overlapping points and equal to zero for separation by the width of the average size of the speckles. Displacing the speckled irradiance patterns by this distance decorrelates them in time, given some relationship between motion of the extended object and that of the dynamic speckle. Then at a known rate of change in extended-object position, the speckle decorrelation is predictable as a function of time. Through the years, a number of researchers have taken this approach, while many others have studied closely-related phenomena that one can easily recast in this manner.

Rigden and Gordon [22], Oliver [23] and Langmuir [24] were among the first scientists to report on dynamic speckle. Allen and Jones [25] offered an explanation of their results based on the diffraction of radio waves. Isenor [26] and Sporton [27] followed up by emphasizing the optical-system geometry and its impact on speckle dynamics in the image plane. Anisimov et al. [28] later derived space-time correlation statistics for the first time, and correlation experiments have been underway ever since [29, 30, 31, 32, 33, 34].

With this rich history in mind, this two-part paper demonstrates the use wave-optic simulations to model the effects of dynamic speckle. In Part I, we formulate closed-form expressions for the analytical irradiance correlation coefficient in the pupil plane of an optical system. Part II then switches gears and formulates closed-form expressions for the analytical irradiance correlation coefficient in the image plane of an optical system. It is worthwhile to consider the pupil plane separately from the image plane, as the structure of speckle turns out to operate independently in each plane under most conditions of interest. As such, this paper focuses solely on the theory and simulation of speckle decorrelation in the pupil plane of an optical system. Because image formation is not yet of concern, the pupil plane (discussed throughout this paper) is equivalent to a plane of observation at some distance from the extended object in a free-space system. In Part II, this distance represents free-space propagation from the object plane to the entrance-pupil plane. A second free-space propagation then focuses the light from the exit-pupil plane to the image plane.

Broadly speaking, Part I aims to fulfill two main goals. The first goal is to establish closed-form expressions for the analytical irradiance correlation coefficient (associated with dynamic speckle in a pupil plane) for (1) the cases of square, circular, and Gaussian scattering spots and (2) four different modes of extended-object motion: in-plane and out-of-plane translation, as well as in-plane and out-of-plane rotation. While meeting this goal does not demand any new theory per se, it does fill several gaps in the dynamic-speckle literature that would otherwise require some inference while compiling all of the closed-form expressions

in a unified notation. It also frames many of these closed-form expressions for the first time as straightforward functions of extended-object motion. The second main goal is to develop a simulation framework within which to study speckle decorrelation in terms of the numerical irradiance correlation coefficient and thereafter compare the numerical results from simulation to the analytical results from theory.

In service of these goals, the following sections formulate the aforementioned closed-form expressions for the analytical irradiance correlation coefficient (cf. Sec. 2.2), the wave-optics simulations used to compute the numerical irradiance correlation coefficient (cf. Sec. 2.3), and the results that compare the analytical and numerical findings (cf. Sec. 2.4). Before moving on to the next section, it is important to note that we wrote Part I so that it complements Part II. In turn, both papers contain overlapping material. So as not to be redundant, this choice enables two things: (1) both papers read independently from each other (i.e., the reader does not have to read Part II in order to understand the results in Part I and vice versa), and (2) the reader can pull up Part II alongside Part I and compare and contrast the results without too much difficulty. As a result, this two-part paper demonstrates the use of wave-optics simulations to model the effects of dynamic speckle.

2.2 Analytical Irradiance Correlation Coefficient

In this section, we formulate closed-form expressions for the analytical irradiance correlation coefficient, $\mu_I(\mathbf{p}_1; \mathbf{p}_2)$. Strictly speaking, these formulations treat $\mu_I(\mathbf{p}_1; \mathbf{p}_2)$ as a measure of correlation between two points in a static-speckled irradiance pattern. In this way, $\mu_I(\mathbf{p}_1; \mathbf{p}_2)$ offers a sense of the average size of the speckles by solving for the spatial separation between two distinct points in space, \mathbf{p}_1 and \mathbf{p}_2 , at which speckle decorrelation occurs. The closed-form expressions formulated in this section are just as effective, however, at defining where speckle decorrelation occurs

for dynamic-speckled irradiance patterns [32, 35, 36]. In practice, we can relate such patterns to the dynamics induced by extended-object motion; thus, $\mu_I(\mathbf{p}_1; \mathbf{p}_2)$ is a useful construct for dynamic speckle, in addition to static speckle, hence the reason we use it in the analysis that follows.

Although speckle is by nature a self-interference effect with respect to the complex-optical field, it manifests as an irradiance measurement (in units of power per unit area) using modern-day optical detectors. Consequently, dynamic speckle involves a correlation function between two speckled irradiance patterns, $I_1(\mathbf{p})$ and $I_2(\mathbf{p})$. The relevant correlation function is

$$\begin{aligned} R_I(\mathbf{p}_1; \mathbf{p}_2) &= \langle I_1(\mathbf{p}_1) I_2(\mathbf{p}_2) \rangle \\ &= \langle U_1(\mathbf{p}_1) U_1^*(\mathbf{p}_1) U_2(\mathbf{p}_2) U_2^*(\mathbf{p}_2) \rangle, \end{aligned} \quad (2.2)$$

where $\langle \circ \rangle$ denotes an ensemble average, while \mathbf{p}_1 and \mathbf{p}_2 are again two distinct points in space. Supposing that the rough-surface scattering from the optically rough extended object lends enough independent phase contributions that the central-limit theorem applies, we model the complex-optical fields $U(\mathbf{p}_1)$ and $U(\mathbf{p}_2)$ as complex-circular Gaussian random variables [37]. In turn,

$$\begin{aligned} R_I(\mathbf{p}_1; \mathbf{p}_2) &= \langle I_1(\mathbf{p}_1) \rangle \langle I_2(\mathbf{p}_2) \rangle + |\langle U_1(\mathbf{p}_1) \rangle \langle U_2^*(\mathbf{p}_2) \rangle|^2 \\ &= \langle I_1(\mathbf{p}_1) \rangle \langle I_2(\mathbf{p}_2) \rangle + |J_U(\mathbf{p}_1; \mathbf{p}_2)|^2, \end{aligned} \quad (2.3)$$

where $J_U(\mathbf{p}_1; \mathbf{p}_2)$ is the mutual intensity between $U_1(\mathbf{p}_1)$ and $U_2(\mathbf{p}_2)$. The complex spatial coherence factor,

$$\mu_U(\mathbf{p}_1; \mathbf{p}_2) = \frac{J_U(\mathbf{p}_1; \mathbf{p}_2)}{\sqrt{J_U(\mathbf{p}_1; \mathbf{p}_1) J_U(\mathbf{p}_2; \mathbf{p}_2)}}, \quad (2.4)$$

is a normalization of mutual intensity having the property $0 \leq \mu_U \leq 1$. Substituting Eq. (2.4) into Eq. (2.3),

$$R_I(\mathbf{p}_1; \mathbf{p}_2) = \langle I_1(\mathbf{p}_1) \rangle \langle I_2(\mathbf{p}_2) \rangle [1 + |\mu_U(\mathbf{p}_1; \mathbf{p}_2)|^2]. \quad (2.5)$$

Equation (2.5) contains both DC and AC components, but it is the fluctuating AC term that carries meaningful information about the speckle decorrelation. Thus,

$$\mu_I(\mathbf{p}_1; \mathbf{p}_2) = |\mu_U(\mathbf{p}_1; \mathbf{p}_2)|^2 \quad (2.6)$$

is a fitting correlation coefficient with respect to irradiance that governs R_I . Also known as the Yamaguchi correlation factor [38], $\mu_I(\mathbf{p}_1; \mathbf{p}_2)$ is effectively a ratio of crosscorrelation to autocorrelation with reference to Eqs. (2.4) and (2.5).

2.2.1 Propagation From the Object Plane to the Pupil Plane

At this stage in the analysis, it is useful to introduce the rough-surface-scattering geometry proposed in this paper. Figure 2.1 illustrates this geometry as a free-space system with the α - β and ξ - η sets of axes placed within the object and pupil planes, respectively. The respective radial coordinates are $\Omega = \sqrt{\alpha + \beta}$ and $\varrho = \sqrt{\xi + \eta}$. A distance Z along the z axis initially separates the object and pupil planes.

We position an optically rough extended object of width W in the object plane, while an observation screen with infinite field of view (for the time being) resides in the pupil plane. Each component starts off centered at the origin of its local coordinate system. Distances $\Delta\Omega$ and Δz are measures of in-plane and out-of-plane translation, respectively. The z axis and optical axis are collinear with the axis of in-plane rotation ($\Delta\vartheta$), while out-of-plane rotation ($\Delta\varphi$) occurs about some axis in the α - β plane. As the object moves under fully coherent illumination, the diffusely scattered speckled irradiance pattern changes and eventually decorrelates from its initial state. Moving forward we assume that both illumination and observation occur on axis (for ease of modeling). We also assume that deviations from theory (i.e., the closed-form expressions formulated in this section) are only appreciable for large angles of incidence and observation.

With Eqs. (2.4) and (2.6) in mind, recall that we can relate the analytical irradiance correlation coefficient, $\mu_I(\mathbf{p}_1; \mathbf{p}_2)$, to the mutual intensity, $J_U(\mathbf{p}_1; \mathbf{p}_2)$. What

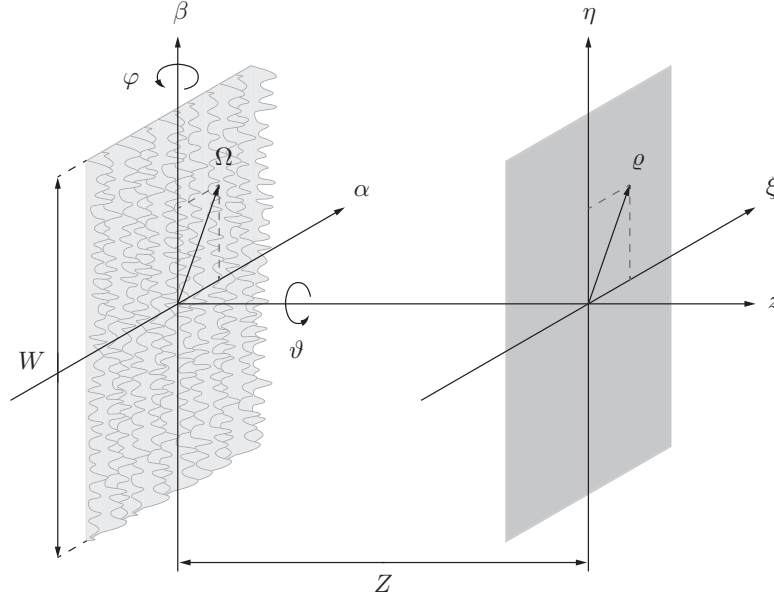


Figure 2.1: Free-space propagation from an optically rough extended object in the object plane to an observation screen in the pupil plane.

is more, we can use scalar diffraction theory to propagate $J_U(\mathbf{p}_1; \mathbf{p}_2)$ from plane to plane to determine $\mu_I(\mathbf{p}_1; \mathbf{p}_2)$ in the appropriate plane. For this purpose, if $U(\alpha, \beta)$ is the source field (i.e., the complex-optical field in the object plane), then the first Rayleigh–Sommerfeld diffraction integral predicts that

$$U(\xi, \eta) = \frac{Z}{j\lambda} \iint_{\Sigma} U(\alpha, \beta) \frac{\exp(jk\ell)}{\ell^2} ds \quad (2.7)$$

in the pupil plane. Here, λ is the optical wavelength, $k = 2\pi/\lambda$ is the angular wavenumber,

$$\ell = \sqrt{(\xi - \alpha)^2 + (\eta - \beta)^2 + Z^2} \quad (2.8)$$

is the Euclidean distance between points (α, β) and (ξ, η) , and ds is a differential surface element of source area Σ . This solution assumes that we satisfy the optical condition $\lambda \ll \ell$. In practice, Eq. (2.7) has the form of a superposition integral in

terms of source field $U(\alpha, \beta)$ and free-space impulse response

$$h(\xi, \eta; \alpha, \beta) = \frac{Z \exp(jk\ell)}{j\lambda\ell^2}. \quad (2.9)$$

Equation (2.9) notably depends only on the differences between points (α, β) and (ξ, η) , and this shift invariance constitutes an isoplanatic system so that Eq. (2.7) becomes a convolution between the source field and the impulse response [39].

To determine the mutual intensity, $J_U(\mathbf{p}_1; \mathbf{p}_2)$, in the pupil plane, we first define a generic point $\mathbf{\Omega} = (\alpha, \beta)$ within the object plane. In the vicinity of the pupil plane, \mathbf{p}_1 and \mathbf{p}_2 are points located at (ξ_1, η_1, Z) and $(\xi_1 + \Delta\xi, \eta_1 + \Delta\eta, Z + \Delta z)$, respectively. Then Eq. (2.7) yields

$$\begin{aligned} J_U(\mathbf{p}_1; \mathbf{p}_2) &= \langle U(\mathbf{p}_1) U^*(\mathbf{p}_2) \rangle \\ &= \iint_{\Sigma_2} \iint_{\Sigma_1} \langle U(\mathbf{\Omega}_1) U^*(\mathbf{\Omega}_2) \rangle h(\mathbf{p}_1; \mathbf{\Omega}_1) h^*(\mathbf{p}_2; \mathbf{\Omega}_2) d^2\mathbf{\Omega}_1 d^2\mathbf{\Omega}_2 \quad (2.10) \\ &= \iint_{\Sigma_2} \iint_{\Sigma_1} J(\mathbf{\Omega}_1; \mathbf{\Omega}_2) h(\mathbf{p}_1; \mathbf{\Omega}_1) h^*(\mathbf{p}_2; \mathbf{\Omega}_2) d^2\mathbf{\Omega}_1 d^2\mathbf{\Omega}_2, \end{aligned}$$

so all that is left to define is the source mutual intensity $J(\mathbf{\Omega}_1; \mathbf{\Omega}_2)$ (i.e., the mutual intensity in the object plane).

According to Goodman [40], the scattered field immediately following an optically rough surface is delta correlated to a first approximation (above the scale of a wavelength). The resulting expression is

$$J_U(\mathbf{\Omega}_1; \mathbf{\Omega}_2) = \kappa U(\mathbf{\Omega}_1) U^*(\mathbf{\Omega}_2) \delta(\mathbf{\Omega}_1 - \mathbf{\Omega}_2), \quad (2.11)$$

where κ is some global loss factor. By the sifting property of the Dirac delta function, $\delta(\circ)$, Eqs. (2.10) and (2.11) combine as

$$J_U(\mathbf{p}_1; \mathbf{p}_2) = \kappa \iint_{\Sigma} |U(\mathbf{\Omega})|^2 h(\mathbf{p}_1; \mathbf{\Omega}) h^*(\mathbf{p}_2; \mathbf{\Omega}) d^2\mathbf{\Omega} \quad (2.12)$$

after setting $\mathbf{\Omega}_1 = \mathbf{\Omega}$ for simplicity.

Making the paraxial approximation (with respect to amplitude) that $\ell_1^2 \approx \ell_2^2 \approx Z^2$, the end result of Eqs. (2.4), (2.6), and (2.12) is

$$\mu_I(\mathbf{p}_1; \mathbf{p}_2) = \left| \frac{\iint_{\Sigma} |U(\mathbf{\Omega})|^2 \exp[jk(\ell_2 - \ell_1)] d^2\mathbf{\Omega}}{\iint_{\Sigma} |U(\mathbf{\Omega})|^2 d^2\mathbf{\Omega}} \right|^2. \quad (2.13)$$

Equation (2.13) reveals that the analytical irradiance correlation coefficient, $\mu_I(\mathbf{p}_1; \mathbf{p}_2)$, is a function of the source irradiance, $|U(\mathbf{\Omega})|^2$, as well as the observation points \mathbf{p}_1 and \mathbf{p}_2 . Much of the foundational work on speckle decorrelation applies a binomial approximation to a power-series expansion of the phasor argument of Eq. (2.13) prior to integrating. This final paraxial approximation (with respect to phase) ultimately gives rise to a scaled Fresnel diffraction integral, since replacing the impulse responses with the well-known Fresnel propagation kernel effectively makes Eq. (2.13) a normalized Fresnel transform of $|U(\mathbf{\Omega})|^2$ in two dimensions.

2.2.2 Four Different Modes of Extended-Object Motion

In what follows, we formulate closed-form expressions for the four different modes of extended-object motion proposed in this paper, including in-plane and out-of-plane translation and rotation. For this purpose, we need to first define a set of unit-amplitude source fields, $U(\mathbf{\Omega}) = U(\alpha, \beta)$. Assuming plane-wave illumination, these so-called scattering spots take the following functional forms [41]:

$$U(\alpha, \beta) = \text{rect}\left(\frac{\alpha}{W}, \frac{\beta}{W}\right) = \text{rect}\left(\frac{\alpha}{W}\right) \text{rect}\left(\frac{\beta}{W}\right), \quad (2.14)$$

where

$$\text{rect}(w) = \begin{cases} 1 & |w| < 1/2 \\ 1/2 & |w| = 1/2 \\ 0 & |w| > 1/2 \end{cases}; \quad (2.15)$$

$$U(\alpha, \beta) = \text{cyl}\left(\frac{\sqrt{\alpha^2 + \beta^2}}{W}\right), \quad (2.16)$$

where

$$\text{cyl}(\rho) = \begin{cases} 1 & 0 \leq \rho < 1/2 \\ 1/2 & \rho = 1/2 \\ 0 & \rho > 1/2 \end{cases} ; \quad (2.17)$$

and

$$U(\alpha, \beta) = \text{Gaus} \left(\frac{\sqrt{\alpha^2 + \beta^2}}{\sqrt{\pi}W/2} \right), \quad (2.18)$$

where

$$\text{Gaus}(\rho) = \exp(-\pi\rho^2). \quad (2.19)$$

Here, Eqs. (2.14) and (2.15) give rise to a square scattering spot of width W , Eqs. (2.16) and (2.17) give rise to a circular scattering spot of diameter W , and Eqs. (2.18) and (2.19) gives rise to a Gaussian scattering spot of 1/e-amplitude diameter W .

Moving forward, we also need to define the following special functions:

$$\text{sinc}(w) = \frac{\sin(\pi w)}{\pi w}, \quad (2.20)$$

$$\text{somb}(\rho) = 2 \frac{J_1(\pi\rho)}{\pi\rho}, \quad (2.21)$$

and

$$\text{Fres}(w) = \frac{S^2(w) + C^2(w)}{w^2}. \quad (2.22)$$

Here, $J_1(\circ)$ is a first-order Bessel function of the first kind (not to be confused with mutual intensity), while $S(\circ)$ and $C(\circ)$ are, respectively, the Fresnel sine and cosine integrals [39]. These special functions readily show up in the closed-form expressions that follow for in-plane and out-of-plane translation and rotation of the object. Furthermore, these special functions [cf. Eqs. (2.18)-(2.22)] readily provide cutoff/rolloff conditions. Such conditions define what we mean by speckle decorrelation and offer a sense of the average size of the speckles.

In-Plane Translation

Assuming in-plane translation of the object (cf. Fig. 2.1), Table 2.1 provides closed-form expressions for the analytical irradiance correlation coefficient, $\mu_I(\Delta\Omega)$, for all three scattering spots (i.e., square, circular, and Gaussian) with corresponding cutoff/rolloff conditions, $\Delta\Omega_{c/r}$. Here, $\Delta\Omega$ is the in-plane translation distance. It is important to note that both the square and circular scattering spots give rise to distinct cutoff conditions (i.e., the special functions go to zero at $\Delta\Omega_c$), whereas the Gaussian scattering spot gives rise to a rolloff condition (i.e., the special function never reaches zero but has a $1/e^2$ magnitude at $\Delta\Omega_r$).

To formulate the closed-form expressions given in Table 2.1, Δz is set to zero in

Table 2.1: Closed-form expressions for in-plane translation.

scattering spot	irradiance correlation coefficient	cutoff/rolloff condition
square	$\mu_I(\Delta\Omega) = \text{sinc}^2\left(\frac{W\Delta\Omega}{\lambda Z}\right)$	$\Delta\Omega_c = \frac{\lambda Z}{W}$
circular	$\mu_I(\Delta\Omega) = \text{somb}^2\left(\frac{W\Delta\Omega}{\lambda Z}\right)$	$\Delta\Omega_c = \frac{1.22\lambda Z}{W}$
Gaussian	$\mu_I(\Delta\Omega) = \text{Gaus}\left(\frac{\sqrt{\pi}W\Delta\Omega}{2\lambda Z}\right)$	$\Delta\Omega_r = \frac{\sqrt{8}\lambda Z}{\pi W}$

Eq. (2.13) for in-plane translation, such that point \mathbf{p}_2 is at $(\xi_1 + \Delta\xi, \eta_1 + \Delta\eta, Z)$. The radial distance between points of observation in the pupil plane is $\Delta\varrho = \sqrt{\Delta\xi^2 + \Delta\eta^2}$, which corresponds directly to an in-plane object translation of $\Delta\Omega = \sqrt{\Delta\alpha^2 + \Delta\beta^2}$. Thus, by substituting $\Delta\varrho$ with $\Delta\Omega$ after integration, the analytical irradiance correlation coefficient, $\mu_I(\Delta\Omega)$, becomes a function of the in-plane translation distance, $\Delta\Omega$. In so doing, we neglect the effects of boiling as we introduce new scatterers into the scattering spot. This assumption is valid as long as the scattering spot is larger than the speckles it produces in the pupil plane.

For a square or circular scattering spot of width or diameter W , the cutoff condition, $\Delta\Omega_c$, corresponds to the average lateral size of the speckles. If dealing with

an oblong rectangular spot, things become separable in the horizontal and vertical directions (using different values for W). These findings agree with published results [42, 43].

For a Gaussian scattering spot of $1/e$ -amplitude diameter W , the rolloff condition, $\Delta\Omega_r$, is consistent with Goodman's theory [16]. The resulting equation is only valid over small translation distances [44], as are all other Gaussian functions presented in this paper. Such analytical curves decrease monotonically out to infinity, when in practice there are oscillatory outer lobes (as with previous expressions), due to periodic overlap of speckles with large translation distances [45]. Moreover, these analytical curves decay asymptotically, which means there is no zero crossing at which to naturally define the average lateral size of the speckles. Instead, the $1/e^2$ point serves as a correlation rolloff condition rather than a cutoff condition. What matters for comparison with discrete irradiance datasets from wave-optics simulations (or experiments) is that there is consistency with theory at least up to this rolloff condition.

Out-of-Plane Translation

Assuming out-of-plane translation of the object (cf. Fig. 2.1), Table 2.2 provides closed-form expressions for the analytical irradiance correlation coefficient, $\mu_I(\Delta z)$, for all three scattering spots (i.e., square, circular, and Gaussian) with corresponding cutoff/rolloff conditions, $\Delta z_{c/r}$. Here, Δz is the out-of-plane translation distance. It is important to note that both the square and circular scattering spots give rise to distinct cutoff conditions (i.e., the special functions go to zero or a minimum at Δz_c), whereas the Gaussian scattering spot gives rise to a rolloff condition (i.e., the special function has a $1/e^2$ magnitude at Δz_r).

To formulate the closed-form expressions given in Table 2.2, $\Delta\Omega$ is set to zero in Eq. (2.13) for out-of-plane translation, confining point \mathbf{p}_2 to $(\xi_1, \eta_1, Z + \Delta z)$. Unlike with in-plane translation (cf. Sec. 2.2.2), the results now vary with radial vantage point $\varrho = \sqrt{\xi + \eta}$ in the pupil plane. Thus, the closed-form expressions given in Table 2.2 are valid only for *on-axis* speckles.

Table 2.2: Closed-form expressions for out-of-plane translation.

scattering spot	irradiance correlation coefficient	cutoff/rolloff condition
square	$\mu_I(\Delta z) = \text{Fres}^2\left(\frac{W}{Z}\sqrt{\frac{\Delta z}{2\lambda}}\right)$	$\Delta z_c = 7.31\lambda\left(\frac{Z}{W}\right)^2$
circular	$\mu_I(\Delta z) = \text{sinc}^2\left[\frac{\Delta z}{8\lambda}\left(\frac{W}{Z}\right)^2\right]$	$\Delta z_c = 8\lambda\left(\frac{Z}{W}\right)^2$
Gaussian	$\mu_I(\Delta z) = \left\{1 + \left[\frac{\pi W^2 \Delta z}{8\lambda Z(Z + \Delta z)}\right]^2\right\}^{-1}$	$\Delta z_r = \frac{Z}{0.155W^2/(\lambda Z) - 1}$

Analogous to the relationship between in-plane translation and the average lateral size of the speckles, the cutoff/rolloff conditions given in Table 2.2 estimate the average longitudinal size of the on-axis speckles. These speckles all point away from the centroid of illumination, meaning they align with the z axis at $\varrho = 0$ and rotate away from it for $\varrho > 0$. They also elongate with increasing distance from the illumination axis, yet they have the same axial projection on average. This behavior implies that they are shortest along the axial dimension with an off-axis length of $\Delta z_c = \sqrt{\xi^2 + \eta^2 + Z^2}$ [42]. A detail worth mentioning is that Li & Chiang numerically derive scaling factors for an exact calculation of the average longitudinal size of the off-axis speckles [46]. Another detail worth mentioning is that Eq. (2.22) does not cross zero but rather decreases to a minimum value of 6.65×10^{-3} before increasing again.

In-Plane Rotation

Assuming in-plane rotation of the object (cf. Fig. 2.1), Table 2.3 provides closed-form expressions for the analytical irradiance correlation coefficient, $\mu_I(\Delta\vartheta)$, for all three scattering spots (i.e., square, circular, and Gaussian) with corresponding cutoff/rolloff conditions, $\Delta\vartheta_{c/r}$. Here, $\Delta\vartheta$ is the in-plane rotation angle. It is

important to note that both the square and circular scattering spots give rise to distinct cutoff conditions (i.e., the special functions go to zero at $\Delta\vartheta_c$), whereas the Gaussian scattering spot gives rise to a rolloff condition (i.e., the special function has a $1/e^2$ amplitude at $\Delta\vartheta_r$).

In essence, in-plane rotation is an extension of in-plane translation (cf.

Table 2.3: Closed-form expressions for in-plane rotation.

scattering spot	irradiance correlation coefficient	cutoff/rolloff condition
square	$\mu_I(\Delta\vartheta) = \text{sinc}^2\left(\frac{W\Delta\vartheta\varrho}{\lambda Z}\right)$	$\Delta\vartheta_c = \frac{\lambda Z}{W\varrho}$
circular	$\mu_I(\Delta\vartheta) = \text{somb}^2\left(\frac{W\Delta\vartheta\varrho}{\lambda Z}\right)$	$\Delta\vartheta_c = \frac{1.22\lambda Z}{W\varrho}$
Gaussian	$\mu_I(\Delta\vartheta) = \text{Gaus}\left(\frac{\sqrt{\pi}W\Delta\vartheta\varrho}{2\lambda Z}\right)$	$\Delta\vartheta_r = \frac{\sqrt{8}\lambda Z}{\pi W\varrho}$

Sec. 2.2.2), given a circular path around the rotational axis. Accordingly, we can substitute arc length $\Delta\vartheta\varrho$ for linear distance $\Delta\Omega$. Doing so produces the relationships given in Table 2.3.

Similar to out-of-plane translation (cf. Sec. 2.2.2), the expressions in this case vary with radial vantage point $\varrho = \sqrt{\xi + \eta}$. Unlike for out-of-plane translation, however, the closed-form expressions given in Table 2.3 readily account for off-axis speckles with the inclusion of variable ϱ . Churnside's work confirms these results after appropriate simplifications [47], as does further analysis by Yura et al. [48]. Saleh makes the point that in-plane rotation at sufficiently large angles warrants the inclusion of a sinusoidal argument factor to account for periodic replication of the signal in time [29]. A detail worth mentioning is that the on-axis correlation is unity with a cutoff/rolloff condition of infinity, since $\varrho = 0$. This result is physically accurate, since the speckle at the very center of rotation remains stationary, independent of in-plane rotation $\Delta\vartheta$.

Out-of-Plane Rotation

Assuming out-of-plane rotation of the object (cf. Fig. 2.1), Table 2.4 provides closed-form expressions for the analytical irradiance correlation coefficient, $\mu_I(\Delta\varphi)$, for all three scattering spots (i.e., square, circular, and Gaussian) with corresponding cutoff/rolloff conditions, $\Delta\varphi_{c/r}$. Here, $\Delta\varphi$ is the out-of-plane rotation angle. It is important to note that both the square and circular scattering spots give rise to distinct cutoff conditions (i.e., the special functions go to zero at $\Delta\varphi_c$), whereas the Gaussian scattering spot gives rise to a rolloff condition (i.e., the special function has a $1/e^2$ magnitude at $\Delta\varphi_r$).

In essence, out-of-plane rotation also mimics the behavior of in-plane translation

Table 2.4: Closed-form expressions for out-of-plane rotation.

scattering spot	irradiance correlation coefficient	cutoff/rolloff condition
square	$\mu_I(\Delta\varphi) = \text{sinc}^2\left(\frac{2W\Delta\varphi}{\lambda}\right)$	$\Delta\varphi_c = \frac{\lambda}{2W}$
circular	$\mu_I(\Delta\varphi) = \text{somb}^2\left(\frac{2W\Delta\varphi}{\lambda}\right)$	$\Delta\varphi_c = \frac{0.61\lambda}{W}$
Gaussian	$\mu_I(\Delta\varphi) = \text{Gaus}\left(\frac{\sqrt{\pi}W\Delta\varphi}{\lambda}\right)$	$\Delta\varphi_r = \frac{\sqrt{2}\lambda}{\pi W}$

(cf. Sec. 2.2.2), given small-angle rotations. Accordingly, we can substitute linear distance $2Z\Delta\varphi$ for linear distance $\Delta\Omega$. Doing so produces the relationships given in Table 2.4.

For near-normal angles of incidence and observation, the speckled irradiance patterns arise from the same set of rough-surface scatters [49]. As such, a linear tilt across the object's surface imposes a linear shift in the far field. This last point relates to the shift theorem of the Fourier transform [41]. Thus, under the small-angle approximation, the appropriate substitution comes about through geometric considerations as the object surface normal subtends an angle of $\Delta\varphi \approx \Delta\varrho/Z$.

Recalling that $\Delta\varrho$ and $\Delta\Omega$ are functionally equivalent for in-plane translation

and free-space propagation, the result is that $Z\Delta\varphi$ replaces $\Delta\Omega$ in a transmission geometry. The reflection geometry then requires that $2Z\Delta\varphi$ replaces $\Delta\Omega$, as an angle doubling occurs due to the double pass through the depth of the tilted object. With this last point in mind, the rough-surface scattering geometry under consideration leads to the closed-form expressions given in Table 2.4. The same results follow from Goodman's use of scattering vectors to characterize the speckle decorrelation at normal incidence and observation [16].

2.2.3 Analytical Exploration

Figure 2.2 plots the closed-form expressions formulated in Tables 2.1–2.4. In particular, Fig. 2.2(a) plots the case of in-plane translation (cf. Table 2.1), Fig. 2.2(b) plots the case of out-of-plane translation (cf. Table 2.2), Fig. 2.2(c) plots the case of in-plane rotation (cf. Table 2.3), and Fig. 2.2(d) plots the case of out-of-plane rotation (cf. Table 2.4). All plots include the respective cutoff conditions for square and circular scattering spots and the rolloff conditions for Gaussian scattering spots.

2.3 Numerical Irradiance Correlation Coefficient

All of the closed-form expressions formulated in Sec. 2.2 make use of continuous speckled irradiance patterns, $I_1(\mathbf{p})$ and $I_2(\mathbf{p})$. In this section, we make use of discrete irradiance datasets, I_1 and I_2 , from wave-optics simulations (or experiments). With this last point in mind, the numerical irradiance correlation coefficient, $\hat{\mu}_I$, takes the following form:

$$\hat{\mu}_I = \frac{\langle I_1 I_2 \rangle - \langle I_1 \rangle \langle I_2 \rangle}{\sqrt{\langle (I_1 - \langle I_1 \rangle)^2 \rangle \langle (I_2 - \langle I_2 \rangle)^2 \rangle}}, \quad (2.23)$$

where $\langle \circ \rangle$ denotes an arithmetic mean. Equation (2.23) turns out to be equivalent to calculating the Pearson's correlation coefficient for a sample [50], which applies

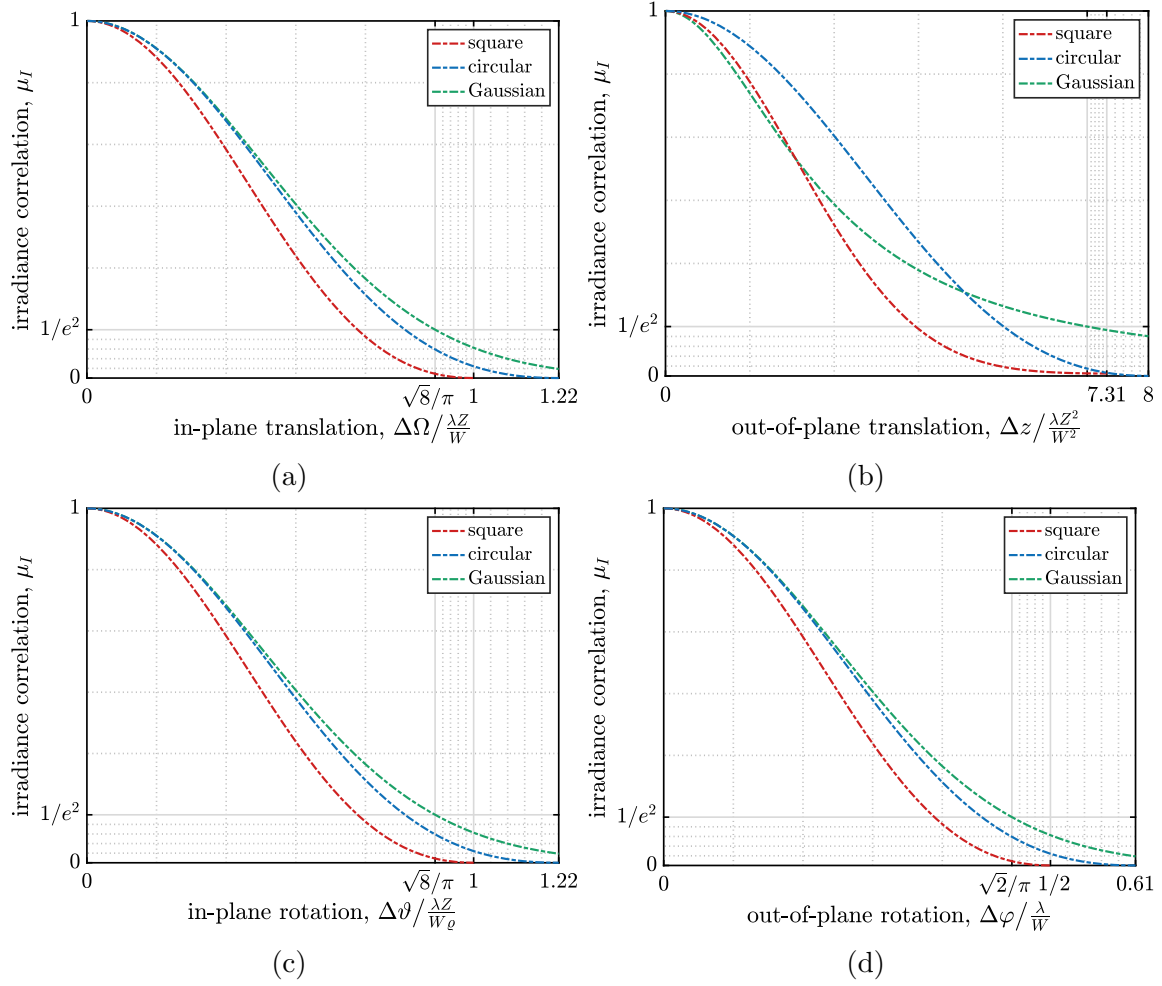


Figure 2.2: Analytical exploration of the trade space in terms of the four different modes of extended-object motion.

to Gaussian random processes. Thus, similar to its analytical counterpart, $\hat{\mu}_I$ is a useful construct for dynamic speckle and we use it in the analysis that follows.

With Eq. (2.23) in mind, the wave-optics simulations setup in this section make use of the following procedure.

1. Create an optically rough extended object using a phase-screen approach.
2. Propagate from the object plane to the pupil plane.
3. Crop the irradiance dataset I_1 and save for reference.
4. Modify the optically rough extended object with the appropriate mode of extended-object motion.
5. Repeat as necessary, saving the frame-to-frame irradiance dataset I_2 .
6. Calculate the numerical irradiance correlation coefficients as a function of extended-object motion.

To illustrate steps 1–3, Fig. 2.3 displays example irradiance and phase datasets. These wave-optics simulations make use of the WaveProp Toolbox for MATLAB [51].

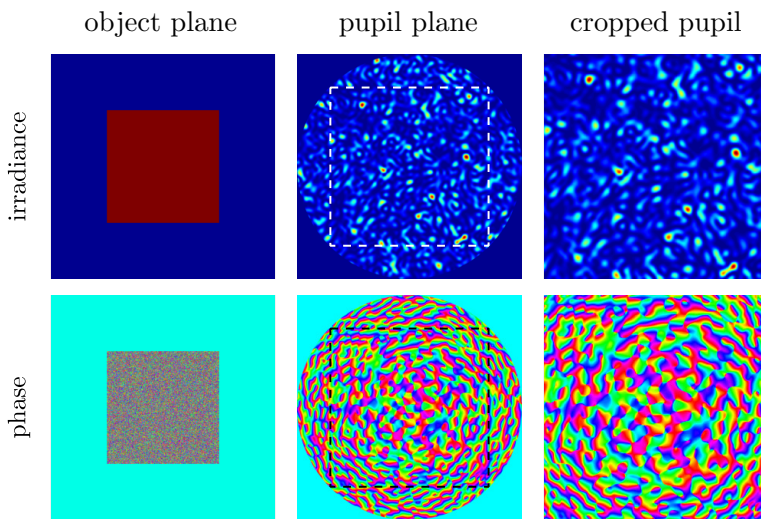


Figure 2.3: Example irradiance and phase datasets from the wave-optics simulations

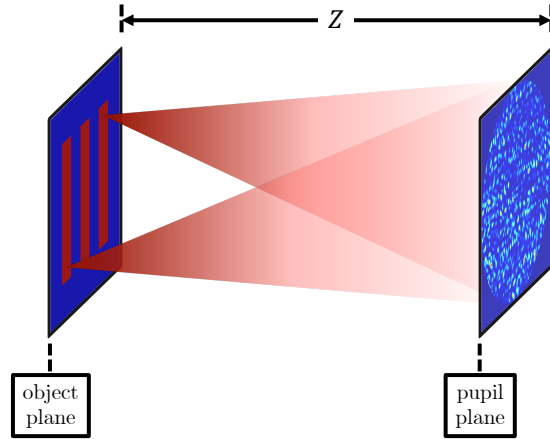


Figure 2.4: Illustration of the free-space system simulated in the wave-optics simulations. Here, we use an optically rough three-bar object (for illustrative purposes).

2.3.1 Simulating Propagation From the Object Plane to the Pupil Plane

Analogous to Fig. 2.1, Fig. 2.4 depicts the free-space system simulated in the wave-optics simulations. These wave-optics simulations used an $N \times N$ grid resolution with $N = 512$. This choice provided an acceptable balance between physical accuracy and computational efficiency [52]. The wave-optics simulations also made use of a free-space wavelength of $\lambda_0 = 1 \mu\text{m}$ and a limiting-aperture (circular-only) diameter of $D = 30 \text{ cm}$, which are typical values for long-range propagation studies.

For simplicity, the wave-optics simulations used unity scaling between the simulated object and pupil planes. They also used 200 grid points across the aperture diameter, while padding the circular pupil with zeros to exceed the recommended factor of 2.4 [53]. As such, the grid spacing, δ , was 1.5 mm, and the grid side length, S , was 76.8 cm. Critical sampling [54] (a.k.a. Fresnel scaling [51]) then stipulated that

$$N = \frac{S^2}{\lambda Z}. \quad (2.24)$$

Satisfying critical sampling typically gives wave-optics results that are free of aliasing. However, the high spatial frequencies contained in diffuse speckle made the wave-optics simulations especially prone to aliasing even with Eq. (2.24) satisfied. Tailored methods such as pupil-plane filtering [55] aim to combat this problem by

eliminating the high spatial frequencies that would cause aliasing. Nonetheless, empirical evidence suggests that first doubling the grid resolution, then propagating the field (via the impulse-response method [54]) and cropping back down has greater resistance to aliasing [51]. Taking this approach, we set $Z = 2.30$ km.

Recalling that the scattering-spot width/diameter W varies inversely with speckle size, it cannot be so large as to cause insufficient sampling of the speckle in the simulated pupil plane. As a result, we set $W = 30.7$ cm, so that the object Fresnel number, $N_{\text{obj}} = DW/(\lambda Z)$, was 40. This choice populated the pupil plane with roughly 40 speckles across D (cf. Fig. 2.3), yielding five grid points per speckle for an average pupil-plane error of $<1\%$ [9, 10]. Table 2.5 summarizes all of the parameters of interest in the wave-optics simulations.

Table 2.5: Parameters of interest in the wave-optics simulations.

	parameter	value(s)
general	grid resolution, $N \times N$ [px]	512×512
	grid spacing, δ [mm]	1.50
	grid side length, S [cm]	76.8
system	illumination wavelength, λ [μm]	1.00
	propagation distance, Z [km]	2.30
	limiting-aperture diameter, D [cm]	30.0
object	object Fresnel number, N_{obj}	40
	scattering-spot width/diameter, W [cm]	30.7

2.3.2 Simulating Four Different Modes of Extended-Object Motion

To simulate an optically rough extended object, we used a phase-screen approach [16, 9, 10]. In so doing, we assumed that the surface heights were uniformly distributed and delta correlated from grid point to grid point. At each grid point within the scattering spot, we then took a random draw from a uniform phase distribution on the interval $[-\pi, \pi)$ and examined four different modes of extended-object motion.

Simulating In-Plane Translation

Simulating in-plane translation required that we move the phase screen laterally across the scattering spot. Since the phase-screen approach used in this paper assumed that the surface heights were uniformly distributed and delta correlated from grid point to grid point, we set the minimum in-plane translation distance to a single grid point of motion between each captured frame. Implementing in-plane translation in this way involved a circular shift of the phase screen in one direction. Since the object width, W , was considerably smaller than the grid side length S , the resultant scattering spot had zero magnitude (or near-zero magnitude in the case of a Gaussian scattering spot) near the edges of the grid. Thus, the phase wraparound resulting from a small circular shift did not affect the phase screen's frame-to-frame randomness.

Simulating Out-of-Plane Translation

Out-of-plane translation was perhaps the most laborious mode of extended-object motion to simulate properly, as it required a different propagation distance between the simulated object and pupil planes for each successive value of Δz . This outcome meant that we inevitably violated critical sampling [cf. Eq. (2.24)] as we moved the simulated object plane closer to the simulated pupil plane. Varying this propagation distance also changed the lateral speckle size, meaning we had to recrop and upsample each speckle pattern (for comparison with the original) as the object moved closer to the pupil plane. Nonetheless, we empirically determined that the wave-optics simulations were robust against the effects of aliasing and resampling for all values of Δz .

As discussed in the Appendix, the simulated out-of-plane translation exhibited a radial dependence. Thus, masking the irradiance datasets restricted the viewing region to a certain radius in order to calculate the numerical irradiance correlation coefficient [cf. Eq. (2.23)]. These masks were of the same thickness as the size of

the speckles, where speckle size was defined by the cutoff/rolloff conditions given in Table 2.2.

Simulating In-Plane Rotation

To simulate in-plane rotation, we applied a rotation matrix at the specified angle $\Delta\vartheta$. We also applied nearest-neighbor interpolation. In turn, we observed reasonable rotation in the resulting dynamic speckle (as expected) without a noticeable loss of fidelity.

Similar to out-of-plane translation, the simulated in-plane rotation also exhibited a radial dependence, as discussed in the Appendix. In turn, masking the irradiance datasets restricted the viewing region to a certain radius in order to calculate the numerical irradiance correlation coefficient [cf. Eq. (2.23)]. In accordance with the cutoff/rolloff conditions given in Table 2.3, these masks were of the same thickness as the average size of the speckles.

Simulating Out-of-Plane Rotation

Simulation of out-of-plane rotation involved multiplying the simulated object plane by the following complex reflectance function:

$$\mathcal{R}(\alpha, \beta) = \exp [j2k (\Delta\varphi_\beta\alpha + \Delta\varphi_\alpha\beta)]. \quad (2.25)$$

Here, we decomposed the tilt angle into rotations about the α and β axes. This decomposition accounted for the change in optical path length, given the small-angle approximation.

2.3.3 Numerical Exploration

In the next section, we compare the results obtained for the numerical irradiance correlation coefficient to those obtained for the analytical irradiance correlation coefficient. To do so, we need to perform Monte Carlo averaging on the numerical results. To explore this numerical trade space, we use root-mean-square error (RMSE), such that

$$\text{RMSE} = \sqrt{\frac{1}{n} \sum_{i=1}^n [\hat{\mu}_I(i) - \mu_I]^2}. \quad (2.26)$$

Here, i is an iterator over the number of Monte-Carlo trials n , $\hat{\mu}_I$ is the numerical irradiance correlation coefficient from simulation, and μ_I is the analytical correlation coefficient from theory.

Figure 2.5 plots Eq. (2.26) to find that the average RMSE becomes asymptotically stable in the neighborhood of 40 Monte Carlo trials. Choosing this number keeps the error below $\sim 1\%$. Note that the average RMSE results displayed in Fig. 2.5 are fairly representative for all four modes of extended-object motion. Also note that we averaged over 100 realizations at each datapoint for curve-smoothing purposes.

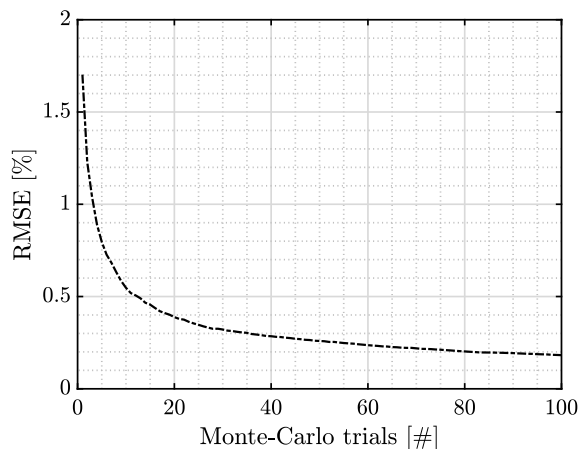


Figure 2.5: Numerical exploration in terms of the average RMSE versus the number of Monte-Carlo trials.

2.4 Analytical and Numerical Results

Figures 2.6–2.9 provide the analytical and numerical results for this paper. Overall, the analytical results from theory are in agreement with the numerical results from simulation. With this agreement in mind, we discuss the four different modes of extended-object motion in the following list.

1. Figure 2.6 shows the analytical and numerical results for *in-plane translation* (also see Visualization 1). Here, the sampling is relatively coarse due to the fact we set the minimum in-plane translation distance to a single grid point of motion between each captured frame. Future efforts could look at using interpolation to increase this sampling. However, doing so could violate the assumptions used throughout this paper; in particular, that the optically rough surface is delta correlated to a first approximation.
2. Figure 2.7 shows the the analytical and numerical results for *out-of-plane translation* (also see Visualization 2). Here, we show results for several values of ϱ but relative to some scattering-spot width W . To calculate numerical results for off-axis observation, where $\varrho \neq 0$, we made use of an annular mask, which we illustrate in Fig. 2.10 in the Appendix. By normalizing the numerical results using the approach presented in Ref. [43], we derived nonlinear scale factors [56] to modify the closed-form expressions presented in Table 2.2. In particular, we normalized the off-axis radial position to the scattering-spot width W , since the scale factors themselves are a normalization of the longitudinal correlation lengths. These scale factors allowed for comparison with the analytical results for off-axis observation, where $\varrho \neq 0$.
3. Figure 2.8 shows the analytical and numerical results for *in-plane rotation* (also see Visualization 3). Here, we show results for several values of ϱ relative to some position P . Similar to out-of-plane translation, we made use of the annular mask, which we illustrate in Fig. 2.10 in the Appendix, to calculate numerical results for off-axis observation, where $\varrho \neq 0$. Recalling that the

closed-form expressions in Table 2.3 are already set up to handle off-axis observation, one does not need scale factors in this particular case. Moreover, we observe the off-axis speckle at relative rather than absolute radial positions because the correlation falloff is linear with radial position.

4. Figure 2.9 shows the analytical and numerical results for *out-of-plane rotation* (also see Visualization 4). These results mirror those contained in Fig. 2.6 for in-plane translation, but the use of Eq. (2.25) at arbitrary out-of-plane rotation angles allowed for better sampling. This similarity comes about because translation of speckle dominates the pupil-plane decorrelation in both cases.

The data points in Figs. 2.6–2.9 also indicate ± 1 standard deviation about the Monte Carlo average (i.e., the average with respect to 40 Monte-Carlo trials). A general observation is that these standard deviations seem to grow with increasing extended-object motion, which is not surprising. Even so, the error bars maintain an upper bound of $\sim 3\%$; thus, the Monte-Carlo averaging did not dramatically affect the mean result for any one trial. Before moving on to the next section, it is important to note that Visualizations 1–4 help in comprehending the results presented in this section. These visualizations show results for a square scattering spot and circular limiting aperture. This particular setup is common between Parts I and II of this two-part paper. Thus, we include both pupil and image planes in these visualizations, so that the results presented here complement those contained in Part II and vice versa.

Note: Annular Masks

Both the simulated out-of-plane translation and the simulated in-plane rotation exhibited a radial dependence. Thus, masking the irradiance datasets restricted the viewing region to a certain radius in order to calculate the numerical irradiance correlation coefficient [cf. Eq. (2.23)]. On-axis observation simply required a circular mask, but off-axis observation required an annular mask as shown in Fig. 2.10(a).

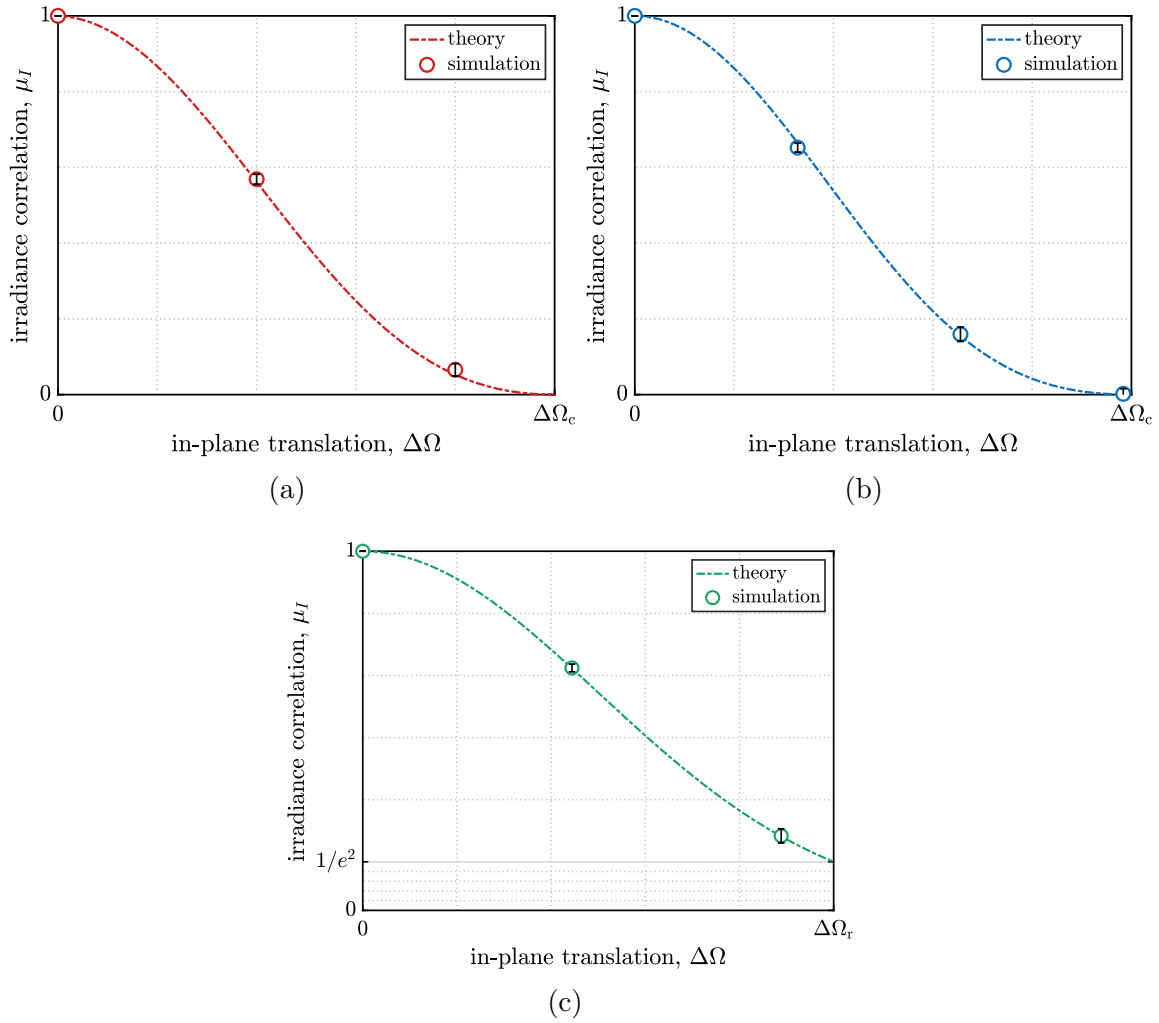


Figure 2.6: Analytical and numerical results for in-plane translation, given (a) square, (b) circular, and (c) Gaussian scattering spots.

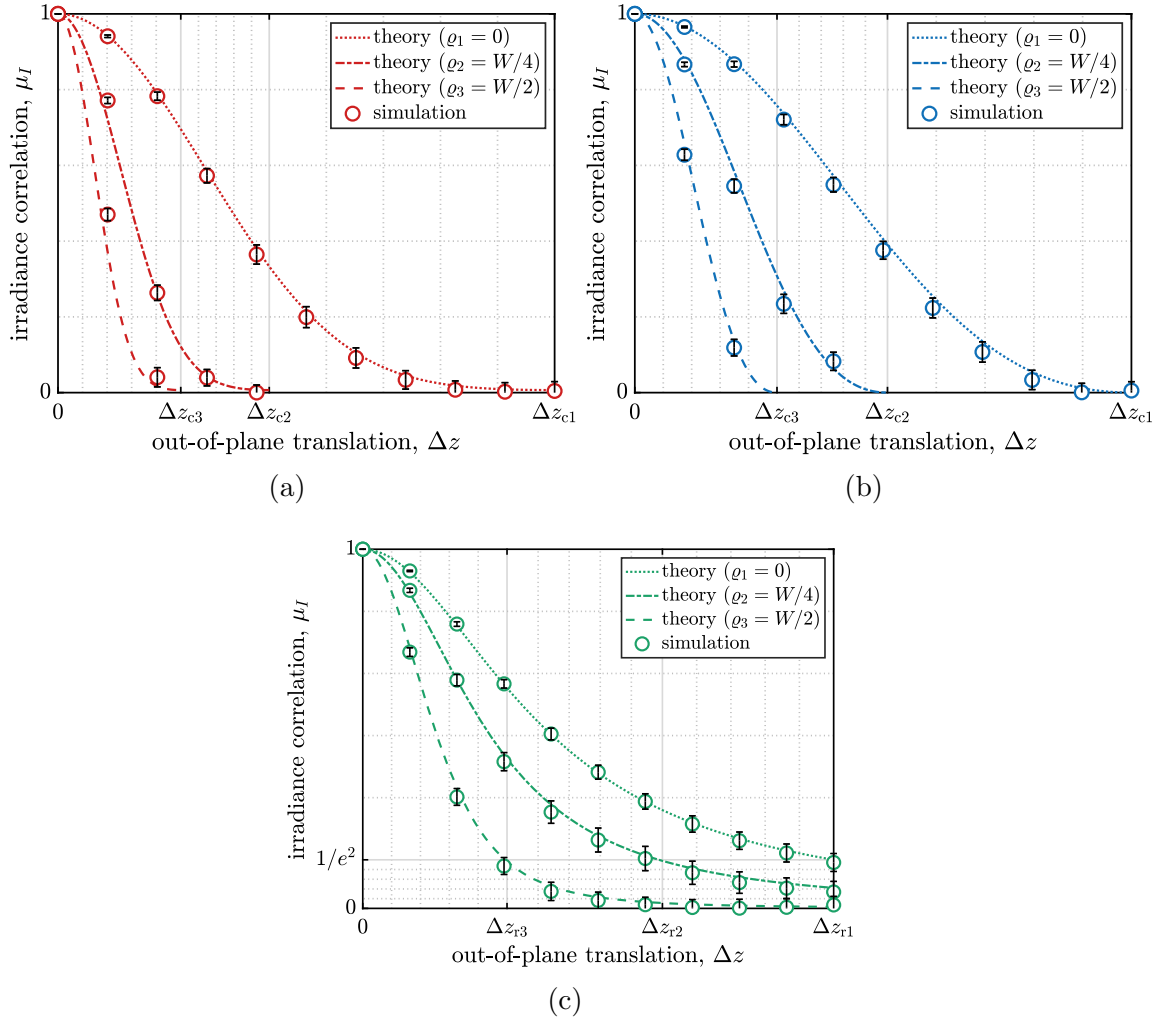


Figure 2.7: Analytical and numerical results for out-of-plane translation, given (a) square, (b) circular, and (c) Gaussian scattering spots.

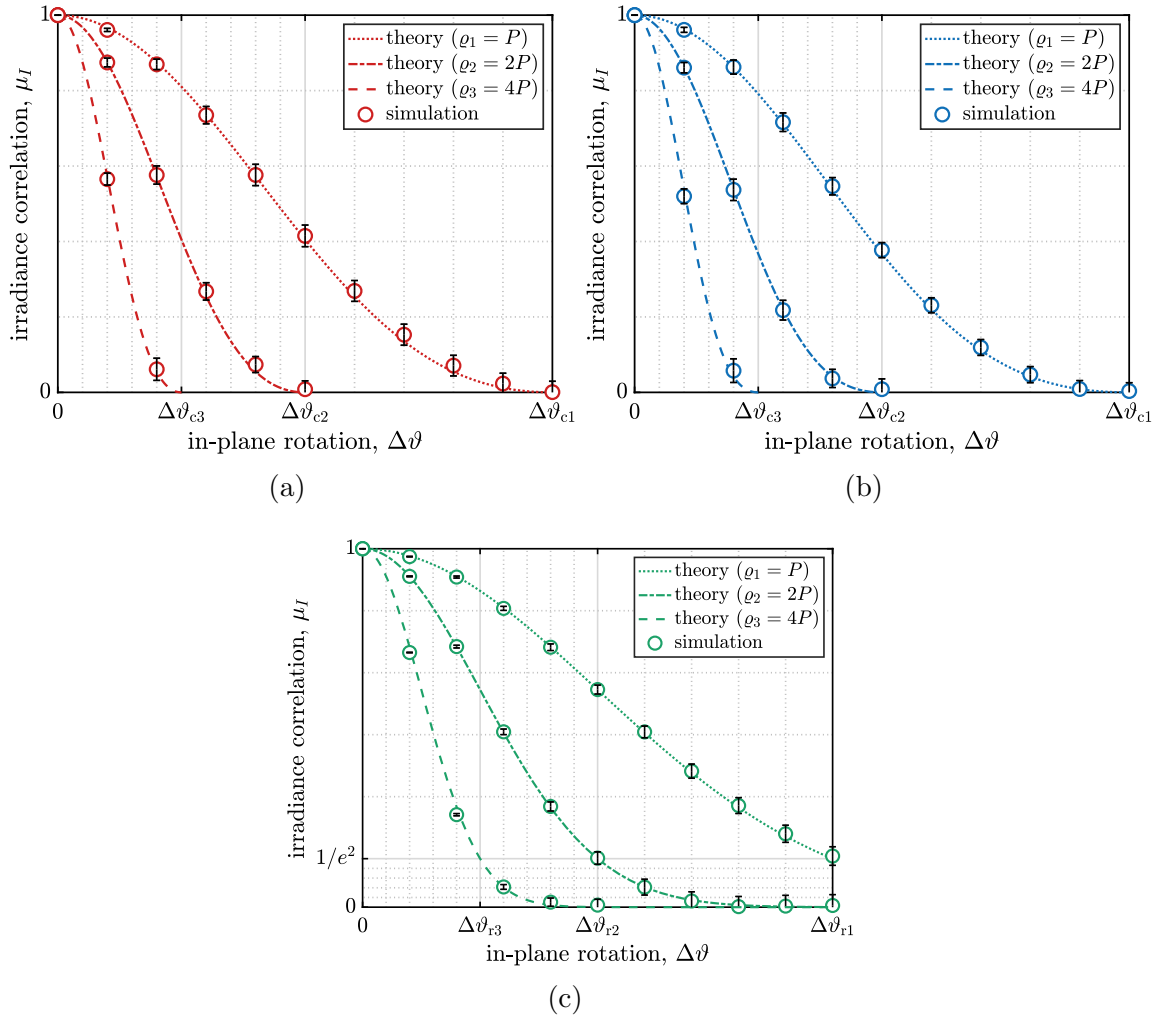


Figure 2.8: Analytical and numerical results for in-plane rotation, given (a) square, (b) circular, and (c) Gaussian scattering spots.

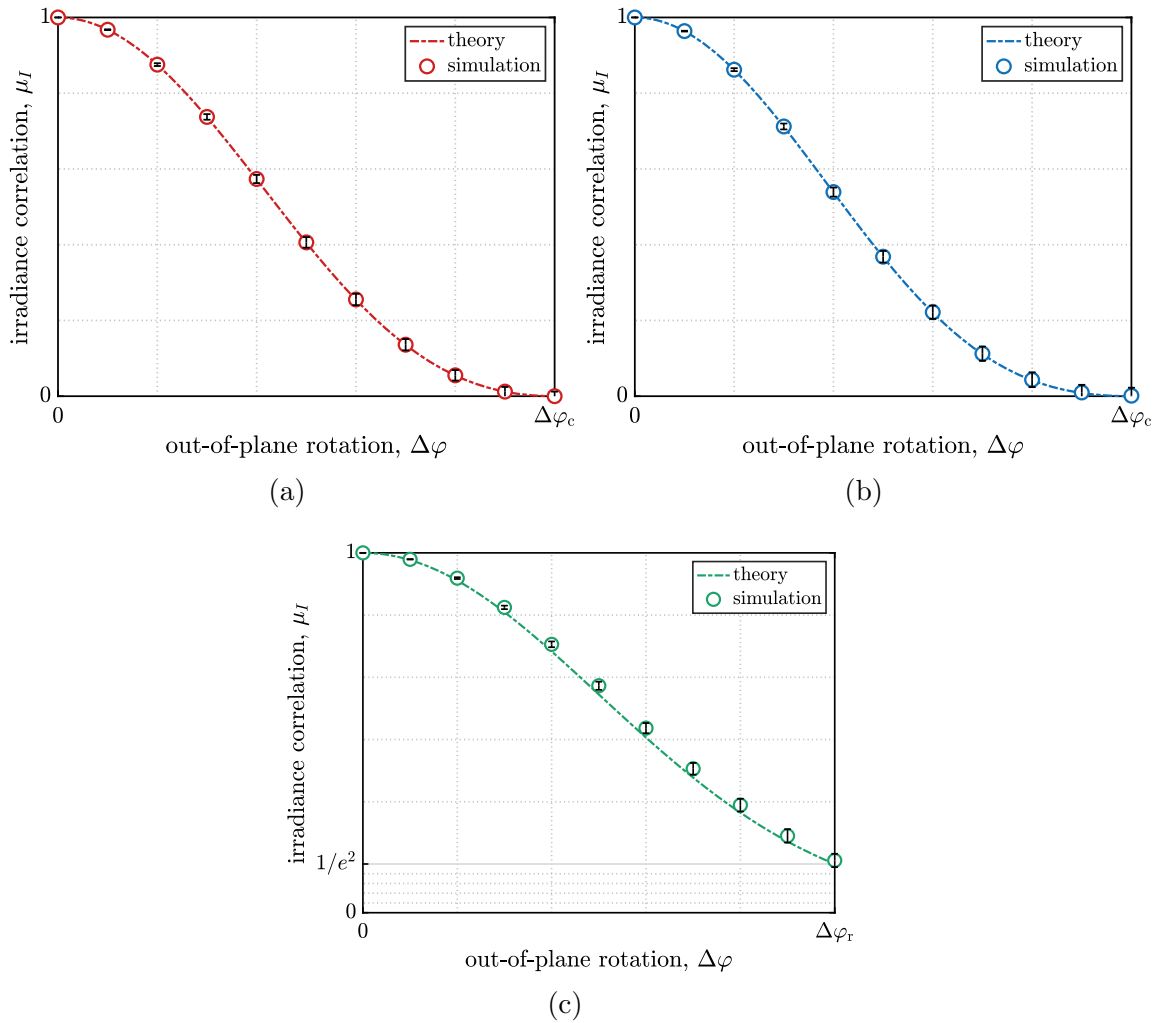


Figure 2.9: Analytical and numerical results for out-of-plane rotation, given (a) square, (b) circular, and (c) Gaussian scattering spots.

In this work, the mask had the same thickness as the average size of the speckles, as portrayed in Fig. 2.10(b). In general, the annular mask had inner and outer radii ϱ_1 and ϱ_2 with an average radius

$$\begin{aligned}\varrho_{\text{ave}} &= \frac{\int_0^{2\pi} \int_{\varrho_1}^{\varrho_2} \varrho^2 d\varrho d\theta}{\int_0^{2\pi} \int_{\varrho_1}^{\varrho_2} \varrho d\varrho d\theta} \\ &= \frac{2}{3} \left(\varrho_2 + \frac{\varrho_1^2}{\varrho_1 + \varrho_2} \right).\end{aligned}\quad (2.27)$$

Thus, for an annular mask of thickness t centered at radial position ϱ_0 , we can rewrite Eq. (2.27) such that

$$\varrho_{\text{ave}} = \varrho_0 + \frac{t^2}{12\varrho_0}, \quad (2.28)$$

where

$$\varrho_0 = \frac{1}{6} \left(3\varrho_{\text{ave}} + \sqrt{9\varrho_{\text{ave}}^2 - 3t^2} \right). \quad (2.29)$$

In the above analysis, we set t such that it equaled the cutoff/rolloff conditions given in Tables 2.2 and 2.3 for the simulated out-of-plane translation and the simulated in-plane rotation, respectively.

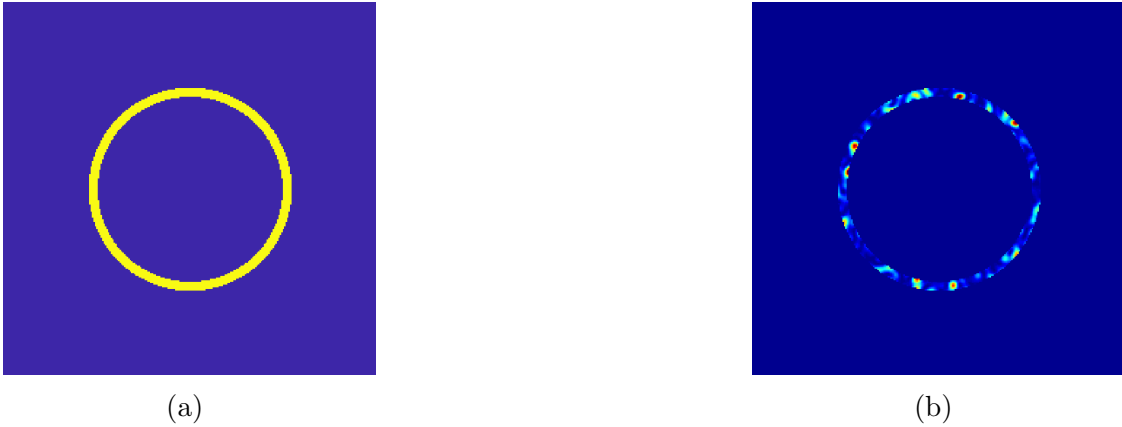


Figure 2.10: An example annular mask for radial isolation of the irradiance datasets (a) without speckle and (b) with speckle.

CHAPTER 3

Wave-Optics Simulation of Dynamic Speckle: II. In an Image Plane[†]

3.1 Background

Speckle plays a pivotal role in directed-energy applications. One cannot actively illuminate a distant object without also introducing speckle. Thus, directed-energy applications like long-range imaging [3, 4, 5, 6, 7], tracking [8, 9], wavefront sensing [10, 11], phase compensation [12, 13], and synthetic-aperture ladar [14, 15] depend on the presence of speckle to achieve their desired outcomes. Whenever possible, however, these applications also look to mitigate the effects of speckle in order to achieve the best possible performance.

Optically rough extended objects (i.e., where the surface roughness is on the order of the wavelength of light) diffusely scatter an incident laser beam to produce a speckled irradiance pattern. The associated speckles, in practice, appear as bright regions of constructive interference. Here, the average size of the speckles is roughly equal to a coherence cell from the scattering spot [16]. These speckles unfortunately act as a noise term that limit performance in the aforementioned directed-energy applications. What is more, different modes of extended-object motion serve to perpetuate this noise term on a frame-by-frame basis, due to the effects of dynamic speckle.

Speckle mitigation, in turn, has been an active area of research since the emergence of the laser itself [17]. For example, researchers often perform speckle averaging to mitigate the effects of dynamic speckle. To quantify the benefits of speckle

[†]This material was published previously as [57] in *Applied Optics* with coauthors M. F. Spencer, N. R. Van Zandt, and R. G. Driggers (<https://doi.org/10.1364/AO.427964>) © 2021 Optica Publishing Group. Users may use, reuse, and build upon the article, or use the article for text or data mining, so long as such uses are for non-commercial purposes and appropriate attribution is maintained. All other rights are reserved.

averaging, one can make use of the signal-to-noise ratio (SNR). In practice, the SNR is inversely proportional to the contrast ratio, C , such that

$$C = \frac{\sigma_I}{\bar{I}}, \quad (3.1)$$

where σ_I is the standard deviation of the speckled irradiance pattern and \bar{I} is the mean [17]. A fully developed speckled irradiance pattern (resulting from fully polarized/coherent light) follows a negative-exponential probability density function (PDF). In turn, C goes to unity [18]. Accumulating K patterns, as a result, decreases C to $1/\sqrt{K}$ as the PDF becomes more Gaussian like in accordance with the central-limit theorem. This last statement is only true if the individual speckled irradiance patterns are uncorrelated on a frame-by-frame basis [19]. From a systems-engineering perspective, it is therefore of great interest to accurately define when speckle decorrelation occurs, especially in the presence of dynamic speckle.

Given a fully developed speckle pattern, the real and imaginary parts of the underlying complex-optical field conform to a complex-circular Gaussian joint PDF [20]. Because of this inherent randomness, there are no deterministic solutions for the size of the speckles and thus for the speckle decorrelation. A general approach to this problem is to derive a correlation function that accounts for the lowest-order statistics of the complex-optical field at two different points in space [21]. Normalizing this function to its peak value yields an analytical irradiance correlation coefficient equal to one for overlapping points and equal to zero for separation by the width of the average size of the speckles. Displacing the speckled irradiance patterns by this distance decorrelates them in time, given some relationship between motion of the extended object and that of the dynamic speckle. Then at a known rate of change in extended-object position, the speckle decorrelation is predictable as a function of time. Through the years, a number of researchers have taken this approach, while many others have studied closely-related phenomena that one can easily recast in this manner.

Rigden and Gordon [22], Oliver [23] and Langmuir [24] were among the first scientists to report on dynamic speckle. Allen and Jones [25] offered an explanation of their results based on the diffraction of radio waves. Isenor [26] and Sporton [27] followed up by emphasizing the optical-system geometry and its impact on speckle dynamics in the image plane. Anisimov et al. [28] later derived space-time correlation statistics for the first time, and correlation experiments have been underway ever since [29, 30, 31, 32, 33, 34].

With this rich history in mind, this two-part paper demonstrates the use wave-optic simulations to model the effects of dynamic speckle. In Part II, we formulate closed-form expressions for the analytical irradiance correlation coefficient in the image plane of an optical system. Part I starts by formulating closed-form expressions for the analytical irradiance correlation coefficient in the pupil plane of an optical system. It is worthwhile to consider the image plane separately from the pupil plane, as the structure of speckle turns out to operate independently in each plane under most conditions of interest. In turn, this paper focuses solely on the theory and simulation of speckle decorrelation in the image plane of an optical system. Because image formation is of concern, the pupil plane (discussed throughout Part I) is equivalent to a plane of observation at some distance from the extended object in a free-space system. Here, this distance represents free-space propagation from the object plane to the entrance-pupil plane. A second free-space propagation then focuses the light from the exit-pupil plane to the image plane.

Broadly speaking, Part II aims to fulfill two main goals. The first goal is to establish closed-form expressions for the analytical irradiance correlation coefficient (associated with dynamic speckle in an image plane) for (1) the cases of square, circular, and Gaussian limiting apertures and (2) four different modes of extended-object motion: in-plane and out-of-plane translation, as well as in-plane and out-of-plane rotation. While meeting this goal does not demand any new theory per se, it does fill several gaps in the dynamic-speckle literature that would otherwise require some inference while compiling all of the closed-form expressions in a unified notation. It also frames many of these closed-form expressions for

the first time as straightforward functions of extended-object motion. The second main goal is to develop a simulation framework within which to study speckle decorrelation in terms of the the numerical irradiance correlation coefficient and thereafter compare the numerical results from simulation to the analytical results from theory.

In service of these goals, the following sections formulate the aforementioned closed-form expressions for the analytical irradiance correlation coefficient (cf. Sec. 3.2), the wave-optics simulations used to compute the numerical irradiance correlation coefficient (cf. Sec. 3.3), and the results that compare the analytical and numerical findings (cf. Sec. 3.4). Before moving on to the next section, it is important to note that we wrote Part II so that it complements Part I. In turn, both papers contain overlapping material. So as not to be redundant, this choice enables two things: (1) both papers read independently from each other (i.e., the reader does not have to read Part I in order to understand the results in Part II and vice versa), and (2) the reader can pull up Part I alongside Part II and compare and contrast the results without too much difficulty. As a result, this two-part paper demonstrates the use of wave-optics simulations to model the effects of dynamic speckle.

3.2 Analytical Irradiance Correlation Coefficient

In this section, we formulate closed-form expressions for the analytical irradiance correlation coefficient, $\mu_I(\mathbf{p}_1; \mathbf{p}_2)$. Strictly speaking, these formulations treat $\mu_I(\mathbf{p}_1; \mathbf{p}_2)$ as a measure of correlation between two points in a static-speckled irradiance pattern. In this way, $\mu_I(\mathbf{p}_1; \mathbf{p}_2)$ offers a sense of the average size of the speckles by solving for the spatial separation between two distinct points in space, \mathbf{p}_1 and \mathbf{p}_2 , at which speckle decorrelation occurs. The closed-form expressions formulated in this section are just as effective, however, at defining where speckle decorrelation occurs for dynamic-speckled irradiance patterns [32, 35, 36]. In practice, we can relate such

patterns to the dynamics induced by extended-object motion; thus, $\mu_I(\mathbf{p}_1; \mathbf{p}_2)$ is a useful construct for dynamic speckle, in addition to static speckle, hence the reason we use it in the analysis that follows.

Although speckle is by nature a self-interference effect with respect to the complex-optical field, it manifests as an irradiance measurement (in units of power per unit area) using modern-day optical detectors. Consequently, dynamic speckle involves a correlation function between two speckled irradiance patterns, $I_1(\mathbf{p})$ and $I_2(\mathbf{p})$. The relevant correlation function is

$$\begin{aligned} R_I(\mathbf{p}_1; \mathbf{p}_2) &= \langle I_1(\mathbf{p}_1) I_2(\mathbf{p}_2) \rangle \\ &= \langle U_1(\mathbf{p}_1) U_1^*(\mathbf{p}_1) U_2(\mathbf{p}_2) U_2^*(\mathbf{p}_2) \rangle, \end{aligned} \quad (3.2)$$

where $\langle \circ \rangle$ denotes an ensemble average, while \mathbf{p}_1 and \mathbf{p}_2 are again two distinct points in space. Supposing that the rough-surface scattering from the optically rough extended object lends enough independent phase contributions that the central-limit theorem applies, we model the complex-optical fields $U(\mathbf{p}_1)$ and $U(\mathbf{p}_2)$ as complex-circular Gaussian random variables [37]. In turn,

$$\begin{aligned} R_I(\mathbf{p}_1; \mathbf{p}_2) &= \langle I_1(\mathbf{p}_1) \rangle \langle I_2(\mathbf{p}_2) \rangle + |\langle U_1(\mathbf{p}_1) \rangle \langle U_2^*(\mathbf{p}_2) \rangle|^2 \\ &= \langle I_1(\mathbf{p}_1) \rangle \langle I_2(\mathbf{p}_2) \rangle + |J_U(\mathbf{p}_1; \mathbf{p}_2)|^2, \end{aligned} \quad (3.3)$$

where $J_U(\mathbf{p}_1; \mathbf{p}_2)$ is the mutual intensity between $U_1(\mathbf{p}_1)$ and $U_2(\mathbf{p}_2)$. The complex spatial coherence factor,

$$\mu_U(\mathbf{p}_1; \mathbf{p}_2) = \frac{J_U(\mathbf{p}_1; \mathbf{p}_2)}{\sqrt{J_U(\mathbf{p}_1; \mathbf{p}_1) J_U(\mathbf{p}_2; \mathbf{p}_2)}}, \quad (3.4)$$

is a normalization of mutual intensity having the property $0 \leq \mu_U \leq 1$. Substituting Eq. (3.4) into Eq. (3.3),

$$R_I(\mathbf{p}_1; \mathbf{p}_2) = \langle I_1(\mathbf{p}_1) \rangle \langle I_2(\mathbf{p}_2) \rangle [1 + |\mu_U(\mathbf{p}_1; \mathbf{p}_2)|^2]. \quad (3.5)$$

Equation (3.5) contains both DC and AC components, but it is the fluctuating AC term that carries meaningful information about the speckle decorrelation. Thus,

$$\mu_I(\mathbf{p}_1; \mathbf{p}_2) = |\mu_U(\mathbf{p}_1; \mathbf{p}_2)|^2 \quad (3.6)$$

is a fitting correlation coefficient with respect to irradiance that governs R_I . Also known as the Yamaguchi correlation factor [38], $\mu_I(\mathbf{p}_1; \mathbf{p}_2)$ is effectively a ratio of crosscorrelation to autocorrelation with reference to Eqs. (3.4) and (3.5).

3.2.1 Propagation From the Object Plane to the Image Plane

At this stage in the analysis, it is useful to introduce the rough-surface-scattering geometry proposed in this paper. Figure 3.1 illustrates this geometry as a single-lens system with the α - β , ξ - η , and x - y sets of axes placed within the object, pupil, and image planes, respectively. The respective radial coordinates are $\Omega = \sqrt{\alpha + \beta}$, $\varrho = \sqrt{\xi + \eta}$, and $r = \sqrt{x + y}$. A distance Z_1 along the z axis initially separates the object and entrance-pupil planes, whereas Z_2 is a fixed distance between the exit-pupil and image planes. Note that Z_1 is simply called Z in Part I. Also note that with the placement of a single lens between the object and image planes, the entrance and exit pupils are coplanar with the lens (which also serves as the aperture stop).

We position an optically rough extended object of width W in the object plane, a limiting aperture of width D in the pupil plane, and an observation screen with infinite field of view (for the time being) in the image plane. Each component starts off centered at the origin of its local coordinate system. Distances $\Delta\Omega$ and Δz are measures of in-plane and out-of-plane translation, respectively. The z axis and optical axis are collinear with the axis of in-plane rotation ($\Delta\vartheta$), while out-of-plane rotation ($\Delta\varphi$) occurs about some axis in the α - β plane. As the object moves under fully coherent illumination, the diffusely scattered speckled irradiance pattern changes and eventually decorrelates from its initial state. These changes are generally differ-

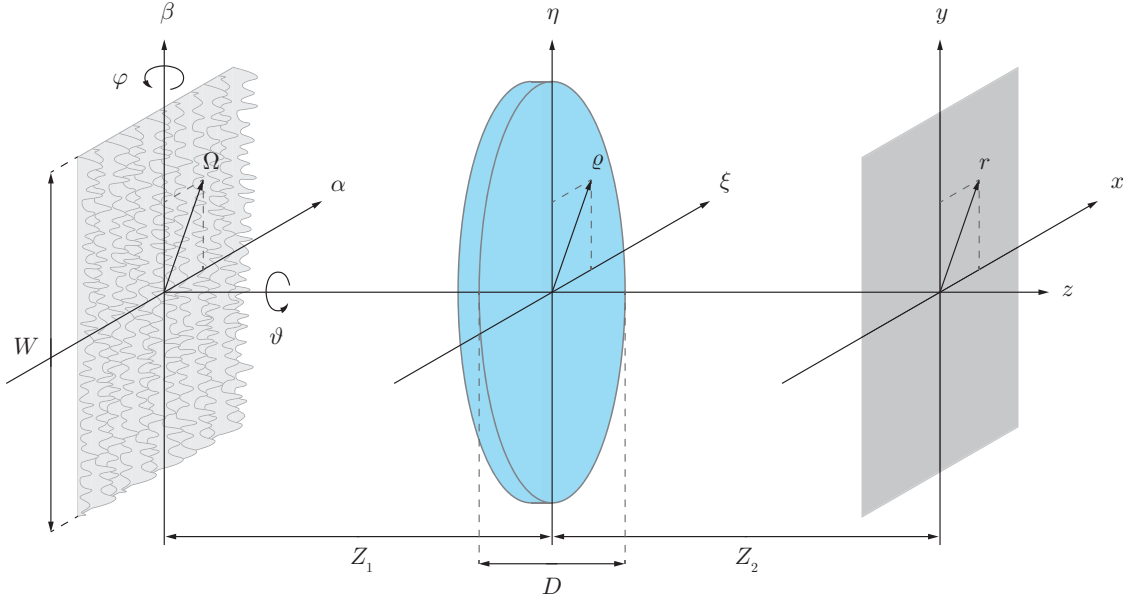


Figure 3.1: Free-space propagation from an optically rough extended object in the object plane to a limiting aperture in the pupil plane followed by another free-space propagation to an observation screen in the image plane.

ent in the pupil and image planes as the speckles propagate through the single-lens system. Moving forward we assume that both illumination and observation occur on axis (for ease of modeling). We also assume that deviations from theory (i.e., the closed-form expressions formulated in this section) are only appreciable for large angles of incidence and observation.

With Eqs. (3.4) and (3.6) in mind, recall that we can relate the analytical irradiance correlation coefficient, $\mu_I(\mathbf{p}_1; \mathbf{p}_2)$, to the mutual intensity, $J_U(\mathbf{p}_1; \mathbf{p}_2)$. What is more, we can use scalar diffraction theory to propagate $J_U(\mathbf{p}_1; \mathbf{p}_2)$ from plane to plane to determine $\mu_I(\mathbf{p}_1; \mathbf{p}_2)$ in the appropriate plane. For this purpose, if $U(\alpha, \beta)$ is the source field (i.e., the complex-optical field in the object plane), then the first Rayleigh–Sommerfeld diffraction integral predicts that

$$U(\xi, \eta) = \frac{Z_1}{j\lambda} \iint_{\Sigma} U(\alpha, \beta) \frac{\exp(jk\ell)}{\ell^2} ds \quad (3.7)$$

in the pupil plane. Here, λ is the optical wavelength, $k = 2\pi/\lambda$ is the angular wavenumber,

$$\ell = \sqrt{(\xi - \alpha)^2 + (\eta - \beta)^2 + Z_1^2} \quad (3.8)$$

is the Euclidean distance between points (α, β) and (ξ, η) , and ds is a differential surface element of source area Σ . This solution assumes that we satisfy the optical condition $\lambda \ll \ell$. In practice, Eq. (3.7) has the form of a superposition integral in terms of source field $U(\alpha, \beta)$ and free-space impulse response

$$h(\xi, \eta; \alpha, \beta) = \frac{Z_1 \exp(jk\ell)}{j\lambda\ell^2}. \quad (3.9)$$

Equation (3.9) notably depends only on the differences between points (α, β) and (ξ, η) , and this shift invariance constitutes an isoplanatic system so that Eq. (3.7) becomes a convolution between the source field and the impulse response [39].

To determine the mutual intensity, $J_U(\mathbf{p}_1; \mathbf{p}_2)$, in the pupil plane, we first define a generic point $\boldsymbol{\Omega} = (\alpha, \beta)$ within the object plane. In the vicinity of the pupil plane, \mathbf{p}_1 and \mathbf{p}_2 are points located at (ξ_1, η_1, Z_1) and $(\xi_1 + \Delta\xi, \eta_1 + \Delta\eta, Z_1 + \Delta z)$, respectively. Then Eq. (3.7) yields

$$\begin{aligned} J_U(\mathbf{p}_1; \mathbf{p}_2) &= \langle U(\mathbf{p}_1) U^*(\mathbf{p}_2) \rangle \\ &= \iint_{\Sigma_2} \iint_{\Sigma_1} \langle U(\boldsymbol{\Omega}_1) U^*(\boldsymbol{\Omega}_2) \rangle h(\mathbf{p}_1; \boldsymbol{\Omega}_1) h^*(\mathbf{p}_2; \boldsymbol{\Omega}_2) d^2\boldsymbol{\Omega}_1 d^2\boldsymbol{\Omega}_2 \quad (3.10) \\ &= \iint_{\Sigma_2} \iint_{\Sigma_1} J(\boldsymbol{\Omega}_1; \boldsymbol{\Omega}_2) h(\mathbf{p}_1; \boldsymbol{\Omega}_1) h^*(\mathbf{p}_2; \boldsymbol{\Omega}_2) d^2\boldsymbol{\Omega}_1 d^2\boldsymbol{\Omega}_2, \end{aligned}$$

so all that is left to define is the source mutual intensity $J(\boldsymbol{\Omega}_1; \boldsymbol{\Omega}_2)$ (i.e., the mutual intensity in the object plane).

According to Goodman [40], the scattered field immediately following an optically rough surface is delta correlated to a first approximation (above the scale of a wavelength). The resulting expression is

$$J_U(\boldsymbol{\Omega}_1; \boldsymbol{\Omega}_2) = \kappa U(\boldsymbol{\Omega}_1) U^*(\boldsymbol{\Omega}_2) \delta(\boldsymbol{\Omega}_1 - \boldsymbol{\Omega}_2), \quad (3.11)$$

where κ is some global loss factor. By the sifting property of the Dirac delta function, $\delta(\circ)$, Eqs. (3.10) and (3.11) combine as

$$J_U(\mathbf{p}_1; \mathbf{p}_2) = \kappa \iint_{\Sigma} |U(\boldsymbol{\Omega})|^2 h(\mathbf{p}_1; \boldsymbol{\Omega}) h^*(\mathbf{p}_2; \boldsymbol{\Omega}) d^2\boldsymbol{\Omega} \quad (3.12)$$

after setting $\boldsymbol{\Omega}_1 = \boldsymbol{\Omega}$ for simplicity.

Making the paraxial approximation (with respect to amplitude) that $\ell_1^2 \approx \ell_2^2 \approx Z_1^2$, the end result of Eqs. (3.4), (3.6), and (3.12) is

$$\mu_I(\mathbf{p}_1; \mathbf{p}_2) = \left| \frac{\iint_{\Sigma} |U(\boldsymbol{\Omega})|^2 \exp[jk(\ell_2 - \ell_1)] d^2\boldsymbol{\Omega}}{\iint_{\Sigma} |U(\boldsymbol{\Omega})|^2 d^2\boldsymbol{\Omega}} \right|^2. \quad (3.13)$$

Equation (3.14) reveals that the analytical irradiance correlation coefficient, $\mu_I(\mathbf{p}_1; \mathbf{p}_2)$, is a function of the source irradiance, $|U(\boldsymbol{\Omega})|^2$, as well as the observation points \mathbf{p}_1 and \mathbf{p}_2 .

Mathematically speaking, Eq. (3.13) accounts for speckle decorrelation in the pupil plane of the single-lens system described in Fig. 3.1. To account for speckle decorrelation in the image plane, we again use Eq. (3.13), but we first replace the source field $U(\boldsymbol{\Omega}) = U(\alpha, \beta)$, which gives rise to a scattering spot of width W , with a pupil function $P(\boldsymbol{\rho}) = P(\xi, \eta)$, which gives rise to a limiting aperture of width D . We also replace the object distance (Z_1) with the image distance (Z_2). In turn, \mathbf{p}_1 and \mathbf{p}_2 are points located at (x_1, y_1, Z_2) and $(x_1 + \Delta x, y_1 + \Delta y, Z_2 + \Delta z)$, respectively, such that in the vicinity of the image plane,

$$\mu_I(\mathbf{p}_1; \mathbf{p}_2) = \left| \frac{\iint_{\Sigma} |P(\boldsymbol{\rho})|^2 \exp[jk(\wp_2 - \wp_1)] d^2\boldsymbol{\rho}}{\iint_{\Sigma} |P(\boldsymbol{\rho})|^2 d^2\boldsymbol{\rho}} \right|^2, \quad (3.14)$$

where

$$\wp = \sqrt{(x - \xi)^2 + (y - \eta)^2 + Z_2^2}. \quad (3.15)$$

These replacements amount to treating the pupil plane as a new delta-correlated source [40], which Zernike first proposed as a means of applying coherence theory

to microscopy problems [58].

In effect, speckle decorrelation in the image plane is then independent of the scattering spot from which the pupil-plane speckles originate. Making this approximation requires that the scattering spot spans many coherence areas in the pupil plane and resolution cells in the object plane [16]. It also requires that lens aberrations do not drastically affect the structure of speckled irradiance pattern.

Much of the foundational work on speckle decorrelation applies a binomial approximation to a power-series expansion of the phasor argument of Eq. (3.14) prior to integrating. This final paraxial approximation (with respect to phase) ultimately gives rise to a scaled Fresnel diffraction integral, since replacing the impulse response with the well-known Fresnel propagation kernel effectively makes Eq. (3.14) a normalized Fresnel transform of $|P(\boldsymbol{\rho})|^2$ in two dimensions.

3.2.2 Four Different Modes of Extended-Object Motion

In what follows, we formulate closed-form expressions for the four different modes of extended-object motion proposed in this paper, including in-plane and out-of-plane translation and rotation. For this purpose, we need to first define a set of unit-amplitude pupil functions, $P(\boldsymbol{\rho}) = P(\xi, \eta)$. These functions take the following functional forms [41]:

$$P(\xi, \eta) = \text{rect}\left(\frac{\xi}{D}, \frac{\eta}{D}\right) = \text{rect}\left(\frac{\xi}{D}\right) \text{rect}\left(\frac{\eta}{D}\right), \quad (3.16)$$

where

$$\text{rect}(w) = \begin{cases} 1 & |w| < 1/2 \\ 1/2 & |w| = 1/2 \\ 0 & |w| > 1/2 \end{cases}; \quad (3.17)$$

$$P(\xi, \eta) = \text{cyl}\left(\frac{\sqrt{\xi^2 + \eta^2}}{D}\right), \quad (3.18)$$

where

$$\text{cyl}(\rho) = \begin{cases} 1 & 0 \leq \rho < 1/2 \\ 1/2 & \rho = 1/2 \\ 0 & \rho > 1/2 \end{cases} ; \quad (3.19)$$

and

$$P(\xi, \eta) = \text{Gaus} \left(\frac{\sqrt{\xi^2 + \eta^2}}{\sqrt{\pi}D/2} \right), \quad (3.20)$$

where

$$\text{Gaus}(\rho) = \exp(-\pi\rho^2). \quad (3.21)$$

Here, Eqs. (3.16) and (3.17) give rise to a square limiting aperture of width D , Eqs. (3.18) and (3.19) give rise to a circular limiting aperture of diameter D , and Eqs. (3.20) and (3.21) gives rise to a Gaussian limiting aperture of 1/e-amplitude diameter D .

Moving forward, we also need to define the following special functions:

$$\text{sinc}(w) = \frac{\sin(\pi w)}{\pi w}, \quad (3.22)$$

$$\text{somb}(\rho) = 2 \frac{J_1(\pi\rho)}{\pi\rho}, \quad (3.23)$$

$$\text{Fres}(w) = \frac{S^2(w) + C^2(w)}{w^2}, \quad (3.24)$$

$$\text{tri}(w) = \begin{cases} 1 - |w| & |w| < 1 \\ 0 & |w| \geq 1 \end{cases}, \quad (3.25)$$

and

$$\text{chat}(\rho) = \begin{cases} \frac{2}{\pi} \left[\arccos(\rho) - \rho\sqrt{1-\rho^2} \right] & \rho < 1 \\ 0 & \rho \geq 1 \end{cases}. \quad (3.26)$$

Here, $J_1(\circ)$ is a first-order Bessel function of the first kind (not to be confused with mutual intensity), while $S(\circ)$ and $C(\circ)$ are, respectively, the Fresnel sine and cosine integrals [39]. These special functions readily show up in the closed-form expressions that follow for in-plane and out-of-plane translation and rotation of

the object. Furthermore, these special functions [cf. Eqs. (3.20)-(3.26)] readily provide cutoff/rolloff conditions. Such conditions define what we mean by speckle decorrelation in the image plane and offer a sense of the average size of the image-plane speckles.

In-Plane Translation

Assuming in-plane translation of the object (cf. Fig. 3.1), Table 3.1 provides closed-form expressions for the analytical irradiance correlation coefficient, $\mu_I(\Delta\Omega)$, for all three limiting apertures (i.e., square, circular, and Gaussian) with corresponding cutoff/rolloff conditions, $\Delta\Omega_{c/r}$. Here, $\Delta\Omega$ is the in-plane translation distance. It is important to note that both the square and circular limiting apertures give rise to distinct cutoff conditions (i.e., the special functions go to zero at $\Delta\Omega_c$), whereas the Gaussian limiting aperture gives rise to a rolloff condition (i.e., the special function never reaches zero but has a $1/e^2$ magnitude at $\Delta\Omega_r$).

To formulate the closed-form expressions given in Table 3.1, we set Δz to zero

Table 3.1: Closed-form expressions for in-plane translation.

aperture shape	irradiance correlation coefficient	cutoff/rolloff condition
square	$\mu_I(\Delta\Omega) = \text{sinc}^2\left(\frac{D\Delta\Omega}{\lambda Z_1}\right)$	$\Delta\Omega_c = \frac{\lambda Z_1}{D}$
circle	$\mu_I(\Delta\Omega) = \text{somb}^2\left(\frac{D\Delta\Omega}{\lambda Z_1}\right)$	$\Delta\Omega_c = \frac{1.22\lambda Z_1}{D}$
Gaussian	$\mu_I(\Delta\Omega) = \text{Gaus}\left(\frac{\sqrt{\pi}D\Delta\Omega}{2\lambda Z_1}\right)$	$\Delta\Omega_r = \frac{\sqrt{8}\lambda Z_1}{\pi D}$

in Eq. (3.14), such that point \mathbf{p}_2 is at $(x_1 + \Delta x, y_1 + \Delta y, Z_2)$. The radial distance between points of observation in the image plane is then $\Delta r = \sqrt{\Delta x^2 + \Delta y^2}$, which corresponds directly to an in-plane object translation of $\Delta\Omega = \sqrt{\Delta\alpha^2 + \Delta\beta^2}$ after accounting for magnification. Thus, by substituting Δr with $\Delta\Omega$ and Z_2 with Z_1

after integration, the analytical irradiance correlation coefficient, $\mu_I(\Delta\Omega)$, becomes a function of the in-plane translation distance, $\Delta\Omega$, and object distance, Z_1 . In so doing, we neglect the effects of boiling as we introduce new speckles into the limiting aperture. This assumption is valid as long as the limiting aperture is larger than the speckles it produces in the image plane.

To make these aforementioned substitutions, one can relate speckle decorrelation in the image plane to a concept known as memory loss, which Cloud describes as the physical movement of a speckled irradiance pattern beyond its original boundaries in any direction [59]. Put another way, the single-lens system described in Fig. 3.1 becomes anisoplanatic with varying shifts. Such shifts give rise to speckle decorrelation in the image plane.

As shown in Part I, only the wavelength, propagation distance, and scattering-spot width can alter the average size of the pupil-plane speckles, and this size determines what we mean by speckle decorrelation in the pupil plane. Image-plane speckles, on the other hand, are roughly the size of a resolution element (a.k.a. “resel”) in the image plane [60]. The average size of the image-plane speckles, again, determines what we mean by speckle decorrelation in the image plane. However, to relate any extended-object motion in the image plane to that in the object plane, we must project the image of the object into object space. For this reason, a shift by a resel on the object (i.e., the conjugate of a resel in the image) is what causes total decorrelation with in-plane translation [61].

With a square limiting aperture, for example, the width of a resel (and therefore the average size of the speckles in the image plane [60]) is

$$\begin{aligned} s_{\text{img}} &= \frac{\lambda Z_2}{D_{\text{XP}}} \\ &= \lambda F_w. \end{aligned} \tag{3.27}$$

Here, D_{XP} is the exit-pupil diameter, $F_w = F(1 + |M|/M_p)$ is the working focal ratio, $F = f_e/D_{\text{EP}}$ is the uncorrected focal ratio, f_e is the effective focal length, D_{EP} is the entrance-pupil diameter, M is the transverse magnification, and M_p is the

pupillary magnification [62, 63, 64]. The resel size on the object is then

$$\begin{aligned} s_{\text{obj}} &= \frac{\lambda Z_1}{D_{\text{EP}}} \\ &= \lambda F_w / |M|. \end{aligned} \tag{3.28}$$

In writing Eqs. (3.27) and (3.28), note that we have assumed the use of an aberration-free, focused imaging system. Also note that with a single-lens system (cf. Fig. 3.1), $f_e = f$ and $D_{\text{XP}} = D_{\text{EP}} = D$. However, one can replace Z_1/D with $F_w/|M|$ to evaluate speckle decorrelation in a generalized imaging system.

For a square or circular limiting aperture of width or diameter D , the cutoff condition, $\Delta\Omega_c$, corresponds to the average lateral resel on the object. If dealing with an oblong rectangular aperture, things become separable in the horizontal and vertical directions (using different values for D). These findings agree with published results [42, 43].

For a Gaussian limiting aperture of 1/e-amplitude diameter D , the rolloff condition, $\Delta\Omega_r$, is consistent with Goodman's theory [16]. The resulting equation is only valid over small translation distances [44], as are all other Gaussian functions presented in this paper. Such analytical curves decrease monotonically out to infinity, when in practice there are oscillatory outer lobes (as with previous expressions), due to periodic overlap of speckles with large translation distances [45]. Moreover, these analytical curves decay asymptotically, which means there is no zero crossing at which to naturally define the average lateral size of the speckles. Instead, the $1/e^2$ point serves as a correlation rolloff condition rather than a cutoff condition. What matters for comparison with discrete irradiance datasets from wave-optics simulations (or experiments) is that there is consistency with theory at least up to this rolloff condition. Here, we consider soft Gaussian apertures, noting that such apertures use apodization filters to allay the strong diffraction effects associated with hard edges [65].

Out-of-Plane Translation

Assuming out-of-plane translation of the object (cf. Fig. 3.1), Table 3.2 provides closed-form expressions for the analytical irradiance correlation coefficient, $\mu_I(\Delta z)$, for all three limiting apertures (i.e., square, circular, and Gaussian) with corresponding cutoff/rolloff conditions, $\Delta z_{c/r}$. Here, Δz is the out-of-plane translation distance. It is important to note that both the square and circular limiting apertures give rise to distinct cutoff conditions (i.e., the special functions go to zero or a minimum at Δz_c), whereas the Gaussian limiting aperture gives rise to a rolloff condition (i.e., the special function has a $1/e^2$ magnitude at Δz_r).

To formulate the closed-form expressions given in Table 3.2, $\Delta \varrho$ is set to zero

Table 3.2: Closed-form expressions for out-of-plane translation.

aperture shape	irradiance correlation coefficient	cutoff/rolloff condition
square	$\mu_I(\Delta z) = \text{Fres}^2\left(\frac{D}{Z_1}\sqrt{\frac{\Delta z}{2\lambda}}\right)$	$\Delta z_c = 7.31\lambda\left(\frac{Z_1}{D}\right)^2$
circle	$\mu_I(\Delta z) = \text{sinc}^2\left[\frac{\Delta z}{8\lambda}\left(\frac{D}{Z_1}\right)^2\right]$	$\Delta z_c = 8\lambda\left(\frac{Z_1}{D}\right)^2$
Gaussian	$\mu_I(\Delta z) = \left\{1 + \left[\frac{\pi D^2 \Delta z}{8\lambda Z_1(Z_1 + \Delta z)}\right]^2\right\}^{-1}$	$\Delta z_r = \frac{Z_1}{0.155D^2/(\lambda Z_1) - 1}$

in Eq. (3.14) for out-of-plane translation, confining point \mathbf{p}_2 to $(x_1, y_1, Z_2 + \Delta z)$. Thus, for a single-lens system and out-of-plane translation, one can substitute Z_2 with Z_1 after integration, and the analytical irradiance correlation coefficient, $\mu_I(\Delta z)$, becomes a function of the object distance, Z_1 .

Analogous to the relationship between in-plane translation and the average lateral resel on the object, the cutoff/rolloff conditions given in Table 3.2 estimate the average longitudinal resel on the object. In turn, the average size of the longitudinal image-plane speckles is proportional to $\lambda(Z_2/D_{\text{xp}})^2$, or more generally λF_w^2 . A detail worth mentioning is that although off-axis observation can change

the behavior of the speckle decorrelation in the pupil plane, as shown in Part I, it has very little influence on the behavior of the speckle decorrelation in the image plane [66]. Another detail worth mentioning is that Eq. (3.24) does not cross zero but rather decreases to a minimum value of 6.65×10^{-3} before increasing again.

In-Plane Rotation

Assuming in-plane rotation of the object (cf. Fig. 3.1), Table 3.3 provides closed-form expressions for the analytical irradiance correlation coefficient, $\mu_I(\Delta\vartheta)$, for all three limiting apertures (i.e., square, circular, and Gaussian) with corresponding cutoff/rolloff conditions, $\Delta\vartheta_{c/r}$. Here, $\Delta\vartheta$ is the in-plane rotation angle. It is important to note that both the square and circular limiting apertures give rise to distinct cutoff conditions (i.e., the special functions go to zero at $\Delta\vartheta_c$), whereas the Gaussian limiting aperture gives rise to a rolloff condition (i.e., the special function has a $1/e^2$ amplitude at $\Delta\vartheta_r$).

In essence, in-plane rotation is an extension of in-plane translation (cf.

Table 3.3: Closed-form expressions for in-plane rotation.

aperture shape	irradiance correlation coefficient	cutoff/rolloff condition
square	$\mu_I(\Delta\vartheta) = \text{sinc}^2\left(\frac{D\Delta\vartheta r}{\lambda Z_1}\right)$	$\Delta\vartheta_c = \frac{\lambda Z_1}{Dr}$
circle	$\mu_I(\Delta\vartheta) = \text{somb}^2\left(\frac{D\Delta\vartheta r}{\lambda Z_1}\right)$	$\Delta\vartheta_c = \frac{1.22\lambda Z_1}{Dr}$
Gaussian	$\mu_I(\Delta\vartheta) = \text{Gaus}\left(\frac{\sqrt{\pi}D\Delta\vartheta \varrho}{2\lambda Z_1}\right)$	$\Delta\vartheta_r = \frac{\sqrt{8}\lambda Z_1}{\pi Dr}$

Sec. 3.2.2), given a circular path around the rotational axis. Accordingly, we can substitute arc length $\Delta\vartheta r$ for linear distance, $\Delta\Omega$. Doing so produces the relationships given in Table 3.3.

Similar to the pupil-plane expressions (cf. Part I), the closed-form expressions

in this case vary with radial vantage point $r = \sqrt{x + y}$. Churnside's work confirms these expressions after appropriate simplifications [47], as does further analysis by Yura et al. [48]. Saleh makes the point that in-plane rotation at sufficiently large angles warrants the inclusion of a sinusoidal argument factor to account for periodic replication of the signal in time [29]. A detail worth mentioning is that the on-axis correlation is unity with a cutoff/rolloff condition of infinity, since $r = 0$. This result is physically accurate, since the speckle at the very center of rotation remains stationary, independent of in-plane rotation $\Delta\vartheta$.

Out-of-Plane Rotation

Assuming out-of-plane rotation of the object (cf. Fig. 3.1), Table 3.4 provides closed-form expressions for the analytical irradiance correlation coefficient, $\mu_I(\Delta\varphi)$, for all three limiting apertures (i.e., square, circular, and Gaussian) with corresponding cutoff/rolloff conditions, $\Delta\varphi_{c/r}$. Here, $\Delta\varphi$ is the out-of-plane rotation angle. It is important to note that both the square and circular limiting apertures give rise to distinct cutoff conditions (i.e., the special functions go to zero at $\Delta\varphi_c$), whereas the Gaussian limiting aperture gives rise to a rolloff condition (i.e., the special function has a $1/e^2$ magnitude at $\Delta\varphi_r$).

In essence, out-of-plane rotation is a unique case of extended-object motion.

Table 3.4: Closed-form expressions for out-of-plane rotation.

aperture shape	irradiance correlation coefficient	cutoff/rolloff condition
square	$\mu_I(\Delta\varphi) = \text{tri}^2\left(\frac{2Z_1\Delta\varphi}{D}\right)$	$\Delta\varphi_c = \frac{D}{2Z_1}$
circle	$\mu_I(\Delta\varphi) = \text{chat}^2\left(\frac{2Z_1\Delta\varphi}{D}\right)$	$\Delta\varphi_c = \frac{D}{2Z_1}$
Gaussian	$\mu_I(\Delta\varphi) = \text{Gaus}\left(\frac{4Z_1\Delta\varphi}{\sqrt{\pi}D}\right)$	$\Delta\varphi_r = \frac{D}{\sqrt{8}Z_1}$

Here, the same set of scatterers occupies the scattering spot within the object plane over a small range of angles. For this reason, the object never moves by a resel in any direction and therefore no speckle decorrelation occurs by memory loss. Cloud's other criterion for speckle decorrelation [59], which says that the phase difference across a resel attains a value of 2π , comes into play now. For example, in terms of object-plane tilt, one can apply a phase change of $\phi = k\Delta\varphi\Omega$ across the optically rough surface in a transmission geometry. The reflection geometry instead requires $\phi = 2k\Delta\varphi\Omega$. As such, one can set the radial difference $\Delta\Omega$ equal to the resel width $\lambda Z_1/D$ and solve for $\Delta\phi = 2\pi$. The out-of-plane rotation angle $\Delta\varphi$ then prompts a cutoff of $D/(2Z_1)$, which proves to be consistent with theory [67, 68].

Marron and Morris studied this problem in the case of rotating objects, deriving a spatio-temporal correlation function with an envelope that follows the analytical irradiance correlation coefficient as a function of rotation angle [67]. The derivation involves propagating mutual intensity through to the image plane, making similar arguments to those preceding Eq. (3.14). Rather than convolve with the free-space impulse response, however, the convolution is between object-plane mutual intensity and the coherent point spread function (PSF) of the imaging system. A rectangular aperture generates the normalized PSF

$$h(x, y; \alpha, \beta) = \text{sinc} \left[\frac{D}{\lambda} \left(\frac{x}{Z_2} - \frac{\alpha}{Z_1} \right), \frac{D}{\lambda} \left(\frac{y}{Z_2} - \frac{\beta}{Z_1} \right) \right], \quad (3.29)$$

whereas

$$h(r; \Omega) = \text{somb} \left[\frac{D}{\lambda} \left(\frac{r}{Z_2} - \frac{\Omega}{Z_1} \right) \right] \quad (3.30)$$

corresponds to a circular aperture, and

$$h(r; \Omega) = \exp \left\{ - \left[\frac{\pi D}{2\lambda} \left(\frac{r}{Z_2} - \frac{\Omega}{Z_1} \right) \right]^2 / 2 \right\} \quad (3.31)$$

to a Gaussian aperture. In turn, convolution with either Eq. (3.29), (3.30) or (3.31) yields the appropriate result for whichever limiting aperture is under consideration. Table 3.4 lists these results, where the first two entries are squared-triangular and

circular-triangular functions, respectively [69].

The closed-form expressions in Table 3.4 are in line with familiar forms of the modulation transfer function (MTF) for equivalent incoherent systems [70]. Taking the squared magnitude of the coherent PSF is an equivalent operation to autocorrelating the pupil function, which determines the MTF of an incoherent system. The second column of Table 3.4 represents an angular cutoff beyond which speckle fully decorrelates, though this is not the same cutoff that describes the coherent spatial-frequency modulation limit [71]. Total decorrelation takes place once the speckles in the pupil plane translate by the aperture width and a new, independent realization takes its place. As a side note, the cutoff in a coherent transmission geometry is twice that of a reflection geometry due to the single pass in optical path length.

3.2.3 Analytical Exploration

Figure 3.2 plots the closed-form expressions formulated in Tables 3.1–3.4. In particular, Fig. 3.2(a) plots the case of in-plane translation (cf. Table 3.1), Fig. 3.2(b) plots the case of out-of-plane translation (cf. Table 3.2), Fig. 3.2(c) plots the case of in-plane rotation (cf. Table 3.3), and Fig. 3.2(d) plots the case of out-of-plane rotation (cf. Table 3.4). All plots include the respective cutoff conditions for square and circular limiting apertures and the rolloff conditions for Gaussian limiting apertures.

3.3 Numerical Irradiance Correlation Coefficient

All of the closed-form expressions formulated in Sec. 3.2 make use of continuous speckled irradiance patterns, $I_1(\mathbf{p})$ and $I_2(\mathbf{p})$. In this section, we make use of discrete irradiance datasets, I_1 and I_2 , from wave-optics simulations (or experiments). With this last point in mind, the numerical irradiance correlation coefficient, $\hat{\mu}_I$,

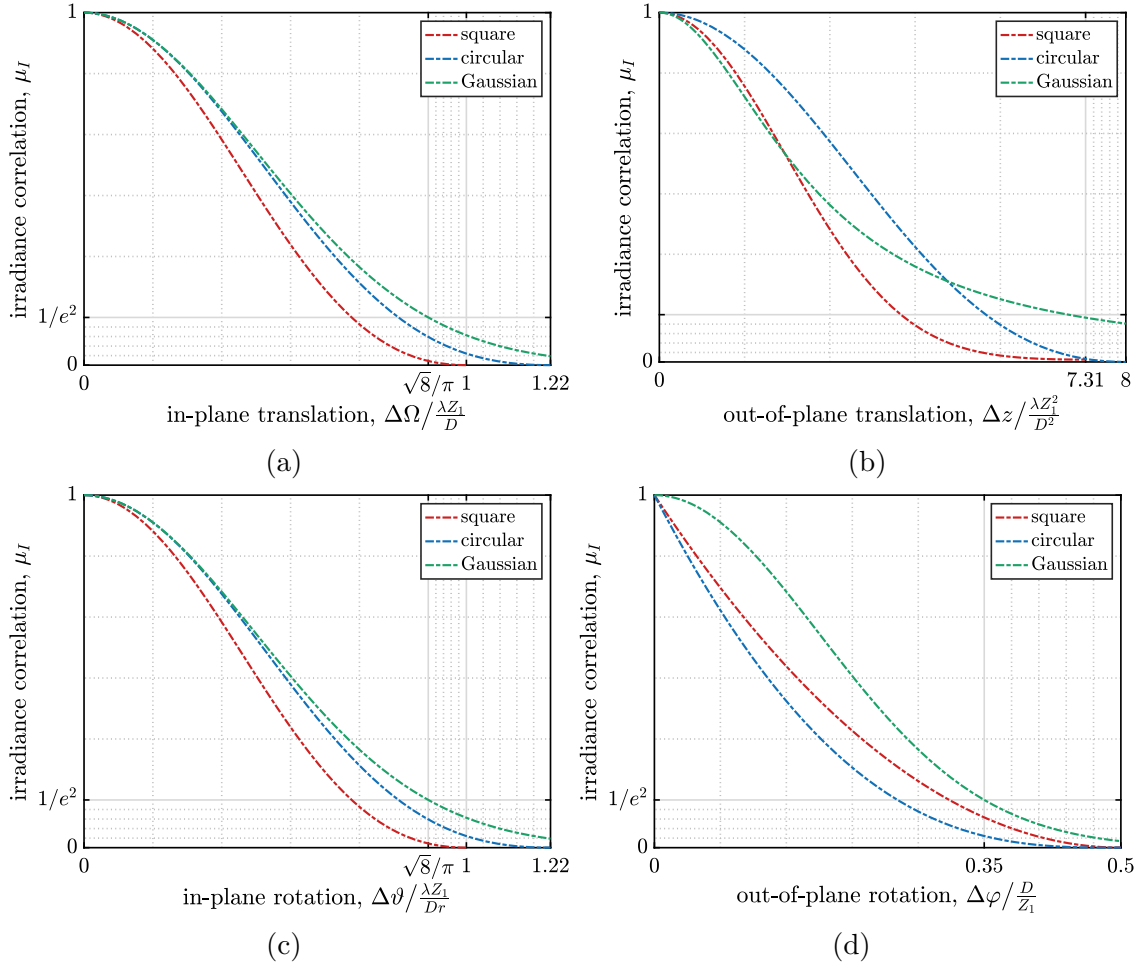


Figure 3.2: Analytical exploration of the trade space in terms of the four different modes of extended-object motion.

takes the following form:

$$\hat{\mu}_I = \frac{\langle I_1 I_2 \rangle - \langle I_1 \rangle \langle I_2 \rangle}{\sqrt{\langle (I_1 - \langle I_1 \rangle)^2 \rangle \langle (I_2 - \langle I_2 \rangle)^2 \rangle}}, \quad (3.32)$$

where $\langle \circ \rangle$ denotes an arithmetic mean. Equation (3.32) turns out to be equivalent to calculating the Pearson's correlation coefficient for a sample [50], which applies to Gaussian random processes. Thus, similar to its analytical counterpart, $\hat{\mu}_I$ is a useful construct for dynamic speckle and we use it in the analysis that follows.

With Eq. (3.32) in mind, the wave-optics simulations setup in this section make use of the following procedure.

1. Create an optically rough extended object using a phase-screen approach.
2. Propagate from the object plane to the image plane.
3. Crop the irradiance dataset I_1 and save for reference.
4. Modify the optically rough extended object with the appropriate mode of extended-object motion.
5. Repeat as necessary, saving the frame-to-frame irradiance dataset I_2 .
6. Calculate the numerical irradiance correlation coefficients as a function of extended-object motion.

To illustrate steps 1–3, Fig. 3.3 displays example irradiance and phase datasets. These wave-optics simulations make use of the WaveProp Toolbox for MATLAB [51].

3.3.1 Simulating Propagation From the Object Plane to the Image Plane

Analogous to Fig. 3.1, Fig. 3.4 depicts the imaging system simulated in the wave-optics simulations. These wave-optics simulations used an $N \times N$ grid resolution with $N = 512$. This choice provided an acceptable balance between physical accuracy and computational efficiency [52]. The wave-optics simulations also made use

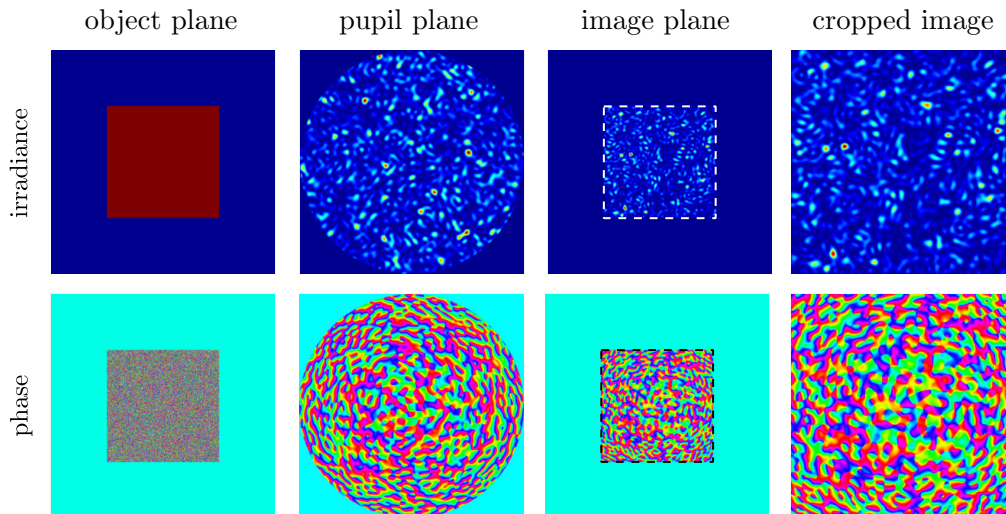


Figure 3.3: Example irradiance and phase datasets from the wave-optics simulations

of a free-space wavelength of $\lambda_0 = 1 \mu\text{m}$ and a limiting-aperture width/diameter of $D = 30 \text{ cm}$, which are typical values for long-range propagation studies.

For simplicity, the wave-optics simulations used unity scaling between the simulated object and pupil planes. They also used 200 grid points across the aperture diameter, while padding the circular pupil with zeros to exceed the recommended factor of 2.4 [53]. As such, the grid spacing, δ , was 1.5 mm, and the grid side length, S , was 76.8 cm. Critical sampling [54] (a.k.a. Fresnel scaling [51]) then stipulated that

$$N = \frac{S^2}{\lambda Z}. \quad (3.33)$$

Satisfying critical sampling typically gives wave-optics results that are free of aliasing. However, the high spatial frequencies contained in diffuse speckle made the wave-optics simulations especially prone to aliasing even with Eq. (3.33) satisfied. Tailored methods such as pupil-plane filtering [55] aim to combat this problem by eliminating the high spatial frequencies that would cause aliasing. Nonetheless, empirical evidence suggests that first doubling the grid resolution, then propagating the field (via the impulse-response method [54]) and cropping back down has greater resistance to aliasing [51]. Taking this approach, we set $Z = 2.30 \text{ km}$.

Recalling that the scattering-spot (square-only) width W varies inversely with

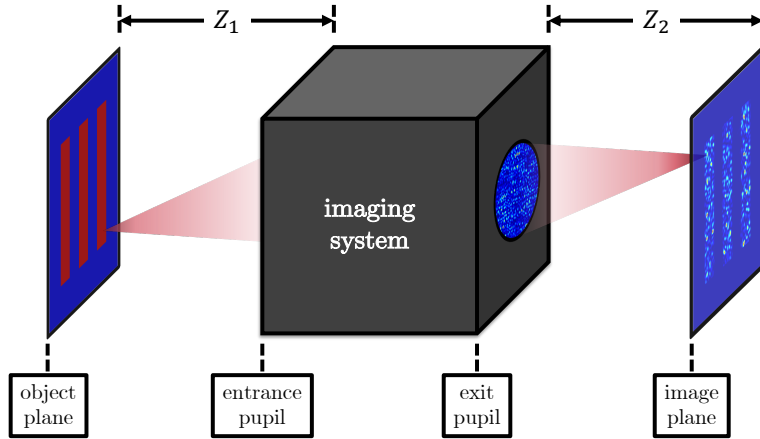


Figure 3.4: Illustration of the imaging system simulated in the wave-optics simulations. Here, we use an optically rough three-bar object (for illustrative purposes).

speckle size, it cannot be so large as to cause insufficient sampling of the speckle in the simulated pupil plane. As a result, we set $W = 30.7$ cm, so that the object Fresnel number, $N_{\text{obj}} = DW/(\lambda Z)$, was 40. This choice populated the pupil plane with roughly 40 speckles across D (cf. Fig. 3.3), yielding five grid points per speckle for an average pupil-plane error of $<1\%$ [9, 10]. In the pupil plane, we used two thin-lens transmittance functions to collimate the light after propagation from the object plane to the entrance pupil and focus the light upon propagation from the exit pupil to the image plane (cf. Fig. 3.4). Unity scaling, in turn, dictated that $Z_1 = Z_2 = Z$, which gave rise to unit-magnification imaging in the wave-optics simulations. Table 3.5 summarizes all of the parameters of interest in the wave-optics simulations.

3.3.2 Simulating Four Different Modes of Extended-Object Motion

To simulate an optically rough extended object, we used a phase-screen approach [16, 9, 10]. In so doing, we assumed that the surface heights were uniformly distributed and delta correlated from grid point to grid point. At each grid point within the scattering spot, we then took a random draw from a uniform phase distribution on the interval $[-\pi, \pi)$ and examined four different modes of

Table 3.5: Parameters of interest in the wave-optics simulations.

	parameter	value(s)
general	grid resolution, $N \times N$ [px]	512×512
	grid spacing, δ [mm]	1.50
	grid side length, S [cm]	76.8
system	illumination wavelength, λ [μm]	1.00
	propagation distance, Z [km]	2.30
	limiting-aperture width/diameter, D [cm]	30.0
object	object Fresnel number, N_{obj}	40
	scattering-spot width, W [cm]	30.7

extended-object motion.

Simulating In-Plane Translation

Simulating in-plane translation required that we move the phase screen laterally across the scattering spot. Since the phase-screen approach used in this paper assumed that the surface heights were uniformly distributed and delta correlated from grid point to grid point, we set the minimum in-plane translation distance to a single grid point of motion between each captured frame. Implementing in-plane translation in this way involved a circular shift of the phase screen in one direction. Since the object width, W , was considerably smaller than the grid side length S , the resultant scattering spot had zero magnitude (or near-zero magnitude in the case of a Gaussian scattering spot) near the edges of the grid. Thus, the phase wraparound resulting from a small circular shift did not affect the phase screen's frame-to-frame randomness.

Simulating Out-of-Plane Translation

Out-of-plane translation was perhaps the most laborious mode of extended-object motion to simulate properly, as it required a different propagation distance between the simulated object and pupil planes for each successive value of Δz . This

outcome meant that we inevitably violated critical sampling [cf. Eq. (3.33)] as we moved the simulated object plane closer to the simulated pupil plane. Varying this propagation distance also changed the image size and added some defocus, meaning we had to recrop and downsample each speckled image (for comparison with the original) as the object moved closer to the pupil plane. Nonetheless, we empirically determined that the wave-optics simulations were robust against the effects of aliasing and resampling for all values of Δz .

Simulating In-Plane Rotation

To simulate in-plane rotation, we applied a rotation matrix at the specified angle $\Delta\vartheta$. We also applied nearest-neighbor interpolation. In turn, we observed reasonable rotation in the resulting dynamic speckle (as expected) without a noticeable loss of fidelity.

The simulated in-plane rotation exhibited a radial dependence, as discussed in the Appendix. In turn, masking the irradiance datasets restricted the viewing region to a certain radius in order to calculate the numerical irradiance correlation coefficient [cf. Eq. (3.32)]. These masks were of the same thickness as the size of the speckles, where speckle size was defined by the cutoff/rolloff conditions given in Table 3.3.

Simulating Out-of-Plane Rotation

Simulation of out-of-plane rotation involved multiplying the simulated object plane by the following complex reflectance function:

$$\mathcal{R}(\alpha, \beta) = \exp [j2k (\Delta\varphi_\beta\alpha + \Delta\varphi_\alpha\beta)]. \quad (3.34)$$

Here, we decomposed the tilt angle into rotations about the α and β axes. This decomposition accounted for the change in optical path length, given the

small-angle approximation.

3.3.3 Numerical Exploration

In the next section, we compare the results obtained for the numerical irradiance correlation coefficient to those obtained for the analytical irradiance correlation coefficient. To do so, we need to perform Monte Carlo averaging on the numerical results. To explore this numerical trade space, we use root-mean-square error (RMSE), such that

$$\text{RMSE} = \sqrt{\frac{1}{n} \sum_{i=1}^n [\hat{\mu}_I(i) - \mu_I(i)]^2}. \quad (3.35)$$

Here, i is an iterator over the number of Monte-Carlo trials n , $\hat{\mu}_I$ is the numerical irradiance correlation coefficient from simulation, and μ_I is the analytical correlation coefficient from theory.

Figure 3.5 plots Eq. (3.35) to find that the average RMSE becomes asymptotically stable in the neighborhood of 40 Monte Carlo trials. Choosing this number keeps the error below $\sim 1\%$. Note that the average RMSE results displayed in Fig. 3.5 are fairly representative for all four modes of extended-object motion. Also note that we averaged over 100 realizations at each datapoint for curve-smoothing purposes.

3.4 Analytical and Numerical Results

Figures 3.6–3.9 provide the analytical and numerical results for this paper. Overall, the analytical results from theory are in agreement with the numerical results from simulation. With this agreement in mind, we discuss the four different modes of extended-object motion in the following list.

1. Figure 3.6 shows the analytical and numerical results for *in-plane translation* (also see Visualization 1). Here, the data-point sampling follows from the

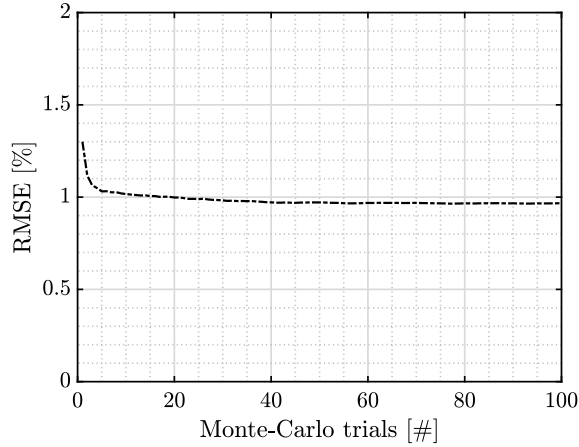


Figure 3.5: Numerical exploration in terms of the average RMSE versus the number of Monte-Carlo trials.

fact that we set the minimum in-plane translation distance to a single grid point of motion between each captured frame. Future efforts could look at using interpolation to increase this sampling. However, doing so could violate the assumptions used throughout this paper; in particular, that the optically rough surface is delta correlated to a first approximation.

2. Figure 3.7 shows the the analytical and numerical results for *out-of-plane translation* (also see Visualization 2). Recalling that speckle decorrelation of this kind does not change significantly with off-axis observation in the image plane, we analyzed the entire speckled irradiance datasets without any masking. This approach provided good agreement between analytical and numerical results, but one could use annular masks, which we illustrate in the Appendix, and derive nonlinear scale factors using Ref. [43] to modify the closed-form expressions presented in Table 3.2 for even greater accuracy.
3. Figure 3.8 shows the analytical and numerical results for *in-plane rotation* (also see Visualization 3). Here, we show results for several values of r relative to some position R . To calculate numerical results for off-axis observation, we made use of an annular mask, which we illustrate in Fig. 3.10 in the Appendix.

The closed-form expressions in Table 3.3 are set up to handle off-axis observation, where $r \neq 0$. Moreover, we observe the off-axis speckle at relative rather than absolute radial positions because the speckle decorrelation is linear with radial position.

4. Figure 3.9 shows the analytical and numerical results for *out-of-plane rotation* (also see Visualization 4). These results have unique functional forms because the decorrelation occurs by dephasing rather than by memory loss. Out-of-plane rotation is the only case where the speckles from either a square or a circular aperture fully decorrelate at the same cutoff condition.

The data points in Figs. 3.6–3.9 also indicate ± 1 standard deviation about the Monte Carlo average (i.e., the average with respect to 40 Monte-Carlo trials). A general observation is that these standard deviations seem to grow with increasing extended-object motion, which is not surprising. Even so, the error bars maintain an upper bound of $\sim 3\%$; thus, the Monte-Carlo averaging did not dramatically affect the mean result for any one trial. Before moving on to the next section, it is important to note that Visualizations 1–4 help in comprehending the results presented in this section. These visualizations show results for a square scattering spot and circular limiting aperture. This particular setup is common between Parts I and II of this two-part paper. Thus, we include both pupil and image planes in these visualizations, so that the results presented here complement those contained in Part I and vice versa.

Note: Annular Masks

The simulated in-plane rotation exhibited a radial dependence. Thus, masking the irradiance datasets restricted the viewing region to a certain radius in order to calculate the numerical irradiance correlation coefficient [cf. Eq. (3.32)]. On-axis observation simply required a circular mask, but off-axis observation required an annular mask as shown in Fig. 3.10(a). In this work, the mask had the same

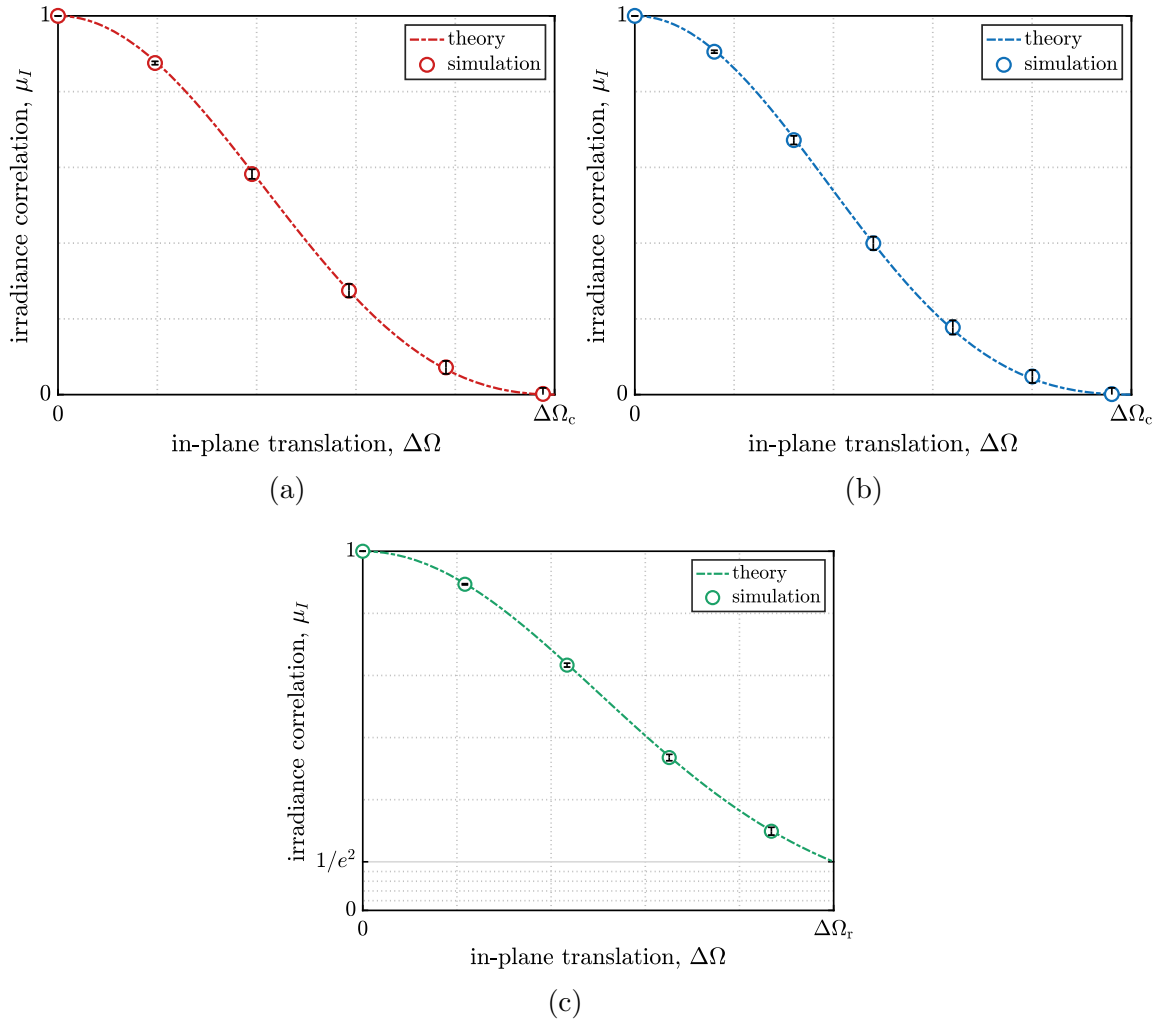


Figure 3.6: Analytical and numerical results for in-plane translation, given (a) square, (b) circular, and (c) Gaussian limiting apertures.

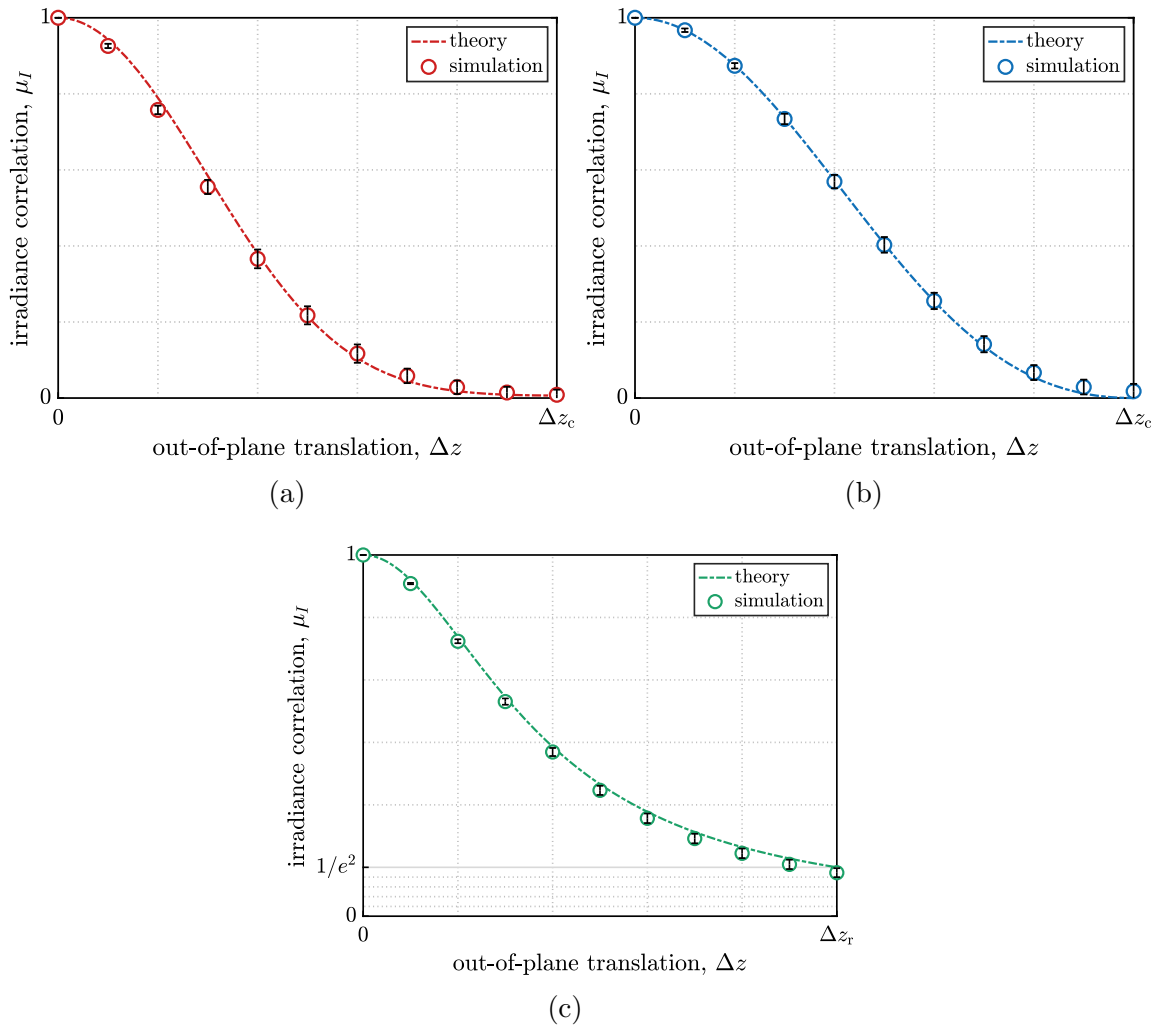


Figure 3.7: Analytical and numerical results for out-of-plane translation, given (a) square, (b) circular, and (c) Gaussian limiting apertures.

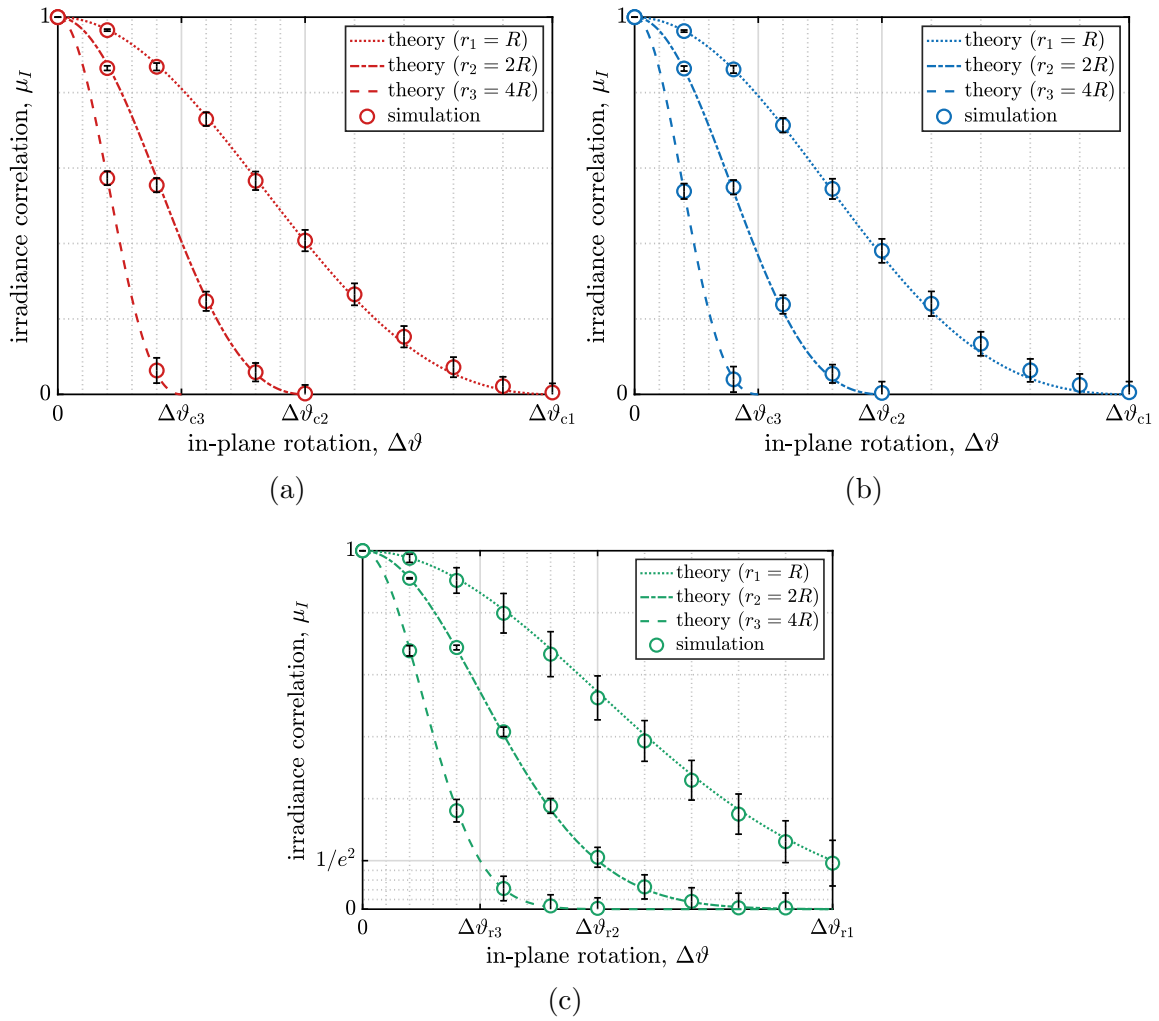


Figure 3.8: Analytical and numerical results for in-plane rotation, given (a) square, (b) circular, and (c) Gaussian limiting apertures.

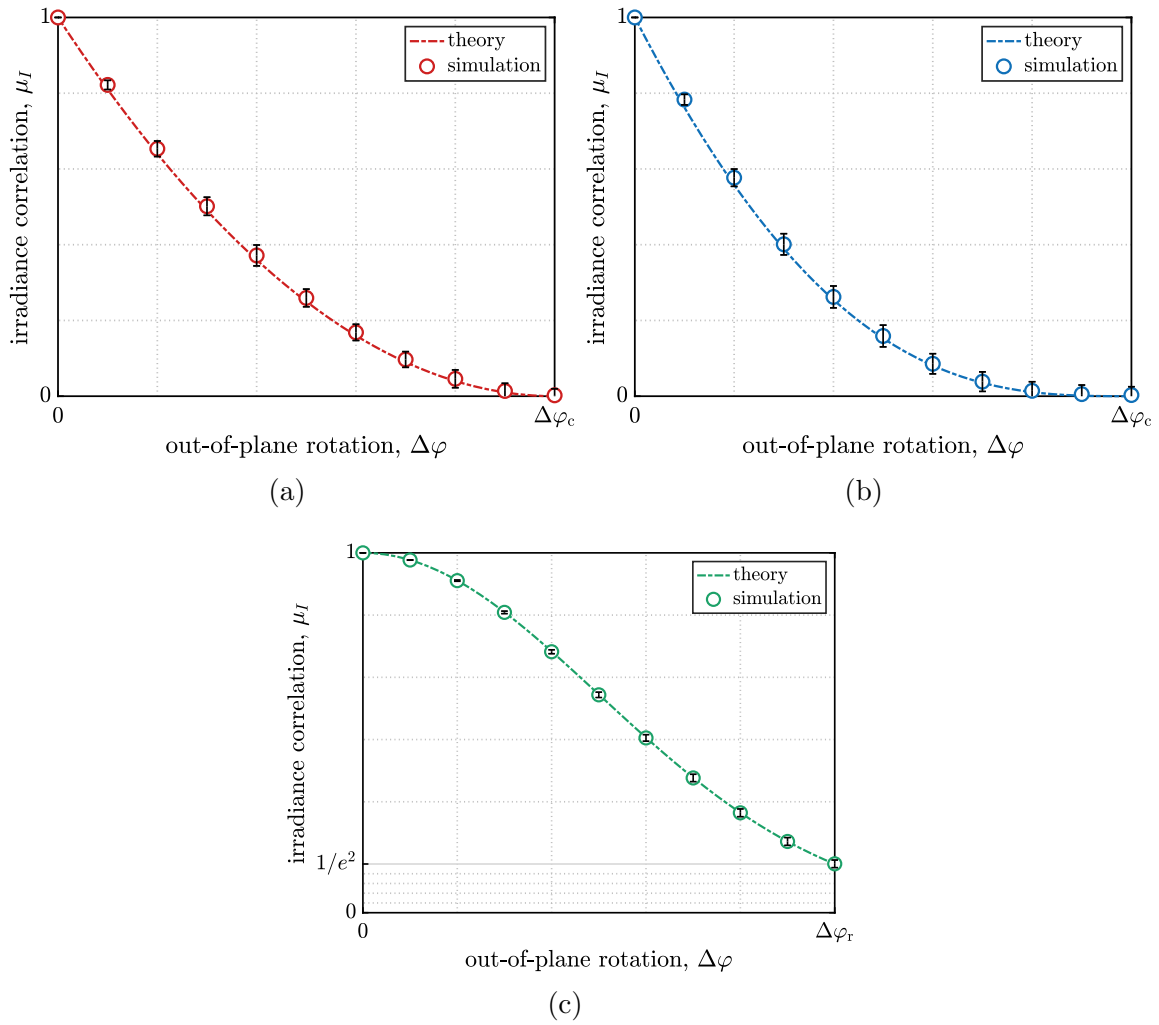


Figure 3.9: Analytical and numerical results for out-of-plane rotation, given (a) square, (b) circular, and (c) Gaussian limiting apertures.

thickness as the average size of the speckles, as portrayed in Fig. 3.10(b). In general, the annular mask had inner and outer radii r_1 and r_2 with an average radius

$$\begin{aligned} r_{\text{ave}} &= \frac{\int_0^{2\pi} \int_{r_1}^{r_2} r^2 dr d\theta}{\int_0^{2\pi} \int_{r_1}^{r_2} r dr d\theta} \\ &= \frac{2}{3} \left(r_2 + \frac{r_1^2}{r_1 + r_2} \right). \end{aligned} \quad (3.36)$$

Thus, for an annular mask of thickness t centered at radial position r_0 , we can rewrite Eq. (3.36) such that

$$r_{\text{ave}} = r_0 + \frac{t^2}{12r_0}, \quad (3.37)$$

where

$$r_0 = \frac{1}{6} \left(3r_{\text{ave}} + \sqrt{9r_{\text{ave}}^2 - 3t^2} \right). \quad (3.38)$$

In the above analysis, we set t such that it equaled the cutoff/rolloff conditions given in Tables 3.2 and 3.3 for the simulated in-plane rotation.

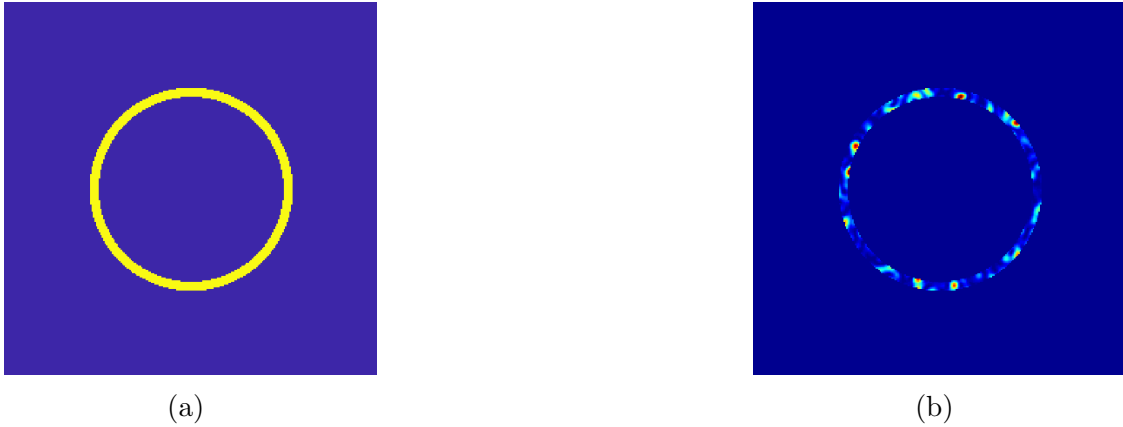


Figure 3.10: An example annular mask for radial isolation of the irradiance datasets (a) without speckle and (b) with speckle.

CHAPTER 4

Active-Tracking Scaling Laws Using the Noise-Equivalent Angle Due to Speckle[†]

4.1 Background

Finding the centroid of an image-plane irradiance pattern is necessary in many cases of object tracking and wavefront sensing. In an idealized noiseless detection scheme, this calculation represents the true geometric center of a resolved object or unresolved spot (assuming uniform illumination and object reflectivity). The presence of any source of noise, however, introduces uncertainty in this measurement that is typically quantified as a noise-equivalent angle (NEA). The general definition of NEA is an offset in angular position that produces unit signal-to-noise ratio (SNR), such that an actual offset by this angle would be indistinguishable from noise. With that in mind, another term for NEA is one-axis, one-sigma track error (denoted mathematically as σ_θ).

In the absence of coherent illumination, Tyler and Fried's foundational work on passive NEA offers a gauge for positional uncertainty of emissive or reflective objects under incoherent illumination [73]. Their treatment assumes the photon and/or sensor noise is what limits performance, giving rise to an NEA that grows without bound for increasingly large well-resolved objects. Though they were studying quad-cell detectors rather than centroid trackers, their results turn out to provide reasonable estimates of the NEA in either scenario [74, 75].

Active electro-optical systems must further contend with the effects of scintillation and speckle associated with coherent-light propagation. Scintillation refers

[†]This material was published previously as [72] in the *Journal of the Optical Society of America A (JOSA A)* with coauthors M. F. Spencer, M. K. Beason, and R. G. Driggers (<https://doi.org/10.1364/JOSAA.482777>) © Optica Publishing Group. Users may use, reuse, and build upon the article, or use the article for text or data mining, so long as such uses are for non-commercial purposes and appropriate attribution is maintained. All other rights are reserved.

to a spatially varying irradiance return arising from distributed-volume phase aberrations. The nonuniformity leads to centroid-tilt, gradient-tilt anisoplanatism, inducing a jitter term that negatively impacts Strehl ratios. Holmes has quantified this track error as a function of log-amplitude variance, among other system-level parameters [76]. Speckle is an unrelated nonuniformity that arises from scattering off an extended, optically rough, and coherently illuminated object. As its effect on received irradiance is statistically independent from that of scintillation, it gives rise to a separate jitter term that is the focus of this paper; namely, the NEA due to speckle.

Fried previously studied the NEA due to speckle in an unpublished technical report [77], which has led over time to an engineering rule of thumb that tracking precision cannot exceed $(1/2)\lambda/D$ in the presence of fully developed speckle. A common mistake, however, is to treat this metric as a one-axis track error when in fact it describes two-axis track error. Shellan later carried out similar analysis for a Shack–Hartmann wavefront sensor, which is essentially a collection of centroid trackers distributed over a lenslet array of square subapertures [78]. Fried and Shellan both relied on the assumption that laser power is sufficiently scalable for other noise sources to become negligible, and we make that same working assumption here. We also follow suit in defining NEA as a function of the object Fresnel number [79, 80, 81, 82], which is a normalization of the object angular extent that gives rise to two distinct imaging conditions: well-resolved and unresolved objects. Only the former condition is considered in the Fried and Shellan reports.

Since neither document is published in the peer-reviewed literature, we set out to provide a rederivation of the NEA due to speckle complete with validation through wave-optics simulations. Along the way, we make several other notable improvements: (1) the results are greatly simplified by leveraging the irradiance correlation coefficient which we have previously reported for dynamic speckle [2, 57]; (2) no radiometry is required to arrive at a mathematically complete result; (3) additional theory is needed to properly account for unresolved objects; and (4) the Strehl ratio due to Gaussian jitter derived by Merritt *et al.* links the NEA due to speckle to an

intuitive scaling law [83, 74]. We find in the well-resolved regime that our results agree with Baribeau’s asymptotic analysis [84]. We also take a related approach to Allan *et al.* in the unresolved regime [85] but make modified statistical arguments that further simplify our expressions. Before validating our theory through wave-optics simulations, we fit saturation curves to the numerical integration of our analytical results and report closed-form expressions for NEA that depend only on the object Fresnel number when speckle is fully developed.

Our end goal in deriving and validating these expressions is to provide scaling laws that predict a track-error limitation due to fully developed speckle. These scaling laws represent both circular- and square-aperture imaging geometries, as commonly found in object-tracking and wavefront-sensing systems, respectively. They are also valid over a full range of object Fresnel numbers, starting from the unresolved into the well-resolved limit. With these goals in mind, Section 4.2 first analyzes NEA in the well-resolved and unresolved limits, then bridges the gap by fitting a single curve to both asymptotic limits. The resultant closed-form expressions lead to the proposed scaling laws in each geometric scenario. Section 4.3 then introduces a wave-optics simulation framework for validation of our proposed scaling laws, and Section 4.4 discusses the agreement between theory and Monte Carlo simulation trials. Appendices A and B contain step-by-step derivations of the analytical overlap integrals introduced in Section 4.2.1.

4.2 Theoretical Analysis

The subsections that follow are concerned with active tracking of both circular and square object–aperture pairings, with the objects being either well resolved or unresolved from a diffraction standpoint. In each case the ultimate goal is to develop an expression for NEA (σ_θ) along one dimension. As we will see, however, even a single-axis centroid depends upon two-dimensional geometry of both the object and aperture. The analysis thus begins in two dimensions and downconverts in later steps, with the two solutions known to differ by a factor of $\sqrt{2}$ [51].

Going forward, a handful of simplifying assumptions help to guide the analysis toward closed-form solutions [cf. Fig. 4.1]: first, a black-box optical system is fully described by its entrance- and exit-pupil sizes and positions relative to the object and image planes; second, the optical system is in focus such that imaging condition $1/Z_1 + 1/Z_2 = 1/f$ is satisfied; third, all analysis takes place in the image plane with transverse magnification ratio $M = Z_2/Z_1$ exactly relating object and image sizes; fourth, the paraxial approximation holds true, such that angular measurements are related to lateral displacements via $\boldsymbol{\theta} = \mathbf{r}/Z_2$; fifth, active illumination is purely monochromatic and linearly polarized (in addition to being uniform over the entire object just before reflection and backscattering from its rough surface); and sixth, well-resolved objects subtend multiple diffraction angles while unresolved objects subtend less than one diffraction angle at range (i.e., the imaging system is diffraction limited rather than detector-sampling limited).

Before moving on, we define the following special functions for reference throughout our analysis [41]:

$$\text{cyl}(\rho) = \begin{cases} 1, & 0 \leq \rho < 1/2 \\ 1/2, & \rho = 1/2 \\ 0, & \rho > 1/2; \end{cases} \quad (4.1)$$

$$\text{somb}(\rho) = 2 \frac{J_1(\pi\rho)}{\pi\rho}; \quad (4.2)$$

$$\text{rect}(w) = \begin{cases} 1, & |w| < 1/2 \\ 1/2, & |w| = 1/2 \\ 0, & |w| > 1/2; \end{cases} \quad (4.3)$$

and

$$\text{sinc}(w) = \frac{\sin(\pi w)}{\pi w}. \quad (4.4)$$

We also point out to the reader that, although analytical curves are referenced throughout this section, they do not appear as plots until Sec. 4.4 where we present our wave-optics simulation results concurrently.

4.2.1 Well-Resolved Objects

An optically rough object that is well resolved by an imaging system presents many independent phase contributions to its entrance pupil, giving rise to irradiance fades called speckles upon propagation to the image plane. A centroid tracker integrates over this entire irradiance pattern, so the image-plane speckle statistics determine uncertainty in the measurement. With reference to Fig. 4.1, the analytical vector expression for an *ordinary* image-plane intensity centroid (i.e., the first moment of the image) is [86]

$$\mathbf{r}_c = \frac{\iint \mathbf{r} I(\mathbf{r}) d^2\mathbf{r}}{\iint I(\mathbf{r}) d^2\mathbf{r}}, \quad (4.5)$$

whereas

$$\begin{aligned} \mathbf{r}_c &= \frac{\iint \mathbf{r} I(\mathbf{r}) d^2\mathbf{r}}{\langle \iint I(\mathbf{r}) d^2\mathbf{r} \rangle} \\ &= \frac{\iint \mathbf{r} I(\mathbf{r}) d^2\mathbf{r}}{\bar{\Phi}} \end{aligned} \quad (4.6)$$

describes the equivalent *simplified* centroid tracker. In Eqs. (4.5) and (4.6), $I(\mathbf{r})$ is the pointwise value of irradiance at vector position \mathbf{r} in the image plane. Note that Eq. (4.6) simply replaces the denominator of Eq. (4.5) with its ensemble average (i.e., the total expected image power $\bar{\Phi}$). This approximation spares us the statistical challenge of taking a random expectation ratio, and Fried argues for its validity on the basis that the numerator and denominator of Eq. (4.5) are mutually statistically independent in the case of an extended, optically rough, and coherently illuminated surface [77].

Our immediate goal is to compute a variance (i.e., the second central moment)

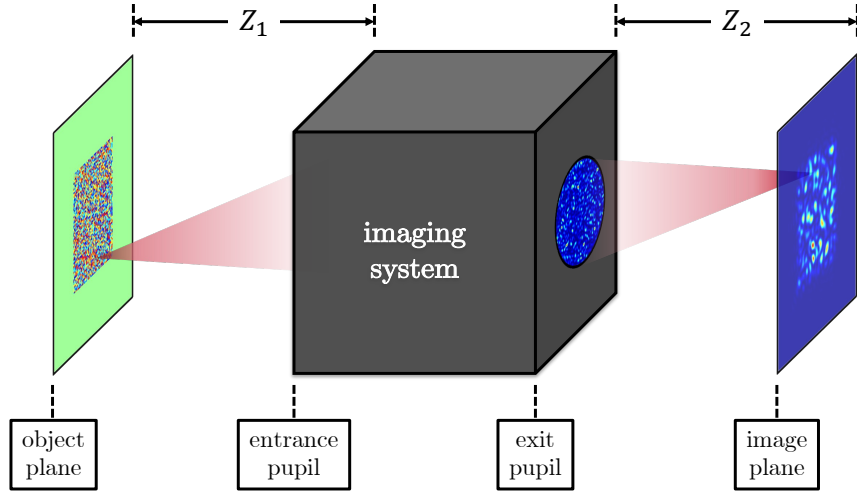


Figure 4.1: Black-box imaging geometry with a rough-surface object in the object plane forming a speckled image in the image plane.

of the random intensity centroid position, which in general is

$$\begin{aligned}\sigma_c^2 &= \text{E}[|\mathbf{r}_c - \text{E}[\mathbf{r}_c]|^2] \\ &= \text{E}[|\mathbf{r}_c|^2] - |\text{E}[\mathbf{r}_c]|^2\end{aligned}\quad (4.7)$$

with $\text{E}[\circ]$ and $|\circ|$ denoting an expected value and vector magnitude, respectively. Given that a speckle-driven centroid is unbiased in any one direction, the second term of Eq. (4.7) goes to zero and the first becomes equivalent to variance. Taking the squared magnitude of Eq. (4.6) amounts to integration over two (generally distinct) position vectors in the image plane; namely, \mathbf{r}_1 and \mathbf{r}_2 :

$$\sigma_c^2 = \left\langle \frac{1}{\Phi^2} \iint_{-\infty}^{\infty} \iint_{-\infty}^{\infty} (\mathbf{r}_1 \cdot \mathbf{r}_2) I(\mathbf{r}_1) I(\mathbf{r}_2) d^2\mathbf{r}_2 d^2\mathbf{r}_1 \right\rangle. \quad (4.8)$$

As the two irradiance factors are the only randomly varying quantities in Eq. (4.8), the orders of integration and averaging are interchangeable [40], such that

$$\sigma_c^2 = \frac{1}{\Phi^2} \iint_{-\infty}^{\infty} \iint_{-\infty}^{\infty} (\mathbf{r}_1 \cdot \mathbf{r}_2) \langle I(\mathbf{r}_1) I(\mathbf{r}_2) \rangle d^2\mathbf{r}_2 d^2\mathbf{r}_1. \quad (4.9)$$

We recognize the quantity enclosed in angle brackets as the statistical autocorrelation function

$$\begin{aligned} R_I(\mathbf{r}_1; \mathbf{r}_2) &= \langle I(\mathbf{r}_1) I(\mathbf{r}_2) \rangle \\ &= \langle U(\mathbf{r}_1) U^*(\mathbf{r}_1) U(\mathbf{r}_2) U^*(\mathbf{r}_2) \rangle, \end{aligned} \quad (4.10)$$

$U(\circ)$ being a complex optical field component and $U^*(\circ)$ its complex conjugate. Assuming the rough-surface scattering process generates enough independent phase contributions that the central-limit theorem is satisfied, $U(\mathbf{r}_1)$ and $U(\mathbf{r}_2)$ obey circular complex Gaussian statistics and

$$\begin{aligned} R_I(\mathbf{r}_1; \mathbf{r}_2) &= \langle I(\mathbf{r}_1) \rangle \langle I(\mathbf{r}_2) \rangle + |\langle U(\mathbf{r}_1) \rangle \langle U^*(\mathbf{r}_2) \rangle|^2 \\ &= \langle I(\mathbf{r}_1) \rangle \langle I(\mathbf{r}_2) \rangle [1 + \mu_I(\mathbf{r}_2 - \mathbf{r}_1)] \end{aligned} \quad (4.11)$$

by the complex Gaussian moment theorem [16]. Here, $\mu_I(\circ) \propto |\mathcal{F}\{\mathcal{P}(\boldsymbol{\rho})\}|^2$ is the image-plane irradiance correlation coefficient, where $\mathcal{F}\{\circ\}$ represents a 2D Fourier transform and $\mathcal{P}(\boldsymbol{\rho})$ a generalized pupil function. Substituting Eq. (4.11) into Eq. (4.9),

$$\sigma_c^2 = \frac{1}{\Phi^2} \iint_{-\infty}^{\infty} \iint_{-\infty}^{\infty} (\mathbf{r}_1 \cdot \mathbf{r}_2) \langle I(\mathbf{r}_1) \rangle \langle I(\mathbf{r}_2) \rangle [1 + \mu_I(\mathbf{r}_2 - \mathbf{r}_1)] d^2\mathbf{r}_1 d^2\mathbf{r}_2. \quad (4.12)$$

For any uniform irradiance pattern that is both finite in extent and symmetric about the optical axis, the first term in Eq. (4.12) integrates to zero and thus

$$\sigma_c^2 = \frac{1}{\bar{\Phi}^2} \iint_{-\infty}^{\infty} \iint_{-\infty}^{\infty} (\mathbf{r}_1 \cdot \mathbf{r}_2) \langle I(\mathbf{r}_1) \rangle \langle I(\mathbf{r}_2) \rangle \mu_I(r_2 - r_1) d^2\mathbf{r}_1 d^2\mathbf{r}_2. \quad (4.13)$$

This result makes the additional assumption of a linear shift-invariant (LSI) system such that the correlation coefficient depends only on scalar differences between vector magnitudes [39].

To proceed, a flat circular object of diameter W and mean irradiance \bar{I} gives

$$\langle I(\mathbf{r}) \rangle = \bar{I} \text{cyl} \left(\frac{\mathbf{r}}{MW} \right) \quad (4.14)$$

in the image plane with $M = Z_2/Z_1$ being the transverse magnification ratio between object–pupil and pupil–image distances Z_1 and Z_2 , respectively. The image-plane irradiance correlation coefficient corresponding to a circular aperture is [57]

$$\mu_I(r_2 - r_1) = \text{somb}^2 \left[\frac{D}{\lambda Z_2} (r_2 - r_1) \right], \quad (4.15)$$

where D is the aperture diameter and λ the wavelength of illumination. Leaving the full derivation to a Appendix A for the sake of brevity, we substitute Eq. (4.15) into Eq. (4.47) and simplify its prefactor by taking average power $\bar{\Phi}$ to be the product of average irradiance \bar{I} and image area

$$A_{\text{img}} = \pi \left(M \frac{W}{2} \right)^2. \quad (4.16)$$

Making this substitution, along with $M = Z_2/Z_1$, $\theta = r/Z_2$ and

$$N_{\text{obj}} = \frac{W/Z_1}{\lambda/D}, \quad (4.17)$$

the final normalized result for a circular object–aperture pairing is

$$\frac{\sigma_\theta}{\lambda/D} = \frac{N_{\text{obj}}}{\sqrt{\pi}} \left\{ \int_0^1 v \left[\cos^{-1}(v) + v\sqrt{1-v^2} (2v^2 - 3) \right] \text{somb}^2(N_{\text{obj}}v) dv \right\}^{1/2}. \quad (4.18)$$

Here, we have also divided the result by 2 for *one-axis* variance and taken its square root for standard deviation. In Eq. (4.17), λ/D is the full-width-at-half-maximum (FWHM) aperture diffraction angle and N_{obj} is the object Fresnel number, which not only normalizes the object angular extent but also counts the estimated number of speckles across one dimension of the aperture. Moreover, $N_{\text{obj}} > 1$ indicates that the object is well resolved with multiple resolution cells spanning the object at range. Equation (4.18) has an asymptotic limit of $1/\pi \approx 0.318$ as N_{obj} tends to infinity.

Pairing a square object of width W with a square aperture of width D gives

$$\langle I(\mathbf{r}) \rangle = \bar{I} \text{rect}\left(\frac{x}{MW}\right) \text{rect}\left(\frac{y}{MW}\right), \quad (4.19)$$

as well as [57]

$$\mu_I(r_2 - r_1) = \text{sinc}^2 \left[\frac{D}{\lambda Z_2} (r_2 - r_1) \right] \quad (4.20)$$

and

$$A_{\text{img}} = (MW)^2. \quad (4.21)$$

Referring the reader to Appendix B and making the appropriate substitutions into Eq. (4.60), we find that our final normalized result for a square object–aperture pairing is

$$\frac{\sigma_\theta}{\lambda/D} = \frac{N_{\text{obj}}}{\sqrt{3}} \left[\int_0^1 (1 - 3v_x + 2v_x^2) \text{sinc}^2(N_{\text{obj}}v_x) dv_x \int_0^1 (1 - v_y) \text{sinc}^2(N_{\text{obj}}v_y) dv_y \right]^{1/2} \quad (4.22)$$

with a saturation value of $\sqrt{3}/6 \approx 0.289$. This time we have simply taken the square root for standard deviation without first dividing by 2, since the full derivation in Appendix B works in one dimension from the outset.

Equations (4.18) and (4.22) result from integration only over the windowed image irradiance, which assumes a full field of view (FOV) equal to the object angular extent. In turn, any presence of background noise or clutter would naturally increase uncertainty in the measurement. The dashed curves of Fig. 4.4 plot these results (i.e., the well-resolved NEA due to speckle for both circle and square objects) over a range of object Fresnel numbers. We note that the asymptotic well-resolved limits of these curves (where $N_{\text{obj}} \gg 1$) remain constant with object Fresnel number due to aperture-limited speckle sizes [57], while their linear predictions are unphysical in the unresolved limits (for which $N_{\text{obj}} \ll 1$) because as an object decreases in angular subtense its image cannot shrink infinitesimally as a consequence of diffraction. This understanding calls for separate treatment of unresolved objects in the analysis that follows.

4.2.2 Unresolved Objects

When an extended, optically rough, and coherently illuminated object is not resolved by the imaging system, it becomes an effective point source producing a single diffraction spot in the image plane. Phase is nonetheless random in the pupil plane, however, which means the centroid position still fluctuates to some degree. Equation (4.17) predicts that speckle width exceeds aperture diameter in the unresolved regime, so the pupil effectively sees a constant phase slope in one direction [87] and the image-plane diffraction spot shifts accordingly. The path forward, then, is to describe this behavior by studying the phase statistics of a fully developed speckle field.

The localized 1D phase slope ($\phi' = d\phi/dx$) of a fully developed speckle field follows the probability-density function (PDF) [16]

$$p(\phi') = \frac{1}{2} \left\{ \frac{g}{[1 + (g\phi')^2]^{3/2}} \right\} \quad (4.23)$$

for an adequately symmetric (e.g. square, circular) object, with corresponding cumulative-distribution function (CDF)

$$P(\phi') = \frac{1}{2} \left\{ 1 + \frac{g\phi'}{[1 + (g\phi')^2]^{1/2}} \right\}. \quad (4.24)$$

In the above, g is a scalar value that depends on the object geometry. Equation (4.23) is defined in theory over an infinitely wide domain, but setting bounds of integration from $-\infty$ to ∞ produces the unphysical result that variance is also infinite. Instead truncating its support to a more realistic interval gives rise to a variance calculation of

$$\sigma_{\phi'}^2 = \frac{\int_{-\phi'_{\max}}^{\phi'_{\max}} (\phi' - \bar{\phi}')^2 p(\phi') d\phi'}{P(\phi'_{\max}) - P(-\phi'_{\max})} \quad (4.25)$$

with ϕ'_{\max} being the maximum phase-slope magnitude of interest. Here, we note that the phase slope of a speckle field is unbiased and thus $\bar{\phi}' = 0$. In deciding where to truncate the phase slopes, we consider the behavior of Eq. (4.25) as ϕ'_{\max} is varied. Plotting its numerator and denominator separately reveals that a vast majority of phase slopes are concentrated toward small values of ϕ'_{\max} . For instance if we draw inspiration from the empirical rule in statistics that says virtually all possible values ($\sim 99.7\%$) of a normally distributed random variable lie within three standard deviations of its mean, we see that the denominator curve has virtually flattened by this point. Likewise it is clear that the numerator curve has flattened significantly here, and little more is contributed to the phase-slope standard deviation by including values of ϕ'_{\max} beyond the point of $\sim 99.7\%$ total probability. Keeping in mind that infinitely large phase slopes (and tilt angles by extension) lose any physical meaning, truncating the distribution at this point is a sound decision given these observations. We therefore solve Eq. (4.24) for a maximum phase slope such that

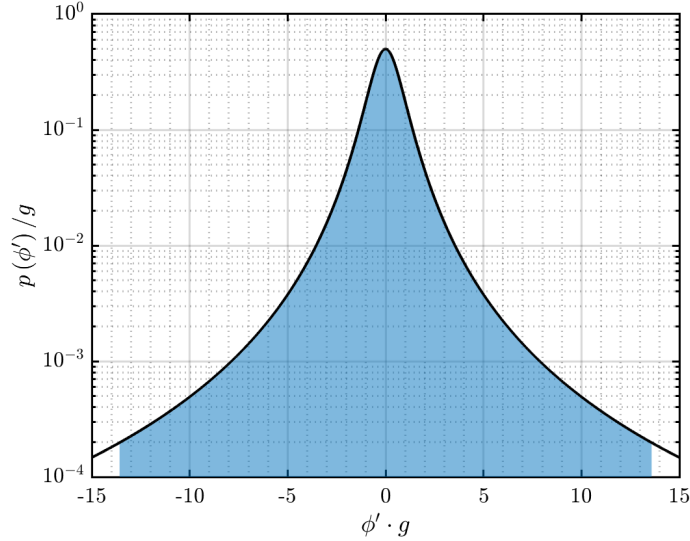


Figure 4.2: Semi-log plot of phase-slope PDF defined in Eq. (4.23); blue shading indicates 99.7% of the area under this curve yielding a realistic range of phase slopes.

$P(\phi'_{\max}) - P(-\phi'_{\max}) = 0.997$. Figure 4.2 illustrates the integration of Eq. (4.23) over this interval on a semi-log plot. As we will see, this heuristic approach is well supported in wave-optics simulation results.

Assuming a circular object [16], $g = 2\lambda Z_1/(\pi W)$ and $\phi'_{\max} = 21.3W/(\lambda Z_1)$. Noting that division by wavenumber $k = 2\pi/\lambda$ converts a phase slope to a tilt angle under the paraxial approximation, this is equivalent to integrating over roughly $7\times$ the object angular extent. Eq. (4.25) then evaluates to $\sigma_{\phi'}^2 = 5.70 [W/(\lambda Z_1)]^2$. From here we simply take the square root for standard deviation and divide by k for an *angular* uncertainty of

$$\frac{\sigma_{\theta}}{\lambda/D} = 0.380 N_{\text{obj}} \quad (4.26)$$

in terms of the aperture diffraction angle and object Fresnel number.

Assuming a square object [16], $g = \sqrt{3}\lambda Z_1/(\pi W)$ and $\phi'_{\max} = 24.6W/(\lambda Z_1)$ or roughly $8\times$ the object extent in angular space. In turn, $\sigma_{\phi'}^2 = 7.61 [W/(\lambda Z_1)]^2$ and

$$\frac{\sigma_\theta}{\lambda/D} = 0.439N_{\text{obj}} \quad (4.27)$$

by the same approach. Comparing Eqs. (4.26) and (4.27) to Eqs. (4.18) and (4.22), we see that the NEA is greater for square geometry in the unresolved limit but greater for circular geometry in the well-resolved limit.

The dotted curves of Fig. 4.4 plot these results (i.e., the unresolved NEA due to speckle for both circle and square objects) over the same range of object Fresnel numbers as in Section 4.2.1. Here, we observe a linear dependence on object Fresnel number in the unresolved limit (where $N_{\text{obj}} \gg 1$), while a constant slope is now unphysical in the well-resolved limit (for which $N_{\text{obj}} \gg 1$) because an image does in fact grow larger with increasing object size and pointwise measurements of phase in the aperture no longer apply.

4.2.3 Scaling Laws

In an effort to develop scaling laws for active tracking that include the NEA due to speckle, we bridge the linear lower limits defined in Section 4.2.2 with the constant upper limits defined in Section 4.2.1 through curve fitting. Synthesizing the lower limit of Eq. (4.26) with the upper limit of Eq. (4.18) in TableCurve 2D yields a saturation-curve fit of

$$\frac{\sigma_\theta}{\lambda/D} = \left(3.21 + \frac{2.56}{N_{\text{obj}}} \right)^{-1} \quad (4.28)$$

for a circular object and aperture, while doing the same with Eqs. (4.27) and (4.22) yields

$$\frac{\sigma_\theta}{\lambda/D} = \left(3.54 + \frac{2.11}{N_{\text{obj}}} \right)^{-1} \quad (4.29)$$

for a square object and aperture. The R^2 value of each fit approaches 1 to within five decimal places, and both fits are also plotted in Fig. 4.4 using dash-dotted lines. As Eqs. (4.28) and (4.29) represent standard noise terms, they decrease with the

square root of the number of independent speckle frames averaged together prior to centroid measurement [88].

Of further interest is quantifying how the NEA due to speckle will ultimately impact system performance. Defining the Strehl ratio according to Merritt's formulation for Gaussian jitter as [83, 74]

$$\langle S_j \rangle = \left[1 + \frac{\pi^2}{2} \left(\frac{\sigma_\theta}{\lambda/D} \right)^2 \right]^{-1} \quad (4.30)$$

gives us insight into the reduction in on-axis, image-plane intensity due to fully developed speckle. With a reduced NEA in the case of speckle averaging, the jitter Strehl ratio increases and track performance improves in response. We explore this improvement by plotting Eq. (4.30) with and without speckle averaging in Fig. 4.5.

4.3 Numerical Simulation

To produce numerical results that accurately represent active-centroid tracking with coherent illumination, we take the standard wave-optics approach of propagating from plane to plane via the Fresnel diffraction integral as a solution to the Helmholtz wave equation. After selecting a realistic illumination wavelength λ , propagation distance $Z_1 = Z_2 = Z$ (for unit magnification) and aperture diameter D , we vary the object width W by controlling the object Fresnel number [cf. Eq. (4.17)]. The next step is to define either a square or circular shape of this width in the object plane with constant amplitude and δ -correlated random phase distributed uniformly over $[-\pi, \pi)$. Propagating this field a distance Z_1 to the pupil plane, applying a thin lens of focal length $f = Z_1$ to collimate the entrance-pupil field, applying a second thin lens of focal length $f = Z_2$ to focus the exit-pupil field, propagating by a second distance Z_2 to the image plane, and taking the field's squared magnitude produces the image-plane irradiance for analysis (cf. Fig. 4.1). Although our simulations represent a two-lens imaging system for the sake of simplicity [89], we remind the reader that any black-box system with known pupil positions relative to the object and image planes would give equally valid results. After windowing out a region

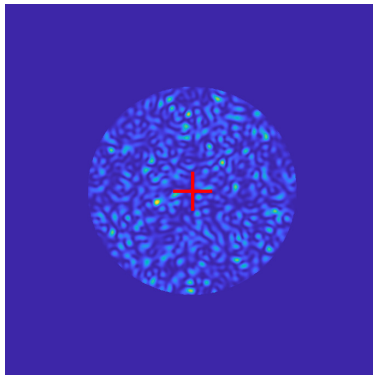


Figure 4.3: Example windowed image for numerical centroid estimation; results from uniform coherent illumination of a circular object such that crosshairs would be perfectly centered on the image if not for the presence of speckle noise.

of interest that is consistent with the image size, we calculate an x -axis centroid estimate as

$$\hat{x}_c = \frac{\sum_{m,n} x_{mn} I_{mn}}{\sum_{m,n} I_{mn}}. \quad (4.31)$$

An example speckled and windowed image is shown in Fig. 4.3 with red crosshairs marking the estimated centroid position. A Monte Carlo average of this estimate over 100 independent speckle realizations for each object Fresnel number increases robustness of the estimates, and finally dividing the average results by $\lambda Z_2/D$ allows for comparison to the appropriate scaling law [cf. Eq. (4.29) or (4.28)]. These results are plotted as circles in Fig. 4.4, noting that the general approach remains valid over the full range of object sizes. Because a minimum of ~ 10 phase samples are required across the object width to generate proper speckle statistics, sampling requirements become much more constrained in the unresolved limit where object sizes grow smaller against a aperture size and propagation distance [90]. With that said, Table 4.1 highlights the critical inputs to an example simulation in the well-resolved limit with unity scaling between each pair of planes.

Table 4.1: Sample wave-optics simulation parameters used to validate scaling laws in the well-resolved limit.

	parameter	value
general	grid resolution, $N \times N$ [px]	1024×1024
	grid spacing, δ [μm]	879
	grid side length, S [cm]	90
system	illumination wavelength, λ [μm]	1
	object–pupil distance, Z_1 [m]	791
	pupil–image distance, Z_2 [m]	791
	effective focal length, f [m]	791
	aperture, diameter, D [cm]	30

4.4 Results and Discussion

Figure 4.4 plots all circular and square integral expressions, curve fits and simulation data for NEA over a wide range of object Fresnel numbers assuming fully developed speckle. It is clear that the curve fits in general provide decent estimates of their rigorous analytical counterparts, and the numerical results provide validation with strong agreement. Furthermore, rigorous analysis cannot account for the transition region from unresolved to well-resolved objects where curve fitting offers the only viable closed-form solutions. Lower object Fresnel numbers tend to show greater variation in the data, which stands to reason since the centroid of a well-resolved object that projects many phase slopes across the aperture represents more of an ensemble average than does a single phase contribution from an unresolved object. Monte Carlo averaging of more than 100 datasets would help to reduce this noise, but overall trends in the data provide meaningful insight nonetheless.

Recalling that our circular and square scaling laws saturate at ~ 0.318 and ~ 0.289 , respectively, we propose a new rule of thumb that says tracking precision of well-resolved objects cannot exceed $(1/3)\lambda/D$. We make the argument that a one-axis definition is more intuitive when considering the idea of a NEA. If one considers instead a two-axis definition, the estimate more closely approaches the familiar $(1/2)\lambda/D$ metric: $\sqrt{2}/\pi \approx 0.450$ and $1/\sqrt{6} \approx 0.408$, respectively for circular and square geometries. We also point out that any discrepancy in the transition

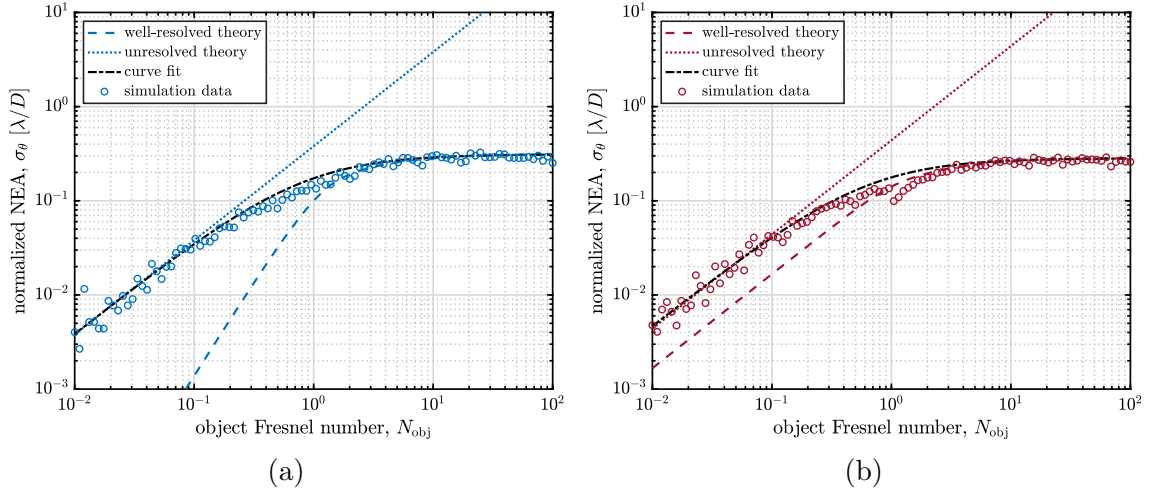


Figure 4.4: Normalized NEA as a function of object Fresnel number for uniform (a) circular [cf. Eqs. (4.18), (4.26) & (4.28)] and (b) square [cf. Eqs. (4.22), (4.27) & (4.29)] object–aperture pairings under coherent illumination.

region from unresolved to well-resolved objects is a conservative overestimate of the NEA, though this discrepancy appears somewhat exaggerated on the log–log scale of Fig. 4.4.

As a matter of interest, comparing the scaling laws presented here to the passive SNR-limited results of Ref. [73] reveals essentially opposite trends. Our active NEA due to speckle increases linearly with object Fresnel number in the unresolved limit. As the object Fresnel number N_{obj} increases, the phase ramps grow steeper over decreasing speckle sizes, until multiple speckles appear across the aperture with $N_{\text{obj}} > 1$ and the effect of ensemble averaging over image-plane speckles of constant size (as set by the exit pupil) saturates the NEA to a constant value. Conversely, in the passive case an incoherent point-spread function fixes the NEA at a constant value in the unresolved regime. Such is the case until the object becomes well resolved for $N_{\text{obj}} > 1$ and the NEA increases linearly with object Fresnel number while the image grows without bound (as allowed by the FOV) without total destructive interference to limit the centroid calculation area. This comparison highlights an inherent tradeoff between active and passive tracking, subject to available SNR from natural illumination.

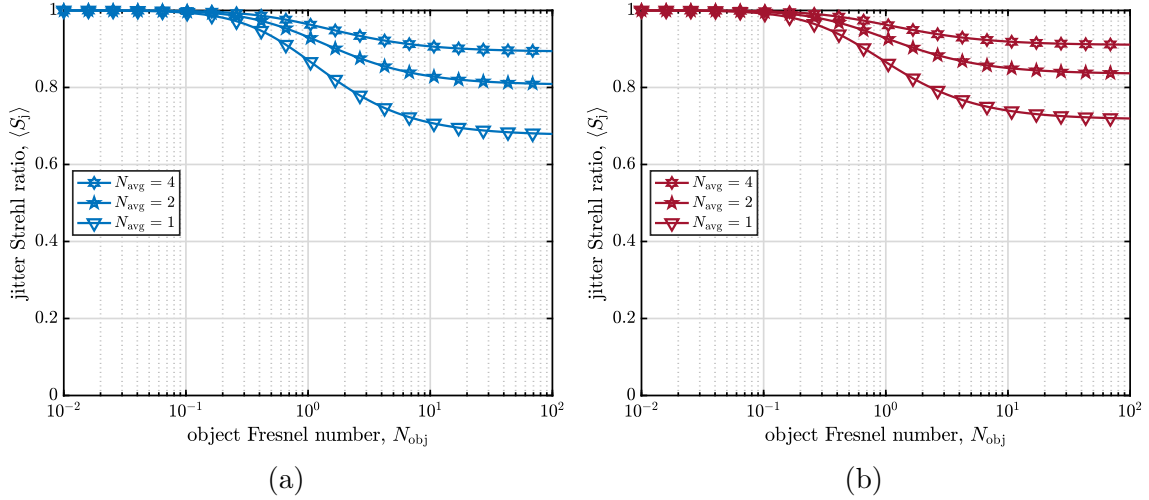


Figure 4.5: Comparison of Strehl ratios as a function of object Fresnel number for uniform (a) circular [cf. Eqs. (4.28) & (4.30)] and (b) square [cf. Eqs. (4.29) & (4.30)] object–aperture pairings.

In order to quantify the on-axis intensity reduction associated with speckle-induced jitter, Eq. (4.30) together with Eqs. (4.28) and (4.29) leads to the plots of Strehl ratio in Fig. 4.5. These plots also illustrate the benefit of reducing NEA through speckle averaging, with Eqs. (4.29) and (4.28) divided by the square root of $N_{\text{avg}} = 2$ and 4 before substitution into Eq. (4.30). In addition to the $(1/3) \lambda/D$ tracking limit for well-resolved objects, a key result of this paper from Fig. 4.5 is that the one-axis jitter Strehl ratio falls below the Maréchal criterion for nominally diffraction-limited imaging ($\langle S \rangle \gtrsim 80\%$) in the well-resolved limit (without speckle averaging). In particular, $\langle S_j \rangle = 2/3$ and ~ 0.709 for circular and square geometries, respectively. A two-axis definition would decrease these numbers respectively to $1/2$ and ~ 0.549 , potentially overestimating the severity of unmitigated speckle and its impact on performance in an active tracking system.

Note A: Full Derivation for Well-Resolved Objects with Circular Geometry

Starting from Eq. (4.13), we define sum and difference vectors as

$$\mathbf{p} = \frac{\mathbf{r}_1 + \mathbf{r}_2}{2} \quad (4.32)$$

and

$$\mathbf{q} = \mathbf{r}_2 - \mathbf{r}_1, \quad (4.33)$$

respectively for a Jacobian determinant of 1. This choice implies that

$$\begin{cases} \mathbf{r}_1 = \mathbf{p} - \mathbf{q}/2 \\ \mathbf{r}_2 = \mathbf{p} + \mathbf{q}/2 \\ \mathbf{r}_1 \cdot \mathbf{r}_2 = p^2 - q^2/4, \end{cases} \quad (4.34)$$

and in turn

$$\sigma_c^2 = \frac{1}{\Phi^2} \iint_{-\infty}^{\infty} \mu_I(q) \iint_{-\infty}^{\infty} \left(p^2 - \frac{q^2}{4} \right) \langle I(\mathbf{p} - \frac{\mathbf{q}}{2}) \rangle \langle I(\mathbf{p} + \frac{\mathbf{q}}{2}) \rangle d^2\mathbf{p} d^2\mathbf{q}. \quad (4.35)$$

Notice that the use of sum and difference vectors here provides us with an iterated integral that we can treat with respect to one vector quantity at a time. A circular object of diameter W now gives us

$$\begin{cases} \langle I(\mathbf{p} - \mathbf{q}/2) \rangle = \bar{I} \text{cyl}[(\mathbf{p} - \mathbf{q}/2) / (MW)] \\ \langle I(\mathbf{p} + \mathbf{q}/2) \rangle = \bar{I} \text{cyl}[(\mathbf{p} + \mathbf{q}/2) / (MW)] \end{cases} \quad (4.36)$$

in the image plane. Making another change of variables,

$$\begin{cases} \mathbf{u} = \mathbf{p} / (MW) \\ \mathbf{v} = \mathbf{q} / (MW) \end{cases} \Rightarrow p^2 - q^2/4 = (MW)^2 \left(u^2 - \frac{v^2}{4} \right) \quad (4.37)$$

and

$$\begin{aligned}
\begin{vmatrix} \frac{\partial \mathbf{p}}{\partial \mathbf{u}} & \frac{\partial \mathbf{p}}{\partial \mathbf{v}} \\ \frac{\partial \mathbf{q}}{\partial \mathbf{u}} & \frac{\partial \mathbf{q}}{\partial \mathbf{v}} \end{vmatrix} &= \begin{vmatrix} (MW)^2 & 0 \\ 0 & (MW)^2 \end{vmatrix} \\
&= (MW)^4.
\end{aligned} \tag{4.38}$$

Equation (4.35) then becomes

$$\sigma_c^2 = \frac{\bar{I}^2 (MW)^6}{\bar{\Phi}^2} \iint_{-\infty}^{\infty} \mu_I(v) \iint_{-\infty}^{\infty} \left(u^2 - \frac{v^2}{4}\right) \text{cyl}\left(\mathbf{u} - \frac{\mathbf{v}}{2}\right) \text{cyl}\left(\mathbf{u} + \frac{\mathbf{v}}{2}\right) d^2\mathbf{u} d^2\mathbf{v}. \tag{4.39}$$

Decomposing \mathbf{u} into Cartesian a and b coordinates while choosing to align u_a with \mathbf{v} allows us to assign a single component of magnitude v to vector \mathbf{v} . In other words, $\mathbf{u} = \langle u_a, u_b \rangle$ and $\mathbf{v} = \langle v, 0 \rangle$. Then according to Eq. (4.1)

$$\begin{aligned}
\left|\mathbf{u} - \frac{1}{2}\mathbf{v}\right| &= \sqrt{\left(u_a - \frac{v}{2}\right)^2 + u_b^2} \\
&\leq \frac{1}{2} \Rightarrow |u_b| \leq \sqrt{\frac{1}{4} - \left(u_a - \frac{v}{2}\right)^2},
\end{aligned} \tag{4.40}$$

which requires that

$$\frac{v-1}{2} \leq u_a \leq \frac{v+1}{2}. \tag{4.41}$$

Similarly,

$$\begin{aligned}
\left|\mathbf{u} + \frac{1}{2}\mathbf{v}\right| &= \sqrt{\left(u_a + \frac{v}{2}\right)^2 + u_b^2} \\
&\leq \frac{1}{2} \Rightarrow |u_b| \leq \sqrt{\frac{1}{4} - \left(u_a + \frac{v}{2}\right)^2}
\end{aligned} \tag{4.42}$$

requires

$$-\frac{1+v}{2} \leq u_a \leq \frac{1-v}{2}. \quad (4.43)$$

Figure 4.6 shows that our overlap integral calls for bounds on u_b in Eq. (4.40) from the lower bound of Eq. (4.41) to $u_a = 0$, as well as those on u_b in Eq. (4.42) from $u_a = 0$ to the upper bound of Eq. (4.43). Thus, the interior integral of Eq. (4.39) becomes

$$\begin{aligned} & \iint_{-\infty}^{\infty} \left(u^2 - \frac{v^2}{4} \right) \text{cyl} \left(\mathbf{u} - \frac{\mathbf{v}}{2} \right) \text{cyl} \left(\mathbf{u} + \frac{\mathbf{v}}{2} \right) d^2 \mathbf{u} \\ &= \int_{(v-1)/2}^0 \int_{-\sqrt{1/4-(u_a-v/2)^2}}^{\sqrt{1/4-(u_a-v/2)^2}} \left(u_a^2 + u_b^2 - \frac{v^2}{4} \right) du_b du_a \\ &+ \int_0^{(1-v)/2} \int_{-\sqrt{1/4-(u_a+v/2)^2}}^{\sqrt{1/4-(u_a+v/2)^2}} \left(u_a^2 + u_b^2 - \frac{v^2}{4} \right) du_b du_a, \end{aligned} \quad (4.44)$$

which evaluates to

$$\frac{1}{16} \left[\cos^{-1}(v) + v\sqrt{1-v^2} (2v^2 - 3) \right]. \quad (4.45)$$

Plugging back into Eq. (4.39),

$$\sigma_c^2 = \frac{\bar{I}^2 (MW)^6}{16\bar{\Phi}^2} \iint_{\Sigma} \left[\cos^{-1}(v) + v\sqrt{1-v^2} (2v^2 - 3) \right] \mu_I(v) d^2 \mathbf{v}. \quad (4.46)$$

Converting to polar coordinates, integrating azimuthally and setting appropriate radial bounds on v [cf. Eq. (4.37)],

$$\sigma_c^2 = \frac{\pi \bar{I}^2 (MW)^6}{8\bar{\Phi}^2} \int_0^1 v \left[\cos^{-1}(v) + v\sqrt{1-v^2} (2v^2 - 3) \right] \mu_I(v) dv. \quad (4.47)$$

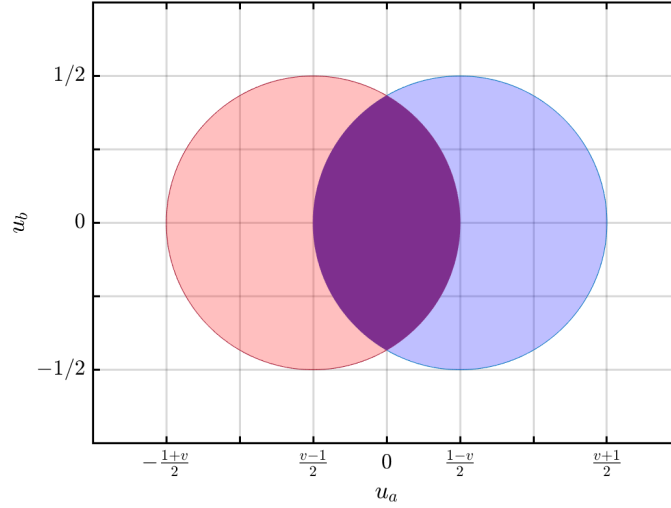


Figure 4.6: Visualization of overlap-integral computation for a circular rough-surface object; limits are shown for $0 < v < 1$.

Bearing in mind that a circular aperture gives us

$$\mu_I(q) = \text{somb}^2\left(\frac{D}{\lambda Z_2}q\right) \quad (4.48)$$

and that $v = q/(MW)$, the abbreviated analysis of Sec. 4.2.1 picks up from this point with Eq. (4.16).

Note B: Full Derivation for Well-Resolved Objects with Square Geometry

For the square case, we convert from polar to Cartesian coordinates using the relationships $x = r \cos(\theta)$ and $y = r \sin(\theta)$. By invoking separability, this conversion allows us to work in only one dimension and arrive at

$$\begin{aligned} \sigma_c^2 = & \frac{1}{\Phi^2} \int_{-\infty}^{\infty} \int_{-\infty}^{\infty} x_1 x_2 \langle I(x_1) \rangle \langle I(x_2) \rangle \mu_I(x_2 - x_1) dx_2 dx_1 \\ & \times \int_{-\infty}^{\infty} \int_{-\infty}^{\infty} \langle I(y_1) \rangle \langle I(y_2) \rangle \mu_I(y_2 - y_1) dy_2 dy_1 \end{aligned} \quad (4.49)$$

in place of Eq. (4.13). Introducing the same sum and difference vectors as in Appendix A gives us the following substitutions:

$$\begin{cases} x_1 = p_x - q_x/2 \\ y_1 = p_y - q_y/2 \\ x_2 = p_x + q_x/2 \\ y_2 = p_y + q_y/2 \\ x_1 x_2 = p_x^2 - q_x^2/4 \end{cases}, \quad (4.50)$$

Then we have

$$\begin{aligned} \sigma_c^2 = & \frac{1}{\Phi^2} \int_{-\infty}^{\infty} \mu_I(q_x) \int_{-\infty}^{\infty} \left(p_x^2 - \frac{q_x^2}{4} \right) \langle I\left(p_x - \frac{q_x}{2}\right) \rangle \langle I\left(p_x + \frac{q_x}{2}\right) \rangle dp_x dq_x \\ & \times \int_{-\infty}^{\infty} \mu_I(q_y) \int_{-\infty}^{\infty} \langle I\left(p_y - \frac{q_y}{2}\right) \rangle \langle I\left(p_y + \frac{q_y}{2}\right) \rangle dp_y dq_y \end{aligned} \quad (4.51)$$

With a square object of width W we now have

$$\begin{cases} \langle I(\mathbf{p} - \mathbf{q}/2) \rangle = \bar{I} \text{rect} [(\mathbf{p} - \mathbf{q}/2) / (MW)] \\ \langle I(\mathbf{p} + \mathbf{q}/2) \rangle = \bar{I} \text{rect} [(\mathbf{p} + \mathbf{q}/2) / (MW)] \end{cases} \quad (4.52)$$

in the image plane. Making the same second change of variables as in Appendix A, Eq. (4.51) becomes

$$\begin{aligned} \sigma_c^2 = & \frac{\bar{I}^2 (MW)^6}{\bar{\Phi}^2} \int_{-\infty}^{\infty} \mu_I(v_x) \int_{-\infty}^{\infty} \left(u_x^2 - \frac{v_x^2}{4}\right) \text{rect}\left(u_x - \frac{v_x}{2}\right) \text{rect}\left(u_x + \frac{v_x}{2}\right) du_x dv_x \\ & \times \int_{-\infty}^{\infty} \mu_I(v_y) \int_{-\infty}^{\infty} \text{rect}\left(u_y - \frac{v_y}{2}\right) \text{rect}\left(u_y + \frac{v_y}{2}\right) du_y dv_y. \end{aligned} \quad (4.53)$$

Establishing limits of integration,

$$\left|u_x - \frac{v_x}{2}\right| \leq \frac{1}{2} \Rightarrow \frac{v_x - 1}{2} \leq u_x \leq \frac{v_x + 1}{2}, \quad (4.54)$$

$$\left|u_x + \frac{v_x}{2}\right| \leq \frac{1}{2} \Rightarrow -\frac{1 + v_x}{2} \leq u_x \leq \frac{1 - v_x}{2}, \quad (4.55)$$

$$\left|u_y - \frac{v_y}{2}\right| \leq \frac{1}{2} \Rightarrow \frac{v_y - 1}{2} \leq u_y \leq \frac{v_y + 1}{2}, \quad (4.56)$$

and

$$\left|u_y + \frac{v_y}{2}\right| \leq \frac{1}{2} \Rightarrow -\frac{1 + v_y}{2} \leq u_y \leq \frac{1 - v_y}{2}. \quad (4.57)$$

Given that both v_x and v_y can range from -1 to 1 , Fig. 4.7 provides a visual for this set of integral bounds when $0 < \{v_x, v_y\} < 1$. In turn, Eq. (4.53) becomes

$$\begin{aligned} \sigma_c^2 = & \frac{\bar{I}^2 (MW)^6}{\bar{\Phi}^2} \left[\int_{-1}^0 \mu_I(v_x) \int_{-(1+v_x)/2}^{(v_x+1)/2} \left(u_x^2 - \frac{v_x^2}{4}\right) du_x dv_x \right. \\ & \left. + \int_0^1 \mu_I(v_x) \int_{(v_x-1)/2}^{(1-v_x)/2} \left(u_x^2 - \frac{v_x^2}{4}\right) du_x dv_x \right] \\ & \times \left[\int_{-1}^0 \mu_I(v_y) \int_{-(1+v_y)/2}^{(v_y+1)/2} du_y dv_y + \int_0^1 \mu_I(v_y) \int_{(v_y-1)/2}^{(1-v_y)/2} du_y dv_y \right], \end{aligned} \quad (4.58)$$

and solving its interior integrals gives us

$$\begin{aligned} \sigma_c^2 = \frac{\bar{I}^2 (MW)^6}{\bar{\Phi}^2} & \left[\int_{-1}^0 \frac{1}{12} (1 + 3v_x - 2v_x^2) \mu_I(v_x) dv_x \right. \\ & \left. + \int_0^1 \frac{1}{12} (1 - 3v_x + 2v_x^2) \mu_I(v_x) dv_x \right] \\ & \times \left[\int_{-1}^0 (1 + v_y) \mu_I(v_y) dv_y + \int_0^1 (1 - v_y) \mu_I(v_y) dv_y \right] \end{aligned} \quad (4.59)$$

or

$$\sigma_c^2 = \frac{\bar{I}^2 (MW)^6}{3\bar{\Phi}^2} \int_0^1 (1 - 3v_x + 2v_x^2) \mu_I(v_x) dv_x \int_0^1 (1 - v_y) \mu_I(v_y) dv_y \quad (4.60)$$

by symmetry. Now recalling that a square aperture gives us

$$\mu_I(q) = \text{sinc}^2\left(\frac{D}{\lambda Z_2} q\right) \quad (4.61)$$

and again $v = q/(MW)$, Eq. (4.21) picks up from this point in Sec. 4.2.1.

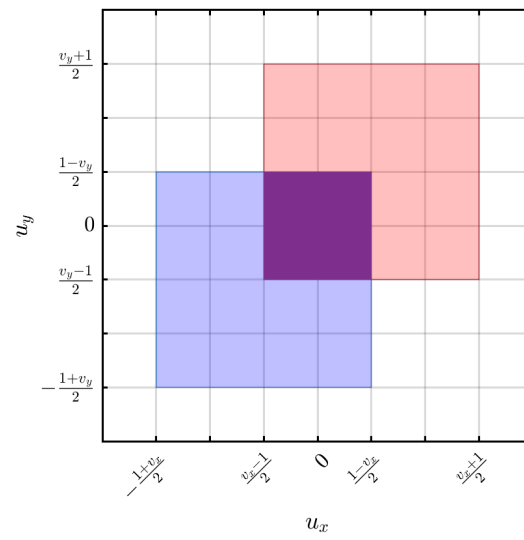


Figure 4.7: Visualization of overlap-integral computation for a square rough-surface object; limits are shown for $0 < \{v_x, v_y\} < 1$.

CHAPTER 5

Open-Loop Wavefront Sensing in the Presence of Speckle and Weak Scintillation
Over Horizontal Paths[†]**5.1 Background**

In many applications of free-space optics (FSO), it is necessary to accurately characterize the phase aberrations due to atmospheric turbulence. Knowledge of a wavefront in the pupil plane enables phase compensation by either physical or computational means, ultimately improving image quality or beam propagation. A conventional wavefront sensor requires some sort of beacon to provide a reference wave for measurement and reconstruction. When available, natural guide stars serve as idealized point-source beacons that sample the atmosphere from space to ground with high fidelity. Often the only option along a horizontal path, however, is to create an artificial beacon that may or may not be cooperative in nature.

An end-to-end FSO communications link has the luxury of including a cooperative beacon on the receiver side for wavefront sensing and precompensation at the transmitter. Long-range imaging, on the other hand, typically calls for projection of a noncooperative beacon from the receiver to the object plane. The beacon in this scenario is subject to both diffractive and refractive beam spreading, atmospheric beam wander, and irradiance fades (i.e., scintillation) resulting from uplink turbulence. Together these effects give rise to a nonuniform, extended source that randomly varies its centroid position in the object plane. As other works have previously explored centroiding limitations due to beam wander [91] and scintillation [76] in horizontal geometries, we restrict our discussion here to the impact of beam spreading on wavefront-sensor performance. Moreover, we limit the scope of this

[†]This material is currently undergoing submission in draft form to *Optics Communications* with coauthors M. F. Spencer and R. G. Driggers.

work to a Shack–Hartmann wavefront sensor (SHWFS) for its robust operation with high dynamic range.

One significant problem associated with extended-source beacons is that all naturally reflective objects possess optically rough surfaces. Wavelength-scale roughness produces an interference pattern called speckle upon propagation back to the receiver plane, along with phase delays that become irretrievably coupled with the turbulence-induced aberrations of interest. These two phenomena generate additional irradiance fluctuation and centroid motion, respectively, in the point-spread functions (PSFs) of an SHWFS image plane. Larger beacons in general correspond to smaller pupil-plane speckles, and therefore greater severity of measurement corruption. Allan *et al.* have studied this problem extensively by quantifying speckle noise in a ground-to-space configuration [85], but the equivalent horizontal-path arrangement remains relatively unexplored.

Another negative consequence of extended-source beacons, unique to the case of distributed-volume turbulence across horizontal paths, is beacon anisoplanatism. This phenomenon is an extension of angular anisoplanatism, whereby the offset in angular position between the beacon and object of interest (or the beacon and projected aimpoint) leads to two different paths through turbulence from the receiver’s perspective. Rather than a single offset, an extended beacon subtends many such paths as it comprises a collection of spherical wavelets per the Huygens–Fresnel principle. In effect, each of these paths samples a slightly different cone of atmospheric turbulence and undergoes different field distortions that introduce shift-varying PSFs. These distorted fields add incoherently in a process called path averaging to produce the image-plane intensity centroids and subsequent pupil-plane phase reconstruction [92]. Even in the absence of speckle, inverting the path-averaged phase function from an optically smooth extended beacon would compare unfavorably to an ideal point source.

In wavefront sensing with artificial beacons, it is standard practice to buy back performance by averaging out speckle however possible; i.e., leveraging speckle diversity through system dynamics [85], spatial decoherence [93], temporal decoherence

[81], depolarization [94] or some combination thereof [16]. Figure 5.1 illustrates the benefits of achieving speckle diversity through any of these mechanisms, with the speckle-averaged wavefront in turbulence converging to the wavefront aberrations from turbulence alone. Unfortunately, beacon anisoplanatism leaves a system vulnerable to path averaging that compounds with other forms of averaging and diminishes system stability overall. In what follows, we explore this tradeoff by first explaining the theory of wavefront error and irradiance skewness as SHWFS defect functions, then quantifying these functions both in vacuum and in weak scintillation through a wave-optics simulation campaign, before finally discussing results and offering conclusions based on our findings.

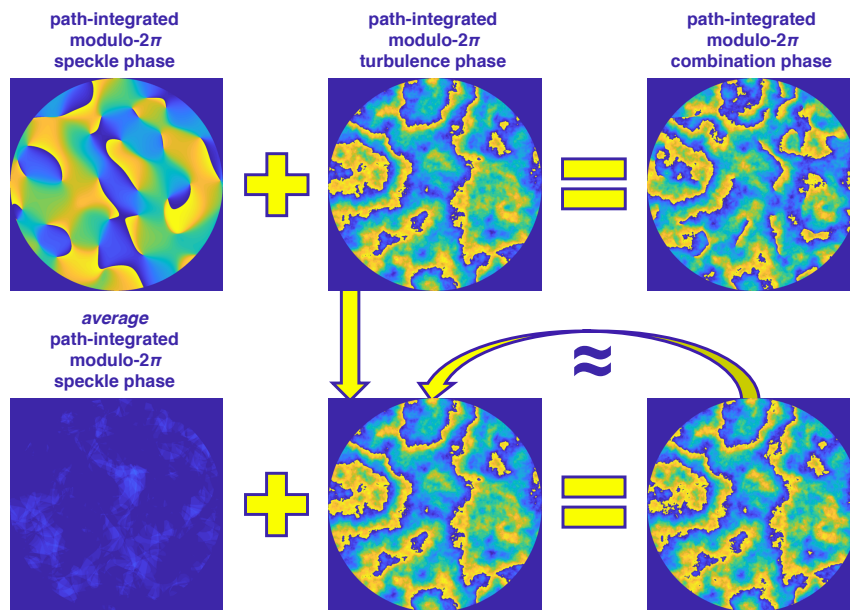


Figure 5.1: Example overview of combined phase aberrations due to rough-surface scattering and weak scintillation, both (top row) without and (bottom row) with intraframe speckle averaging.

5.2 Background and Theory

Despite a growing interest in alternative sensing modalities (e.g., pyramid and curvature wavefront sensors), the SHWFS has maintained its reputation for technological

readiness that helps us ground our results and establish a baseline understanding of performance limits. We assume in our model that each subaperture is a square of roughly Fried’s coherence diameter (r_0) in width, and the extended beacon is square in shape as well. The subapertures are defined by a lenslet array in the x - y plane. Our approach to speckle mitigation in this paper is impose motion on the beacon object such that speckle decorrelates from one frame to the next. For reasons we will explain in Sec. 5.3, we choose to implement speckle decorrelation specifically by translating the rough surface underlying the beacon light a distance $\Delta\Omega$ in the object plane. We make the assumption throughout this paper that all speckle realizations are of equal average irradiance I_0 , and that speckle is fully developed on a frame-by-frame basis such that $\sigma_I = I_0$.

5.2.1 Wavefront Error

In a recent journal publication, we analytically derived closed-form scaling laws that predict centroid-tracking performance in the limit of speckle noise [72]. Quantifying single-aperture track error by a noise-equivalent angle (NEA), we found that solutions depend only on object size. It is common to express the latter quantity as an object Fresnel number, which for a multi-subaperture SHWFS is

$$n_{\text{obj}} = \frac{W/Z_1}{\lambda/d}. \quad (5.1)$$

Here, W is the transverse object width, Z_1 is the longitudinal distance from object to pupil plane, λ is the wavelength of light, and d is the width of a subaperture. The numerator and denominator of Eq. (5.1) represent the object angular extent and full-width-at-half-max (FWHM) subaperture diffraction angle, respectively. Rearranging variables,

$$n_{\text{obj}} = \frac{d}{\lambda Z_1/W} \quad (5.2)$$

also counts the approximate number of speckles across the width of a subaperture (since its denominator is on the order of pupil-plane speckle width [95]). We gener-

ally refer to n_{obj} as a subaperture–object Fresnel number as a way of differentiating it from the usual full-aperture metric. Normalizing to the subaperture diffraction angle, we found in our analysis that NEA is approximately

$$\frac{\sigma_{\theta}}{\lambda/d} = \left(3.54 + \frac{2.11}{n_{\text{obj}}} \right)^{-1} \quad (5.3)$$

in the case of a square beacon and square subapertures. Equation (5.3) saturates at a value of ~ 0.289 .

Our main goal in this paper is to quantify standard deviations in wavefront slope from subaperture to subaperture, measured in optical path difference (OPD) and normalized to wavelength ($\sigma_{\text{wf}}/\lambda$). The slope or gradient of phase function ϕ in the x direction is

$$\begin{aligned} g &= \frac{\partial \phi}{\partial x} \\ &= k\theta, \end{aligned} \quad (5.4)$$

where $k = 2\pi/\lambda$ is the angular wavenumber,

$$\theta = \frac{\Delta z}{d} \quad (5.5)$$

is the angle of wavefront tilt and Δz is the OPD between opposite edges of a subaperture. Noting that Eqs. (5.1)–(5.5) assume the paraxial approximation holds true,

$$\frac{\theta}{\lambda/d} = \frac{\Delta z}{\lambda}, \quad (5.6)$$

which gives the needed equivalence with Eq. (5.3):

$$\frac{\sigma_{\text{wf}}}{\lambda} = \left(3.54 + \frac{2.11}{n_{\text{obj}}} \right)^{-1}. \quad (5.7)$$

In vacuum propagation to the far field, phase function ϕ describes a perfectly flat

wavefront. Thus any nonzero σ_{wf} is due to speckle and indicates deviation from ground truth. In turbulence, however, the ground truth consists of atmospheric aberrations with speckle acting as bias in the estimator. We therefore refer to σ_{wf} as root-mean-square (RMS) wavefront *error* in the case of speckle only, and as RMS wavefront *aberration* when both speckle and turbulence are present.

5.2.2 Speckle Contrast

Equation (5.7) provides an estimate for normalized σ_{wf} when speckle is fully developed. If averaging together M fully uncorrelated speckle realizations, we can expect σ_{wf} to scale inversely with the square root of M [85]. What we still lack is a method of estimating σ_{wf} when speckle only partially decorrelates between frames. Speckle contrast,

$$C = \frac{\sigma_I/\bar{I}}{\sqrt{M}}, \quad (5.8)$$

takes on a value between 0 and 1 where σ_I and \bar{I} are the standard deviation and mean irradiance, respectively [16]. Because of this built-in normalization and the fact that C scales in the way as σ_{wf} , we can use it as a scale factor to modify our expected wavefront error/aberration as

$$\sigma'_{\text{wf}} = C\sigma_{\text{wf}}. \quad (5.9)$$

Taking a similar approach to Egge *et al.* [96] in the context of speckle reduction for laser projection displays, we derive our own equation for modified speckle contrast the applies to successive speckle realizations presented to the pupil plane with mutual partial correlation. Considering how the total irradiance detected at a point in space is

$$\Sigma I = \sum_{m=1}^M I_m, \quad (5.10)$$

where I_m is the m th of M total speckle patterns in a sum, the speckle contrast of

our final sum is then

$$C = \frac{\sigma_{\Sigma I}}{\overline{\Sigma I}}. \quad (5.11)$$

The Bienaymé formula tells us that irradiance variance is [97]

$$\begin{aligned} \text{var}(\Sigma I) &= \sum_{m=1}^M \text{var}(I_m) + 2 \sum_{m<n} \text{cov}(I_m, I_n) \\ &= \sum_{m=1}^M \text{var}(I_m) + 2 \sum_{m<n} \text{cor}(I_m, I_n) \sqrt{\text{var}(I_m) \text{var}(I_n)} \\ &= I_0^2 \left[M + 2 \sum_{m<n} \mu_I(I_m, I_n) \right] \end{aligned} \quad (5.12)$$

where $\mu_I(I_m, I_n)$ is the irradiance correlation coefficient between a pair of consecutive subframes, while

$$\begin{aligned} \overline{\Sigma I} &= \sum_{m=1}^M \overline{I_m} \\ &= MI_0 \end{aligned} \quad (5.13)$$

follows from linearity of expectation [98]. Note that Eq. (5.12) makes use of the framewise fully developed assumption that $\sigma_I = I_0$. Then according to Eq. (5.11),

$$C = \frac{[M + 2 \sum_{m<n} \mu_I(I_m, I_n)]^{1/2}}{M}. \quad (5.14)$$

Simplifying further,

$$\begin{aligned} \sum_{m<n} \mu_I(I_m, I_n) &= (M-1) \mu_I(\Delta\Omega_0) + (M-2) \mu_I(2\Delta\Omega_0) \\ &\quad + \cdots + \mu_I[(M-1)\Delta\Omega_0], \end{aligned} \quad (5.15)$$

such that

$$C = \frac{\left[M + 2 \sum_{m=1}^{M-1} (M-m) \mu_I(m\Delta\Omega_0) \right]^{1/2}}{M}. \quad (5.16)$$

Since equations for $\mu_I(\circ)$ are highly nonlinear with potentially many sidelobes, we cannot generalize beyond the series notation of Eq. (5.16); solving algorithmically is rather straightforward as shown in Alg. 1.

Algorithm 1 Calculation of speckle contrast for a sum of M partially correlated frames.

Require: $M \in \mathbb{N}, \Delta\Omega_0 \geq 0$ ▷ frame count, translation distance

Ensure: $0 \leq C \leq 1$ ▷ speckle contrast

procedure SPECKLECONTRAST($M, \Delta\Omega_0$)

$B \leftarrow 0$

for $m = 1$ to $M - 1$ **do**

$B \leftarrow B + (M - m) \mu_I(m\Delta\Omega_0)$

end for

$C \leftarrow \sqrt{M + 2B} \div M$

return C

end procedure

Since we are assuming a square beacon, our formula for the pupil-plane irradiance coefficient is

$$\mu_I(\Delta\Omega) = \text{sinc}^2\left(\frac{W\Delta\Omega}{\lambda Z_1}\right) \text{tri}^2\left(\frac{\Delta\Omega}{W}\right) \quad (5.17)$$

where

$$\text{sinc}(w) = \frac{\sin(\pi w)}{\pi w} \quad (5.18)$$

and

$$\text{tri}(w) = \begin{cases} 1 - |w| & |w| < 1 \\ 0 & |w| \geq 1 \end{cases}. \quad (5.19)$$

The first and second factors in Eq. (5.17) are attributed to translation and boil of the

speckle pattern, respectively [95, 99]. We determine our initial translation distances $\Delta\Omega_0$ by numerically solving Eq. (5.17) for 25%, 50%, 75% and 100% decorrelation of speckle between frames. Then by substituting Eq. (5.17) into Eq. (5.16) and using the result with Eqs. (5.7) in Eq. (5.9), we produce the plots in Fig. 5.2 and theoretically predict from them modified RMS wavefront error with intraframe averaging of partially correlated speckle. As one would expect, mitigation is most efficient when frame-to-frame decorrelation is at its maximum. We note, however, that there is more nuance to Fig. 5.2d than a simple reduction by \sqrt{M} , the reason being only consecutive frames are 100% decorrelated from one another while certain subsequent frames occupy the sidelobes. This detail sets our simulations of 100% decorrelation apart from the common assumption of mutually uncorrelated frames. Even so, we can very loosely approximate the error reduction by a factor of $\sqrt{(1 - \mu_I) M}$.

5.2.3 Kolmogorov Turbulence

Because we are interested in propagation of speckle fields both through vacuum and through turbulence, we briefly review the theory of physical quantities that parameterize our atmospheric conditions. Arguably the most critical of these for our purposes is the Rytov number, which for a spherical wave is [100]

$$\begin{aligned} \mathcal{R}_{\text{sw}} &= 0.563k^{7/6} \int_0^{Z_1} C_n^2(z) \left[z \left(1 - \frac{z}{Z_1} \right) \right]^{5/6} dz \\ &\xrightarrow{\text{horiz.}} 0.124k^{7/6} C_n^2 Z_1^{11/6} \end{aligned} \quad (5.20)$$

where the second line corresponds to a horizontal path assuming constant refractive-index structure parameter C_n^2 . As for the other variables in Eq. (5.20), $k = 2\pi/\lambda$ is the angular wavenumber and z is an arbitrary point along the path of length Z_1 . Throughout this study we restrict our attention to weak scintillation conditions with $\mathcal{R}_{\text{sw}} \lesssim 0.25$, as scintillation begins to saturate at higher Rytov numbers and branch points in the phase function due to total-destructive interference eventually sabotage our ability to perform phase compensation effectively [101, 102, 103, 104, 105]. In

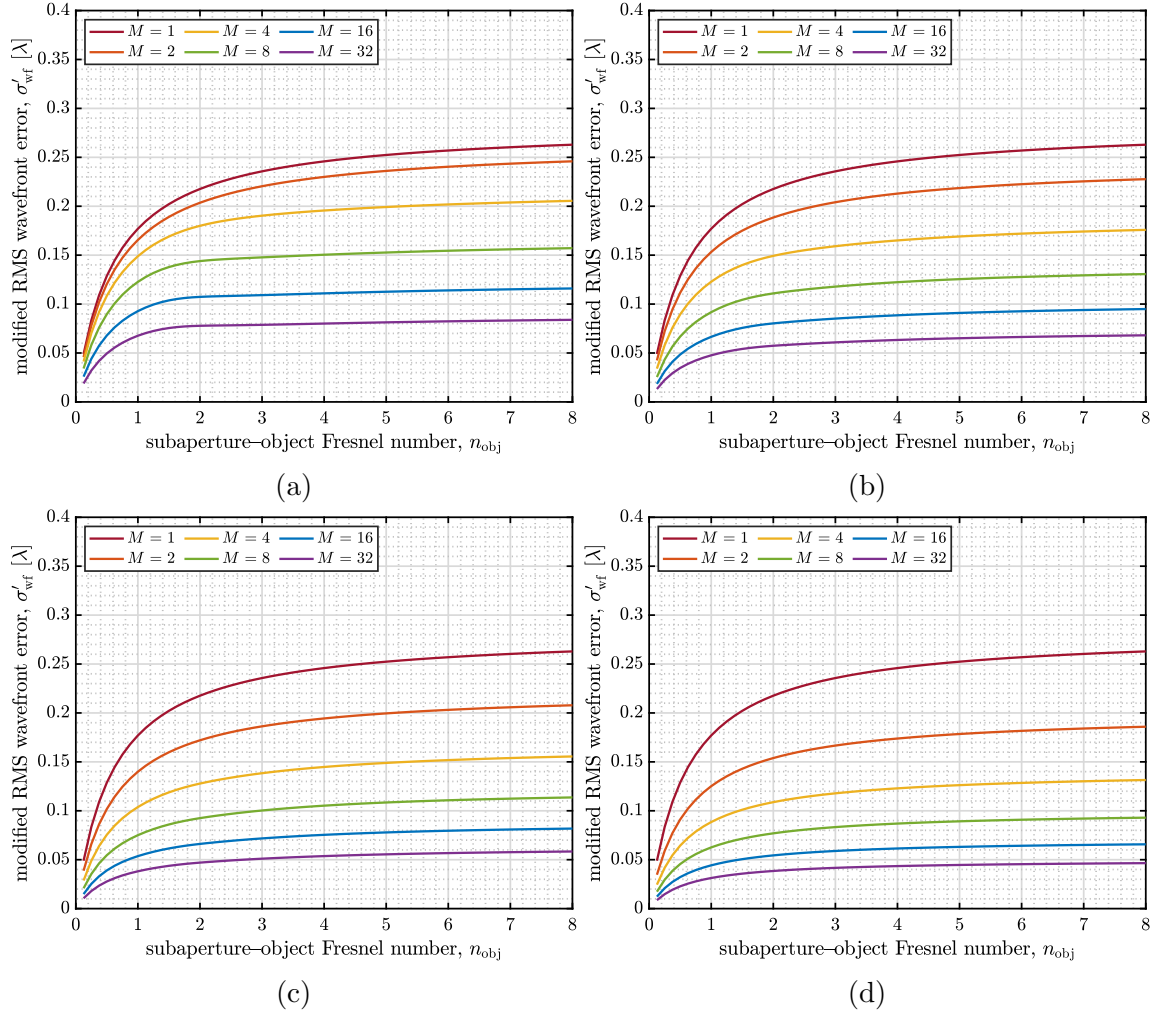


Figure 5.2: Theoretical expectation of RMS wavefront error calculated from Eq. (5.9) for various subaperture-object Fresnel numbers and levels of intraframe averaging with (a) $\mu_I = 75\%$, (b) $\mu_I = 50\%$, (c) $\mu_I = 25\%$, and (d) $\mu_I = 0\%$.

this regime, \mathcal{R}_{sw} also provides an estimation for log-amplitude variance (σ_χ^2) in the pupil plane [106]—the recent analysis of Beck et al. is particularly insightful [107].

The Fried parameter (r_0) is the diameter of a circle in the pupil plane over which phase variance due to turbulence is no greater than $\sim 1 \text{ rad}^2$. Its value for a spherical wave is [108, 109]

$$r_{0,\text{sw}} = \left[0.423k^2 \int_0^{Z_1} C_n^2(z) \left(\frac{z}{Z_1} \right)^{5/3} dz \right]^{-3/5} \quad (5.21)$$

$$\xrightarrow{\text{horiz.}} (0.159k^2 C_n^2 Z_1)^{-3/5},$$

with turbulence-limited atmospheric seeing limited to a blur angle of λ/r_0 rather than the diffraction limit of λ/D . The ratio D/r_0 therefore serves as another gauge of turbulence strength, with smaller values indicating weaker turbulence. Subaperture width d should be on the order of r_0 such that localized phase is predominantly wavefront tilt, with turbulence-induced wavefront aberration directly related to the ratio d/r_0 [110]. Applying Shaw and Tomlinson's treatment on analytic propagation variances, we can quantify the object-plane centroid motion associated with this aberration as [111, 112]

$$\begin{aligned} \sigma_c^2 &= 0.652C_n^2 \int_0^{Z_1} (Z_1 - z)^2 \int_0^\infty \kappa^{-2/3} \text{somb}^2 \left[d \left(1 - \frac{z}{Z_1} \right) \kappa \right] d\kappa dz \\ &= 0.577 \frac{C_n^2 Z_1^3}{d^{1/3}} \end{aligned} \quad (5.22)$$

in uniform turbulence with

$$\text{somb}(\rho) = 2 \frac{J_1(\pi\rho)}{\pi\rho}. \quad (5.23)$$

Rearranging Eq. (5.21) to make the substitution

$$C_n^2 = 0.160 \frac{\lambda^2}{Z_1 r_0^{5/3}}, \quad (5.24)$$

taking the square root for standard deviation, multiplying by transverse magnification $M = Z_2/Z_1$ and dividing by FWHM PSF width $\lambda Z_2/d$ [113], we find the normalized centroid jitter to be

$$\frac{\sigma_\theta}{\lambda/d} = 0.303 \left(\frac{d}{r_0} \right)^{5/6}. \quad (5.25)$$

Although the above derivation assumes circularly symmetric aperture stops, Eq. (5.25) provides us with a rough estimate of normalized RMS wavefront aberration for a point source in turbulence.

In dealing with extended beacons we must also consider the isoplanatic angle (θ_0), an angular extent over which path differences from beacon to pupil induce at most ~ 1 rad² of mean-squared wavefront error. This angle is independent of wavefront shape, with a value of [114]

$$\theta_0 = \left[2.91k^2 \int_0^{Z_1} C_n^2(z) z^{5/3} dz \right]^{-3/5} \quad (5.26)$$

$$\xrightarrow{\text{horiz.}} \left(1.09k^2 C_n^2 Z_1^{8/3} \right)^{-3/5}.$$

Multiplying Eq. (5.26) by path length Z_1 defines the isoplanatic patch of width $W_0 \approx 0.314r_0$ in the object plane given uniform turbulence. In the open-loop domain, we are concerned only with these spatial (and not temporal) characteristics of the atmosphere.

5.2.4 Irradiance Skewness

The presence of speckle contaminating slope measurements means we cannot reconstruct the proper wavefront information for phase compensation. We often rely on point-source performance as a benchmark to study speckle mitigation in modeling and simulation, but in field experiments the effects of speckle and turbulence are not easily decoupled. We do have the option, however, of analyzing pupil-plane irradiance statistics in real time to explore the useful limits of speckle averaging [115].

A fully developed speckle pattern follows the well-known negative exponential probability density function (PDF) [16]

$$p_I(I) = \frac{1}{\bar{I}} \exp\left(-\frac{I}{\bar{I}}\right), \quad (5.27)$$

while a common model for irradiance fluctuations due to weak scintillation is the lognormal PDF [116]

$$p_I(I) = \frac{1}{I\sqrt{2\pi \ln(1 + \sigma_I^2)}} \exp\left[-\frac{\ln^2\left(I\sqrt{1 + \sigma_I^2}/\bar{I}\right)}{2 \ln(1 + \sigma_I^2)}\right]. \quad (5.28)$$

Here, σ_I^2 is the scintillation index; i.e., the variance in irradiance normalized by squared mean irradiance. An advantage of comparing an observed irradiance pattern to Eqs. (5.27) and (5.28) is that the peak value of each PDF is forced on and off the zero-irradiance point, respectively. When unmitigated speckle is present, exponential probability tends to dominate the statistics regardless of turbulence strength. Mitigation through speckle averaging makes the lognormal model a better fit. This behavior is illustrated in Fig. 5.3, where we have simulated propagation through weak scintillation and generated multiple frames of speckle within a single atmospheric coherence time.

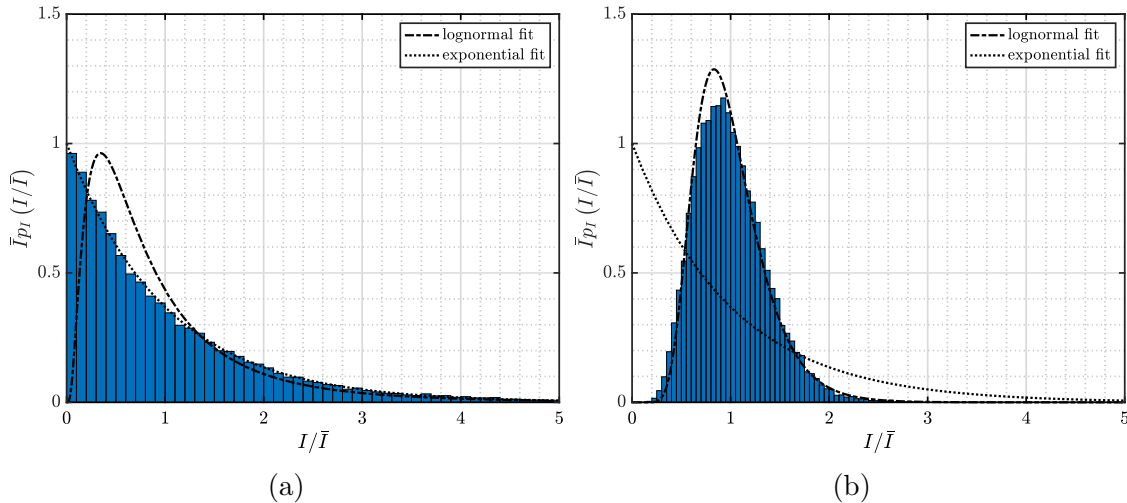


Figure 5.3: Irradiance histograms with lognormal and exponential fits after propagation through weak scintillation of (a) one speckle subframe and (b) eight subframes averaged together. Note a decrease in skewness from (a) to (b).

Under the working assumption that we have sufficiently characterized the atmosphere to ensure weak-turbulence conditions, we can quickly relate the comparison between Eqs. (5.27) and (5.28) to a single moment of the irradiance distribution; namely, the third standardized moment or *skewness*:

$$\gamma_I = \frac{(E [I - \bar{I}])^3}{(\sigma_I^2 \bar{I}^2)^{3/2}} \quad (5.29)$$

The exponential PDF has an associated skewness of 2, while the skewness associated with the lognormal PDF is [116]

$$\begin{aligned} \gamma_I &= \{ \exp [\ln (1 + \sigma_I^2)] + 2 \} \sqrt{\exp [\ln (1 + \sigma_I^2)] - 1} \\ &\approx \{ \exp [\ln (1 + 4\mathcal{R}_{\text{sw}})] + 2 \} \sqrt{\exp [\ln (1 + 4\mathcal{R}_{\text{sw}})] - 1} \end{aligned} \quad (5.30)$$

where σ_I^2 is the scintillation index and is approximately equal to $4\mathcal{R}_{\text{sw}}$ in weak scintillation [106].

Accumulating multiple speckle realizations after propagation through different strengths of simulated turbulence, we calculate Eq (5.29) over each irradiance pattern received and plot the results in Fig. 5.4. We see that skewness settles on a value that increases with turbulence strength in the limit of many averaged speckle frames, but it serves as a useful metric for speckle averaging nonetheless. For this reason, we include skewness calculations in our simulation tradespace as a secondary measure to RMS wavefront error/aberration.

5.2.5 Dynamic Range

Through some basic geometric relationships, one finds that

$$n_{\text{lod}} = \frac{d^2}{\lambda f} \quad (5.31)$$

provides a measure of dynamic range in a SHWFS. Short for “number of lambdas over d ,” n_{lod} counts the maximum waves of tilt across each subaperture without

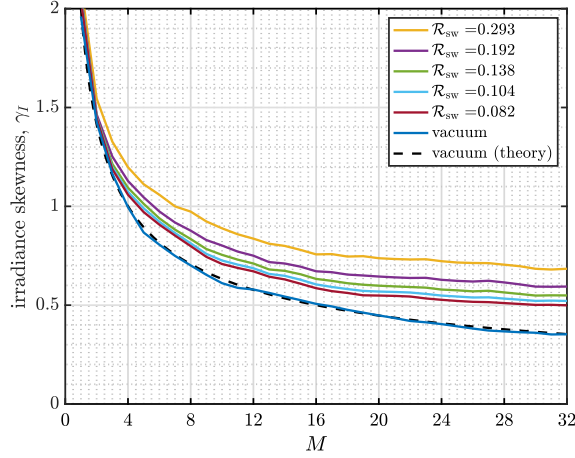


Figure 5.4: Skewness calculated from wave-optics simulation data according to Eq. (5.29) for various levels of intraframe averaging and turbulence strengths (including vacuum).

causing drift into neighboring subapertures. The image of an extended beacon having width W in the far field has width

$$W' = \frac{f}{Z_1} W \quad (5.32)$$

in the image plane. W' must be less than d to prevent drift due to image size, and it is straightforward to show that n_{obj} cannot exceed n_{lod} if this condition is to be met.

5.3 Modeling and Simulation

In this section, we review the simulation setup and methods used in this paper.

5.3.1 Simulation Setup

To begin defining our simulation tradespace, we assume arbitrary but realistic values for beacon wavelength and aperture diameter of 1 μm and 30 cm, respectively. We further assume $D/r_0 = 10$ and $d/r_0 = 1$ for simplicity; greater values of d/r_0 would overly constrain sampling requirements and make it difficult to study extended beacons under isoplanatic conditions. Enforcing the conditions that $\mathcal{R}_{\text{sw}} < 0.25$

per Eq. (5.20) and the isoplanatic patch size exceeds a subaperture–object Fresnel number of at least 1, we arrive at a propagation distance of $Z_1 = 283$ m, a spherical-wave Rytov number of $\mathcal{R}_{\text{sw}} = 0.064$, and an isoplanatic angle of $\theta_0 = 33.3$ μrad . In addition to $n_{\text{obj}} = 1$, we study a range of beacon sizes on either side of the isoplanatic cutoff with subaperture–object Fresnel numbers from $1/8$ to 8. We set $n_{\text{od}} = 8$ in order to accept the largest of these beacon sizes.

With our physical parameter space fully defined, we can begin working with numerical constraints. We define our simulation grid to be of size 2048×2048 , as we find this to be the upper limit on fidelity given available high-performance computing resources and $O(n^2)$ time complexity. Satisfying Nyquist sampling [52], critical sampling [54], and speckle sampling [117] constraints while allowing for nonunity scaling between planes, our sample spacing in the object, pupil and image planes is 259, 534 and 103 μm , respectively. Table 5.1 outlines the full set of physical and numerical parameters in our simulations.

5.3.2 Simulation Methods

We now turn our attention implementing speckle decorrelation between successive frames. In general, in-plane translation and out-of-plane translation are most straightforward in that decorrelation is uniform across the pupil in both cases [95]. If we were to choose the latter, pupil-plane phase would repeat itself whenever the coarse phase tilt simulated across the object is a multiple of $\lambda/(2\delta_{\text{obj}}) = 0.111^\circ$ according to Table 5.1. As Fig. 5.5a shows, it would therefore take only 5 frames for phase to repeat itself for the smallest object size in the case of full decorrelation.

Instead simulating in-plane translation would allow us to translate indefinitely while drawing continuous random phase without repetition. However, translating in the spatial domain is either limited by pixelwise shifts (making small translations difficult/impossible) or subject to interpolation between phase samples (possibly yielding unphysical results). A way forward, then, is to apply the shift theorem of

Table 5.1: Physical and numerical parameters used in wave-optics simulations of open-loop wavefront sensing.

	parameter	value(s)
physical	optical wavelength, λ [μm]	1
	propagation distance, Z_1 [m]	283
	aperture diameter, D [cm]	30
	subaperture width, d [cm]	3
	subaperture-object Fresnel number, n_{obj}	[1/8, 8]
	lenslet Fresnel number, n_{lod}	8
	lenslet focal length, $f = Z_2$ [m]	113
	refractive-index structure constant, C_n^2 [$\text{m}^{-2/3}$]	1.96×10^{-13}
	spherical-wave Rytov number, \mathcal{R}_{sw}	0.0658
	spherical-wave Fried parameter, r_0 [cm]	3
	isoplanatic angle, θ_0 [μrad]	33.3
	piston-removed isoplanatic angle, θ_1 [μrad]	40.9
numerical	grid points per side, $N \times N$	2048×2048
	object-plane grid spacing, δ_{obj} [μm]	259
	pupil-plane grid spacing, δ_{pup} [μm]	534
	image-plane grid spacing, δ_{img} [μm]	103
	object-plane side length, S_{obj} [mm]	529
	pupil-plane side length, S_{pup} [m]	1.09
	image-plane side length, S_{img} [mm]	211

the Fourier transform as follows:

$$U'(\alpha, \beta) = \mathcal{F}^{-1} \{ \mathcal{F} \{ U(\alpha, \beta) \} \exp [j2\pi (\nu_\alpha \Delta\Omega_\alpha + \nu_\beta \Delta\Omega_\beta)] \}. \quad (5.33)$$

Sample spacing in the Fourier domain is $1/(S_{\text{obj}})$, so repetition doesn't occur until the translation distance is a multiple of $S_{\text{obj}} = 529$ mm. Figure 5.5b shows that, even in the worst case where $\Delta\Omega = 16.5$ mm, we can generate 32 successive frames of speckle decorrelation without repetition by this method.

In the results that follow, we used the WavePlex Toolbox for MATLAB from Prime Plexus¹ to simulate rough-surface scattering, propagation through vacuum or turbulence, wavefront sensing with a SHWFS model in the Fried geometry, and least-squares phase reconstruction. After exposing our SHWFS to the desired number of

¹T. J. Brennan is the sole author of the WavePlex Toolbox for MATLAB[®] with correspondence to the following address: Prime Plexus, 650 N Rose Drive #439, Placentia, CA 92870, USA.

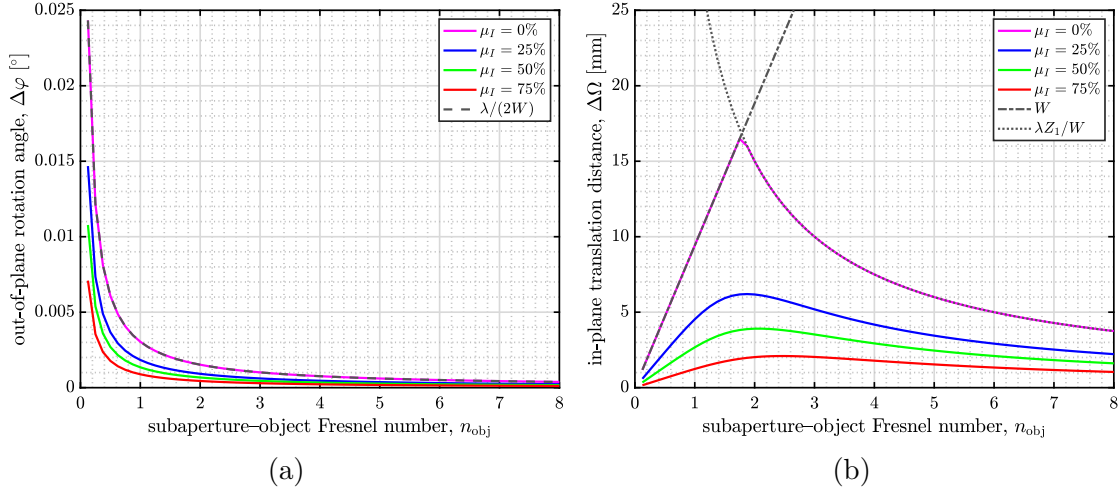


Figure 5.5: Object motion required to achieve various levels of subframe decorrelation based on the parameterization specified in Table 5.1 when the mode of object motion is (a) out-of-plane rotation and (b) in-plane translation.

speckle frames (modified by in-plane translation as described above), we read out the accumulated irradiance to reset the focal plane and reconstructed pupil-plane phase. Taking vector \mathbf{g} to contain all reconstructed phase gradients in the x direction stacked atop those in the y direction, we calculated RMS wavefront error/aberration from simulation data as

$$\sigma_{\text{wf}} = \sqrt{\frac{\sum_{n=1}^{2N_{\text{sub}}} |g_n - \bar{g}|^2}{2N_{\text{sub}} - 1}} \quad (5.34)$$

where N_{sub} is the total number of subapertures in the array. We calculated skewness directly from pupil-plane irradiance according to Eq. (5.29). Each result that we report represents the Monte Carlo average of 40 simulation trials, with error bars indicating standard deviation about the mean. We ran all simulations in parallel across multiple supercomputing clusters consisting of IBM System x, Lenovo NeXtScale and Penguin Computing Altus compute nodes.

5.4 Results and Discussion

Figure 5.6 displays all vacuum results in terms of RMS wavefront error, with curves representing different amounts of intraframe averaging and subfigures corresponding to different amounts of subframe correlation. The general shapes of these curves follow those of Fig. 5.2, although the physics of speckle decorrelation are not perfectly captured according to theory. Still, we see the expected behavior that RMS wavefront error drops off with increased speckle averaging and does so most efficiently with decreased correlation between subframes. In each subfigure, we observe for unmitigated speckle (i.e., $M = 1$) that RMS wavefront error matches Eq. (5.7). We also notice that RMS wavefront error takes on a nonzero value when the beacon is infinitesimally small, suggesting a general mismatch between true phase gradients in the pupil plane and those produced through SHWFS measurement and least-squares reconstruction. As our SHWFS design is unoptimized and based on the study of specific use cases, we remind the reader that such measurement errors are not unexpected [118, 119].

Figure 5.7 contains all vacuum results in terms of skewness, showing some fairly straightforward trends. With unmitigated speckle, skewness climbs to 2 as the aperture–object Fresnel number approaches 10. Although a skewness of 2 is characteristic of the exponential PDF representing fully developed speckle, an adequately large sample size is required for the statistics to reflect this distribution. This observation underscores the importance of monitoring pupil-plane irradiance over the full aperture rather than individual subapertures for meaningful skewness data. Just as with RMS wavefront error, we note that skewness decreases roughly in proportion to $\sqrt{(1 - \mu_I) M}$.

In Fig. 5.8, we reproduce the results of Fig. 5.6 following propagation through weak scintillation rather than vacuum. We see here that our baseline RMS wavefront aberration does indeed follow the prediction of Eq. (5.25) in the point-source case where $n_{\text{obj}} \rightarrow 0$. At higher subaperture–object Fresnel numbers in isoplanatic conditions, jitter adds nearly in quadrature. Take, for instance, the dark red line

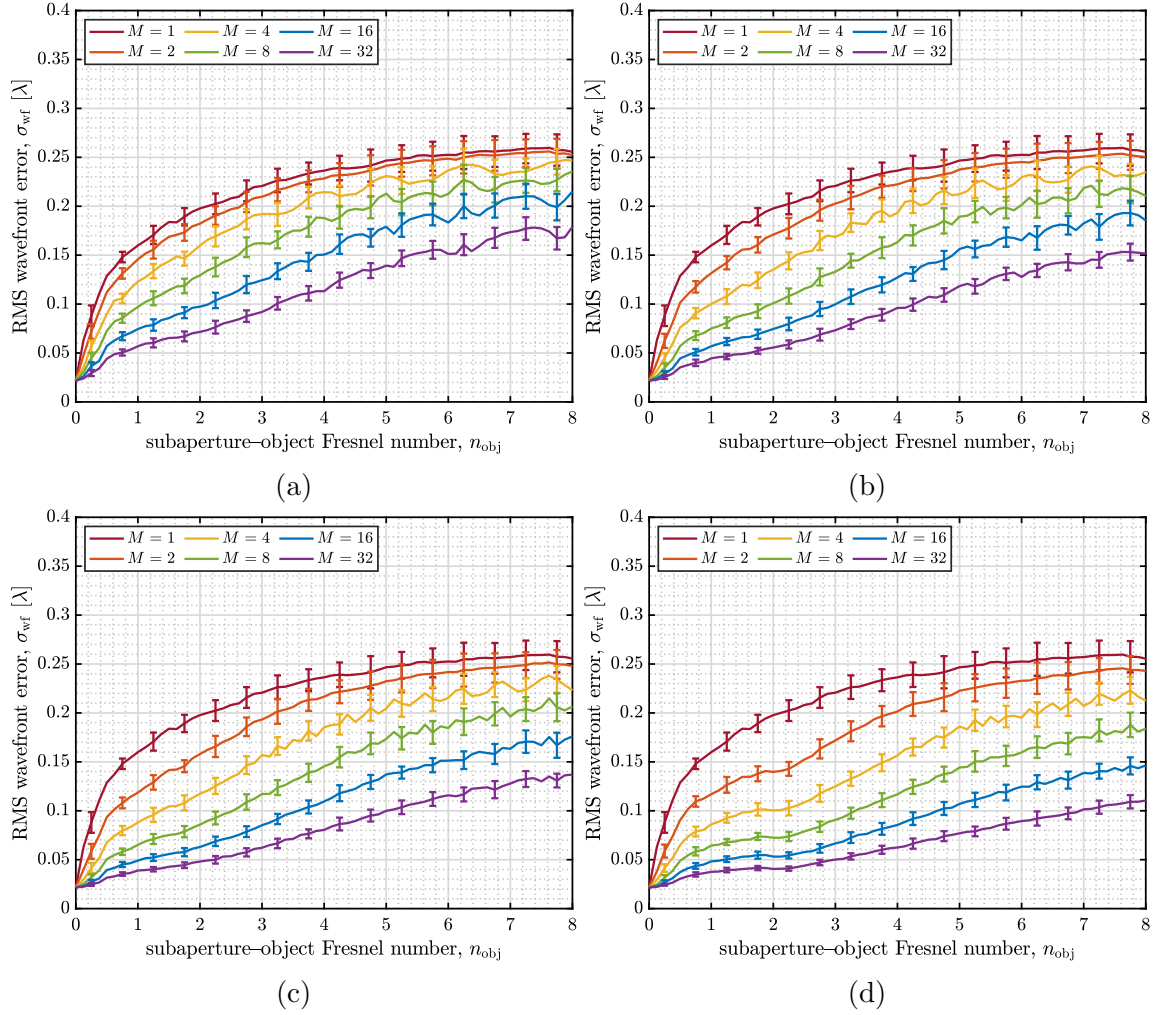


Figure 5.6: RMS wavefront error from subaperture to subaperture after propagating beacons of various sizes through vacuum and averaging together various numbers of subframes at (a) 25%, (b) 50%, (c) 75% and (d) 100% decorrelation.

in any of Figs. 5.8a–5.8d for $M = 1$ and compare at $n_{obj} = 1$ with Eqs. (5.7) and (5.25): $\sqrt{0.177^2 + 0.303^2} \approx 0.351$. As we know from the peer-reviewed literature, turbulence cannot compound the phase perturbations already present in fully developed speckle, but it does introduce compounding amplitude fluctuations that give rise to this uptick in centroid jitter [120]. Looking to larger subaperture-object Fresnel numbers, we now see the effects of beacon anisoplanatism begin to take hold. Whereas wavefront error follows intuition by growing with beacon size in vacuum, it

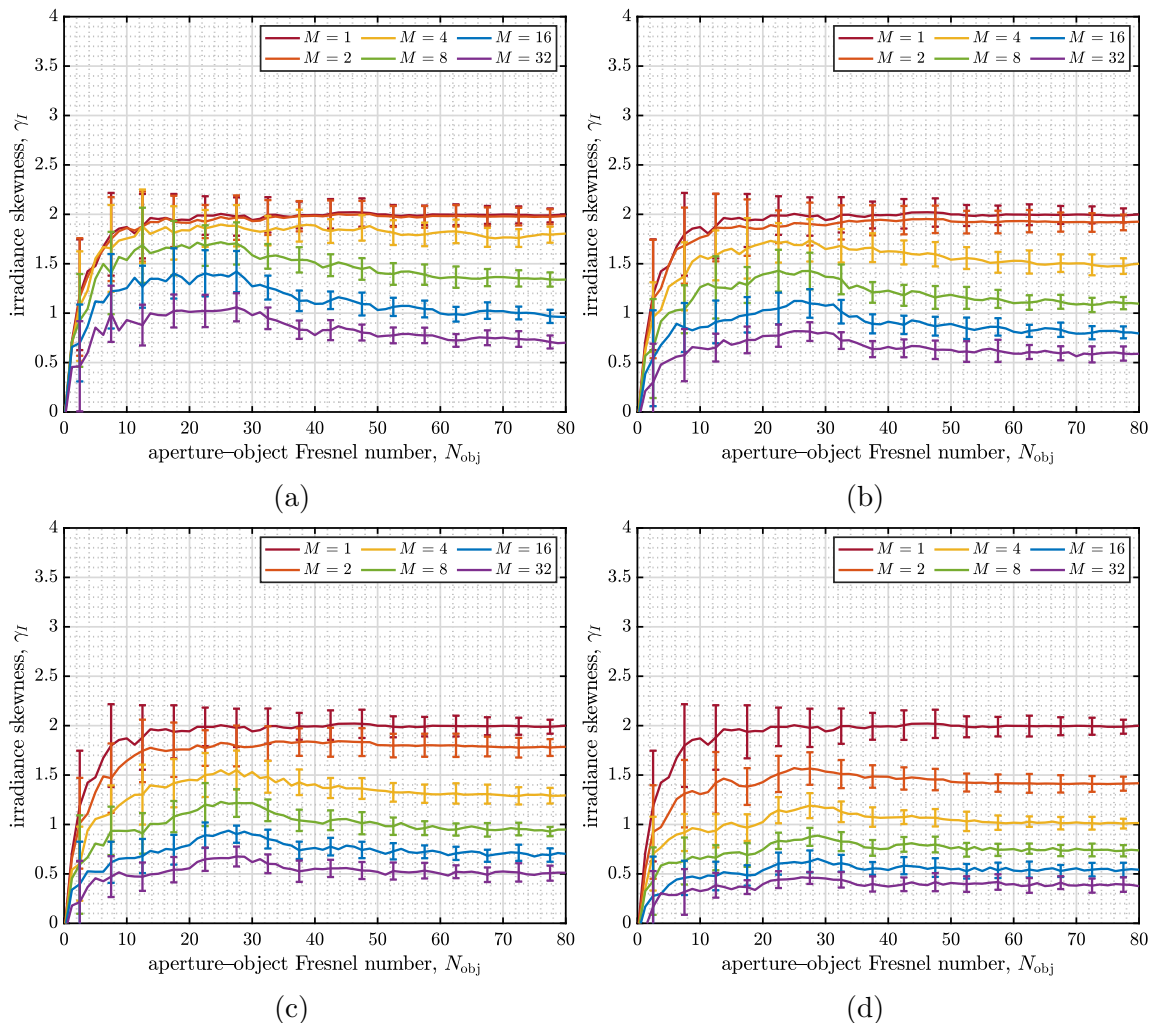


Figure 5.7: Irradiance skewness over the full aperture after propagating beacons of various sizes through vacuum and averaging together various numbers of subframes at (a) 25%, (b) 50%, (c) 75% and (d) 100% decorrelation.

steadily drops in distributed-volume turbulence as the beacon outgrows the isoplanatic patch size by a greater margin. The cause of this behavior is a phenomenon known as path averaging, which describes the aberrations from multiple return paths through the atmosphere summing together and averaging out wavefront aberrations at the receiver [121]. This reduction in overall wavefront aberration is deceptive of course, as it would seem to imply reduced turbulence but actually represents poorer characterization of the ground truth.

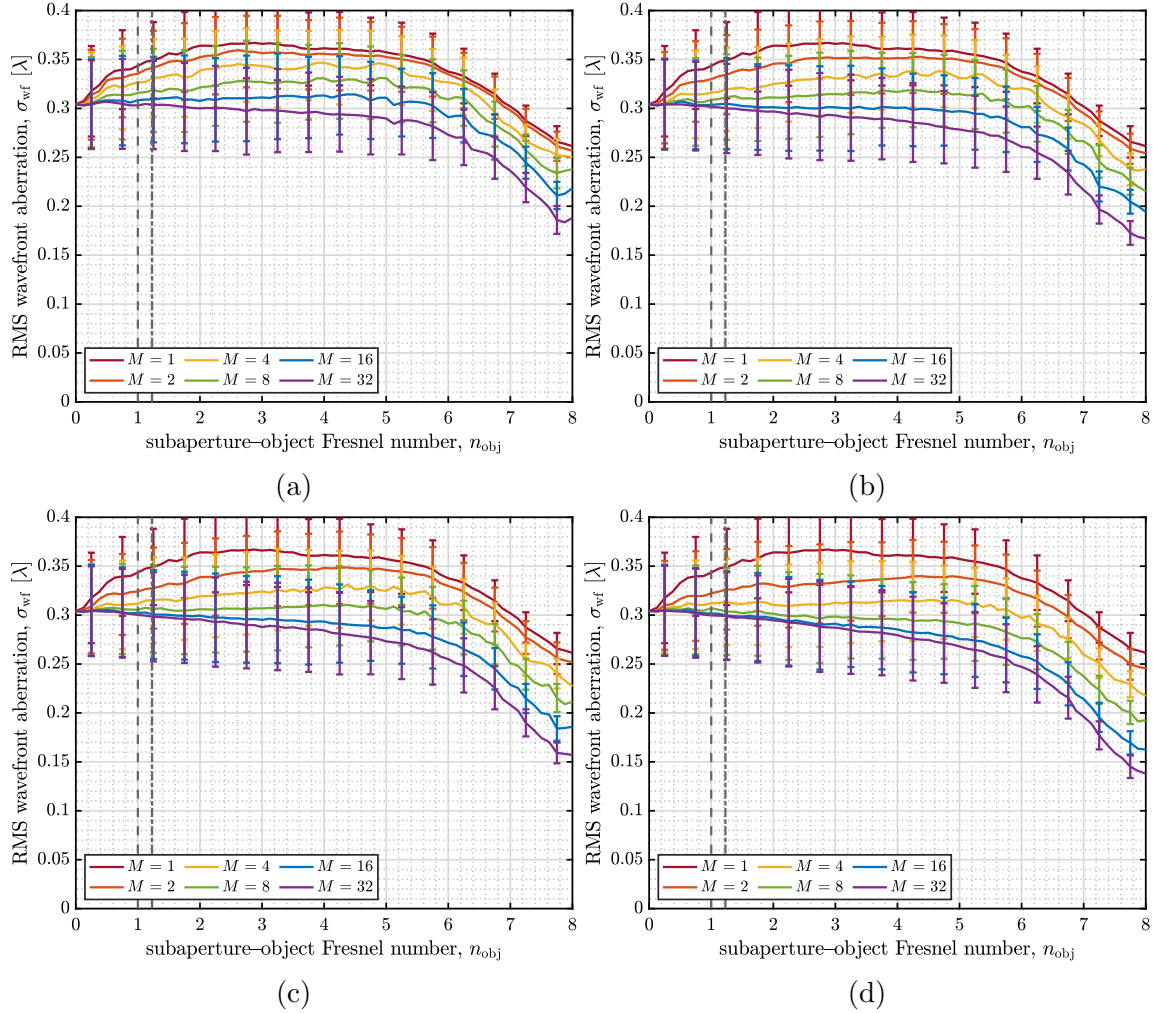


Figure 5.8: RMS wavefront aberration from subaperture to subaperture after propagating beacons of various sizes through weak scintillation and averaging together various numbers of subframes at (a) 25%, (b) 50%, (c) 75% and (d) 100% decorrelation. Vertical dashed and dash-dotted reference lines delineate fully aberrated and piston-removed isoplanatic patch size, respectively.

We see similar trends in Fig. 5.9 as in Fig. 5.8, but we remind the reader that skewness has the advantage of real-time monitoring with comparison between figures while RMS wavefront aberration is only available after readout and reconstruction. Equation (5.30) predicts a point-source skewness of ~ 1.67 , which we closely approximate here as $N_{obj} \rightarrow 0$. We also see a similar reduction across all subaperture-object Fresnel numbers to what we saw in Fig. 5.7, even though reductions in both

wavefront error and skewness are trivial when path averaging occurs due to beacon anisoplanatism and may actually hurt performance in such instances.

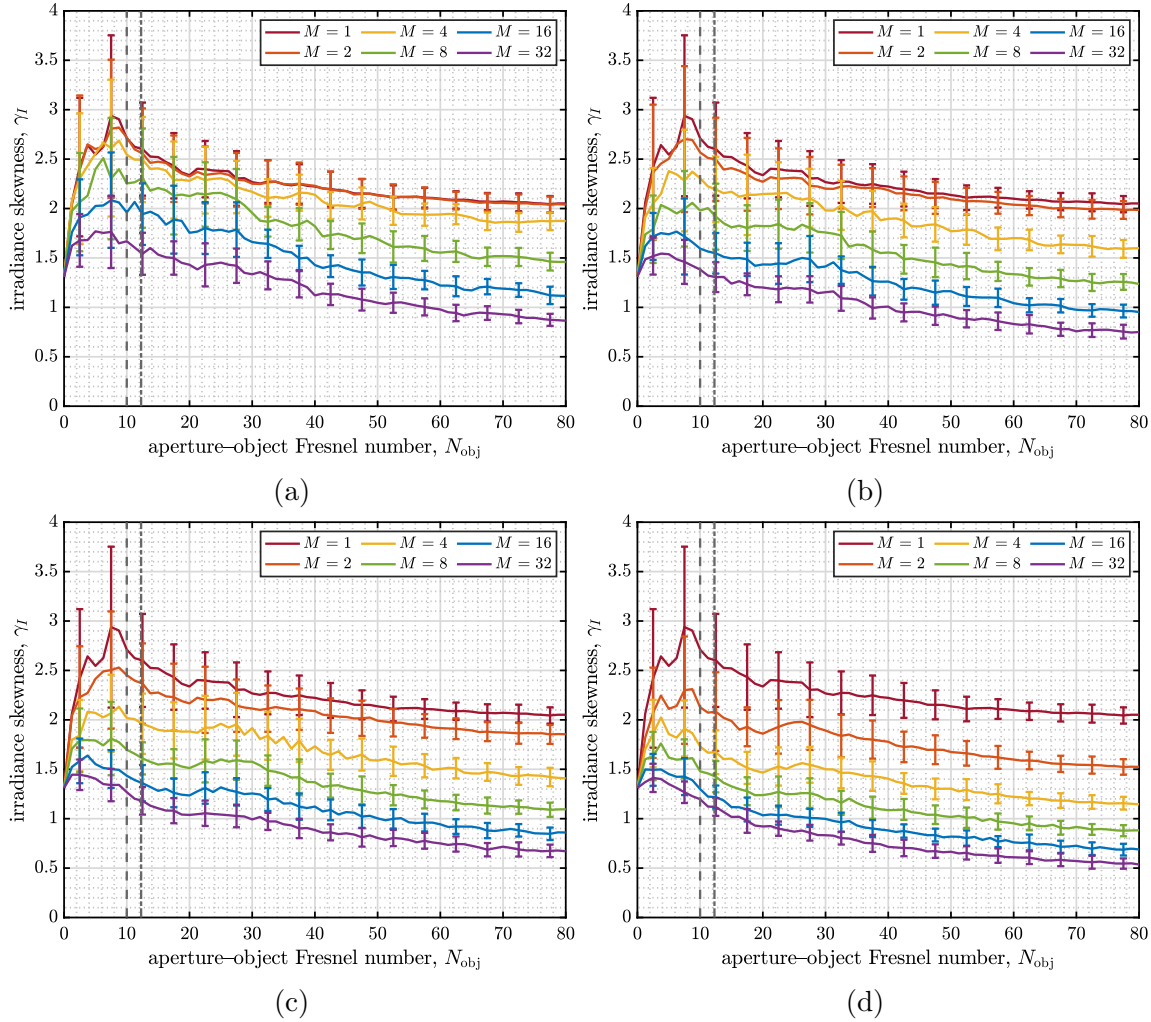


Figure 5.9: Irradiance skewness over the full aperture after propagating beacons of various sizes through weak scintillation and averaging together various numbers of subframes at (a) 25%, (b) 50%, (c) 75% and (d) 100% decorrelation. Vertical dashed and dash-dotted reference lines delineate fully aberrated and piston-removed isoplanatic patch sizes, respectively.

To summarize, the key lessons learned from these results are as follows:

1. Larger objects correspond to greater speckle severity and therefore increased RMS wavefront error/aberration and irradiance skewness.

2. Speckle averaging universally reduces both RMS wavefront error/aberration and irradiance skewness and does so with greatest efficiency with minimal subframe correlation of speckle.
3. Real-time monitoring of irradiance skewness over the total aperture can provide a gauge for unknown intraframe speckle averaging over time.
4. The reduction in both RMS wavefront aberration and irradiance skewness due to path averaging in distributed-volume turbulence outweighs speckle severity.
5. Leveraging speckle averaging in the presence of beacon anisoplanatism is fruitless and perhaps even harmful to performance.

Note: Fully Uncorrelated Speckle

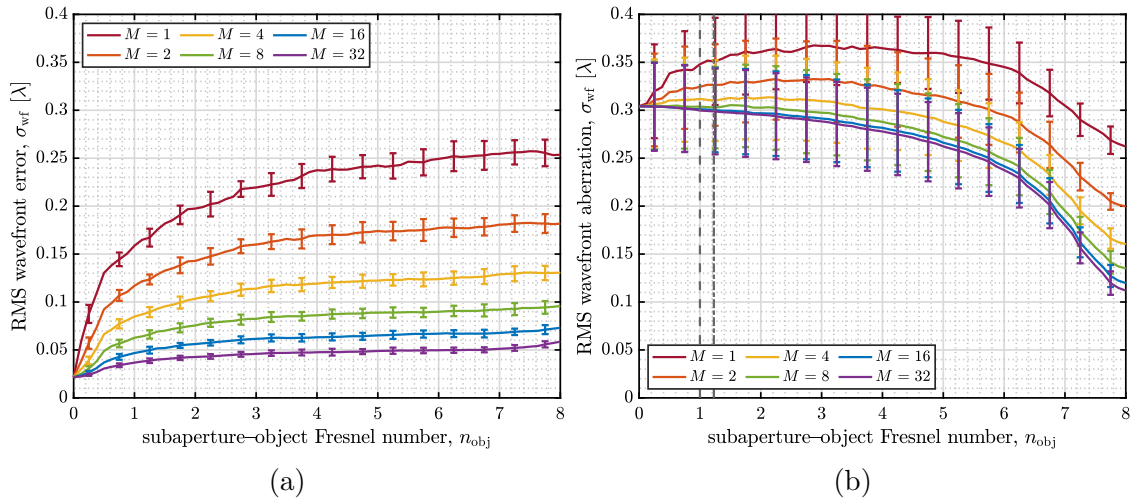


Figure 5.10: RMS wavefront error/aberration from subaperture to subaperture after propagating beacons of various sizes through (a) vacuum and (b) weak scintillation and averaging together various numbers of subframes with fully mutually uncorrelated speckle realizations; compare with Figs. 5.6d and 5.8d, respectively. Vertical dashed and dash-dotted reference lines delineate fully aberrated and piston-removed isoplanatic patch size, respectively.

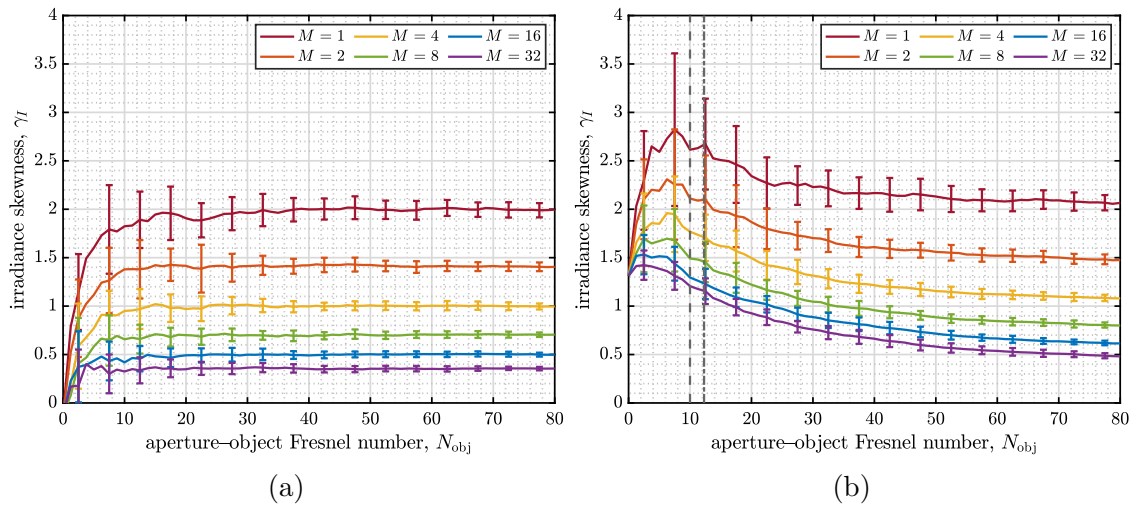


Figure 5.11: Irradiance skewness over the full aperture after propagating beacons of various sizes through weak scintillation and averaging together various numbers of subframes with fully mutually uncorrelated speckle realizations; compare with Figs. 5.7d and 5.9d, respectively. Vertical dashed and dash-dotted reference lines delineate fully aberrated and piston-removed isoplanatic patch size, respectively.

CHAPTER 6

Closed-Loop Adaptive Optics in the Presence of Speckle and Weak Scintillation
Over Horizontal Paths[†]**6.1 Background**

Speckle is an interference phenomenon arising from coherent illumination that reflects off of an optically rough surface. As it propagates to a pupil plane, the backscattered illumination self-interferes to form bright and patches individually known as “speckles.” Assuming quasimonochromatic illumination, linear polarization, and surface-height variations that exceed half the optical wavelength, the speckle pattern is “fully developed” with contrast going to unity. In long-range imaging applications, speckle acts as multiplicative noise with deleterious effects on image quality.

Though not an imaging system in the traditional sense, a Shack-Hartmann wavefront sensor (SHWFS) uses individual lenslets to divide the receiver aperture into subapertures that sample the incoming wavefront and focus the samples onto a detector array. The relative centroid positions of these focused spots correspond to local tilts (a.k.a. phase gradients) present in each subaperture. Accordingly, we can use the centroid measurements to reconstruct a pupil-plane phase function that estimates path-integrated phase aberrations resulting from atmospheric turbulence. A predistorting optic, such as a continuous-face-sheet deformable mirror (DM), can then invert this pupil-plane phase function on an outgoing beam so that it focuses to a nearly diffraction-limited spot at the object plane. Repeating this process in a null-seeking control loop (that employs, for example, a leaky-integrator control law) makes up the nominal phase-compensation system diagrammed in Fig. 6.1 [74].

[†]This material is currently undergoing submission in draft form to *Optics Communications* with coauthors M. F. Spencer and R. G. Driggers.

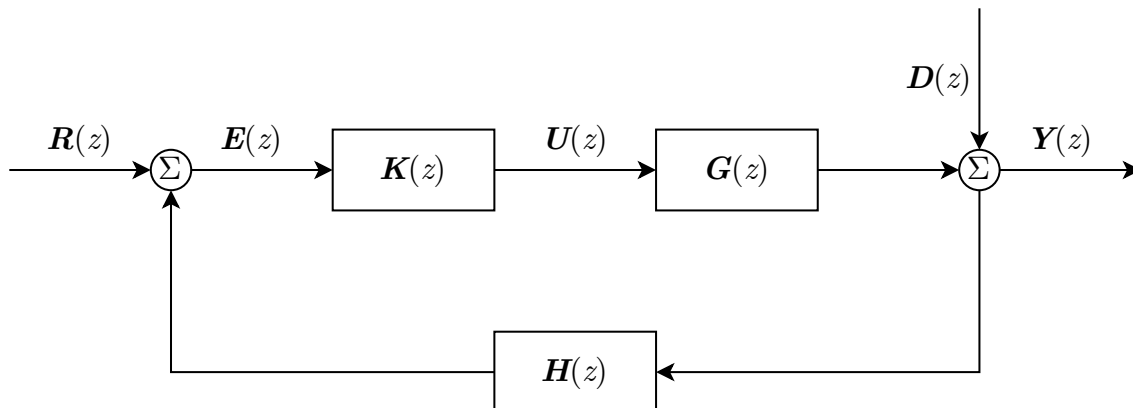


Figure 6.1: Block diagram of a nominal phase-compensation system operating in a null-seeking control loop using a leaky-integrator control law. Here, the matrices \mathbf{K} , \mathbf{G} and \mathbf{H} represent, respectively, the leaky-integrator controller, a continuous-face-sheet DM, and an SHWFS in the Fried geometry; the vectors \mathbf{R} , \mathbf{E} , \mathbf{U} , \mathbf{D} and \mathbf{Y} refer to, respectively, the reference input, the error signal, the control signal, the input disturbance (i.e., aberrated beacon) and the phase-compensated output. Note that the SHWFS and DM sense and correct for the phase aberrations induced by atmospheric turbulence using the compensation offered by the integrator in this multiple-input, multiple-output control loop (hence the use of matrices).

With Fig. 6.1 in mind, the closed-loop performance of an AO system becomes compromised with the use of an extended beacon. Such a beacon manifests as scattering of coherent illumination from an optically rough surface. The resultant speckle adds noise to the pupil-plane phase function, as shown in the upper row of heatmaps in Fig. 6.2. For ideal closed-loop performance (i.e., maximize power in the bucket), the AO system must sense and correct for atmosphere-induced phase aberrations (resulting in scintillation) separately from target-induced phase aberrations (resulting in speckle). However, what the SHWFS actually reconstructs is a sum of path-integrated contributions from both phase-aberration sources. Subaperture to subaperture, the presence of speckle also means that the SHWFS collects and resolves nonuniform irradiance in the pupil and image planes, respectively. Since the centroid represents an irradiance-weighted center of mass, these irradiance fades skew the wavefront measurement further. Thus, we must mitigate the effects of speckle—both the target-induced phase aberrations and the target-induced irradi-

ance fades—to obtain good closed-loop performance.

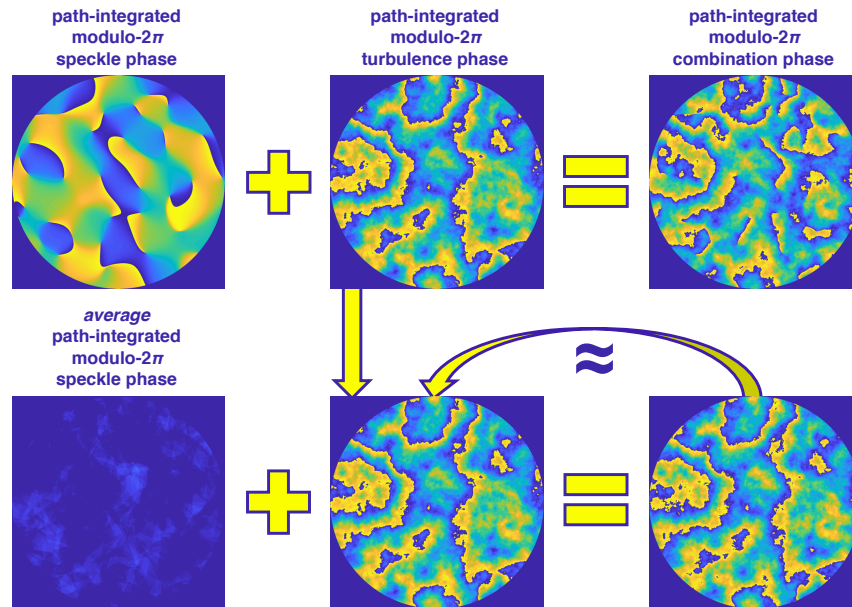


Figure 6.2: Example overview of combined phase aberrations due to rough-surface scattering and weak turbulence, both (top row) without and (bottom row) with intraframe speckle averaging.

One way to mitigate the effects of speckle is to perform speckle averaging. In so doing, it is common to assume that frame-to-frame speckle decorrelates at a faster rate than the scintillation. This assumption can be a sound one¹ given dynamically vibrating targets, but at high frame rates it is possible that speckle only partially decorrelates between observations. Although more frames are required with partially correlated than with fully uncorrelated speckle to achieve the same effect, sufficient energy accumulation in either case effectively averages out unwanted speckle noise as shown in the lower row of heatmaps in Fig. 6.2.

Despite the benefits of speckle averaging, there are limitations to keep in mind regarding its effectiveness. For one, fast framing is required of the focal plane array

¹There are straightforward cases where frame-to-frame speckle averaging could be uncorrelated with highly dynamic targets and correlated with highly static targets. In general, more research needs to be done to know for sure whether the uncorrelated assumption is true or not for a certain set of targets at tactical ranges. For the trade-space analysis contained in this paper, we simply assume uncorrelated speckle throughout.

(FPA) for the most effective speckle averaging—a limitation we will explore in more detail in the analysis that follows. Another limitation stems from the presence of beacon anisoplanatism.

As shown in Fig. 6.3, anisoplanatism results from an extended beacon coupled with distributed-volume phase aberrations. In essence, this coupling causes multiple point-spread functions (PSFs) to appear within the phase-compensation system’s field of view (FOV) due to returns from different points on the object sampling different portions of the atmosphere. A phase-compensation system, especially one incorporating an SHWFS in the Fried geometry and a least-squares phase reconstructor, relies on the use of a point-source beacon for optimal performance with shift invariance. As such, we will also explore anisoplanatic limitations in the analysis that follows.

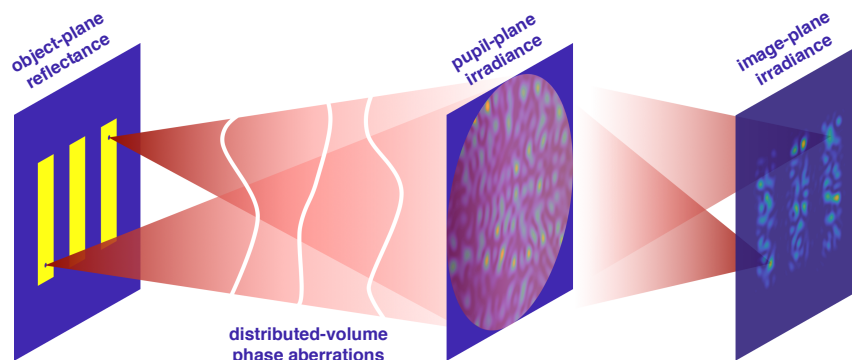


Figure 6.3: Illustration of anisoplanatism giving rise to distinct PSFs over the image of an extended object.

With the above limitations in mind, we model extended beacons of various sizes using plane-wave illumination of square targets ². We assume varying degrees of speckle correlation from one frame to the next, up to and including total decorrelation. We also assume that there is potential for beacon anisoplanatism when the beacon size exceeds that of the isoplanatic patch. We then model horizontal-path propagation with Kolmogorov turbulence and frozen flow through wave-optics sim-

²In so doing, we neglect the effects of uplink scintillation. Such effects are beyond the scope of the present analysis. Future studies should quantify the impacts of uplink scintillation using both compensated and uncompensated illumination to create the extended beacon.

ulations. Finally, we model a closed-loop phase-compensation system comprised of a Shack–Hartmann wavefront sensor in the Fried geometry, a least-squares phase reconstructor, a continuous-face-sheet deformable mirror, and a leaky-integrator control law.

In our approach, we characterize the severity of the speckle and anisoplanatism using the object Fresnel number and object angular extent relative to the isoplanatic angle, respectively. It is important to note that the degree of speckle correlation between frames plays a significant role in our ability to perform speckle averaging [122]; thus, truly uncorrelated speckle comprises a “best-case scenario” in the sense that it draws independent and identically distributed (i.i.d.) speckle data from one frame to the next. In addition to this limiting case, we explore the cases of 25%, 50%, 75% and 100% speckle decorrelation between frames by simulating dynamic speckle with high fidelity.

Dynamic speckle averaging represents just one possible solution to the speckle-mitigation problem, of which several others exist [123]. Such methods generally impose some condition of partial coherence or polarization. For example, we could reduce the spatial coherence of our illumination using dynamic diffusers [16], multimode waveguides [124], DMs [125], or tiled apertures [126]. Similarly, we could reduce the temporal coherence of our illumination via spectral-linewidth broadening [79, 80, 127, 82]. The coherence and polarization trade space is rich with potential ideas [128, 129, 130, 81]. Dynamic speckle averaging offers a unique advantage over other mitigation strategies in that no changes are required to the existing footprint of phase-compensation systems (cf. Fig. 6.1). With that said, our discussion here is not limited strictly to dynamic speckle averaging. In fact, one can generalize the concept of uncorrelated speckle frames as “degrees of freedom” afforded through any of the aforementioned techniques (or combination thereof). At the very least, dynamic speckle averaging provides a baseline method for developing more refined speckle-mitigation strategies.

In what follows, we first explain the setup used for our wave-optics simulations by parameterizing the Kolmogorov turbulence and frozen flow used in our horizontal-

propagation path. We further explore this trade space by examining the impact of various beacon sizes on the speckle observed in the pupil plane. Next, we present our results from both a time-domain and steady-state perspective. Both perspectives allow us to discuss the significance of our results while establishing specifications for a nominal phase-compensation system that incorporates speckle averaging. In closing, we compare our recommendations to commercial-off-the-shelf (COTS) product availability.

Before moving on to the next section, it is worth mentioning that the results presented in this paper demonstrate speckle averaging as an effective strategy for reducing measurement error associated with extended beacons. Even so, these performance gains steadily diminish as beacon anisoplanatism grows in its influence. This outcome serves as novel contribution to the phase-compensation research community, as a thorough trade-space exploration over horizontal paths is not currently found within the peer-reviewed literature.

6.2 Background and Theory

To set the stage for the analysis that follows, it is our intention to model extended beacons of various sizes. We do so via plane-wave illumination of square targets, so that the scattered-beacon illumination experiences both object- and atmosphere-induced phase aberrations as it propagates from the object plane to the pupil plane. These phase aberrations give rise to both speckle and scintillation, respectively, in the received irradiance.

Provided the received irradiance, we close the loop on a nominal phase-compensation system comprised of an SHWFS in the Fried geometry, a least-squares phase reconstructor, a continuous-face-sheet DM, and a leaky integrator control law. Subsequently, we compensate a focused flat-top beam and propagate it from the pupil plane to the object plane along the same horizontal propagation path with Kolmogorov turbulence and frozen flow. In the object plane, we score closed-loop performance as a function of the strength of uncorrelated speckle and anisopla-

natism. We also investigate the framerates needed to achieve good closed-loop performance (i.e., maximize the power in the bucket).

With these concepts in mind, we review in this section the theoretical inputs needed for our wave-optics simulations as discussed in Sec. 6.1.

6.2.1 Kolmogorov Turbulence

To characterize the strength of Kolmogorov turbulence, we first define the refractive-index structure parameter C_n^2 at an altitude h according to the Hufnagel–Valley (H–V) 5/7 model as [131, 132, 133]

$$\begin{aligned} C_n^2(h) &= 3.59 \times 10^{-23} h^{10} \exp(-h) \\ &\quad + 2.70 \times 10^{-16} \exp(-2h/3) \\ &\quad + 1.70 \times 10^{-14} \exp(-10h). \end{aligned} \tag{6.1}$$

with h in kilometers. Since a constant h defines horizontal propagation, C_n^2 has no dependence on the point z along such a path.

The Fried parameter (r_0) defines a circular area in the pupil plane over which the RMS phase error is approximately 1 rad [134]. Because we are comparing closed-loop performance from an extended beacon to that from a point-source beacon, we assume spherical-wave propagation throughout the following analysis. Accordingly, we take the spherical-wave expression for r_0 as [109]

$$\begin{aligned} r_{0,\text{sw}} &= \left[0.423k^2 \int_0^{Z_1} C_n^2(z) \left(\frac{z}{Z_1} \right)^{5/3} dz \right]^{-3/5} \\ &\xrightarrow{\text{horiz.}} (0.159k^2 C_n^2 Z_1)^{-3/5}, \end{aligned} \tag{6.2}$$

where $k = 2\pi/\lambda$ is the angular wavenumber, λ is the wavelength of light, z is an arbitrary point along the propagation path, and Z_1 is the propagation distance from the object plane to the pupil plane (i.e., $0 \leq z \leq Z_1$).

In order to begin prescribing numerical values to our nominal phase-compensation system, we first take the overall pupil-plane aperture diameter D to be 30 cm (typical of modern-day beam-control systems [135]). We then assume $D/r_0 = 10$ for moderate seeing conditions without centroid anisoplanatism becoming a significant issue [136]. Subaperture width d should be no larger than r_0 [110], but taking d to be no smaller than r_0 maximizes flexibility in exploring larger objects under isoplanatic conditions. We can now rearrange Eq. (6.2) to back out our constant-valued refractive-index structure parameter C_n^2 in terms of r_0 as

$$C_n^2 = \frac{0.160\lambda^2}{Z_1 r_0^{5/3}}. \quad (6.3)$$

Knowing C_n^2 also allows us to calculate the Rytov number, which for a spherical wave takes the form [100]

$$\begin{aligned} \mathcal{R}_{\text{sw}} &= 0.563k^{7/6} \int_0^{Z_1} C_n^2(z) \left[z \left(1 - \frac{z}{Z_1} \right) \right]^{5/6} dz \\ &\xrightarrow{\text{horiz.}} 0.124k^{7/6} C_n^2 Z_1^{11/6}. \end{aligned} \quad (6.4)$$

In weak turbulence (i.e., when $\mathcal{R}_{\text{sw}} \lesssim 0.25$), the Rytov number estimates the log-amplitude variance (σ_χ^2) observed in the pupil plane. In other words, \mathcal{R} provides a gauge for the amount of scintillation due to weak Kolmogorov turbulence. This is the regime in which we choose to operate, as scintillation begins to saturate with higher Rytov numbers and branch points in the phase function due to total-destructive interference eventually sabotage our ability to perform phase compensation effectively [101, 102, 103, 104].

The isoplanatic angle also plays a role in our analysis as the beacon grows in size. For all intents and purposes, θ_0 describes an angular path difference that causes a residual RMS wavefront error of approximately 1 rad (much like r_0 for the pupil-plane coherence area). We calculate θ_0 as [114]

$$\theta_0 = \left[2.91k^2 \int_0^{Z_1} C_n^2(z) z^{5/3} dz \right]^{-3/5} \quad (6.5)$$

$$\xrightarrow{\text{horiz.}} \left(1.09k^2 C_n^2 Z_1^{8/3} \right)^{-3/5}.$$

Under the paraxial approximation, we can then multiply this angle by the propagation distance to find the total length across our isoplanatic patch in linear space as $W_0 = \theta_0 Z_1$ [137].

We now turn our attention to the temporal dynamics of Kolmogorov turbulence, specifically as it relates to sampling requirements. Assuming Taylor's frozen-flow hypothesis, the Greenwood frequency represents the 3-dB bandwidth at which a continuous AO system produces 1 rad of residual RMS wavefront error. We calculate the Greenwood frequency as [138]

$$f_G = 2.31\lambda^{-6/5} \left[\int_0^{Z_1} C_n^2(z) v_w^{5/3}(z) dz \right]^{3/5} \quad (6.6)$$

$$\xrightarrow{\text{horiz.}} \left(0.102k^2 C_n^2 v_w^{5/3} Z_1 \right)^{3/5},$$

assuming not only C_n^2 but also transverse wind speed v_w remains constant along a horizontal propagation path.

6.2.2 Digital Controls

Modern control systems favor digital computers for controller implementation as they tend to be more robust, adaptable, compact, and cost effective than their analog counterparts [139]. A rule of thumb in digital control theory is that sampling at a minimum of $30\times$ the system bandwidth (i.e., the Greenwood frequency in our case) yields adequate closed-loop performance [140]. Because a sample rate (f_s) of $10\text{--}20\times$ the Greenwood frequency is also frequently cited [141], we expand the trade space to cover three distinct cases: $f_s = 10f_G$, $f_s = 20f_G$ and $f_s = 40f_G$.

The reader should note that the three distinct cases mentioned above represent base sample rates without taking any speckle averaging into consideration. With speckle averaging, these cases instead correspond to the “effective” sample rate (f_{eff}) and we count the number of averaged subframes as M . As an example, an effective sample rate of $f_{\text{eff}} = 40f_G$ with subframe averaging of $M = 2$ would require the actual sampling frequency $f_s = Mf_{\text{eff}} = 80f_G$. With this example in mind, we now determine the total number of samples (N_s) required to close the loop in simulation.

We assume that the servomechanism of our control loop is a basic leaky integrator with rest initial conditions. Looking back to Fig. 6.1, the difference equation governing control block \mathbf{K} is thus [142]

$$\mathbf{u}[nT] = a\mathbf{u}[(n-1)T] + b\mathbf{e}[nT], \quad (6.7)$$

where u is the control signal, n is a control variable for iteration, T is the sampling period, $a < 1$ is the servo leakage coefficient, $b > 0$ is the forward-loop gain coefficient, and e is the error signal that feeds into the controller. Aside from its straightforward implementation as a control law, this leaky integrator provides both the smoothing qualities of a low-pass filter and the stabilization benefits of leakage [74]. The Z-transform of Eq. (6.7) gives a closed-loop transfer function of

$$\begin{aligned} \mathbf{K}(z) &= \frac{\mathbf{U}(z)}{\mathbf{E}(z)} \\ &= \frac{bz}{z-a} \end{aligned} \quad (6.8)$$

Assuming a flattened DM, the sensitivity (a.k.a. disturbance-rejection) function is

$$\begin{aligned}
\mathbf{S}(z) &= \frac{\mathbf{Y}(z)}{\mathbf{D}(z)} \\
&= \frac{1}{1 + \mathbf{K}(z)} \\
&= \frac{z - a}{(1 + b)z - a}
\end{aligned} \tag{6.9}$$

with a single closed-loop pole at

$$z = \frac{a}{1 + b}. \tag{6.10}$$

The 2% settling time is then

$$T_s = \frac{\ln(0.02)T}{\ln[a/(1+b)]}. \tag{6.11}$$

To understand steady-state performance trends while minimizing simulation run-times, we thus simulate

$$N_s = \left\lceil \frac{2 \ln(0.02)}{\ln[a/(1+b)]} \right\rceil \tag{6.12}$$

time steps on each run for twice the 2% settling time. For reference, Fig. 6.4 shows discrete-time Bode plots of Eq. (6.8) with the substitution $z = e^{j2\pi fT}$. Sampling at 10, 20 and 40 times the Greenwood frequency yields 3-dB temporal bandwidths (f_{bw}) of 118, 236 and 472 Hz, respectively.

6.2.3 Beacon Characteristics

We now consider the size of our extended beacon and its effect on observed speckle in the pupil plane. For this purpose, we estimate the average linear distance across a single speckle corresponding to a beacon of width W as $\lambda Z_1/W$ [143]. We then introduce the subaperture-object Fresnel number as

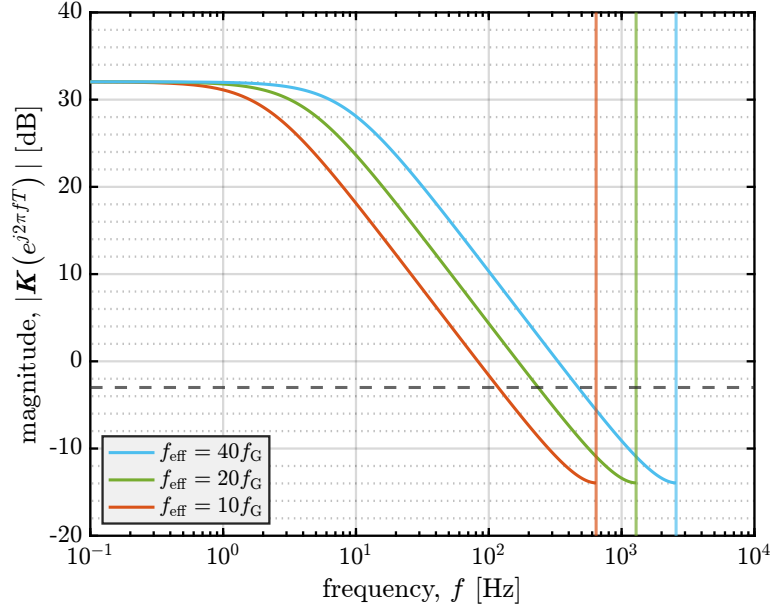


Figure 6.4: Bode magnitude plots of closed-loop sensitivity functions corresponding to servos implementing leaky-integrator control at various sample rates, relative to the Greenwood frequency.

$$n_{\text{obj}} = \frac{d}{\lambda Z_1 / W} \quad (6.13)$$

Equation (6.13) provides us with a gauge for the average number of speckles across the width of each SHWFS subaperture [79, 80]. We can also rearrange variables to show that

$$n_{\text{obj}} = \frac{W/Z_1}{\lambda/d} \quad (6.14)$$

counts the number of diffraction-limited resolution spots across the width of the object. Together, Eqs. (6.13) and (6.14) indicate that larger subaperture–object Fresnel numbers correspond to greater speckle severity from beacons that are more resolved.

For practical reasons in simulation, we impose different degrees of speckle decorrelation by in-plane translation of the phase underlying the beacon illumination in the object plane. Specifically, we do this by solving for in-plane translation distance

in the expression for an irradiance correlation coefficient. Assuming the beacon is a square plate, the irradiance correlation coefficient is [95]

$$\mu_I(\Delta\Omega) = \text{sinc}^2\left(\frac{W\Delta\Omega}{\lambda Z_1}\right) \text{tri}^2\left(\frac{\Delta\Omega}{W}\right) \quad (6.15)$$

where

$$\text{sinc}(w) = \frac{\sin(\pi w)}{\pi w} \quad (6.16)$$

and

$$\text{tri}(w) = \begin{cases} 1 - |w| & |w| < 1 \\ 0 & |w| \geq 1 \end{cases}. \quad (6.17)$$

For the purpose of studying partial through total decorrelation of speckle between subframes, we set Eq. (6.15) equal to 75%, 50%, 25% and 0% so that we can numerically solve for $\Delta\Omega_0$.

6.2.4 Performance Metrics

We now consider two different performance metrics that help us to assess closed-loop performance: normalized power in the bucket (nPIB) and peak Strehl ratio (S_{pk}). For the former, we define a diffraction-limited bucket diameter as

$$B = 2.44 \frac{\lambda Z_1}{D} \quad (6.18)$$

where D is the full aperture diameter. This quantity describes the central lobe of an Airy disk in the far field, resulting from diffraction-limited propagation of a focused flat-top beam at range $z = Z_1$. A “bucket” of this diameter encircles 83.8% of the initial beam power leaving the pupil plane under diffraction-limited conditions [144]. The nPIB is then a normalization of phase-compensated, turbulence-limited power by the diffraction-limited power measured in this bucket [74]:

$$\text{nPIB} = \frac{\int_0^{2\pi} \int_0^{B/2} E_{\text{tl}}(\Omega, \theta) \Omega d\Omega d\theta}{\int_0^{2\pi} \int_0^{B/2} E_{\text{dl}}(\Omega, \theta) \Omega d\Omega d\theta}. \quad (6.19)$$

Here, E_{tl} and E_{dl} are the turbulence- and diffraction-limited irradiance values, respectively.

Because the position of our diffraction-limited bucket is fixed in the object plane, nPIB is sensitive to residual tilt in the outgoing beam. For this reason, we also consider the peak Strehl ratio in our data analysis:

$$S_{\text{pk}} = \frac{\max(E_{\text{tl}})}{\max(E_{\text{dl}})}. \quad (6.20)$$

To provide a baseline for comparison of simulation results against theory, we can use the extended Maréchal approximation to calculate an expected Strehl ratio as [145]

$$\langle S \rangle = \exp(-\sigma_{\text{tot}}^2). \quad (6.21)$$

Here, σ_{tot}^2 is the total variance associated with wavefront error which goes as [141].

$$\sigma_{\text{tot}}^2 = \sigma_{\text{fit}}^2 + \sigma_{\text{tmp}}^2 + \sigma_{\text{iso}}^2 \quad (6.22)$$

assuming we can safely neglect sensor noise. The first term of Eq. (6.22) is spatial fitting error, which we have from Noll as [146]

$$\sigma_{\text{fit}}^2 = 0.294 (D/r_0)^{5/3} N_{\text{act}}^{-\sqrt{3}/2}. \quad (6.23)$$

with N_{act} being the number of active actuators behind the deformable mirror. The second term of Eq. (6.22) describes temporal lag, which we calculate from the Greenwood frequency as [138]

$$\sigma_{\text{tmp}}^2 = (f_G/f_{\text{bw}})^{5/3}. \quad (6.24)$$

The third term of Eq. (6.22) refers to isoplanatic error, which Fried first derived as

[114]

$$\sigma_{\text{iso}}^2 = (\theta/\theta_0)^{5/3}. \quad (6.25)$$

It is important to keep in mind that the quadrature sum in Eq. (6.22) assumes mutual independence of all noise sources involved. If surface-based aberrations were truly uncorrelated from atmospheric aberrations, we could in theory add a fourth term describing speckle noise as [72]:

$$\sigma_{\text{spck}}^2 = \left[2\pi C \left(3.54 + \frac{2.11}{n_{\text{obj}}} \right)^{-1} \right]^2. \quad (6.26)$$

However, we already know that noise from speckle and scintillation couples in ways that we do not fully understand [120]. Because of this, we will rely on Eq. (6.22) to predict point-source performance only and investigate further degradation from extended beacons through wave-optics simulations.

6.3 Modeling and Simulation

In setting up our wave-optics simulations, we used the split-step beam propagation method to simulate propagation of complex optical fields along horizontal paths through the atmosphere. To model the distributed-volume phase aberrations, we used 40 independent realizations of six equally spaced Kolmogorov phase screens with frozen flow. Thus, in the results that follow we report the associated Monte Carlo averages.

To create extended beacons of various sizes, we simulated on-axis, plane-wave illumination of square objects. For this purpose, we defined our target length W by the subaperture–object Fresnel number from Eq. (6.13). We then tested six different values of n_{obj} in increasing powers of two. As a visual aid, Fig. 6.5 highlights the inverse relationship between object size and the total number of received speckles. The object sizes that correspond to these values are roughly equidistant from our fixed isoplanatic patch size W_0 on either side of the inequality. As we will see in

the results that follow, the interplay between W and W_0 gives us a gauge for when anisoplanatism becomes a performance-limiting factor.

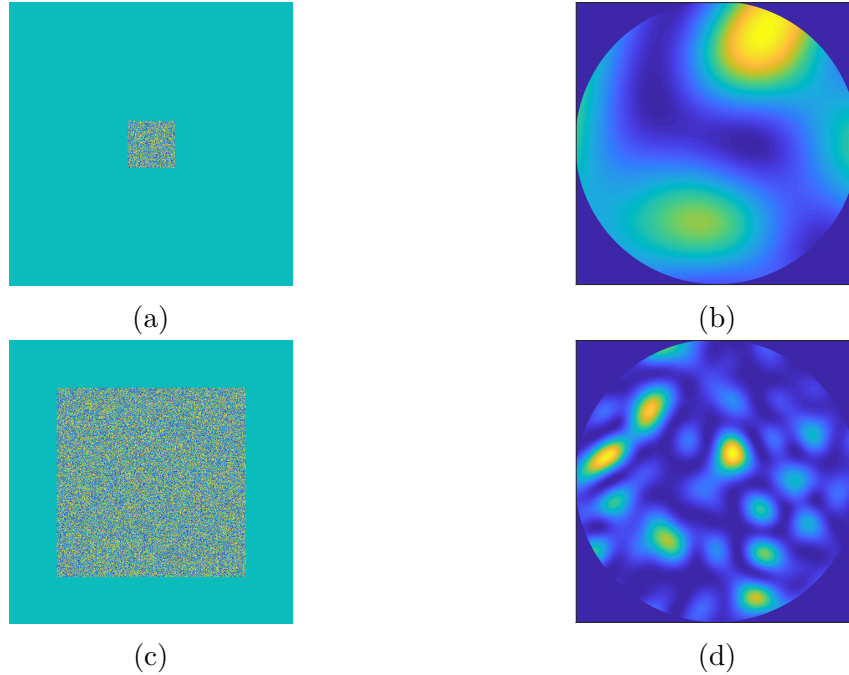


Figure 6.5: Exploration of the subaperture-object Fresnel number (n_{obj}). In general, n_{obj} provides us with a gauge for the average number of speckles across the width of our receiving aperture. As the object size increases from (a) to (c), we see that n_{obj} increases and the total number of received speckles increases from (b) to (d).

As shown in Figs. 6.5a and 6.5c, we assumed that the rough-surface statistics were delta-correlated over the extent of our square objects. To satisfy this assumption, we defined the phase at each object mesh point as a uniformly distributed random draw on the interval $[-\pi, \pi)$. For each simulated time step, we then solved Eq. (6.15) for the incremental translation distance $\Delta\Omega_0$ of underlying phase that decorrelated pupil-plane speckle by 25%, 50%, 75% or 100%. Alternatively, we reseeded the random phase drawn in the object plane for fully uncorrelated frame-to-frame speckle.

To prevent numerical artifacts such as aliasing due to the periodic nature of discrete Fourier transforms involved in propagation, we defined our sampling pa-

rameters such that Nyquist sampling [52], critical sampling [54], and speckle sampling [117] constraints were all satisfied. We used the WavePlex Toolbox for MATLAB from Prime Plexus³ to simulate rough-surface scattering, propagation through turbulence, wavefront sensing with an SHWFS model in the Fried geometry, least-squares phase reconstruction, and phase compensation using a continuous-face-sheet deformable mirror.

Given the vast number of simulation inputs available within our modeling tradespace, an exhaustive matrix test of all possible combinations is neither practical nor would it be digestible to the reader. For this reason, we provided different perspectives by defining two different parameterizations of the general simulation routines described. The first prioritizes study of partial speckle decorrelation according to Eq. (6.15) under isoplanatic conditions. One of the main implications of this approach is that sampling resolution in the pupil plane is sacrificed ($d/r_0 = 1$) in exchange for beacon isoplanatism, which means limited peak performance even in the case of a point-source beacon due to fitting error. The second parameterization therefore emphasizes better peak performance by improving spatial resolution ($d/r_0 = 0.5$) at the expense of beacon isoplanatism, restricting the beacon sizes that we can expect to allow for speckle averaging under isoplanatic conditions. The numerical values associated with these parameterizations are summarized in Tables 6.1 and 6.1, respectively.

6.4 Results and Discussion

In this section, we first present a selection of closed-loop results for both steady-state and time-domain performance with partially correlated frame-to-frame speckle. We then present a selection of closed-loop results for both steady-state and time-domain performance with relaxed isoplanatic constraints and uncorrelated frame-to-frame speckle. In all cases, point-source results in both closed and open loop (OL) are also provided for reference. Provided these results, we also discuss the impacts of

³T. J. Brennan is the sole author of the WavePlex Toolbox for MATLAB[®] with correspondence to the following address: Prime Plexus, 650 N Rose Drive #439, Placentia, CA 92870, USA.

Table 6.1: Physical and numerical parameters used in wave-optics simulations of closed-loop wavefront sensing with partially correlated frame-to-frame speckle.

	parameter	value(s)
physical	optical wavelength, λ [μm]	1
	propagation distance, Z_1 [m]	283
	aperture diameter, D [cm]	30
	subaperture width, d [cm]	3
	subaperture-object Fresnel number, n_{obj}	{1/8, 1/4, 1/2, 1, 2, 4, 8}
	lenslet Fresnel number, n_{lod}	8
	lenslet focal length, $f = Z_2$ [m]	113
	total actuator count, N_{act}	101
	refractive-index structure constant, C_n^2 [$\text{m}^{-2/3}$]	1.96×10^{-13}
	spherical-wave Rytov number, \mathcal{R}_{sw}	0.0658
	spherical-wave Fried parameter, r_0 [cm]	3
	isoplanatic angle, θ_0 [μrad]	33.3
	piston-removed isoplanatic angle, θ_1 [μrad]	40.9
	piston/tip/tilt-removed isoplanatic angle, θ_3 [μrad]	43.9
	Greenwood frequency, f_G [Hz]	129
	effective sample rate, f_{eff} [kHz]	{1.29, 2.57, 5.14}
servo leakage coefficient, a	0.99	
servo gain coefficient, b	0.40	
numerical	grid points per side, $N \times N$	2048×2048
	object-plane grid spacing, δ_{obj} [μm]	259
	pupil-plane grid spacing, δ_{pup} [μm]	534
	image-plane grid spacing, δ_{img} [μm]	103
	object-plane side length, S_{obj} [mm]	529
	pupil-plane side length, S_{pup} [m]	1.09
image-plane side length, S_{img} [mm]	211	

anisoplanatism and sampling rates.

6.4.1 Partially Correlated Speckle

Figure 6.6 displays selected nPIB results in the time domain with $f_{\text{eff}} = 40f_G$ and partially correlated speckle. Specifically, Fig. 6.6a shows the case of no speckle averaging, whereas Figs. 6.6b–6.6e each correspond to 32 subframes averaged per frame with 25%, 50%, 75% and 100% decorrelation between consecutive subframes, respectively. In general, larger extended beacons give rise to poorer closed-loop performance in terms of final nPIB value. Speckle averaging mitigates this perfor-

Table 6.2: Physical and numerical parameters used in wave-optics simulations of closed-loop wavefront sensing with uncorrelated frame-to-frame speckle.

	parameter	value(s)
physical	optical wavelength, λ [μm]	1
	propagation distance, Z_1 [km]	1
	aperture diameter, D [cm]	30
	subaperture width, d [cm]	1.5
	subaperture-object Fresnel number, n_{obj}	$\{1/20, 1/10, 1/5, 2/5, 4/5, 8/5\}$
	lenslet Fresnel number, n_{lod}	4.4
	lenslet focal length, $f = Z_2$ [m]	51.1
	total actuator count, N_{act}	357
	refractive-index structure constant, C_n^2 [$\text{m}^{-2/3}$]	5.53×10^{-14}
	spherical-wave Rytov number, \mathcal{R}_{sw}	0.189
	spherical-wave Fried parameter, r_0 [cm]	3
	isoplanatic angle, θ_0 [μrad]	9.42
	piston-removed isoplanatic angle, θ_1 [μrad]	11.6
	piston/tip/tilt-removed isoplanatic angle, θ_3 [μrad]	12.4
	Greenwood frequency, f_G [Hz]	129
	effective sample rate, f_{eff} [kHz]	$\{1.29, 2.57, 5.14\}$
	servo leakage coefficient, a	0.99
servo gain coefficient, b	0.40	
numerical	grid points per side, $N \times N$	512×512
	object-plane grid spacing, δ_{obj} [mm]	1.40
	pupil-plane grid spacing, δ_{pup} [mm]	1.40
	image-plane grid spacing, δ_{img} [μm]	71.4
	object-plane side length, S_{obj} [cm]	71.6
	pupil-plane side length, S_{pup} [cm]	71.6
	image-plane side length, S_{img} [mm]	36.6

mance degradation to some extent, with the smallest extended beacons and degrees of correlation enabling the greatest performance buyback. The diminishing returns of speckle averaging are readily apparent as the extended beacon size outgrows the isoplanatic patch size in the neighborhood of $n_{\approx}1$, especially when comparing Fig. 6.6b to Fig. 6.6e. In these best-case scenarios, extended beacons closely approach point-source performance.

Figure 6.7 displays selected S_{pk} results in the time domain with $f_{\text{eff}} = 40f_G$ and partially correlated speckle. Specifically, Fig. 6.7a shows the case of no speckle averaging, whereas Figs. 6.7b–6.7e each correspond to 32 subframes averaged per

frame with 25%, 50%, 75% and 100% decorrelation between consecutive subframes, respectively. The trends are similar to those observed in Fig. 6.6, but the lack of dependence on peak-power position in the object plane has the effect of smoothing out the curves and making trends somewhat clearer.

Figure 6.8 displays selected nPIB results in steady state with $f_{\text{eff}} = 40f_G$ as a function of partially correlated speckle averaging. Specifically, Figs. 6.8a–6.8d correspond to 25%, 50%, 75% and 100% decorrelation between consecutive subframes, respectively. We again see here that smaller beacons, especially those with less correlated speckle averaging, begin to approximate point-source performance. However, the temporal noise present in Fig. 6.6 produces instability in the trends that would be alleviated through further time and/or ensemble averaging.

Figure 6.9 displays selected S_{pk} results in steady state with $f_{\text{eff}} = 40f_G$ as a function of partially correlated speckle averaging. Specifically, Figs. 6.9a–6.9d correspond to 25%, 50%, 75% and 100% decorrelation between consecutive subframes, respectively. Again we see similar trends in the data to Fig. 6.8 with increased smoothness on account of positional independence.

6.4.2 Fully Uncorrelated Speckle

Two lessons Figure 6.10 displays selected nPIB results in the time domain with $f_{\text{eff}} = 40f_G$ and fully uncorrelated speckle. Specifically, Figs. 6.10a–6.10f correspond to averaging 1, 2, 4, 8, 16 and 32 mutually uncorrelated subframes within a single frame. Rather than simulating only the number of time steps necessary to double the 2% settling time, these cases simulate twice the time it takes for transverse wind to clear the aperture twice under Taylor’s frozen-flow hypothesis. We see now that the improved fitting parameters from Table 6.2 have afforded better approximation of point-source performance with smaller beacons as compared with Fig. 6.6.

Figure 6.11 displays selected nPIB results in steady state with f_{eff} from $10f_G$ to $40f_G$ as a function of fully uncorrelated speckle averaging. Specifically, Figs. 6.11a–6.11f correspond to subaperture–object Fresnel numbers of $1/20$, $1/10$, $1/5$, $2/5$, $4/5$ and $8/5$, respectively. As predicted, we see better smoothing here than in Fig. 6.8

as a result of the increase in simulated runtimes allowing for more time averaging beyond settling times. For succinctness, we therefore omit peak Strehl ratio from this part of the discussion. Note that in Fig. 6.11a speckle averaging actually reduces the steady-state nPIB with insufficient temporal sampling at $10f_G$; this is because of outdated atmospheric data compounding in the the temporal equivalent of path averaging.

With the above data and observations in mind, overall lessons learned in these studies are as follows:

1. The presence of speckle noise harms closed-loop performance, with the worst cases corresponding to larger extended beacons.
2. Speckle averaging buys back performance under isoplanatic conditions, with the best cases corresponding to minimal speckle correlation between averaged subframes.
3. Path averaging due to anisoplanatism precludes any performance gains through speckle averaging once the extended beacon size exceeds the isoplanatic patch size.
4. Point-source performance dictates potential for performance buyback through speckle averaging, in our cases ranging from $\sim 9\%$ relative performance boost ($\sim 5\%$ absolute) with $d/r_0 = 1$ to $\sim 17\%$ relative performance boost ($\sim 10\%$ absolute) with $d/r_0 = 0.5$.
5. Inadequate temporal sampling not only impacts closed-loop performance in the absence of speckle, but can actually cause speckle averaging to impair performance even further with speckle averaging versus without.

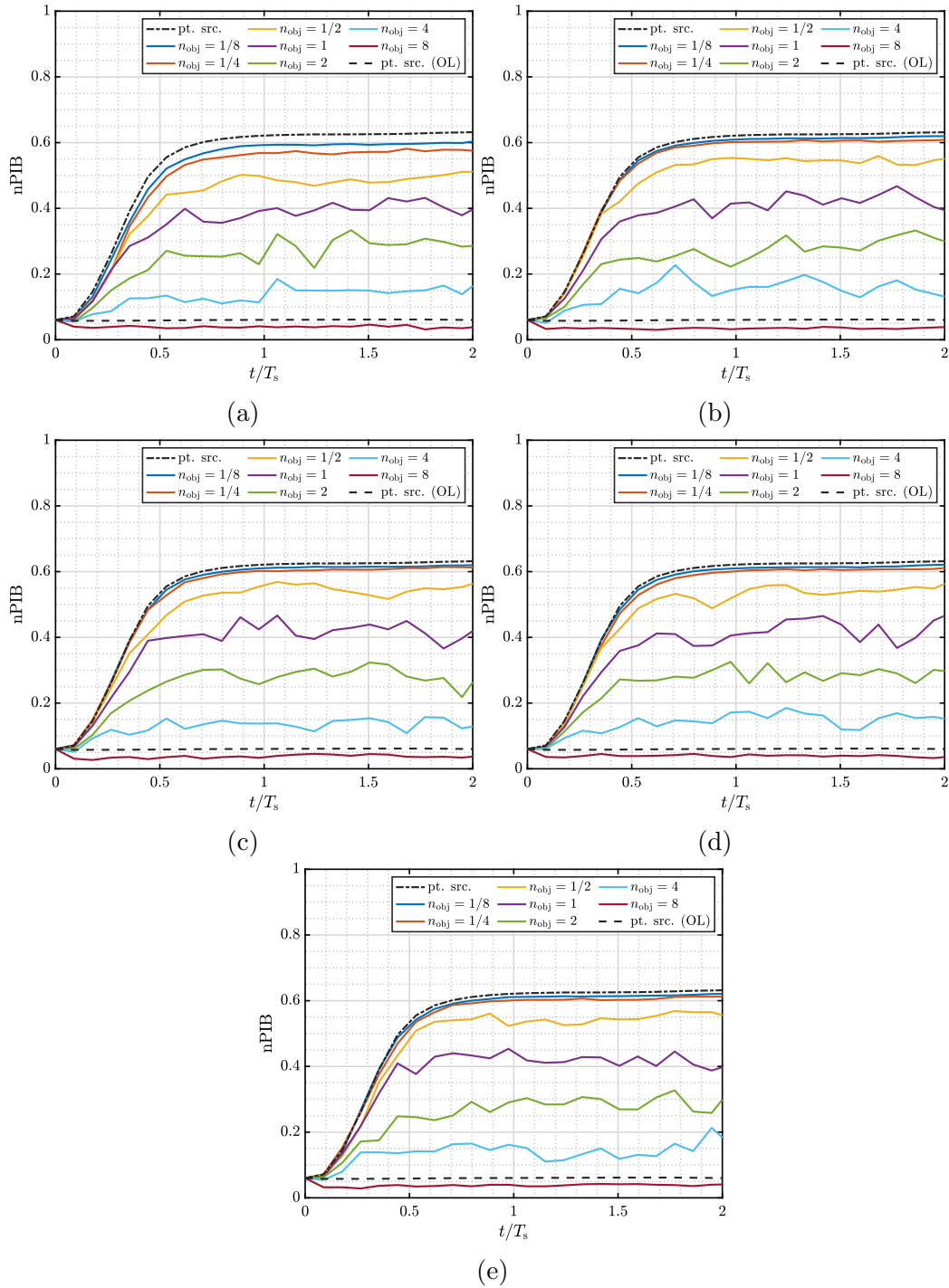


Figure 6.6: Time-domain nPIB results with $f_{\text{eff}} = 40f_G$ and (a) no speckle averaging, as well as 32-subframe averaging at (b) 25% decorrelation, (c) 50% decorrelation, (d) 75% decorrelation and (e) 100% decorrelation of speckle between consecutive subframes.

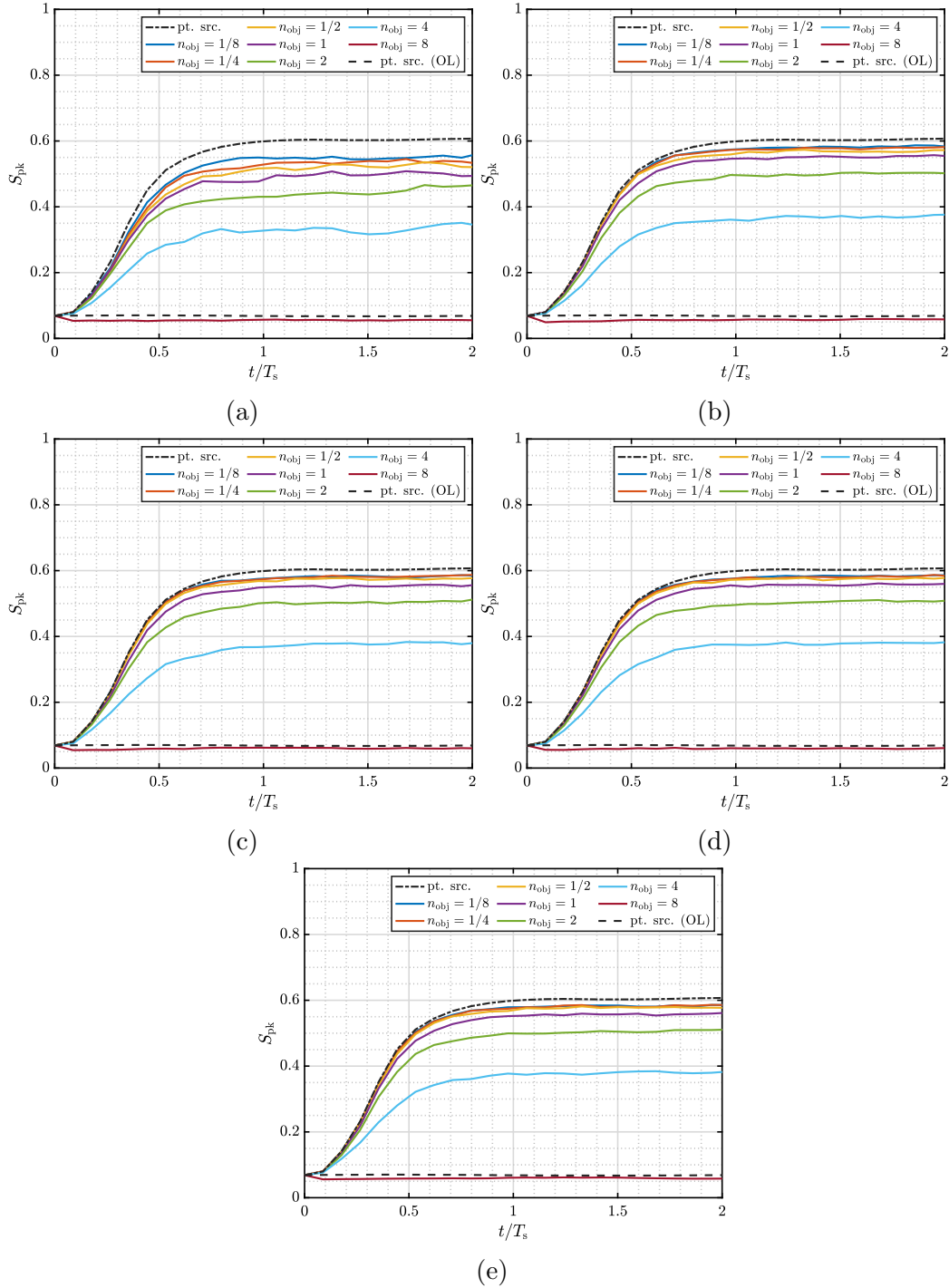


Figure 6.7: Time-domain S_{pk} results with $f_{eff} = 40f_G$ and (a) no speckle averaging, as well as 32-subframe averaging at (b) 25% decorrelation, (c) 50% decorrelation, (d) 75% decorrelation and (e) 100% decorrelation of speckle between consecutive subframes.

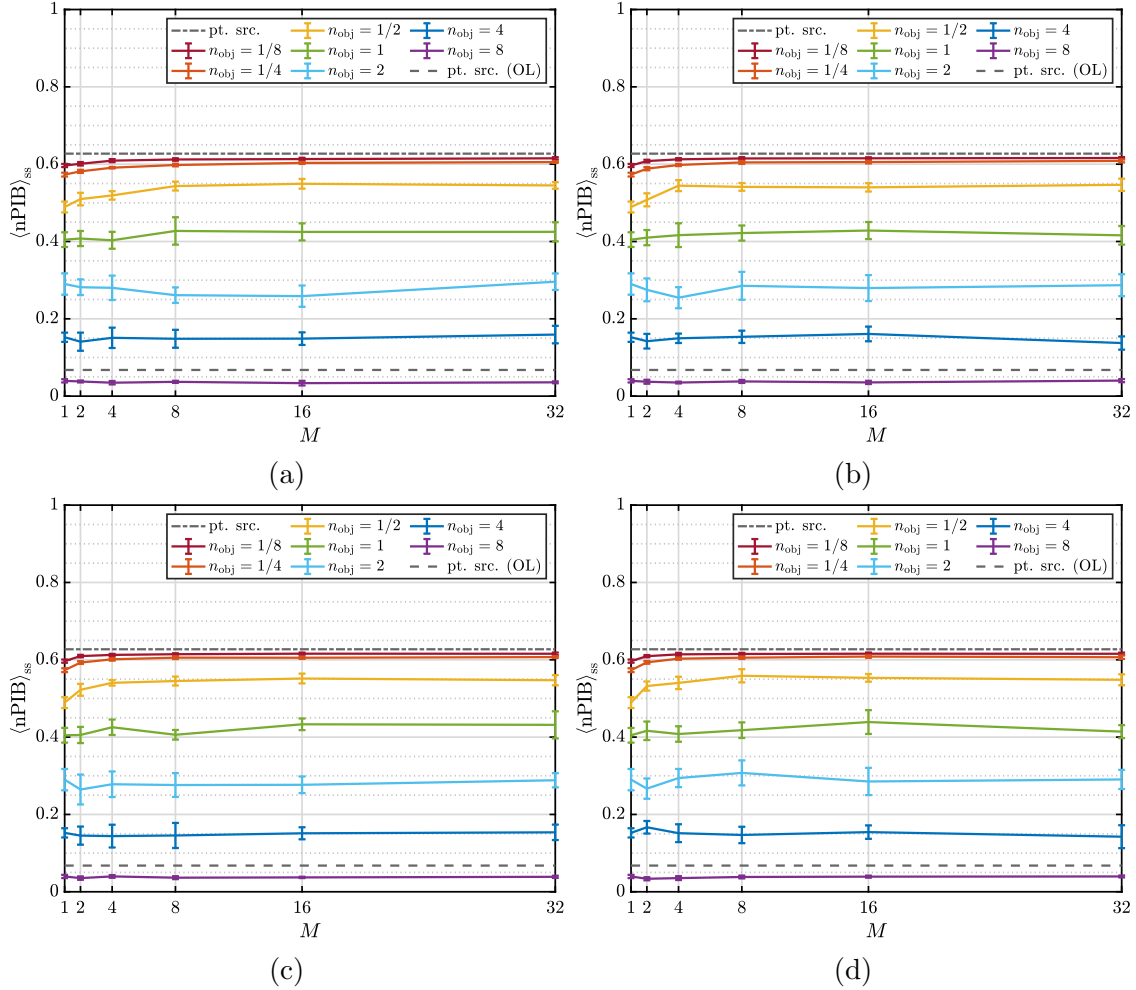


Figure 6.8: Steady-state nPIB results with $f_{\text{eff}} = 40f_G$ and various degrees of subframe averaging at (a) 25% decorrelation, (b) 50% decorrelation, (c) 75% decorrelation and (d) 100% decorrelation of speckle between consecutive subframes.

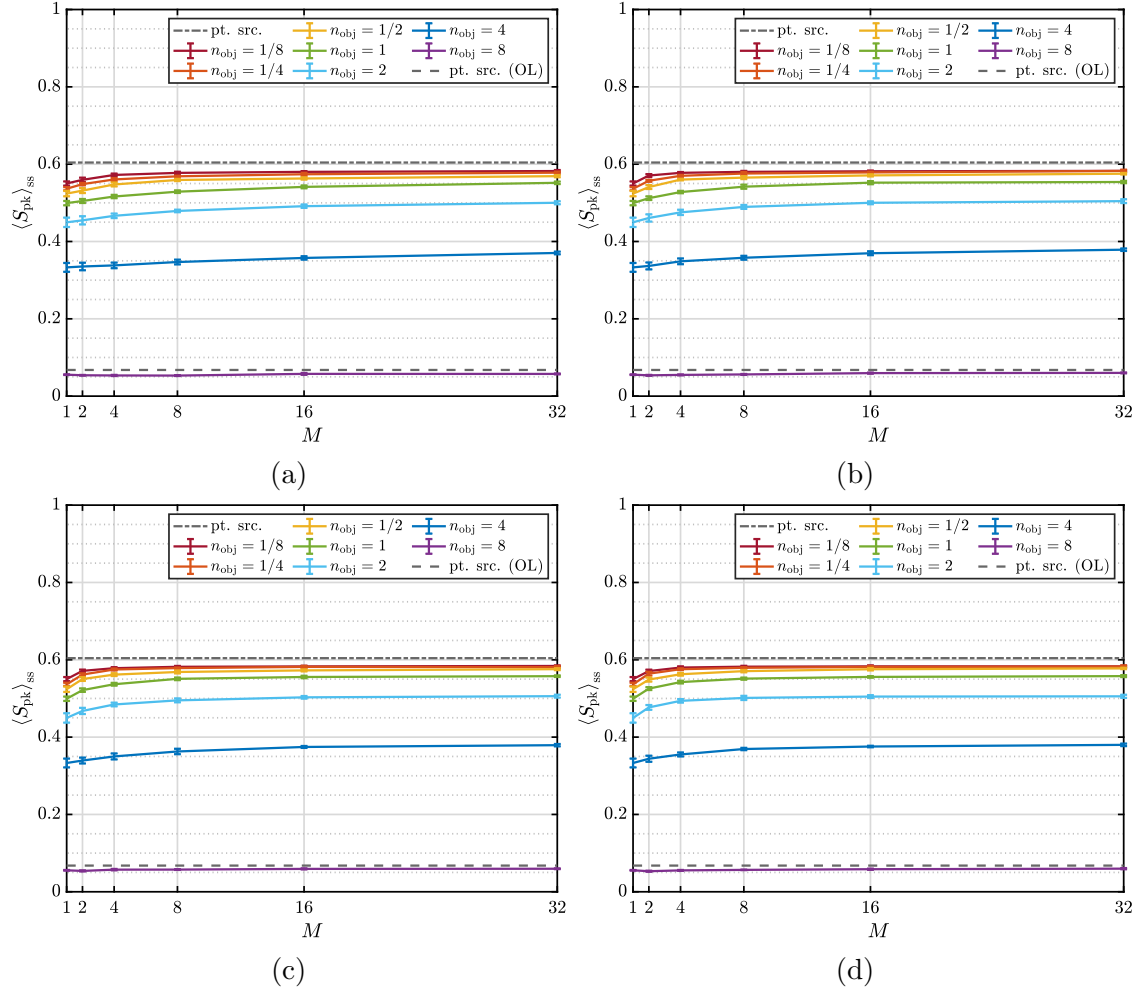


Figure 6.9: Steady-state S_{pk} results with $f_{\text{eff}} = 40f_G$ and various degrees of subframe averaging at (a) 25% decorrelation, (b) 50% decorrelation, (c) 75% decorrelation and (d) 100% decorrelation of speckle between consecutive subframes.

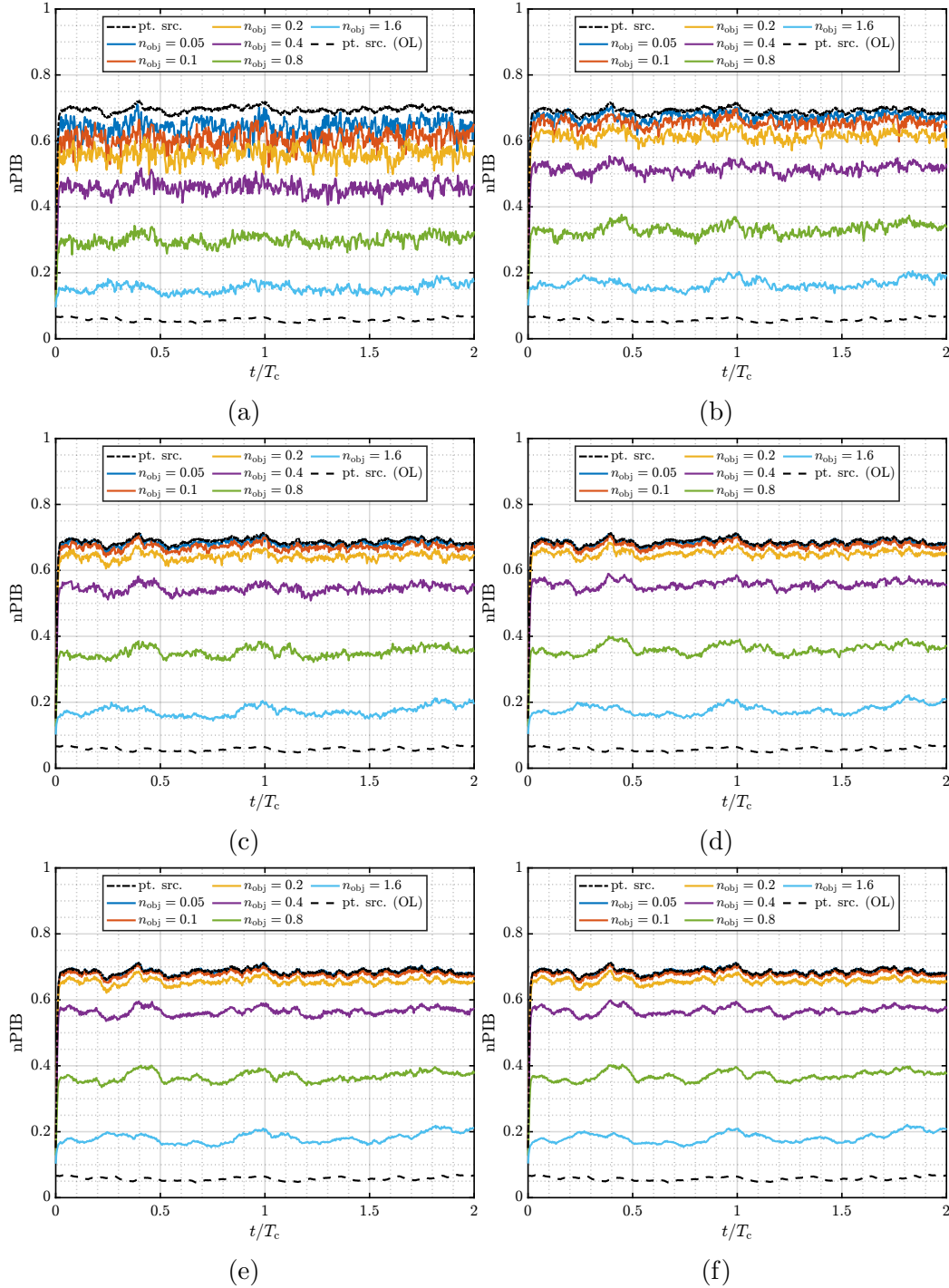


Figure 6.10: Time-domain nPIB results with $f_{\text{eff}} = 40f_G$ and (a) no speckle averaging, (b) 2-subframe averaging, (c) 4-subframe averaging, (d) 8-subframe averaging, (e) 16-subframe averaging and (f) 32-subframe averaging for fully uncorrelated speckle between consecutive subframes.

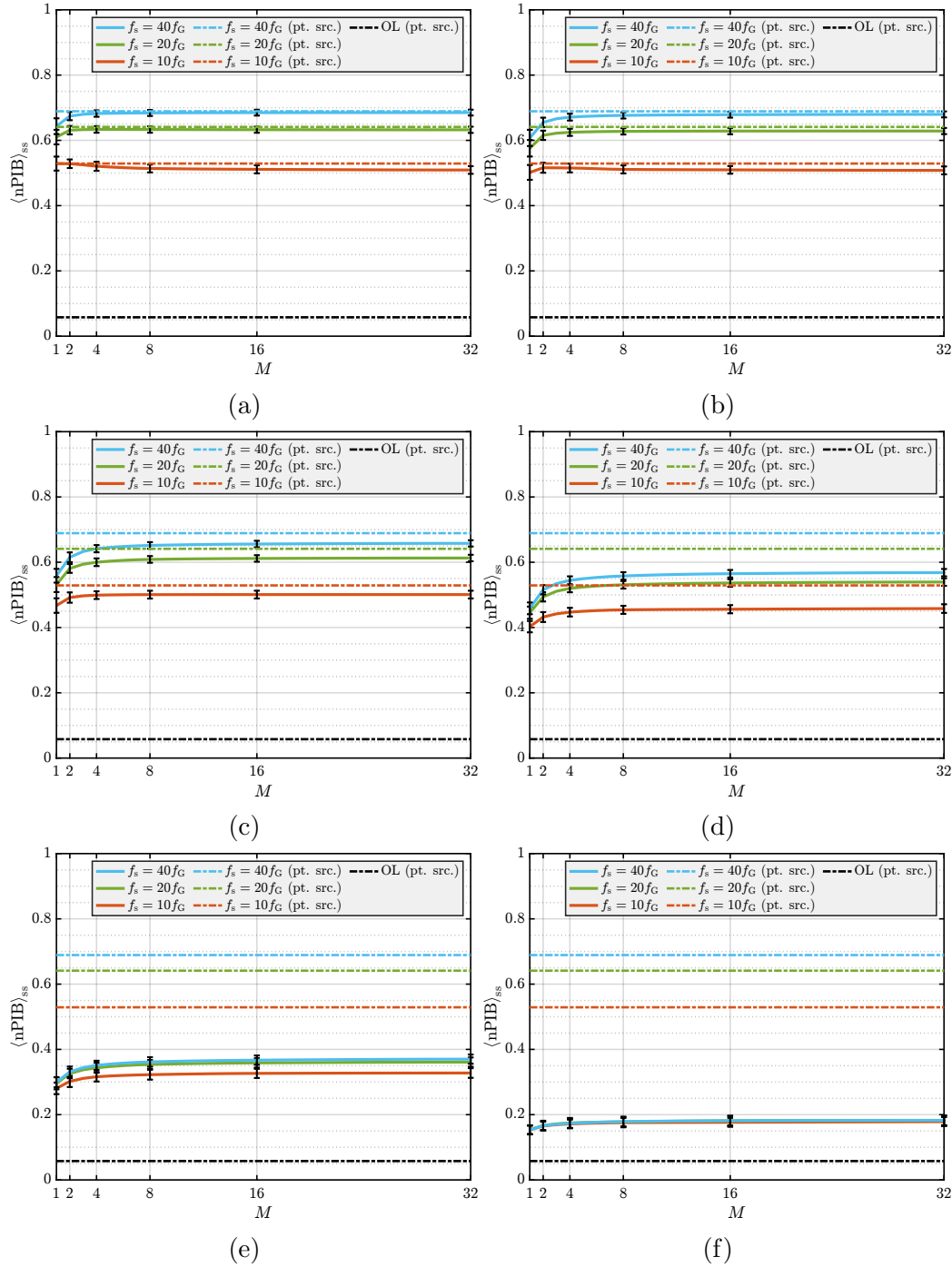


Figure 6.11: Steady-state nPIB results comparing $f_{\text{eff}} = 40f_G$, $20f_G$ and $10f_G$ for various degrees of speckle averaging with fully uncorrelated speckle between consecutive subframes at (a) $n_{\text{obj}} = 1/20$, (b) $n_{\text{obj}} = 1/10$, (c) $n_{\text{obj}} = 1/5$, (d) $n_{\text{obj}} = 2/5$, (e) $n_{\text{obj}} = 4/5$ and (f) $n_{\text{obj}} = 8/5$.

CHAPTER 7

System-Level Noise Performance of Coherent Imaging Systems[†]**7.1 Background**

In designing electro-optical and infrared (EO/IR) systems, resolution and sensitivity play the most impactful roles in determining overall performance [1]. The point-spread function (PSF) and optical transfer function (OTF) of an *incoherent* imaging system fully describe its resolution in the spatial and frequency domains, respectively [147]. Analogously, the amplitude-spread function (ASF) and amplitude transfer function (ATF) provide complete descriptions of a *coherent* imaging system's resolution [39]. The metric of interest for sensitivity is often a signal-to-noise ratio (SNR) or contrast-to-noise ratio (CNR), depending on the imaging task at hand. Accurate estimates of all relevant signals and noise sources are necessary to make such calculations, and considerable effort has gone into radiometric analysis and scaling-law modeling with this very goal.

As a prominent example of imager modeling, the U.S. Army Night Vision and Electronic Sensors Directorate (NVESD) maintains the Night Vision Integrated Performance Model (NV-IPM) to evaluate resolution and sensitivity among many other outputs. Though initially conceived with only passive imaging in mind, the model has grown over time to include pulsed and continuous-wave active sources as well. In spite of these developments, there is no noise component to account for interference of coherent light as it scatters from an optically rough surface or propagates through a distributed-volume turbulent medium; we refer to these effects as speckle and scintillation, respectively.

It is possible to safely neglect scintillation in a physical model by assuming steep

[†]This material is currently undergoing peer review for publication in *Optics Express* with coauthors J. H. Follansbee, M. F. Spencer, and R. G. Driggers.

slant-path geometries or simply very low turbulence over horizontal paths. The absence of speckle effects is particularly problematic, however, as the usual simplifying assumption of a Lambertian surface in radiometric calculations necessarily implies diffuse backreflections. As we will see, speckle noise is often so pronounced that it becomes the limiting factor in coherent imaging performance.

There does not currently appear to be a comprehensive, system-level treatment of imaging sensitivity that covers both conventional and coherent noise anywhere else in the peer-reviewed literature. Riker *et al.* proposed a simple expression for speckle SNR that varies directly with normalized object size [148, 149] based on technical reports analyzing three-bar targets [150, 151]. In their examples, the total SNR is then an inverse quadrature sum of the speckle and radiometric SNRs. In a similar vein, Andrews *et al.* suggested an effective SNR that goes inversely as the radiometric SNR scaled by the scintillation index [152].

In our approach, we posit that an expression for effective SNR in its traditional form of a mean over a quadrature sum should be realizable on the basis of two observations: (1) that truly uncorrelated noise terms (whether additive or multiplicative) always add up in quadrature, and (2) that dependence on a common variable doesn't necessarily imply correlation. With that said, the next section presents analytical expressions for both conventional and coherent noise before exploring possibilities for mutual coupling between them. The sections beyond that introduce a wave-optics simulation methodology for the purpose of verifying theory, compare the theory against numerical results, and make recommendations as to proper treatment of system-level noise in coherent imaging.

7.2 Noise Theory

In what follows, we first offer a brief review of conventional noise sources in digital imagery. Namely, these noise sources include photon shot noise, dark shot noise, and read noise. After introducing each and explaining their quadrature addition, we move on to discussing the coherent noise sources that are central to the theme

of this paper: speckle and scintillation. We tabulate straightforward analytical expressions, reinterpreted from a literature review, that can predict respective noise values due to speckle or scintillation alone. We then pose the question of whether such coherent noise is subject to quadrature addition with conventional sources, and under which conditions if so. As is customary in this sort of analysis, we take all noise calculations to be in an image plane on a per-pixel basis.

7.2.1 Conventional Noise Sources

The quantum properties of light give rise to natural photon fluctuations about the average signal reaching a detector. Being a discrete process, this fluctuating behavior obeys Poisson statistics where the variance is equal to the mean arrival rate. Shot noise associated with photodetection is therefore related to the mean spectral signal $\langle Q(\lambda) \rangle$ in units of photons $[\gamma]$ by

$$\begin{aligned}\sigma_{\text{ps}}(\lambda) &= \sqrt{\langle Q(\lambda) \rangle} \\ &= \sqrt{\eta(\lambda) \langle E_{\text{q}}(\lambda) \rangle \tau \mathcal{A}_{\text{p}}},\end{aligned}\tag{7.1}$$

where σ_{ps} is a standard deviation in photoelectrons $[\text{e}^-]$ at wavelength λ $[\text{m}]$, η is the detector quantum efficiency $[\text{e}^-/\gamma]$, $\langle E_{\text{q}}(\lambda) \rangle$ is the mean *actinometric* irradiance $[\gamma/\text{s}/\text{m}^2]$, τ is the camera integration time $[\text{s}]$, and \mathcal{A}_{p} is the detector pixel area $[\text{m}^2]$. We also note that $\langle E_{\text{q}}(\lambda) \rangle = \langle E_{\text{e}}(\lambda) \rangle \div (hc/\lambda)$, where $\langle E_{\text{e}}(\lambda) \rangle$ is the mean *energetic* irradiance $[\text{W}/\text{m}^2]$, h the Planck constant $[\text{J} \cdot \text{s}]$ and c the speed of light $[\text{m}/\text{s}]$. Often it is convenient to estimate total photon noise (and thus the signal itself) by evaluating Eq. (7.1) under the assumption of quasimonochromatic light at central wavelength $\bar{\lambda}$, eliminating any spectral dependence such that

$$\begin{aligned}\sigma_{\text{ps}} &= \sqrt{\bar{\eta} \langle \bar{E}_{\text{q}} \rangle \tau \mathcal{A}_{\text{p}}} \\ &= \sqrt{\langle \bar{Q} \rangle}.\end{aligned}\tag{7.2}$$

In the above,

$$\bar{\eta} = \frac{1}{\lambda_{\text{hi}} - \lambda_{\text{lo}}} \int_{\lambda_{\text{lo}}}^{\lambda_{\text{hi}}} \eta(\lambda) d\lambda \quad (7.3)$$

and

$$\langle \bar{E}_{\text{q}} \rangle = \int_{\lambda_{\text{lo}}}^{\lambda_{\text{hi}}} \frac{\langle E_{\text{e}}(\lambda) \rangle}{hc/\lambda} d\lambda \quad (7.4)$$

are the average quantum efficiency and band-integrated irradiance with λ_{lo} and λ_{hi} being the passband cut-on and cut-off wavelengths, respectively. This assumption is especially valid for active imaging systems, which tend to operate over finite spectral bands for coherence purposes (and filter down accordingly to preserve sensitivity). As an aside, coherent noise arising from interference depends on the mean incoming signal level as well. We will therefore revisit the subject of photon shot noise when we move on to discuss coupling in Sec. 7.2.3.

Moving on to the charge domain, photoelectrons intermix with thermal electrons originating from sensor electronics as they heat up during exposure. This time-dependent charge buildup in the pixel well occurs independently of any signal accumulation, comprising a pedestal of dark current with its own associated shot noise. The discrete nature of electron counting induces statistical variations that also follow a Poisson distribution, by which

$$\sigma_{\text{ds}} = \sqrt{i_{\text{d}}\tau}. \quad (7.5)$$

Here, σ_{ds} is a standard deviation in electrons [e^-] while i_{d} is the time-average dark current [$e^-/\text{px}/\text{s}$], which manufacturers of focal plane arrays (FPAs) usually specify.

Unlike the previous instances of time-dependent shot noise, each detector readout event produces a fixed level of read noise denoted as σ_{rd} [e^-]. FPA datasheets generally specify this RMS value as well to account for several physical processes inherent in the readout integrated circuit (ROIC) electronics, including pixel (i.e., Johnson) noise, reset (i.e., kTC) noise, and flicker (i.e., $1/f$) noise. Read noise is

typically Gaussian distributed with zero mean. We choose to stop here and work in the charge domain as we are not considering any post-readout sources of noise in the signal chain. Ultimately the ROIC converts all charges to digital numbers (DNs) set by the camera gain factor K [e^-/DN], constituting a digital signal; working in either domain would thus give equivalent SNRs as unitless ratios.

Taken together, the total effective noise up to this point is

$$\begin{aligned}\sigma_{\text{eff}} &= \sqrt{\sigma_{\text{ps}}^2 + \sigma_{\text{ds}}^2 + \sigma_{\text{rd}}^2} \\ &= \sqrt{\langle \bar{Q} \rangle + i_{\text{d}}\tau + \sigma_{\text{rd}}^2}.\end{aligned}\tag{7.6}$$

It is worth pointing out here that Gaussian noise is additive in nature, whereas Poisson noise is nonstationary and hence neither additive nor multiplicative. Nonetheless, taking a quadrature sum of uncorrelated noise levels as in Eq. (7.6) is a widely accepted practice verified through empirical observations [153]. It stands to reason, then, that multiplicative noise such as speckle or scintillation might reasonably add in quadrature too (indicating no correlation with conventional noise). With that in mind, we proceed by deriving similar noise variances characteristic of speckle and scintillation.

7.2.2 Coherent Noise Sources

Our goal in this section is to establish analytical expressions for coherent noise in the charge domain. We define coherent noise broadly as interference due to propagation of coherent light in both a spatial and temporal sense. Our interests include noise due to speckle (σ_{sp}) and scintillation (σ_{sc}), as well as the total coherent noise (σ_{ch}) due to their combined effect. Assuming no coupling between this coherent noise and the aforementioned conventional noise, we would then propose

$$\sigma'_{\text{eff}} = \sqrt{\sigma_{\text{ps}}^2 + \sigma_{\text{ds}}^2 + \sigma_{\text{rd}}^2 + \sigma_{\text{ch}}^2}\tag{7.7}$$

for use in the denominator of an SNR calculation to predict noise performance of

coherent imagery.

Noise Due to Speckle

Speckle is a result of rough-surface scattering, which scrambles the phase of otherwise coherent light such as emission from a laser, followed by propagation to some observation plane where interference patches form. To assess the severity of image-plane speckle noise, we turn to known expressions for partially developed speckle contrast C . In general C is a ratio of standard deviation to mean irradiance of a speckle field, such that

$$\sigma_{\text{sp}} = C \langle \bar{Q} \rangle \quad (7.8)$$

relates speckle contrast and mean signal level to absolute speckle noise. Irradiance follows negative-exponential statistics in a fully developed speckle pattern, meaning signal fluctuations are equal in magnitude to the mean signal itself (i.e., C goes to unity). When we mitigate speckle by any of several mechanisms, however, C is less than one and the pattern is only partially developed. Our immediate goal, then, is to attain a generalized expression for C that applies to various active imaging scenarios.

Solving for C in Van Zandt's validated analysis of modified speckle contrast [154] leads to the result

$$\begin{aligned} C &= \left(\frac{1 + \mathcal{P}^2}{2} \right)^{1/2} \left\{ 1 + \sqrt{\left| \sqrt{1 + \frac{8 [\pi \sigma_h \Delta \lambda \cos(\varphi)]^2}{\bar{\lambda}^4}} - 1 \right|^2 + \left| \frac{3.5 \bar{\lambda} Z_1 \tan(\varphi)}{D l_c} \right|^2} \right\}^{-1/2} \\ &\approx \left(\frac{1 + \mathcal{P}^2}{2} \right)^{1/2} \left\{ 1 + \sqrt{\left| \frac{4 [\pi \sigma_h \Delta \lambda \cos(\varphi)]^2}{\bar{\lambda}^4} \right|^2 + \left| \frac{3.5 \bar{\lambda} Z_1 \tan(\varphi)}{D l_c} \right|^2} \right\}^{-1/2}, \end{aligned} \quad (7.9)$$

where \mathcal{P} is the backscattered degree of polarization (i.e., a ratio of polarized to unpolarized intensity), σ_h is the surface-height standard deviation, $\Delta\lambda$ is the source's $1/e$ spectral linewidth about a central wavelength $\bar{\lambda}$, φ is the object's out-of-plane rotation (i.e., tilt) angle, Z_1 is the longitudinal distance between object and entrance-pupil planes, D is the entrance-pupil diameter, and l_c is the light source's coherence length. The leading factor in Eq. (7.9) represents contrast due to polarization, while the first and second terms within the radical sign account for interaction of finite linewidths with surface roughness and surface tilt, respectively. Note that second line of Eq. (7.9) makes use of the binomial approximation for a somewhat simplified result.

In the case of unresolved *sampling-limited* imagery, we must further consider the effects of pixel averaging on speckle contrast. Assuming the equivalent *diffraction-limited* image would be well resolved, the coherence area associated with image-plane speckle is [16]

$$\mathcal{A}_c = \frac{\bar{\lambda}Z_2}{\mathcal{A}_s}. \quad (7.10)$$

Here, Z_2 is the longitudinal distance between exit-pupil and image planes, while \mathcal{A}_s is the area of the exit pupil itself. Given a pixel integration area \mathcal{A}_p , Speckle contrast reduces by a factor of $\sqrt{\mathcal{A}_p/\mathcal{A}_c}$ when $\mathcal{A}_c < \mathcal{A}_p$, with this factor being no less than 1 as there is always a minimum of one speckle per pixel [17].

In the interest of maximizing applicability, we can recast all mechanisms of contrast reduction in terms of individual factors used to calculate speckle noise as

$$\sigma_{\text{sp}} = \left(\frac{NPX}{1 + \sqrt{B_{\text{rgh}}^2 + B_{\text{tlt}}^2}} \right)^{1/2} \langle \bar{Q} \rangle \quad (7.11)$$

where $X = 1$ for well-resolved imagery. With the exception of N , we break these factors down in Table 7.1 where pixel averaging is now cast in such a way that $X \leq 1$. For our purposes, N is the number of uncorrelated speckle frames averaged within

Table 7.1: Speckle-reduction factors used in calculations of absolute coherent noise.

quantity	symbol	expression
band-averaging roughness factor	B_{rgh}	$[2\pi\sigma_h\Delta\lambda\cos(\varphi)/\bar{\lambda}^2]^2$
band-averaging tilt factor	B_{tilt}	$3.5\bar{\lambda}Z_1\tan(\varphi)/(Dl_c)$
polarization-averaging factor	P	$(1 + \mathcal{P}^2)/2$
pixel-averaging factor (unresolved)	X	$[2\bar{\lambda}Z_2/(pD_{\text{XP}})]^2/\pi$ (circular aperture) $[\bar{\lambda}Z_2/(pD_{\text{XP}})]^2$ (square aperture)

a single camera integration time; we refer the reader to [2, 57] for a framework to calculate N from known system dynamics. It is clear at this point that narrowband (i.e., temporally coherent) and linearly polarized illumination with $\Delta\lambda \rightarrow 0$, $l_c \rightarrow \infty$ and $\mathcal{P} \rightarrow 1$ indicates unit contrast. At the other extreme, broadband (i.e., temporally incoherent) and unpolarized illumination with $\Delta\lambda \rightarrow \infty$, $l_c \rightarrow 0$ and $\mathcal{P} \rightarrow 0$ becomes virtually speckle free. Shorter wavelengths also imply less speckle noise overall, which is consistent with $\bar{\lambda} \rightarrow 0$ marking the geometrical-optics limit where there is no interference and, in turn, no speckle.

Noise Due to Scintillation

Scintillation occurs when the turbulent atmosphere introduces phase and/or amplitude aberrations along the path of a traveling wavefront, resulting in irradiance fades that degrade SNRs. Added propagation distance past these aberrations converts phase to amplitude and vice versa, so scintillation is most severe in the case of long-range imaging across a distributed volume of turbulence (as in a horizontal path). It is common to gauge the “strength” of scintillation by the Rytov number (\mathcal{R}) or Rytov variance ($\sigma_R^2 = 4\mathcal{R}$), which in weak-to-moderate conditions (corresponding to $\sigma_R^2 \lesssim 1$) approximate the log-amplitude variance (σ_χ^2) and log-irradiance variance ($\sigma_{\ln I}^2 = 4\sigma_\chi^2$), respectively [152]. Also assuming weak scintillation, the log-irradiance—and therefore Rytov—variance approximates the normalized irradiance

variance a.k.a. scintillation index ($\sigma_I^2 = \sigma_Q^2 / \langle \bar{Q} \rangle^2 = \exp(4\sigma_\chi^2) - 1 \approx \exp(4\mathcal{R}) - 1 \approx 4\mathcal{R}$). Thus if we estimate the scintillation index from Rytov number, we can predict absolute scintillation noise to be

$$\sigma_{\text{sc}} = \sqrt{\sigma_I^2 \langle \bar{Q} \rangle}. \quad (7.12)$$

Again in the case of *sampling-limited* unresolved imagery, we must consider the effects of aperture averaging on optical scintillation. To a first order, we can quantify this image-plane scintillation index as the pupil-plane expression modified by an aperture-averaging factor $A \leq 1$. Andrews has provided interpolation formulae for such effects [155] as functions of the Fresnel number

$$N_{\text{F}} = \frac{(D/2)^2}{\lambda Z_1}, \quad (7.13)$$

since scintillated correlation widths are on the order of the first Fresnel zone radius $\sqrt{\lambda Z_1}$ and N_{F} counts the number of Fresnel zones contained within the entrance pupil. Scintillation index reduces further through the use of polychromatic light, which Fante [156] and Baykal [157] have both shown to produce a bandwidth-averaging factor that applies to either spherical- or plane-wave illumination. Korotkova [158] more recently demonstrated how scintillation scales with polarization in the same way as speckle [cf. Eq. (7.9)].

In effect, scintillation decreases by all the same mechanisms as speckle except surface roughness which does not apply to turbulent media. Restricting our attention to the regime of weak-to-moderate turbulence (i.e., before scintillation begins to saturate), we proceed to recast all physical processes that affect the scintillation index such that

$$\sigma_{\text{sc}} = 2 (\mathcal{R}ABNP)^{1/2} \langle \bar{Q} \rangle \quad (7.14)$$

where $A = 1$ for well-resolved imagery and N is again the number of averaged frames over a long exposure. Table 7.2 lists each of these factors; we state plane-wave ex-

Table 7.2: Scintillation-reduction factors in calculations of absolute coherent noise.

quantity	symbol	expression
Rytov number	\mathcal{R}	$0.124C_n^2k^{7/6}Z_1^{11/6}$ (spherical wave)
		$0.307C_n^2k^{7/6}Z_1^{11/6}$ (plane wave)
aperture-averaging factor (unresolved)	A	$(1 + 1.54N_F^{5/6})^{-7/5}$ (spherical wave)
		$(1 + 6.67N_F)^{-7/6}$ (plane wave)
bandwidth-averaging factor	B	$1 - 0.445(\Delta\lambda/\bar{\lambda})^{5/6}$
polarization-averaging factor	P	$(1 + \mathcal{P}^2)/2$

pressions for completeness but prefer the spherical-wave versions in practice, as they agree well with our simulation results and infinite plane-wave analysis is known to poorly approximate horizontal-path imaging anyhow [159]. The above relationships suggest that longer wavelengths, shorter propagation paths, larger aperture sizes (when unresolved), broader bandwidths and greater depolarization all contribute to reduced scintillation. Its wavelength dependence is not strictly monotonic, however, due to $\bar{\lambda}$ appearing multiple places in the expression. We note that this analysis only covers scintillation on the downlink path, neglecting the effects of uplink scintillation. Andrews *et al.* derive more complete expressions for scintillation index concerning two-way propagation from either a monostatic or bistatic system [152].

7.2.3 Coupled Noise Effects

With noise parameters defined in the isolated cases of either speckle or scintillation, we now turn our attention to whether their shared dependence on mean signal level gives rise to correlation with photon noise. Recalling that photoevents are in general Poisson distributed, the conditional probability mass function (PMF) describing photon noise is [40]

$$P(K|\bar{Q}) = \frac{\bar{Q}^K}{K!} \exp(-\bar{Q}) \quad (7.15)$$

where K represents the photoevent count and \bar{Q} is the classical energy accumulated at each point in the image. We are ultimately interested in an unconditional variance of photoelectron arrival, which the law of total variance dictates is [160]

$$\text{var} [K] = \text{E} [\text{var} [K|\bar{Q}]] + \text{var} [\text{E} [K|\bar{Q}]]. \quad (7.16)$$

Here, $\text{E} [o]$ denotes an expected value and $\text{var} [o]$ a variance. From Eq. (7.15),

$$\begin{aligned} \text{E} [K|\bar{Q}] &= \sum_{K=0}^{\infty} K \frac{\bar{Q}^K}{K!} \exp(-\bar{Q}) \\ &= \bar{Q} \end{aligned} \quad (7.17)$$

and

$$\begin{aligned} \text{var} [K|\bar{Q}] &= \sum_{K=0}^{\infty} K^2 \frac{\bar{Q}^K}{K!} \exp(-\bar{Q}) - \text{E}^2 [K|\bar{Q}] \\ &= \bar{Q}, \end{aligned} \quad (7.18)$$

confirming the known property of a Poisson distribution that its sole parameter (in this case \bar{Q}) determines both its mean and variance.

In vacuum, speckle statistics generally obey the gamma probability density function (PDF) [16]

$$P(\bar{Q}) = \frac{\beta^\alpha}{\Gamma(\alpha)} \bar{Q}^{\alpha-1} \exp(-\beta\bar{Q}) \quad (7.19)$$

in canonical form with parameters $\alpha = 1/C^2$ and $\beta = 1/(C^2\langle\bar{Q}\rangle)$. Equations (7.17) and (7.18) imply

$$\begin{aligned} \text{E} [\text{var} [K|\bar{Q}]] &= \frac{\beta^\alpha}{\Gamma(\alpha)} \int_0^\infty \bar{Q}^\alpha \exp(-\beta\bar{Q}) d\bar{Q} \\ &= \frac{\alpha}{\beta} \end{aligned} \quad (7.20)$$

and

$$\begin{aligned} \text{var} [\text{E} [K|\bar{Q}]] &= \frac{\beta^\alpha}{\Gamma(\alpha)} \int_0^\infty \bar{Q}^{\alpha+1} \exp(-\beta\bar{Q}) d\bar{Q} - \text{E}^2 [\text{var} [K|\bar{Q}]] \\ &= \frac{\alpha}{\beta^2}, \end{aligned} \quad (7.21)$$

such that

$$\begin{aligned} \sigma_{\text{ps}} &= \sqrt{\frac{\alpha}{\beta} + \frac{\alpha}{\beta^2}} \\ &= \sqrt{\langle \bar{Q} \rangle + C^2 \langle \bar{Q} \rangle^2} \end{aligned} \quad (7.22)$$

for a Poisson-gamma distribution. Note that Eq. (7.19) reduces to the negative-exponential PDF commonly associated with fully developed speckle when $C = 1$, while Eq. (7.22) converges to the incoherent result of Eq. (7.2) as $C \rightarrow 0$. Since noise resulting from the presence of both photon noise and speckle noise is clearly a quadrature sum, we can conclude that there is no correlation between the two despite their common dependence on $\langle \bar{Q} \rangle$. It is worth noting that speckle noise will tend to dominate over photon noise due to its stronger proportionality with $\langle \bar{Q} \rangle$, meaning substantial mitigation of speckle is required to reach the photon-noise limit.

In the absence of speckle but the presence of weak-to-moderate scintillation, the Rytov approximation gives rise to the lognormal PDF [116]

$$P(\bar{Q}) = \frac{1}{\bar{Q}\sigma\sqrt{2\pi}} \exp\left(-\frac{\ln(\bar{Q}) - \mu}{2\sigma^2}\right) \quad (7.23)$$

in canonical form with parameters $\mu = \ln(\langle\bar{Q}\rangle/\sqrt{1+\sigma_I^2})$ and $\sigma = \sqrt{\ln(1+\sigma_I^2)}$. In this case, Eqs. (7.17) and (7.18) tell us

$$\begin{aligned} \mathbb{E}[\text{var}[K|\bar{Q}]] &= \frac{1}{\sigma\sqrt{2\pi}} \int_0^\infty \exp\left(-\frac{\ln(\bar{Q}) - \mu}{2\sigma^2}\right) d\bar{Q} \\ &= \exp\left(\mu + \frac{\sigma^2}{2}\right) \end{aligned} \quad (7.24)$$

and

$$\begin{aligned} \text{var}[\mathbb{E}[K|\bar{Q}]] &= \frac{1}{\sigma\sqrt{2\pi}} \int_0^\infty \bar{Q} \exp\left(-\frac{\ln(\bar{Q}) - \mu}{2\sigma^2}\right) d\bar{Q} - \mathbb{E}^2[\text{var}[K|\bar{Q}]] \\ &= \exp(2\mu + \sigma^2) [\exp(\sigma^2) - 1], \end{aligned} \quad (7.25)$$

such that

$$\begin{aligned} \sigma_{\text{ps}} &= \sqrt{\exp\left(\mu + \frac{\sigma^2}{2}\right) + \exp(2\mu + \sigma^2) [\exp(\sigma^2) - 1]} \\ &= \sqrt{\langle\bar{Q}\rangle + \sigma_I^2 \langle\bar{Q}\rangle^2} \end{aligned} \quad (7.26)$$

for a Poisson-lognormal distribution. Once again, we find no correlation between photon noise and scintillation noise although they share a dependence on $\langle\bar{Q}\rangle$. We also note the same proportionality with scintillation as we saw with speckle before, indicating scintillation noise will also tend to dominate over photon noise.

We now must ask the question of what happens when *both* speckle and scintillation are present in an active imaging scenario, as is often the case in horizontal-path geometries. Gudimetla and Holmes proposed the two-parameter K (a.k.a. gamma-

gamma) distribution as a general model to parameterize irradiance statistics by degrees of freedom with respect to both speckle and scintillation [161]. However, they demonstrated both analytically and experimentally that normalized variance does not increase monotonically with turbulence strength in the presence of speckle [120, 162, 163]. Rather, it remains at a constant unity for very low scintillation strengths where speckle phase dominates, rises above 1 as atmospheric log-amplitude perturbations grow stronger until peaking around 1.25 for $\sigma_\chi^2 \approx 0.1$, and finally decays back down to unity as scintillation saturates and atmospheric phase perturbations take over [164]. These trends are relatively indifferent to specific beam parameters and propagation geometries [165], and they are consistent with what we've seen in our own simulations and experimental trials.

Since we cannot simply add in quadrature the theoretical expressions of Secs. 7.2.2 and 7.2.2, we seek an alternative closed-form expression for the combined effects of speckle and scintillation that we encounter in active imaging. The covariance calculations of Refs. [120, 162, 163] remain in integral form, however, requiring involved numerical calculations to produce meaningful results. We can instead use the relatively constant shape of their normalized irradiance curves to our advantage by fitting a four-parameter lognormal function of the form

$$\varsigma(\mathcal{R}) = c_1 \exp \left\{ -\frac{\ln(2)}{\ln^2(c_4)} \ln^2 \left[1 + \frac{(\mathcal{R} - c_2)(c_4^2 - 1)}{c_3 c_4} \right] \right\} \quad (7.27)$$

with $c_1 = 0.125$, $c_2 = 0.1$, $c_3 = 0.3$ and $c_4 = 3.3$ using TableCurve 2D. Figure 7.1 shows a semilog plot of this function, which we treat as a scale factor in calculating the coupled variance for coherent noise according to the K distribution model as

$$\sigma_{\text{ch}} = \sqrt{[1 + C^2][1 + \varsigma(\mathcal{R})] - 1} \langle \bar{Q} \rangle. \quad (7.28)$$

Here, $\varsigma(\mathcal{R})$ has replaced $(4\mathcal{R})^2$ in the expression for scintillation noise variance as compared with Eq. (7.14). The argument of the radical sign in Eq. (7.28) works out to be a sum of individual variances with the product of variances, which is identical to the form of combined variances that Bufton *et al.* derived in a related problem

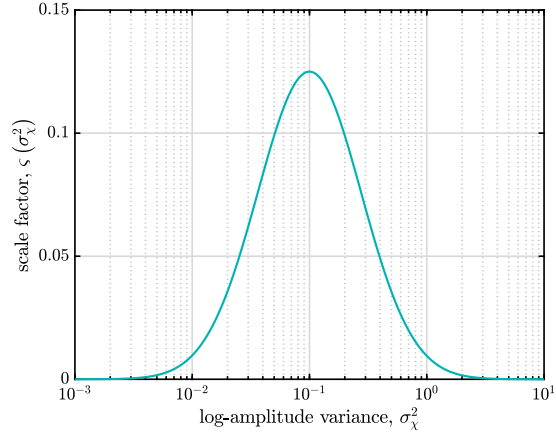


Figure 7.1: Scale factor describing additional coherent noise due to scintillation when speckle noise is already present [cf. Eq. (7.27)].

involving ground-to-space laser ranging of a retroreflector array [166]. All told, our conditional expression for system-level coherent noise is now

$$\begin{aligned}
 \sigma'_{\text{eff}} &= \sqrt{\sigma_{\text{ps}}^2 + \sigma_{\text{ds}}^2 + \sigma_{\text{rd}}^2 + \sigma_{\text{ch}}^2} \\
 &= \begin{cases} \sqrt{\langle \bar{Q} \rangle + i_d \tau + \sigma_{\text{rd}}^2 + C^2 \langle \bar{Q} \rangle^2} & \text{(speckle only)} \\ \sqrt{\langle \bar{Q} \rangle + i_d \tau + \sigma_{\text{rd}}^2 + \sigma_I^2 \langle \bar{Q} \rangle^2} & \text{(scintillation only)} \\ \sqrt{\langle \bar{Q} \rangle + i_d \tau + \sigma_{\text{rd}}^2 + \{[1 + C^2][1 + \varsigma(\mathcal{R})] - 1\} \langle \bar{Q} \rangle^2} & \text{(speckle and scintillation)} \end{cases} \\
 & \hspace{20em} (7.29)
 \end{aligned}$$

with reference to Tables 7.1 and 7.2. We reiterate at this stage that coherent noise (which is directly proportional to the signal) will always outweigh the conventional shot noise (which is proportional to its square root) unless sufficiently mitigated by naturally occurring or deliberately engineered means.

7.3 Modeling and Simulation

With the goal of verifying the theory of Sec. 7.2, we take a wave-optics simulation approach with Monte Carlo averaging to handle the stochastic nature of speckle and



Figure 7.2: Amplitude mask of four-bar target for use in numerical simulations.

scintillation. To that end, we first define the amplitude of our object as a binary four-bar target on an $N \times N$ grid with each bar one-seventh as wide as it is tall. Figure 7.2 shows a visual of this definition, which also serves as the geometrical-optics prediction of its own image at unit magnification. With the initial amplitude of $U_0 = 1 \sqrt{W}/m$ at each nonzero pixel, we update it to

$$U = U_0 \sqrt{\frac{\Phi_e}{\sum_{x=1}^N \sum_{y=1}^N U_0^2(x, y) \delta^2}} \quad (7.30)$$

where Φ_e is the optical source power [W/m^2] and δ our simulation grid spacing [m]. Going forward, we will say for simplicity δ matches our simulated pixel pitch p .

To simulate the effects of diffraction through a coherent optical system, we define the circular pupil in Fig. 7.3a and take its 2D discrete Fourier transform (DFT) to find the ASF in Fig. 7.3b. Convolution of the geometrical image in Fig. 7.2 with this ASF yields the diffraction-limited image in Fig. 7.3c, which we take as our “noiseless” (with respect to conventional noise) and “pristine” (i.e., speckle- and scintillation-free) image to compare against various noise degradations.

From here, we take the squared modulus of our image-plane field for radiant power [W/m^2], multiply by integration time for radiant fluence [J/m^2], multiply by pixel area for radiant energy [J] and divide by photon energy for units of photons [γ]. We then proceed to simulate conventional noise in our diffraction-limited image. To apply photon shot noise, we generate random numbers from a pixelwise Poisson distribution with its rate parameter set to the pre-noise photon count at each

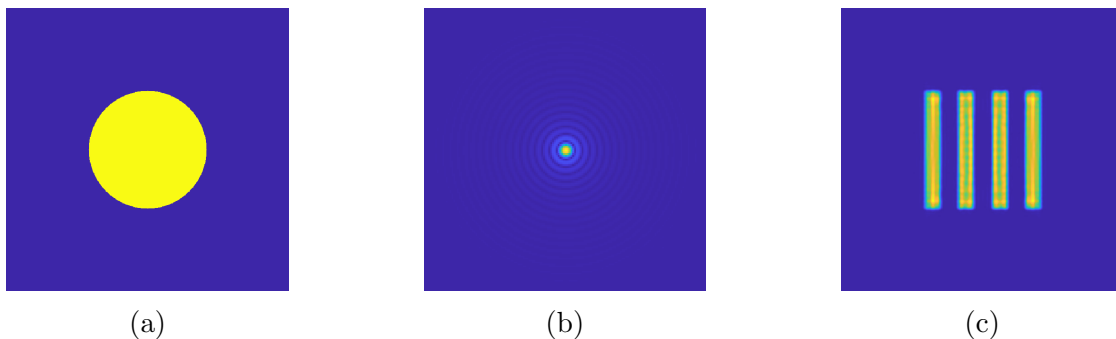


Figure 7.3: Amplitudes of (a) circular pupil and (b) complex-valued ASF; (c) pristine coherent image of four-bar target (not drawn to scale).

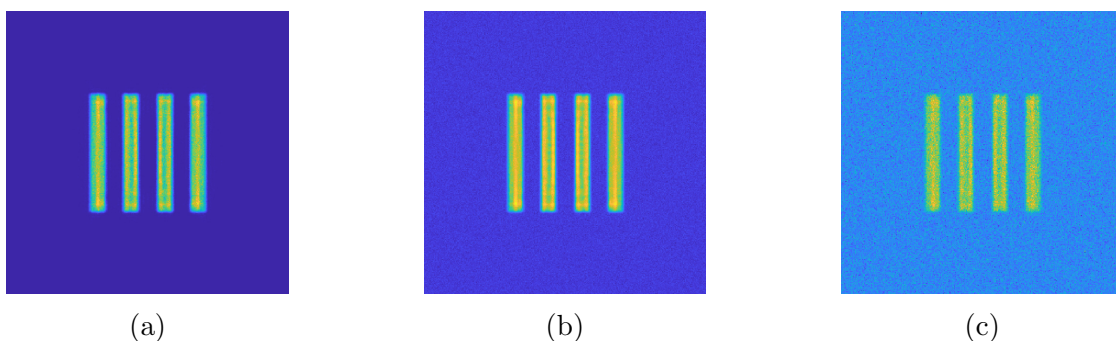


Figure 7.4: Four-bar target image after adding simulated (a) photon shot noise, (b) dark shot noise and (c) read noise.

pixel. Figure 7.4a shows the result of applying this noise. Multiplying by quantum efficiency (η) converts this image to the charge domain, where we add a pedestal and apply a second layer of Poisson-distributed random numbers to represent dark shot noise with $i_d\tau$ setting the mean and overall rate parameter. Figure 7.4b shows the result of this step. Lastly, we add read noise in the form of random numbers drawn from a zero-mean Gaussian distribution with a standard deviation of σ_{rd} , before nullifying any negative values to zero to mimic the measurement uncertainty of a realistic analog-to-digital converter (ADC). Figure 7.4c shows our final pristine image with conventional noise degradations.

To simulate speckle, we define not only a flat amplitude over our four-bar target but also a uniformly distributed random phase between $-\pi$ and π . This approach rests on the assumption of δ -correlated phase on the scale at which we're simulating

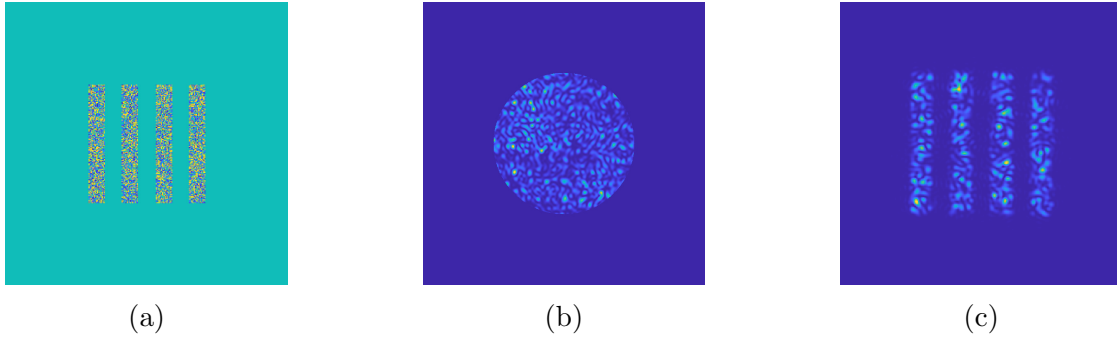


Figure 7.5: (a) Underlying phase function of rough-surface target; resulting speckle patterns in the (b) pupil and (c) image planes (not drawn to scale).

the object plane (i.e., $\delta \gg w_c$ where w_c is the surface-height correlation width). With the amplitude in Fig. 7.2 and phase in Fig. 7.5a defining the complex phasor of our object-plane field, we propagate to the pupil plane via the Fresnel diffraction integral and crop the resulting speckle field down to the pupil size as in Fig. 7.5b. We then collimate this field (invoking far-field conditions) and propagate by one focal length of a thin lens to the image plane as in Fig. 7.5c.

The remaining steps between Fig. 7.5c and the speckled, conventionally noisy image in Fig. 7.6a are identical to those starting from the pristine, diffraction-limited image in Fig. 7.3c. As for simulating scintillation, we revert to a flat object phase function and carry out split-step propagation through six Kolmogorov phase screens of equal strength and spacing between the object and pupil planes. We decompose the pupil-plane wavefront into Zernike modes in order to remove atmospheric tip and tilt so that the image stays roughly centered at its vacuum position [52], then propagate a second time through vacuum to arrive at the scintillated and conventionally noisy image in Fig. 7.6b. Here we make note of some distortion due to anisoplanatism, but Monte Carlo averaging largely alleviates any error this would introduce in our calculations. Figure 7.6c follows from the same procedure as Fig. 7.6b but begins by reinstating the δ -correlated phase of Fig. 7.5a, simulating all relevant noise sources in unison. Finally, we can reuse the amplitude definition of Fig. 7.2 as a binary mask with any of the images in Figs. 7.4c or 7.6a–7.6c for the purpose of calculating and comparing standard deviations to test for mutual independence.

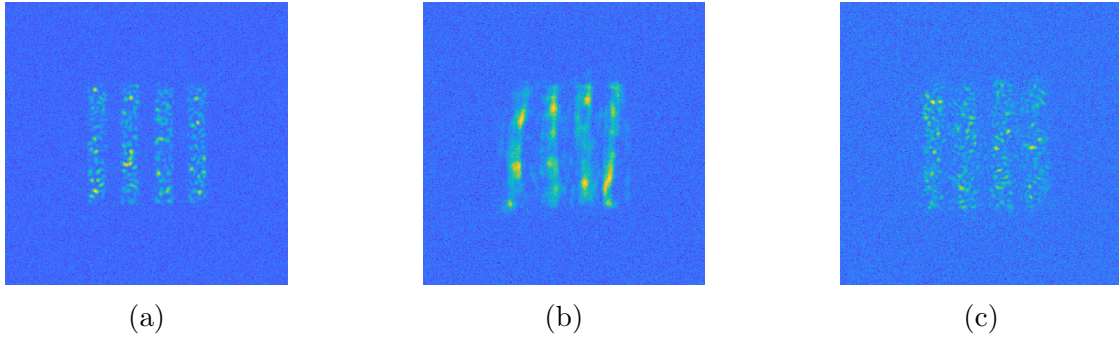


Figure 7.6: Final image of four-bar target including all conventional noise terms in addition to (a) speckle, (b) scintillation and (c) combined speckle and scintillation.

Before doing so, we subtract our noiseless and pristine image in Fig. 7.3c from each to remove the influence of pure diffraction from such calculations.

7.4 Results and Discussion

As an example use case, we reference the datasheet of an Allied Vision Goldeye CL-033 TEC1 for noise specifications [167]. The dark current of this particular model is $110 \text{ ke}^-/\text{px}/\text{s}$, while its read noise is $390 \text{ e}^- \text{ RMS}$. It has a quantum efficiency of 78.5% at a wavelength of 1550 nm. We set our source power to 1 mW so that various contributions to the effective noise are all on the same order of magnitude. Because it gives us a single knob to turn without affecting other parameters, we choose to vary our read noise from 0 to 400 e^- in 5-e^- increments while holding all other noise sources constant. We set our object size such that the object Fresnel number $N_{\text{obj}} = D/(\lambda Z_1/W) = 16$ where W is the object width; in other words, our imaging system fully resolves the object [79]. We also enforce the weak-turbulence condition that $D/r_0 = 3$, where r_0 is the Fried coherence width, leading to a spherical-wave Rytov number $\mathcal{R} = 0.06$.

The results of these tests are plotted in Fig. 7.7, which shows strong agreement between the theory that Eqs. (7.11) and (7.14) predict and the effective noise that we calculate from simulation data. Similarly, Fig. 7.8 shows promising results that suggest the scaling in Eqs. (7.27) and (7.28) provides an accurate depiction of the

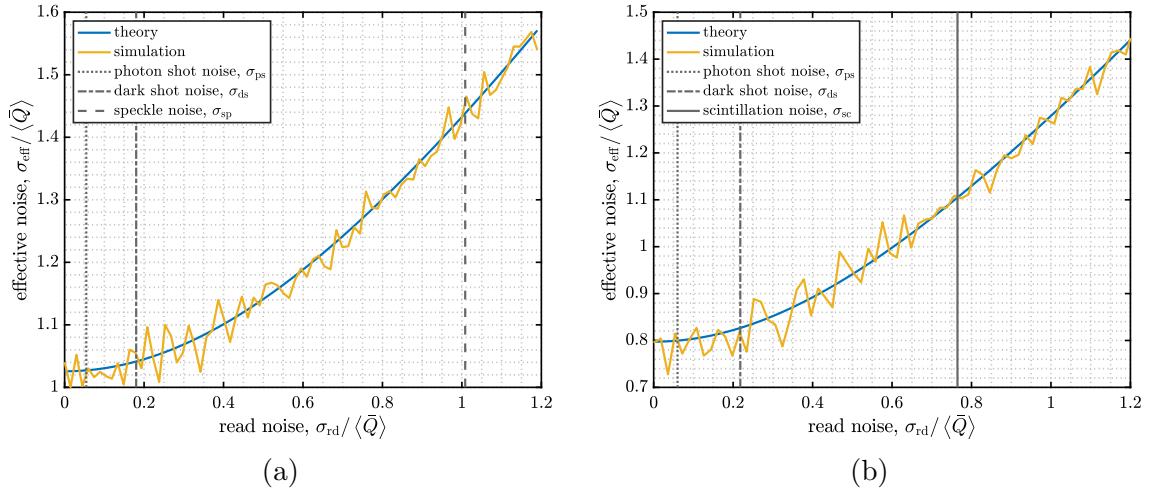


Figure 7.7: Comparison of theoretical and numerical effective noise as a function of variable read noise with other conventional noise and either (a) speckle or (b) scintillation fixed; vertical lines show fixed values for reference.

coupling that takes place between speckle and scintillation when both effects are present. The green line shows our working theory based on the work of Holmes *et al.* that provides good estimates. By contrast, the red lines represent alternative approaches that provide much poorer estimates: the sum of individual variances and their products from pure speckle and pure scintillation, a simple quadrature addition of the two, pure speckle only and pure scintillation only. Although not proper descriptions of the problem, the scintillation-only and speckle-only predictions do converge as the read noise surpasses the mean number of photoelectrons contained within the signal.

In addition to the radiometric calculations we present here, there is significant interest among the community in how speckle and scintillation affect SNR when the “signal” is an object’s angular position rather than an optical energy. We typically quantify this track error as a noise-equivalent angle (NEA; in other words, an object angular displacement at which $\text{SNR} = 1$). Tyler and Fried derived an expression for NEA as a function of SNR_0 , which is the radiometric SNR referring only to conventional noise (i.e., without speckle or scintillation included) [73]. Likewise, we showed in a recently published paper that the normalized NEA due to speckle

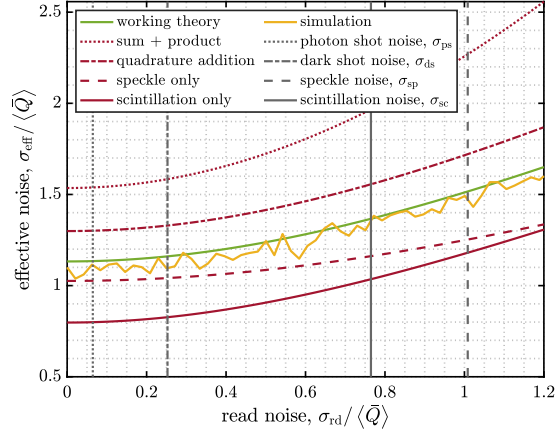


Figure 7.8: Comparison of theoretical and numerical effective noise as a function of variable read noise with other conventional and coherent (speckle and scintillation combined) noise fixed; vertical lines show fixed values for reference.

depends only on object Fresnel number [72]. Although not yet approximated in closed form, Holmes published an analytical approach to finding the NEA due to scintillation as a function of beam parameters and propagation geometry; in this case it is the discrepancy between C- and G-tilt that manifests as track error [76]. Assuming Gaussian-distributed noise, we can expect these three error quantities to decrease in the same way as Eqs. (7.11) and (7.14) with reduced speckle contrast and root scintillation index, respectively [85]. Calling them NEA_0 , NEA_{sp} and NEA_{sc} , respectively, it is therefore reasonable to assume that

$$\frac{\sigma'_\theta}{\lambda/D} = \begin{cases} \sqrt{NEA_0^2 + NEA_{sp}^2} & \text{(speckle only)} \\ \sqrt{NEA_0^2 + NEA_{sc}^2} & \text{(scintillation only)} \\ \sqrt{NEA_0^2 + \{[1 + NEA_{sp}^2][1 + \varsigma(\mathcal{R})] - 1\}} & \text{(speckle and scintillation)} \end{cases} \quad (7.31)$$

based on the findings of this paper.

CHAPTER 8

Conclusion

Chapters 2 and 3 of this dissertation demonstrated the use of wave-optic simulations to model the effects of dynamic speckle. In Ch. 2, we formulated closed-form expressions for the analytical irradiance correlation coefficient in the pupil plane of an optical system. These expressions were for square, circular, and Gaussian scattering spots and four different modes of extended-object motion, including in-plane and out-of-plane translation and rotation. In Ch. 3, we formulated closed-form expressions for the analytical irradiance correlation coefficient in the image plane of an optical system. These expressions were for square, circular, and Gaussian limiting apertures and four different modes of extended-object motion, including in-plane and out-of-plane translation and rotation. Using a phase-screen approach, we then simulated the equivalent scattering from an optically rough extended object, where we assumed that the surface heights were uniformly distributed and delta correlated from grid point to grid point. For comparison to the analytical irradiance correlation coefficient, we also calculated the numerical irradiance correlation coefficient from the dynamic speckle after simulated propagation from the object plane to a pupil plane and an image plane. Overall, the analytical and numerical results definitely demonstrated that, relative to theory, the dynamic speckle in the simulated pupil plane is properly correlated from one frame to the next. Such validated wave-optics simulations provide the framework needed to model more sophisticated setups and obtain accurate results for system-level studies.

When rough-surface scattering from a coherently illuminated object introduces speckle, it randomly shifts the centroid of its image. As such, we formulated closed-form expressions in Ch. 4 that accurately predict the NEA due to speckle. In an effort to make our results broadly applicable, we separately treated the cases of well-resolved and unresolved objects for both circular and square apertures. Overall, the

analytical results showed excellent agreement when compared with the numerical results from wave-optics simulations. Both sets of results also showed a track-error limitation of $(1/3)\lambda/D$, where λ/D is the diffraction-limited half angle. Because the Strehl ratio due to Gaussian jitter links the NEA to an intuitive scaling law, system engineers can now use these validated, closed-form expressions to account for active-tracking performance in a straightforward way.

Shack–Hartmann wavefront sensors are well-established tools for characterizing phase aberrations present in an optical field. The performance of such devices is optimized when provided a cooperative point-source beacon at range. If the beacon is instead a noncooperative extended source, the speckle that arises from rough-surface scattering introduces errors into the measurements. In distributed-volume turbulence over horizontal paths, beacon anisoplanatism acts as another source of error due to path averaging. Both types of error grow in severity with growing beacon size. Operating in the weak-turbulence regime where Shack–Hartmann wavefront sensors offer robust performance and using in-plane translation of the beacon to accomplish speckle diversity, we showed in Ch. 5 that speckle averaging helps to reduce isoplanatic measurement error but is rendered ineffective for highly anisoplanatic beacons. Understanding these system limitations is critical for performing effective wavefront sensing in horizontal propagation scenarios with noncooperative beacons.

In Ch. 6, we investigated the use of an extended beacon with a nominal phase-compensation system. An extended beacon, in general, manifests due to the scattering of coherent illumination off of an optically rough surface and results in two phenomena: (1) speckle, which adds noise to the phase measurement, and (2) anisoplanatism, which causes multiple point-spread functions to arise within the field of view of the phase-compensation system. Together, these phenomena remain relatively unexplored in the open literature, as phase-compensation research typically relies on the use of a point-source beacon for optimal performance. A point-source beacon, in practice, does not give rise to speckle or anisoplanatism and is unrealistic for tactical applications. As such, we created extended beacons of various sizes using

the plane-wave illumination of square objects. We then assumed that the resultant speckle was uncorrelated from one frame to the next and that there was the potential for anisoplanatism. These assumptions allowed us to explore the trade space using straightforward wave-optics simulations. Provided these wave-optics simulations, we modeled a horizontal-propagation path with Kolmogorov turbulence and frozen flow. Our approach characterized the severity of the uncorrelated speckle and anisoplanatism using the object Fresnel number and the size of the object relative to the size of the isoplanatic patch, respectively. In addition, our approach employed two speckle-averaging methods to investigate the framerates needed to achieve good closed-loop performance (i.e., maximize the power in the bucket at the object). Overall, the closed-loop results showed that speckle averaging is an effective strategy for mitigating the noise induced by uncorrelated speckle. However, as the extended beacon grows in size, anisoplanatism seems to become the limiting factor with respect to performance and negates the benefits of speckle averaging.

Chapter 7 provided an in-depth analysis of noise considerations in coherent imaging, accounting for speckle and scintillation in addition to “conventional” image noise. Specifically, we formulated closed-form expressions for total effective noise in the presence of speckle only, scintillation only (with weak-to-moderate conditions), and speckle combined with scintillation. We found analytically that photon shot noise is uncorrelated with speckle and scintillation, despite their shared dependence on the mean signal. Furthermore, unmitigated coherent noise tends to dominate performance limitations due to a squared mean-signal dependence. Strong coupling occurs between speckle and scintillation when both are present, and we characterized this behavior by fitting a scale factor capable of generating variances in closed form. We verified each of these claims through a series of wave-optics simulations, and we saw strong agreement in general between numerical results and theoretical predictions. Our findings allow us to confidently gauge signal-to-noise ratio (SNR) expectations when active illumination produces coherent noise.

Broad conclusions and contributions to the active EO community drawn from Chs. 2–7 are as follows:

1. We can now accurately predict speckle decorrelation (as quantified by the **irradiance correlation coefficient**) in the pupil and image planes of a generalized optical system based on object motion, as well as invert the problem to induce object motion for a controlled degree of speckle decorrelation.
2. We can now accurately predict centroiding error (as quantified by the **noise-equivalent angle**) due to speckle based on normalized object size in tracking applications.
3. We can now accurately predict open-loop wavefront sensing performance in the presence of speckle (as quantified by **RMS wavefront error** and **irradiance skewness**), as well as understand limitations due to anisoplanatism.
4. We can now understand performance trades of closed-loop adaptive optics in the presence of speckle (as quantified by **normalized power in the bucket** and **peak Strehl ratio**), including anisoplanatic limitations.
5. We can now include coherent noise terms in signal-to-noise ratio (SNR) calculations; namely, **speckle noise** and **scintillation noise**.

Looking ahead to future work on this topic, the near-, medium- and long-term goals are as follows:

- Finalize and publish simulation-based and experimental data on speckle mitigation in active tracking through manipulation of spatial coherence (**near term**).
- Process and publish field data on open-loop wavefront sensing in the presence of speckle and weak scintillation (**medium term**).
- Develop and publish slope-discrepancy theory backed by results from wave-optics simulations and field experiments (**medium term**).
- Work with Army Space and Missile Defense Command (SMDC) collaborators to validate tracking and wavefront sensing performance in the presence of speckle through laboratory testing (**long term**).

- Work with incoming graduate student(s) on quantifying effects of centroid anisoplanatism and speckle–scintillation coupling in active tracking, wavefront sensing and adaptive optics (**long term**).
- Work with Naval Surface Warfare Center (NSWC) collaborators to describe and test angular/beacon/diffractive anisoplanatism as it pertains to finite-aperture systems (**long term**).

APPENDIX A

Target Pose Estimation from Dual-Plane Speckle Return[†]**A.1 Background**

Active imaging is imperative to long-range identification of reflective, non-cooperative targets in low-light conditions. In particular, pose information describing target size, range to target, and tilt orientation is often of interest. Various lidar schemes can provide such inputs, but they tend to be technologically sophisticated, reliant on time-of-flight data for ranging, and prone to corruption from speckle in the case of coherent detection [169].

To simplify matters, we propose an alternative setup consisting of an optical system that exploits and simultaneously monitors the speckle return in two different planes. The technique assumes a reflective, optically rough, extended target under coherent illumination. For illustrative purposes the diagram in Fig. A.1 shows a laser source illuminating such a rough surface, which diffusely reflects the incident light to produce far-field speckle in the pupil plane. This pupil-plane field is then split between two optical paths, one of which relays the pupil to a lensless beam profiler. The other path introduces a lens to transform the pupil, focusing down to the image plane of a conventional camera. Through straightforward analysis of this image along with the structure of speckle in each plane, we can derive a series of relationships that reveal a rich dataset concerning the target object.

[†]This material was presented previously as [168] (<https://doi.org/10.1109/RAPID54472.2022.9911586>) © 2022 IEEE. Reprinted, with permission, from D. Burrell and R. Driggers, "Target Pose Estimation from Dual-Plane Speckle Return," *2022 IEEE Research and Applications of Photonics in Defense Conference (RAPID)*, October 2022.

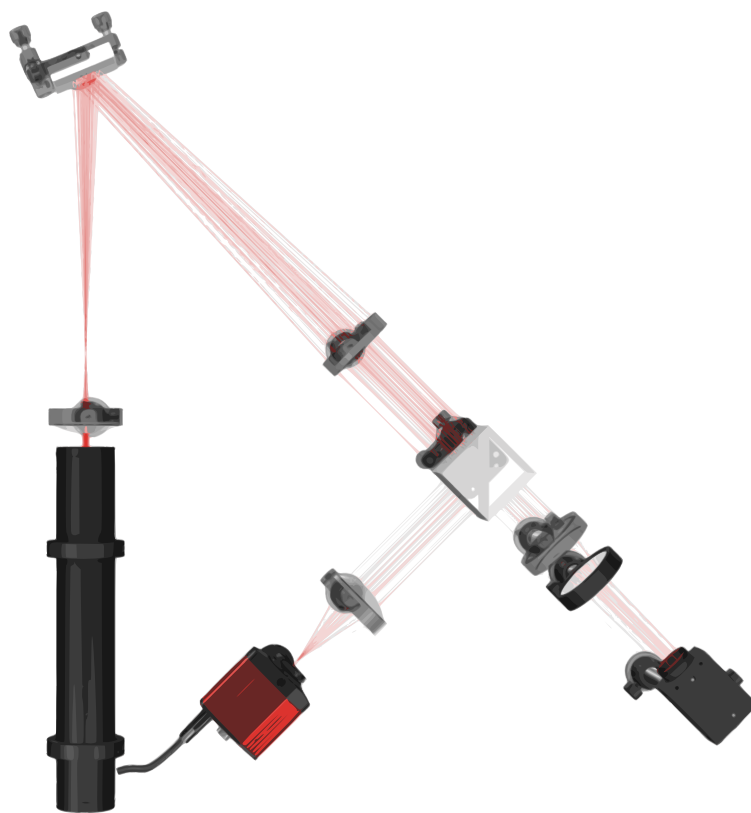


Figure A.1: Illustrative schematic of active target illumination with dual-plane monitoring of speckle return.

A.2 Theory

When a fully resolved, speckled image forms at focus in an imaging system, average lateral speckle size goes as [59]

$$\begin{aligned} w_{\text{img}} &= b\lambda F_w \\ &= b\lambda F \left(1 + \frac{|M|}{M_p} \right). \end{aligned} \quad (\text{A.1})$$

Here, b is a scale factor related to the aperture shape, λ is the wavelength of illumination, F_w refers to the working focal ratio, $F = f_{\text{eff}}/D_{\text{EP}}$ is the uncorrected focal ratio, f_{eff} is the effective focal length, D_{EP} is the entrance-pupil diameter, M is the lateral magnification, and M_p is the pupillary magnification. Rearranging Eq. (A.1) and recognizing that $|M| = W_{\text{img}}/W_{\text{obj}}$ —where W_{obj} and W_{img} are respective overall target widths in the object and image planes—we have

$$W_{\text{obj}} = \frac{\lambda F W_{\text{img}}}{M_p (w_{\text{img}}/b - \lambda F)}. \quad (\text{A.2})$$

In the pupil plane, on the other hand, average lateral speckle size following free-space propagation is [59]

$$\max(w_{\text{pup}}) = \frac{a\lambda Z}{W_{\text{obj}}} \quad (\text{A.3})$$

where a is another scale factor corresponding to the target shape and Z is the path length separating target and pupil. We consider only the *maximum* width in this case since projected speckle shrinks in the direction of any induced tilt. With only one unknown variable remaining in Eq. (A.3), we solve for

$$Z = \frac{F W_{\text{img}} \max(w_{\text{pup}})}{a M_p (w_{\text{img}}/b - \lambda F)}. \quad (\text{A.4})$$

When tilt is applied to the target at some arbitrary out-of-plane angle φ ,

$$\min(w_{\text{pup}}) = \max(w_{\text{pup}}) \cos(\varphi) \quad (\text{A.5})$$

such that

$$\varphi = \arccos \left[\frac{\min(w_{\text{pup}})}{\max(w_{\text{pup}})} \right] \quad (\text{A.6})$$

and

$$\vartheta = \angle \min(w_{\text{pup}}). \quad (\text{A.7})$$

In the above, ϑ is the rotation angle of the in-plane axis about which the target tilts out of plane.

A.3 Methods

Looking back at Eqs. (A.1)–(A.7), the known system parameters are b , λ , F and M_p . Image width W_{img} is directly measurable from the number of pixels spanning the focused image, and we can quantitatively estimate a from the shape of the resolved image. For instance, a is ~ 1.22 for a circular target and 1 for a square (and likewise with b for a given aperture shape).

Average speckle sizes w_{pup} and w_{img} follow from a 2D autocorrelation of the appropriate irradiance pattern [16]. Simulated speckle irradiance in the pupil and image planes is displayed in Fig. A.2 with corresponding autocorrelation functions for visual reference. We determine $\min(w_{\text{pup}})$ and $\max(w_{\text{pup}})$ by taking cross sections of the pupil-plane autocorrelation at azimuthal angles from 0° to 180° , fitting the expected function according to our image-plane observation (e.g. a sombrero function if circular or a sinc if the target appears square as in Fig. A.2), then determining null-crossing widths from the resulting fits. In the image plane we can simply take w_{img} to be the mean correlation width over all azimuthal angles, as an aperture is assumed parallel to the image plane in a practical system.

To generate blind speckle data for analysis, we randomize target sizes, propa-

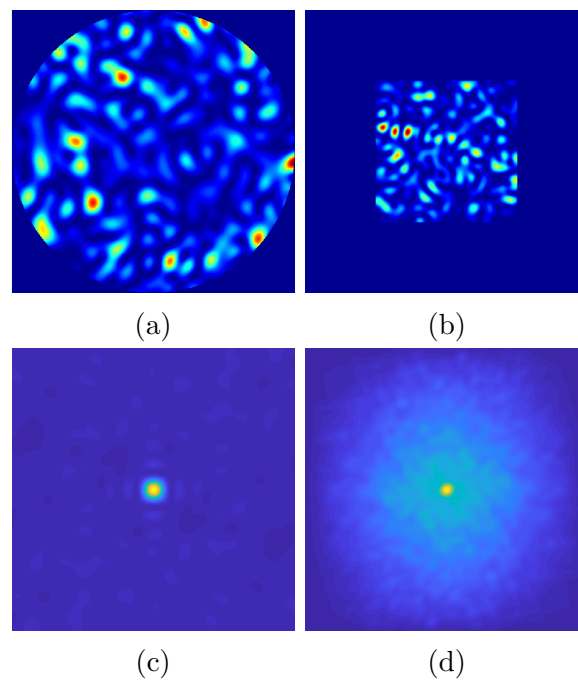


Figure A.2: Simulated irradiance maps of the (a) speckle-filled aperture in the pupil plane and (b) speckled image in the image plane; corresponding autocorrelation maps in the (c) pupil and (d) image planes.

gation distances and tilts on a simulation basis and propagate from plane to plane using standard wave-optics codes. We then perform the necessary discrete, aperture-removed autocorrelation in both planes and calculate our estimates of size, range, tilt and rotation axis via Eqs. (A.2), (A.4), (A.6) and (A.7), respectively.

A.4 Results and Discussion

In numerical Monte Carlo trials utilizing simulation data for blind tests, all calculations are in agreement with the theory of Sec. A.2 at a maximum percent error of 10%. In general we find that calculations involving $\min(w_{\text{pup}})$ or $\max(w_{\text{pup}})$ set this upper limit due to the sensitivity of isolating autocorrelation at individual angles, whereas the azimuthally averaged w_{img} is a far more robust value.

APPENDIX B

Laser Speckle Mitigation Through Substandard Compressive Sensing[†]**B.1 Background**

Laser speckle is a persistent issue affecting quality of coherent imaging as well as performance of active target tracking and wavefront sensing. Optical techniques exist for averaging out speckle that decorrelates over time, but they can be taxing from a hardware standpoint and unreliable in the presence of stationary objects [171]. Digital filters targeting speckle are often effective but struggle with the task of edge preservation [172]. Here we examine a computational approach that averages together multiple image reconstructions after compressively sensing at suboptimal sample rates.

Leportier & Park in 2016 [173] proposed a novel speckle-reduction filter inspired by compressive sensing (CS), which is the field of mathematics devoted to reconstructing a given signal from fewer measurements m than the number n of signal components. An underlying assumption is that some sparse representation exists such that the signal or its transform to a suitable domain consists of far more zeros than nonzeros. This condition generally holds true for the discrete cosine transform (DCT) of natural images.

If we intentionally set $m \ll n$ and randomize the composition of measurement matrices, speckle content diversifies from one reconstruction to the next and averages to an overall lesser effect. This effectively reduces strain on data-collection resources while helping to preserve fidelity of edges. We demonstrate these advan-

[†]This material was presented previously as [170] in *Computational Optical Sensing and Imaging (COSI) 2020* with coauthors B. Berry, M. Spencer, and R. Driggers (<https://doi.org/10.1364/COSI.2020.JW4D.5>) © 2020 Optica Publishing Group. One print or electronic copy may be made for personal use only. Systematic reproduction and distribution, duplication of any material in this paper for a fee or for commercial purposes, or modifications of the content of this paper are prohibited.

tages numerically by testing various CS configurations and gauging our success via several different performance metrics.

B.2 Methods

The familiar quantity that we take as a baseline is speckle contrast, defined as

$$K = \frac{\sigma_I}{\langle I \rangle}. \quad (\text{B.1})$$

Here, σ_I is the standard deviation of irradiance over the area of interest and $\langle I \rangle$ is the arithmetic mean over the same irradiance distribution. When $K = 1$, the speckle is “fully developed” in the sense that irradiance fluctuates on the same order of magnitude as its average value.

Our next calculation is what we call visibility factor, based on the concept of fringe visibility in interferometry and calculated as

$$V = \frac{\langle I_1 \rangle - \langle I_0 \rangle}{\langle I_1 \rangle + \langle I_0 \rangle}. \quad (\text{B.2})$$

$\langle I_1 \rangle$ and $\langle I_0 \rangle$ for our purposes are simply average irradiances in the “on” and “off” state (or the image-plane conjugate of reflective and nonreflective object features), respectively.

The final metric that we assess is reconstruction error given by

$$e = \frac{\|\hat{I} - I\|_2}{\|I\|_2}, \quad (\text{B.3})$$

where $\|\circ\|_p$ denotes the ℓ_p norm and \hat{I} is our best estimate of ground-truth irradiance I . Within the context of our problem, we consider the estimate to be a running average of reconstructed speckled images and the ground truth to be a diffraction-limited image of the equivalent mirrored object.

Formalizing the CS framework, our goal is to solve the basis pursuit problem

$$\hat{x} = \arg \min_x \|x\|_1 \quad \text{subject to } y = \Phi\Psi x, \quad (\text{B.4})$$

where x and \hat{x} respectively are the 1-D vectorization of our speckled image and its estimate, y is our measurement, Φ is a projection matrix of our choosing and Ψ is the sparsifying basis set. Provided sufficient sparsity along with minimal coherence between Φ and Ψ , Eq. (B.4) is a convex optimization problem that we can solve via linear programming for efficient image reconstruction.

B.3 Results and Discussion

The most significant outcome of reconstruction is a strong dependence on m , shown in Fig. B.1 for a weighted binary Φ with a row weight of 50 and a DCT-II Ψ matrix. Noting that Eqs. (B.1) & (B.3) represent defect functions whereas Eq. (B.2) is a figure of merit, low speckle contrast and reconstruction error with a high visibility factor comprise the ideal recovery scenario. Figures B.1a & B.1b expose the shortcoming of evaluation by either K or V as the two variables appear to be directly related. Figure B.1c suggests that e accounts for this loss of visibility by rating the crude least-squares reconstruction lower than in Fig. B.1a.

In these simulation trials, we have shown that there are clear benefits to performing CS averaging of speckled imagery in terms of reconstruction error. The challenge lies in striking proper balance between speckle contrast and visibility for optimal reconstruction; initial results imply that $m/n \approx 10\%$ is satisfactory. Looking to the comparison in Fig. B.2, CS can greatly assist in deciphering images that contain speckle. We can use this strategy to better image static objects or to relax sampling constraints in dynamic systems.

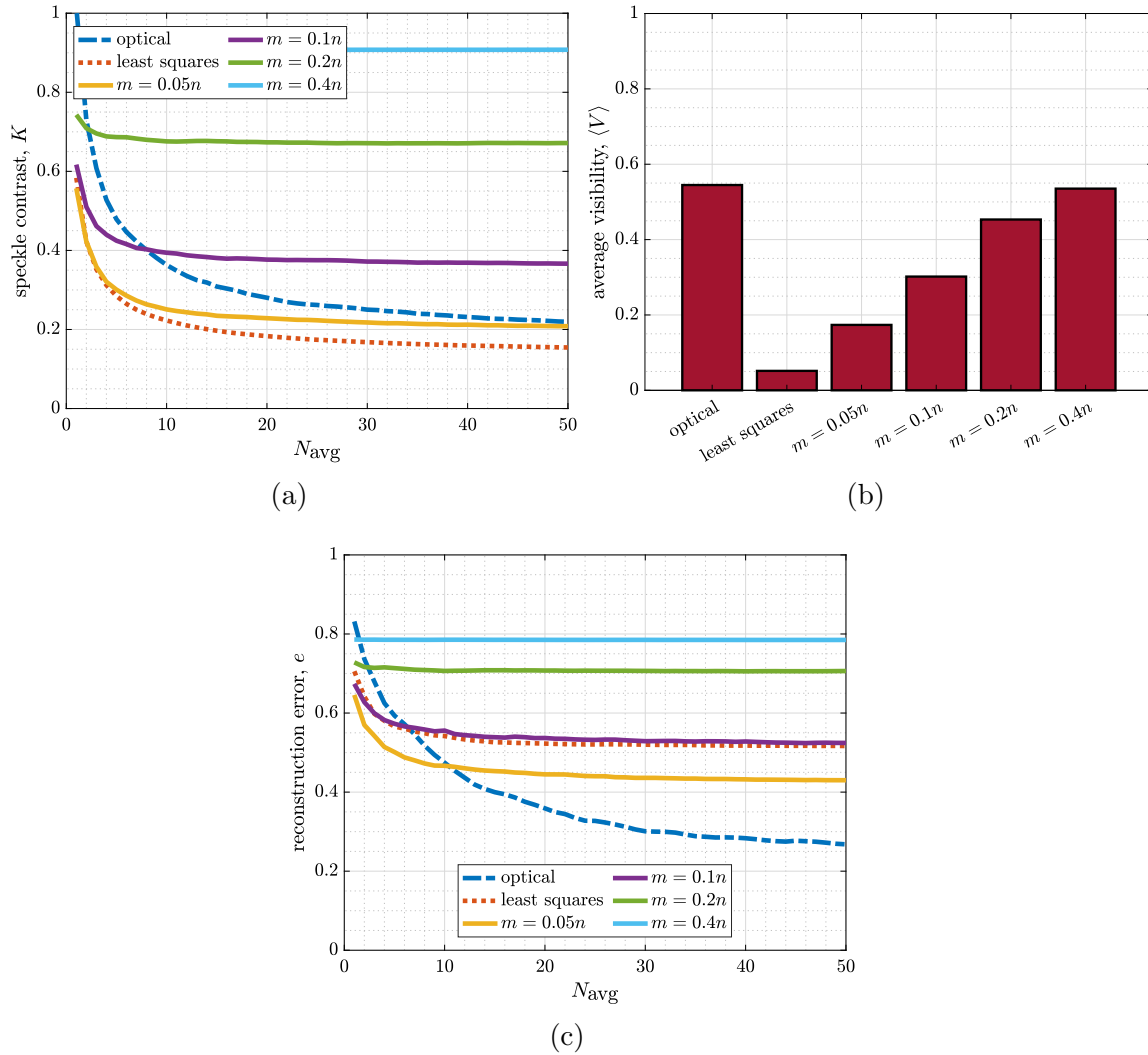


Figure B.1: Monte Carlo performance metrics versus average count (N_{avg}) and number of measurements (m).

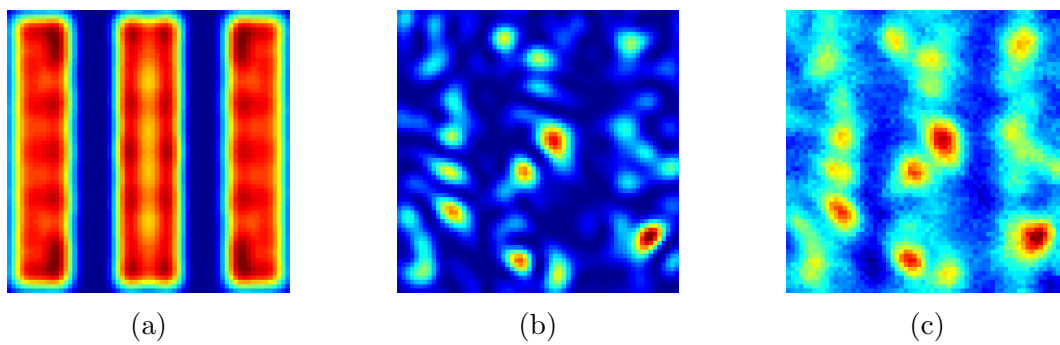


Figure B.2: Irradiance maps of (a) diffraction-limited, (b) speckle-limited and (c) CS-averaged image.

APPENDIX C

Efficiently Calculating Extended Isoplanatic Angles Over Horizontal Paths[†]**C.1 Background**

Angular anisoplanatism has a deleterious effect on image quality in astronomy and directed-energy applications [175]. The isoplanatic angle (θ_0) describes an offset between two point sources that results in no more than 1 rad^2 of mean-squared error (MSE) between their pupil-plane wavefronts after propagating through distributed-volume turbulence. However, this error metric accounts for even the lowest-order wavefront aberrations; namely piston, which is of no consequence to system performance in most cases [176], and tip/tilt, which is often addressed in a separate track loop and is altogether absent from artificial beacon measurements [175]. We therefore seek extended isoplanatic angles with these aberrations removed.

C.2 Analysis

From Stone *et al.* [176] we have an integral expression for piston/tip/tilt-removed anisoplanatic MSE as

$$\overline{\sigma_{\text{iso}}^2} = 0.821k^2D^{5/3} \int_0^Z C_n^2(z) \int_0^\infty u^{-8/3} \left[1 - J_0\left(\frac{2\theta zu}{D}\right) \right] \times \left\{ 1 - 4 \left[\frac{J_1(u)}{u} \right]^2 - 16 \left[\frac{J_2(u)}{u} \right]^2 \right\} du dz. \quad (\text{C.1})$$

[†]This material was presented previously as [174] in *Propagation Through and Characterization of Atmospheric and Oceanic Phenomena (pcAOP) 2022* with coauthors M. Kemnetz, J. Beck, and M. Beason (<https://doi.org/10.1364/PCAOP.2022.PW4F.6>) © 2022 Optica Publishing Group. One print or electronic copy may be made for personal use only. Systematic reproduction and distribution, duplication of any material in this paper for a fee or for commercial purposes, or modifications of the content of this paper are prohibited.

Here, D is the aperture-averaging receiver diameter, $k = 2\pi/\lambda$ is the angular wavenumber, λ is the wavelength of radiation, Z is the total propagation distance, $C_n^2(z)$ is the refractive-index structure parameter at distance z from the source, θ is an angular offset between incoming beams and $J_n(\circ)$ is an n th-order Bessel function of the first kind. Note that the 1st- and 2nd-order Bessel terms in Eq. (C.1) are filter functions corresponding to piston and tip/tilt, respectively.

Setting Eq. (C.1) equal to 1 and solving for θ does not generally converge to an isoplanatic angle, in which case we must rely on time-consuming graphical methods. Assuming horizontal propagation, however, allows us to treat C_n^2 as a constant for integration purposes. Then by conditioning and evaluating the proper integral in Eq. (C.1) we can represent piston-removed anisoplanatic error in quasi-closed form as

$$\begin{aligned} \overline{\sigma_{\text{iso}}^2} = \frac{C_n^2 D^{5/3} Z}{\lambda^2} \times & \left\{ \left| \frac{Z\theta}{D} \right|^{14/3} {}_4F_3 \left(-\frac{1}{2}, \frac{1}{2}, \frac{3}{2}, \frac{17}{6}; \frac{10}{3}, \frac{10}{3}, \frac{23}{6}; \left| \frac{Z\theta}{D} \right|^2 \right) K_1 \right. \\ & + \left| \frac{Z\theta}{D} \right|^{5/3} K_2 \\ & \left. + \left[{}_4F_3 \left(-\frac{17}{6}, -\frac{11}{6}, -\frac{5}{6}, \frac{1}{2}; -\frac{4}{3}, 1, \frac{3}{2}; \left| \frac{Z\theta}{D} \right|^2 \right) - 1 \right] K_3 \right\}, \end{aligned} \quad (\text{C.2})$$

where constants K_n are defined in Table C.1, $\Gamma(\circ)$ is the complete gamma function and ${}_pF_q(a_1, \dots, a_p; b_1, \dots, b_q; \circ)$ is the generalized hypergeometric function.

Table C.1: Definitions of constants appearing in calculation of piston-removed anisoplanatic error.

K_1	K_2	K_3
$\frac{729\pi^{3/2}\Gamma(11/6)}{833\Gamma(1/3)}$	$\frac{\pi^{7/2}}{\Gamma(2/3)\Gamma(11/6)}$	$\frac{1,280\sqrt[3]{2}\pi^{5/2}\Gamma(-5/6)}{6,171\Gamma^2(11/6)}$

Further removing tip and tilt leads instead to the solution

$$\begin{aligned}
\overline{\sigma_{\text{iso}}^2} = \frac{C_n^2 D^{5/3} Z}{\lambda^2} & \left\{ \left| \frac{Z\theta}{D} \right|^{14/3} \left[{}_4F_3 \left(-\frac{1}{2}, \frac{1}{2}, \frac{3}{2}, \frac{17}{6}; \frac{10}{3}, \frac{10}{3}, \frac{23}{6}; \left| \frac{Z\theta}{D} \right|^2 \right) K_4 \right. \right. \\
& \left. \left. + {}_4F_3 \left(-\frac{3}{2}, \frac{1}{2}, \frac{5}{2}, \frac{17}{6}; \frac{10}{3}, \frac{10}{3}, \frac{23}{6}; \left| \frac{Z\theta}{D} \right|^2 \right) K_5 \right] \right. \\
& \left. + \left| \frac{Z\theta}{D} \right|^{5/3} K_6 - {}_4F_3 \left(-\frac{17}{6}, -\frac{11}{6}, -\frac{5}{6}, \frac{1}{2}; -\frac{4}{3}, 1, \frac{3}{2}; \left| \frac{Z\theta}{D} \right|^2 \right) \right. \\
& \left. + {}_4F_3 \left(-\frac{23}{6}, -\frac{11}{6}, \frac{1}{6}, \frac{1}{2}; -\frac{4}{3}, 1, \frac{3}{2}; \left| \frac{Z\theta}{D} \right|^2 \right) K_8 + K_9 \right\} \quad (\text{C.3})
\end{aligned}$$

with constants K_n now defined in Table C.2. Note that $K_6 = K_2$ but is redefined here for legibility.

Table C.2: Definitions of constants appearing in calculation of piston/tip/tilt-removed anisoplanatic error.

K_4	K_5	K_6	K_7	K_8	K_9
$\frac{40 \sqrt[3]{2} \pi^2 \Gamma(-7/3)}{51 \Gamma(1/3) \Gamma(10/3)}$	$\frac{160 \sqrt[3]{2} \pi^2 \Gamma(-7/3)}{51 \Gamma(1/3) \Gamma(10/3)}$	$\frac{\pi^{7/2}}{\Gamma(2/3) \Gamma(11/6)}$	$\frac{3,520 \sqrt[3]{2} \pi^{7/2}}{1,377 \Gamma^3(17/6)}$	$\frac{70,400 \sqrt[3]{2} \pi^{7/2}}{31,671 \Gamma^3(17/6)}$	$\frac{3,520 \sqrt[3]{2} \pi^{7/2}}{10,557 \Gamma^3(17/6)}$

C.3 Results and Discussion

Using MATLAB's numerical solver, we can quickly predict extended isoplanatic angles from Eqs. (C.2) and (C.3) over a range of aperture diameters as in Fig. C.1a. To remain consistent with accepted notation we let subscript j index the number of lowest-order aberrations removed, i.e. $j = 0, 1$ and 3 for full aberration, piston removal and piston/tip/tilt removal, respectively. The spherical-wave formula for θ_0 is obtainable from standard references on atmospheric optics. We produce the results in Fig. C.1b by propagating a simulated on-axis point source through six evenly spaced layers of Kolmogorov turbulence, shifting a second point source off axis by distance $\theta_0 Z$ and propagating through the same

turbulence volume, then taking the mean-squared difference between their unwrapped phase functions ($\langle |\Delta\phi|^2 \rangle$) in the pupil plane and subtracting off successive Zernike polynomials. We see in the right-hand column that $\Delta\phi$ grows flatter with each subtraction for a fixed θ . As expected, $\langle |\Delta\phi|^2 \rangle \lesssim 1 \text{ rad}^2$ when $\theta = \theta_j$ in each of the three cases.

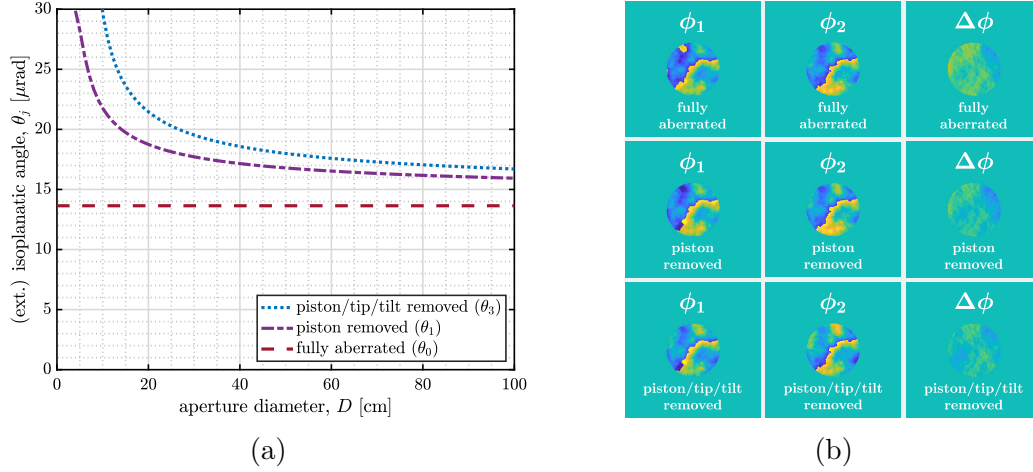


Figure C.1: (a) Fully aberrated, piston-removed & piston/tip/tilt-removed isoplanatic angles versus aperture diameter ($\lambda = 1 \text{ }\mu\text{m}$, $Z = 1.15 \text{ km}$, $C_n^2 = 2.05 \times 10^{-14} \text{ m}^{-2/3}$); (b) qualitative wave-optics simulation results ($D = 30 \text{ cm}$).

In our trials, numerical integration of Eq. (C.1) at a single offset angle consumed an average $\sim 192.6 \text{ ms}$ of CPU processing time. Evaluating Eq. (C.2) or (C.3) on an equivalent system now takes only $\sim 13.2 \text{ ms}$ on average, while solving either equation for the isoplanatic angle requires just $\sim 114.7 \text{ ms}$. In other words, the inverse problem is less resource intensive with our approach than the forward solution was previously.

APPENDIX D

Fast Statistical Testing of Scintillated, Speckled Irradiance[†]**D.1 Motivation and Background**

When we perform adaptive optics without a cooperative point-source beacon, the spatial extent of artificial beacon light typically causes speckle through backscattered rough-surface reflections. The presence of speckle contaminates our slope measurements such that we reconstruct improper wavefront information for phase compensation. Introducing geometric and/or spectral diversity shows promise as a mitigation technique, but we often rely on point-source performance as a benchmark to quantify the improvement in modeling and simulation. In field experiments, however, we have the option of analyzing pupil-plane irradiance statistics in real time to explore the useful limits of speckle averaging.

We are assuming operation in weak turbulence where scintillation does not yet saturate due to atmospheric aberrations. It is common to model the irradiance fluctuations in this regime by a lognormal probability density function (PDF) [116], which has the associated cumulative distribution function (CDF)

$$P_I(I \leq I_t) = \frac{1}{2} \left\{ 1 + \operatorname{erf} \left[\frac{\ln \left(I_t \sqrt{1 + \sigma_I^2} / \bar{I} \right)}{\sqrt{2 \ln(1 + \sigma_I^2)}} \right] \right\}. \quad (\text{D.1})$$

Here, I_t is a set threshold irradiance level, σ_I^2 is the scintillation index (i.e. variance in irradiance normalized by squared mean irradiance), and \bar{I} signifies a spatial ensemble average over all irradiance values.

Fully-developed speckle arises from diffuse reflection of coherent light off a large number of randomly-distributed surface scatterers [16]. Such an irradiance pattern follows the

[†]This material was presented previously as [177] in *Propagation Through and Characterization of Atmospheric and Oceanic Phenomena (pcAOP) 2021* with coauthor M. Beason (<https://doi.org/10.1364/PCAOP.2021.PW4F.5>) © 2021 Optica Publishing Group. One print or electronic copy may be made for personal use only. Systematic reproduction and distribution, duplication of any material in this paper for a fee or for commercial purposes, or modifications of the content of this paper are prohibited.

well-known exponential probability density with corresponding CDF

$$P_I(I \leq I_t) = 1 - \exp\left(-\frac{I_t}{\bar{I}}\right). \quad (\text{D.2})$$

When unmitigated speckle is present in the received field, probability of this form tends to dominate the observed statistics regardless of turbulence strength.

D.2 Test Methods

Under the working assumption that we have separately characterized the atmosphere to ensure weak-turbulence conditions, we can apply goodness-of-fit (GOF) testing principles to determine whether Eq. (D.1) or (D.2) provides a better fit to the available irradiance data. The latter result in this case indicates a wavefront dominated by speckle and thus a need for further averaging. The chi-square test statistic for a histogram of N total irradiance samples grouped into k bins is [178]

$$\chi^2 = \sum_{i=1}^k \frac{(O_i - E_i)^2}{E_i}, \quad (\text{D.3})$$

where O_i is the observed frequency, $E_i = N [P_I(I \leq B_i^+) - P_I(I \leq B_i^-)]$ is the expected frequency, and B_i^+ and B_i^- respectively are upper and lower boundaries of the bin at index i . Once we identify the lowest value of χ^2 between Eqs. (D.1) and (D.2), it is more computationally efficient to relate this result back to a single moment of the irradiance distribution; namely, the third standardized moment or *skewness*:

$$\gamma = \frac{(E [I - \bar{I}])^3}{(\sigma_I^2 \bar{I}^2)^{3/2}} \quad (\text{D.4})$$

D.3 Results and Discussion

By simulating propagation through weak turbulence and sampling within one atmospheric coherence time, we generate Monte-Carlo numerical results and assess the pupil-plane irradiance that accumulates. Figure D.1 shows qualitatively that the exponential PDF yields a closer fit given a single frame of speckle, while the lognormal PDF matches more closely after sufficient speckle averaging. Although other models such as the gamma-gamma

distribution are likely to improve curve fitting, the utility of lognormal and exponential functions is that their respective peaks are forced off and on the zero-irradiance point.

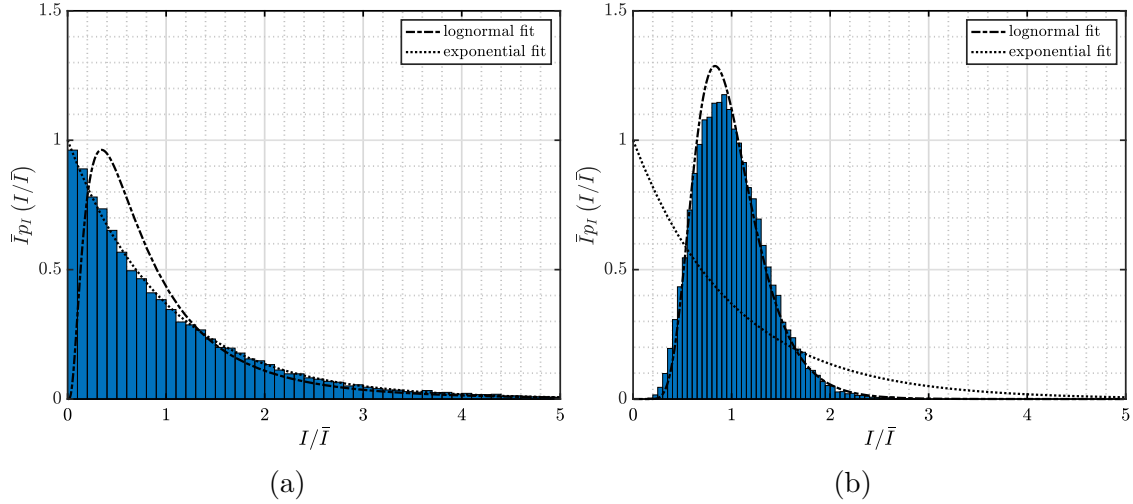


Figure D.1: Irradiance histogram with lognormal and exponential fits after propagation through weak turbulence with (a) one frame of speckle and (b) eight frames averaged together. Note a decrease in skewness from (a) to (b).

In Fig. D.2a, we observe the root-mean-square error (RMSE) tapering off with greater numbers of averages and stabilizing once lognormal statistics begin to better represent the irradiance accumulation (i.e. for $N_{\text{avg}} \geq 8$). Comparing to Fig. D.2b, we see that this same point corresponds to a skewness of approximately 1. The takeaway is that continuously monitoring the pupil plane for unit skewness optimizes performance by imposing minimal RMSE without setting camera integration times to be longer than necessary. Ultimately this approach enables fast frame rates while averaging out speckle to the fullest extent, as skewness continues to drop below 1 for additional averages while RMSE remains relatively constant.

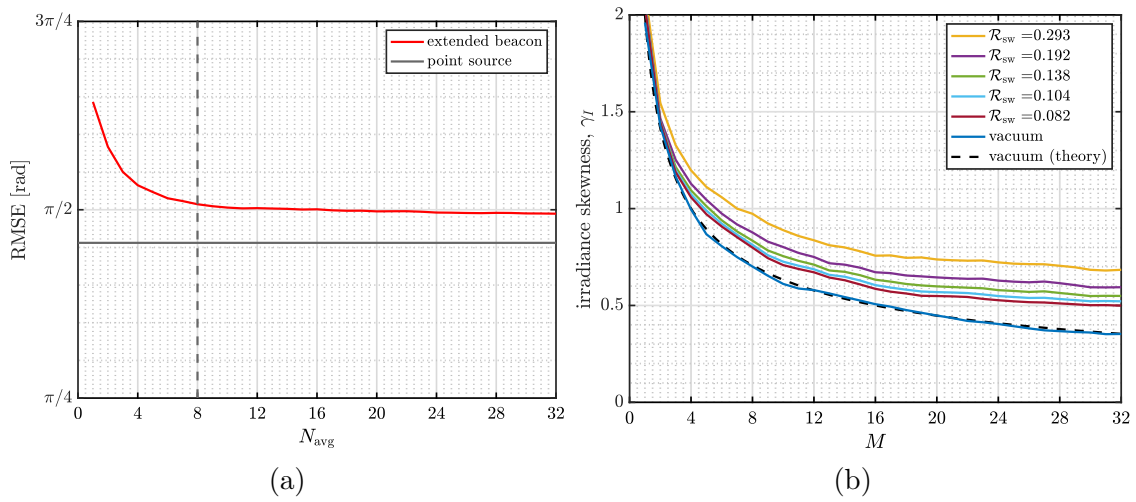


Figure D.2: (a) Residuals between actual phase and wavefront reconstruction; (b) skewness in irradiance as a function of uncorrelated averages. Dashed vertical lines indicate the transition from exponential to lognormal GOF outcomes.

APPENDIX E

Wave-Optics Sampling Constraints in the Presence of Speckle and Anisoplanatism[†]**E.1 Background**

Wave-optics simulations of adaptive optics (AO) systems traditionally assume point-source beacons for the purpose of wavefront sensing. If instead using extended-object beacons, it is tempting to attribute the additional error to speckle and/or centroid-tracking limitations for resolved objects. In turbulence, however, extended objects are also subject to angular anisoplanatism in that different object points traverse different cones of the atmosphere. Since both speckle and anisoplanatism arise naturally from the use of extended objects as beacons, it can be difficult (and in some cases impossible) to decouple their effects in simulation. This is especially true when enforcing a condition of unity scaling between planes, in which case fine sampling of both a rough-surface object and its resulting speckle pattern tends to automatically violate isoplanatic conditions. Because of these sampling difficulties, we set out to explicitly bound the problem for maximum computational efficiency without extreme mismatches in scaling from plane to plane of an imaging simulation.

With this goal in mind, Sec. E.2 details an analytic procedure for writing out systems of equations from which a symbolic solver such as Mathematica can readily determine simulation parameters. These parameters are both physical and numerical in nature, with the latter depending heavily upon the former with regard to workflow. Section E.3 presents wave-optics simulation results using the WaveProp Toolbox for MATLAB. These results justify a minimum number of samples across the extended object as well as the speckle that it produces. We apply the results to prior calculations and use them to tabulate one possible parameterization as an example.

[†]This material was presented previously as [179] in *Unconventional Imaging and Adaptive Optics 2021*. Used with permission of SPIE, from “Wave-optics sampling constraints in the presence of speckle and anisoplanatism,” D. Burrell, J. Beck, M. Beason, and B. Berry, vol. 11836, 2021 (<https://doi.org/10.1117/12.2595469>); permission conveyed through Copyright Clearance Center, Inc.

E.2 Procedure

This section is divided into two parts. The first outlines physical constraints for a wave-optics simulation involving both speckle and anisoplanatism, then shows how to calculate a maximum target size and propagation distance under the supplied conditions. With a propagation geometry fully defined, the second part goes on to identify numerical constraints and solves to create a sampling grid for digital propagation from one plane to the next.

E.2.1 Physical Constraints

Throughout the analysis that follows, we assume for simplicity an ideal horizontal turbulence scenario in which atmospheric conditions are constant along the entire propagation path. We take this approach in part to consider only straightforward algebraic expressions for the relevant atmospheric parameters, noting that path-integral expressions for varying turbulence strength are widely available in the open literature. Our goal is not to present a rigorous study of the atmospheric, but rather to explain a general setup procedure that one might follow for a scenario of any given complexity. However, we also note that a horizontal-path propagation geometry exhibits distributed-volume aberrations that give us the most significant anisoplanatic cases of interest. Going forward, we take our extended object to be a square, flat plate of width W and the pupil function to be a circular, thin lens of diameter D .

Often the first parameter that comes to mind in setting up an atmospheric simulation is related to the strength of turbulence. Fried's coherence diameter, r_0 , defines a circle within the receiving aperture (often a telescope's objective lens) over which RMS wavefront distortion is limited to ~ 1 rad. Its value reduces to [86]

$$r_0 = (0.159 C_n^2 k^2 Z_1)^{-3/5} \quad (\text{E.1})$$

for a spherical wave in constant turbulence, where C_n^2 is the refractive-index structure constant gauging local turbulence strength, $k = 2\pi/\lambda$ is the angular wavenumber, λ is the wavelength of light and Z_1 is the total path length from object to pupil. Since a circle of diameter r_0 effectively constitutes a coherence cell in the pupil plane, D/r_0 provides a metric for the resolution limit of astronomical seeing. As a general rule, $D/r_0 \leq 1$ suggests

diffraction-limited operation while $D/r_0 > 1$ corresponds to turbulence-limited operation. In practice, seeing first becomes an issue when $D/r_0 \gtrsim 0.5$ (i.e. in weak turbulence) [180] and renders AO correction ineffective when $D/r_0 \gtrsim 40$ (i.e. in strong turbulence) [181]. When $D/r_0 \gtrsim 10$ (i.e. in moderate-to-strong turbulence), centroid anisoplanatism takes effect and leads to errors in tilt estimates for tracking or wavefront reconstruction [136]. For these reasons, it is often useful to establish D/r_0 at the outset of building a simulation and proceed with setup from there.

Another key parameter concerning the atmosphere is Rytov number, as it is directly proportional to turbulence strength and identifies a saturation regime in which scintillation overwhelms the capabilities of conventional phase-compensation schemes. Generally a Rytov number on the interval $\sim[0.05, 0.25]$ is of interest to beam-control studies, as this loosely defines weak turbulence in which branch points begin to appear but scintillation does not yet saturate [182]. The Rytov number gives a close approximation of empirical log-amplitude variance calculations within these limits [106]. To directly calculate Rytov number, we first rearrange Eq. (E.1) for the index structure constant in terms of r_0 as

$$C_n^2 = \frac{0.160\lambda^2}{Z_1 r_0^{5/3}}. \quad (\text{E.2})$$

The spherical-wave Rytov number is then [183]

$$\begin{aligned} \mathcal{R} &= 0.124 C_n^2 k^{7/6} Z_1^{11/6} \\ &= 0.169 r_0^{-5/3} (\lambda Z_1)^{5/6}. \end{aligned} \quad (\text{E.3})$$

Recall that, in our wave-optics simulations, we are interested in studying the use of noncooperative and reflective extended objects as beacons for an AO system. This type of beacon introduces two primary degradations to the performance of such a system. The first is speckle, which results from diffuse reflection by a random distribution of surface scatterers that are collectively rough compared to the wavelength of coherent light. Speckle severity in the pupil plane is typically quantified by the object Fresnel number,

$$N_{\text{obj}} = \frac{DW}{\lambda Z_1}. \quad (\text{E.4})$$

$N_{\text{obj}} \leq 1$ indicates an aperture that is relatively free of speckle, with more speckles appearing as N_{obj} grows larger. In the interest of studying speckle effects, it is therefore a necessary condition that $N_{\text{obj}} > 1$. Assuming a diffraction-limited system, this also implies that the object would be well resolved by the full aperture in an imaging geometry.

The second effect that degrades performance for our purposes is anisoplanatism, which arises from an angular offset between the aperture and different points on the object such that backreflected light samples multiple return paths through the atmosphere. The isoplanatic angle is an offset resulting in an RMS wavefront error of ~ 1 rad, and an approximation of this angle over a horizontal path is [184]

$$\begin{aligned}\theta_0 &= \left(1.09C_n^2 k^2 Z_1^{8/3}\right)^{-3/5} \\ &= 0.314 \frac{r_0}{Z_1}.\end{aligned}\tag{E.5}$$

Here, we have once again made use of Eq. (E.2) as a substitution for C_n^2 . The so-called isoplanatic patch at the range of the object is then $W_0 = \theta_0 Z_1 = 0.314 r_0$. As such, a necessary condition to study speckle in the absence of anisoplanatism is $W \leq W_0$ with W being the object width.

Finally for a given wavelength λ and aperture diameter D , as well as a desired turbulence strength D/r_0 and *maximum* object Fresnel number $\max(N_{\text{obj}}^{\text{iso}})$ under isoplanatic conditions, the appropriate set of physical constraints is

$$\begin{cases} \min(\mathcal{R}) \leq 0.169 r_0^{-5/3} (\lambda Z_1)^{5/6} \leq \max(\mathcal{R}) \\ \lambda Z_1 / D < W \leq 0.314 r_0 \\ DW / (\lambda Z_1) = \max(N_{\text{obj}}^{\text{iso}}) \end{cases}.\tag{E.6}$$

Using Mathematica to solve this overdetermined system of equations yields a range of acceptable values for object width W , along with a propagation range Z_1 that varies as a function of W . The upper bound on W determines the largest possible object before introducing anisoplanatism. Calculating a fixed Z from this W then serves two purposes: it maximizes the Rytov number on the specified interval, and it forces a lower object Fresnel number for all other values of W .

E.2.2 Numerical Constraints

In this work we are considering a simulated imaging system comprised of object, pupil and image planes that are sampled at spacings of δ_{obj} , δ_{pup} and δ_{img} , respectively. Distances Z_1 and Z_2 separate the three planes in the order given. Following Schmidt's treatment on Fresnel diffraction [52], Nyquist sampling stipulates that

$$\frac{W\delta_{\text{pup}}/\delta_{\text{obj}} + D}{2Z_1} \leq \frac{\lambda}{2\delta_{\text{obj}}}, \quad (\text{E.7})$$

while

$$D \leq \frac{W\delta_{\text{pup}} + \lambda Z_1}{\delta_{\text{obj}}} \quad (\text{E.8})$$

is required for the illumination area to overfill the aperture. Furthermore,

$$N \geq \frac{W_{\text{max}}}{2\delta_{\text{obj}}} + \frac{D}{2\delta_{\text{pup}}} + \frac{\lambda Z_1}{2\delta_{\text{obj}}\delta_{\text{pup}}} \quad (\text{E.9})$$

ensures that any aliasing that occurs due to wraparound does not encroach into the observing aperture. Imposing what Voelz refers to as the critical sampling condition [54],

$$\begin{cases} \delta_{\text{pup}} &= \lambda Z_1 / (N\delta_{\text{obj}}) \\ \delta_{\text{img}} &= \lambda Z_2 / (N\delta_{\text{pup}}) \end{cases}, \quad (\text{E.10})$$

utilizes the full spatial extent and effective bandwidth of our setup.

In order to reproduce the expected physical behavior of speckle on a computational basis, it is imperative that we properly sample the rough surface itself as well as its resultant speckle field within some region of interest. It is generally a valid assumption that a simulation grid of practical size will sample a rough surface much more coarsely than its correlation width in surface heights. Therefore, we treat the rough surface as delta correlated from point to point and randomly draw the phase at each point from a uniform distribution between $-\pi$ and π upon reflection.

When a fully coherent and polarized wave impinges on such a surface, a fully developed speckle pattern will form if there are sufficiently many independent contributions to the observed intensity that the central limit theorem applies. When it does, the optical field behaves as a circular complex Gaussian random process with amplitude, phase,

and irradiance components that follow Rayleigh, uniform, and exponential distributions, respectively. Figure E.1 illustrates the simulated statistics of fully developed speckle separated into these three components.

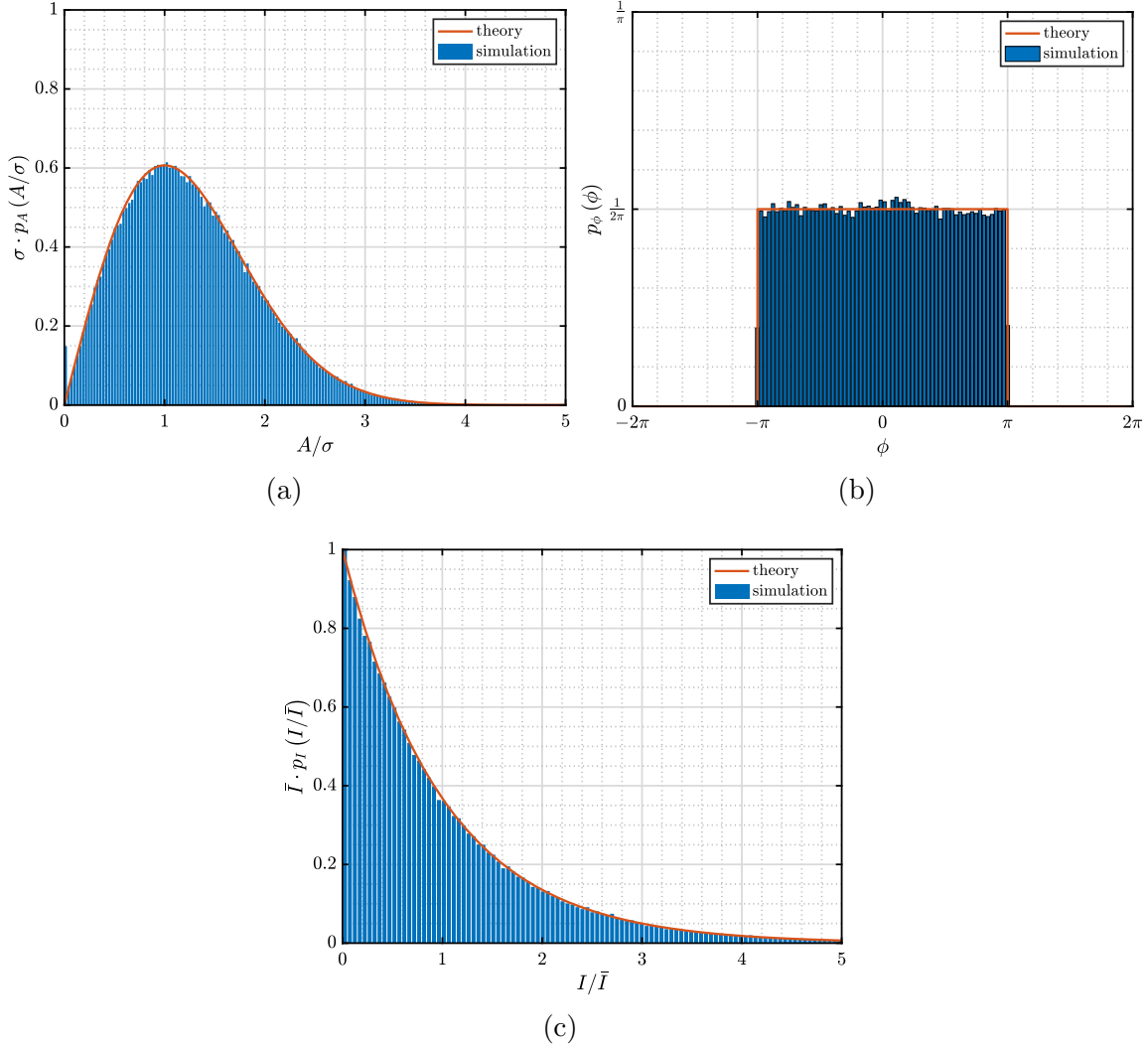


Figure E.1: Normalized histograms of (a) amplitude, (b) phase and (c) irradiance data representing the Monte Carlo average of 100 independently simulated speckle fields.

A common measure for “strength” of speckle noise is its contrast ratio, calculated as

$$C = \frac{\sigma_I}{\bar{I}} \tag{E.11}$$

where σ_I and \bar{I} are respectively its standard deviation and mean irradiance. Since standard deviation is equal to the mean in an exponential distribution, a simple test for fully developed speckle is to check that $C \approx 1$ according to Eq. (E.11). Checking this condition for different numbers of independent scattering contributions requires setting the object size to be

$$W = N_{\text{smp}}^{\text{obj}} \delta_{\text{obj}}, \quad (\text{E.12})$$

where $N_{\text{smp}}^{\text{obj}}$ is the number of samples spanning the object in one dimension. As such, the approach we take here is to simply increase $N_{\text{smp}}^{\text{obj}}$ for a square object until C goes to unity. For that number of samples, object-plane sampling must be such that

$$\min(N_{\text{obj}}) \frac{\lambda Z_1}{D} \geq \min(N_{\text{smp}}^{\text{obj}}) \delta_{\text{obj}} \quad (\text{E.13})$$

where $\min(N_{\text{obj}})$ is the minimum desired object Fresnel number in simulation.

Conventional wisdom suggests at least meeting the Nyquist criterion when sampling speckle, i.e. ensuring 2 or more pixels per speckle in the plane of observation. Empirical evidence finds that even an undersampled speckle pattern arising from a sufficient number of random scatterers retains unit contrast over the total number of pixels. In other words, undersampling fully developed speckle upon propagation does not see the same contrast reduction as spatially averaging a well sampled speckle pattern. To test whether Nyquist sampling is sufficient, then, we induce speckle decorrelation by simulating object tilt and calculate root-mean-square error (RMSE) between known analytical expressions for the irradiance correlation coefficient and the equivalent results in simulation.

A square object of width

$$W = \frac{\lambda Z_1}{N_{\text{smp}}^{\text{pup}} \delta_{\text{pup}}} \quad (\text{E.14})$$

produces $N_{\text{smp}}^{\text{pup}}$ pixels across the width of an average speckle in the pupil plane, while a circular exit pupil of diameter

$$D = \frac{1.22 \lambda Z_2}{N_{\text{smp}}^{\text{img}} \delta_{\text{img}}} \quad (\text{E.15})$$

produces $N_{\text{smp}}^{\text{img}}$ pixels across the width of an average speckle in the image plane. Due to the inverse relationship between scattering-spot or aperture size and speckle size, sampling in the pupil and image planes should allow for

$$\frac{\lambda Z_1}{W_{\text{max}} \delta_{\text{pup}}} \geq \min(N_{\text{smp}}^{\text{pup}}) \quad (\text{E.16})$$

and

$$\frac{1.22 \lambda Z_2}{D \delta_{\text{img}}} \geq \min(N_{\text{smp}}^{\text{img}}) \quad (\text{E.17})$$

after identifying $\min(N_{\text{smp}}^{\text{pup}})$ and $\min(N_{\text{smp}}^{\text{img}})$, respectively. We note that, as a direct consequence of satisfying the critical sampling condition, $N_{\text{smp}}^{\text{img}}$ cannot exceed 1.22 without the object going out of bounds with respect to the simulation grid. For this same reason $N_{\text{smp}}^{\text{pup}}$ and $N_{\text{smp}}^{\text{obj}}$ cannot exceed 1 and N , respectively. As a final sampling constraint, we enforce the condition that there are at least $\min(N_{\text{smp}}^{r_0}) = 10$ samples across Fried's coherence diameter to accurately simulate the seeing resolution limit [185].

Taken together, Eqs. (E.7)–(E.10) and (E.16)–(E.17) culminate in

$$\left\{ \begin{array}{l} \min(N_{\text{obj}}) \lambda Z_1 / D \geq \min(N_{\text{smp}}^{\text{obj}}) \delta_{\text{obj}} \\ (D \delta_{\text{obj}} - \lambda Z_1) / W_{\text{min}} \leq \delta_{\text{pup}} \leq (\lambda Z_1 - D \delta_{\text{obj}}) / W_{\text{max}} \\ N \geq W_{\text{max}} / (2 \delta_{\text{obj}}) + D / (2 \delta_{\text{pup}}) + \lambda Z_1 / (2 \delta_{\text{obj}} \delta_{\text{pup}}) \\ \delta_{\text{obj}} \delta_{\text{pup}} = \lambda Z_1 / N \\ \lambda Z_1 / (W_{\text{max}} \delta_{\text{pup}}) \geq \min(N_{\text{smp}}^{\text{pup}}) \\ \delta_{\text{pup}} \delta_{\text{img}} = \lambda Z_2 / N \\ 1.22 \lambda Z_2 / (D \delta_{\text{img}}) \geq \min(N_{\text{smp}}^{\text{img}}) \\ r_0 / \delta_{\text{pup}} \geq \min(N_{\text{smp}}^{r_0}) \end{array} \right. \quad (\text{E.18})$$

Solving this system in Mathematica gives a range of solutions for δ_{obj} , a solution for δ_{pup} that goes inversely as δ_{obj} , a range of solutions for δ_{img} with an upper limit inversely related to δ_{pup} , and a solution for Z_2 that depends directly on both δ_{pup} and δ_{img} . Taking the largest allowed solution for δ_{obj} and plugging in for δ_{pup} minimizes scaling between the object and pupil planes. Similarly, the largest allowed solution for δ_{img} minimizes scaling

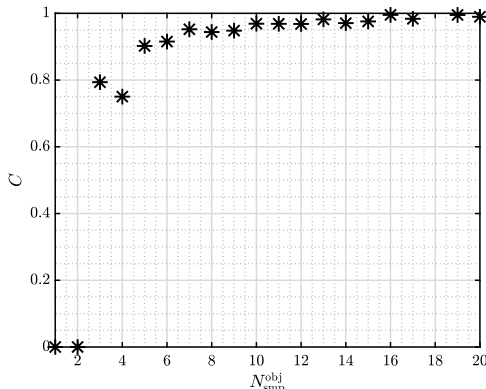


Figure E.2: Speckle contrast as a function of samples across the object.

while relating the image- and object-plane scales as closely as possible.

E.3 Results and Discussion

Figure E.2 shows the average result of 100 Monte Carlo trials calculating speckle contrast in the pupil plane as a function of the number of samples over one dimension of a simulated rough object. Contrast reaches a value of $\sim 97\%$ with 10 or more samples across, and it stabilizes at $\sim 99\%$ for 16 or more samples. We find in general that $\min(N_{\text{smp}}^{\text{obj}}) = 10$ samples (yielding $\sim 97\%$ contrast accordingly) is sufficient for accurate simulation results with regard to other error metrics such as RMSE. For this reason, we fix the object to be at least 10 pixels wide in each subsequent test.

Figure E.3 shows the average result of 100 Monte Carlo trials calculating RMSE in the pupil plane as a function of the number of samples across one dimension of a generated speckle. RMSE drops below 1% with $\min(N_{\text{smp}}^{\text{pup}}) = 3$ samples across an average speckle and remains more or less stable thereafter. Figure E.4, on the other hand, shows the same calculations for speckle in the image plane. Here, we have fixed the target width such that $N_{\text{smp}}^{\text{pup}} = 3$ in order to isolate image-plane sampling dependencies. RMSE drops more gradually in this case and instead reaches a minimum of $\sim 1.5\%$ with $\min(N_{\text{smp}}^{\text{img}}) = 5$. Purely tilting the object plane gives rise to speckle decorrelation by pure displacement and pure boil in the pupil and image planes, respectively. Thus a generalization of these results is that boiling is more sensitive to sampling effects than displacement. With these minimum values known, Table E.1 lists all inputs and outputs as calculated from Eqs. (E.6)

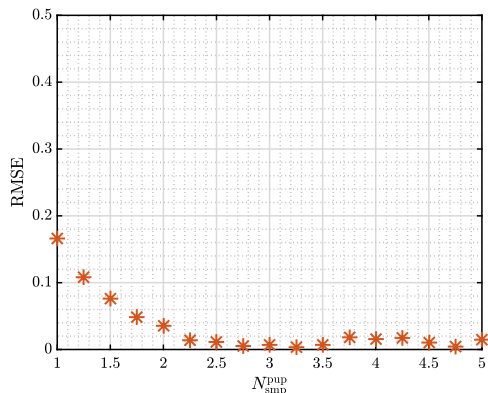


Figure E.3: Root-mean-square error between numerical and analytical irradiance correlation coefficient as a function of samples per pupil-plane speckle.

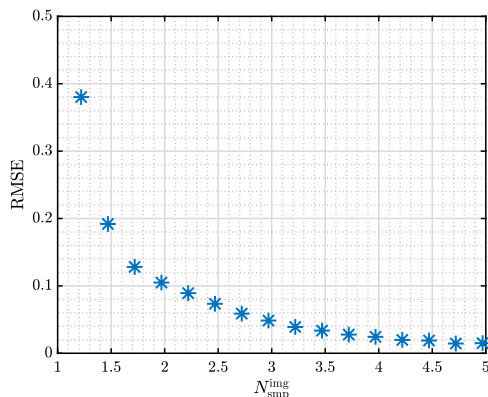


Figure E.4: Root-mean-square error between numerical and analytical irradiance correlation coefficient as a function of samples per image-plane speckle.

and (E.18).

The most important takeaway from this investigation is that the tradespace is quite constrained when looking to simulate extended objects that cause speckle without anisoplanatism. On the side of physical constraints, the only available options for increasing Rytov number are to increase D/r_0 (which may complicate wavefront sensing for phase compensation) or decrease $\max(N_{\text{obj}}^{\text{iso}})$ (which is counterproductive to our goal of studying speckle in the absence of anisoplanatism). For instance, a Rytov number at or above 0.2 would require either a maximum isoplanatic N_{obj} of only 2 or a D/r_0 value of at least 16 in this particular case. As for numerical constraints, we note that non-unity scaling (i.e. $\delta_{\text{obj}} \neq \delta_{\text{pup}} \neq \delta_{\text{img}}$) is necessary for the sake of sufficiently sampling both the object itself and the speckle that it generates. From Table E.1, the scaling factor between pupil and

Table E.1: Summary of simulation inputs and physical/numerical derived quantities.

	parameter	value
inputs	wavelength, λ [μm]	1
	aperture diameter, D [cm]	30
	Fried coherence diameter, r_0 [cm]	3
	minimum Rytov number, $\min(\mathcal{R})$	0.1
	maximum Rytov number, $\max(\mathcal{R})$	0.25
	minimum object Fresnel number, $\min(N_{\text{obj}})$	0.5
	maximum <i>isoplanatic</i> object Fresnel number, $\max(N_{\text{obj}}^{\text{iso}})$	4
	minimum samples per Fried coherence diameter, $\min(N_{\text{pup}}^{\text{r}_0})$	10
	grid points per side, N [#]	2048
physical	minimum object width, W_{min} [mm]	1.18
	maximum object width, W_{max} [mm]	9.42
	object–pupil propagation distance, Z_1 [m]	707
	pupil–image propagation distance, Z_2 [m]	707
	spherical-wave Rytov number, \mathcal{R}	0.137
numerical	object-plane grid spacing, δ_{obj} [mm]	0.118
	pupil-plane grid spacing, δ_{pup} [mm]	2.93
	image-plane grid spacing, δ_{img} [mm]	0.118
	minimum samples per pupil-plane speckle, $\min(N_{\text{smp}}^{\text{pup}})$	25.6
	samples per image-plane speckle, $N_{\text{smp}}^{\text{img}}$	24.4

object planes is $\delta_{\text{pup}}/\delta_{\text{obj}} \approx 25$ before scaling back down by $\delta_{\text{img}}/\delta_{\text{pup}} \approx 1/25$. The only remedy to approach unity scaling is to increase the number of grid points per side, keeping in mind the discrete Fourier transform algorithm is of $O(n^2)$ complexity. Doubling N along one dimension means quadrupling the total number of grid points and ultimately taking $16\times$ longer to perform the operation. A potential workaround that would relax both the physical and numerical constraints is to numerically derive a piston-removed isoplanatic angle that is less restrictive, since we are dealing with finite apertures and beam control is insensitive to overall phase for most practical purposes [176]. In short, a larger isoplanatic angle yields a greater maximum object size, which then allows for a longer propagation distance to achieve the same maximum isoplanatic object Fresnel number, ultimately enabling both higher Rytov numbers and reduced scaling between planes [cf. Eq. (E.18)].

REFERENCES

- [1] R. G. Driggers, M. H. Friedman, J. W. Devitt, O. Furxhi, and A. Singh, *Introduction to Infrared and Electro-Optical Systems*, 3rd ed., ser. Remote Sensing Library. Norwood, MA: Artech House, 2022.
- [2] D. J. Burrell, M. F. Spencer, N. R. V. Zandt, and R. G. Driggers, “Wave-optics simulation of dynamic speckle: I. In a pupil plane,” *Appl. Opt.*, vol. 60, no. 25, pp. G64–G76, 2021.
- [3] C. J. Pellizzari, M. F. Spencer, and C. A. Bouman, “Phase-error estimation and image reconstruction from digital-holography data using a Bayesian framework,” *J. Opt. Soc. Am. A*, vol. 34, no. 9, pp. 1659–1669, 2017.
- [4] C. J. Pellizzari, M. T. Banet, M. F. Spencer, and C. A. Bouman, “Demonstration of single-shot digital holography using a Bayesian framework,” *J. Opt. Soc. Am. A*, vol. 35, no. 1, pp. 103–107, 2018.
- [5] C. J. Pellizzari, M. F. Spencer, and C. A. Bouman, “Imaging through distributed-volume aberrations using single-shot digital holography,” *J. Opt. Soc. Am. A*, vol. 36, no. 2, pp. A20–A33, 2019.
- [6] C. J. Radosevich, C. J. Pellizzari, S. Horst, and M. F. Spencer, “Imaging through deep turbulence using single-shot digital holography data,” *Opt. Express*, vol. 28, no. 13, pp. 19 390–19 401, 2020.
- [7] C. J. Pellizzari, M. F. Spencer, and C. A. Bouman, “Coherent plug-and-play: Digital holographic imaging through atmospheric turbulence using model-based iterative reconstruction and convolutional neural networks,” *IEEE Tran. Comp. Img.*, vol. 6, pp. 1607–1621, 2020.
- [8] N. R. Van Zandt, J. E. McCrae, and S. T. Fiorino, “Modeled and measured image-plane polychromatic speckle contrast,” *Opt. Eng.*, vol. 55, no. 2, p. 024106, 2016.
- [9] N. R. Van Zandt, J. E. McCrae, M. F. Spencer, M. J. Steinbock, M. W. Hyde IV, and S. T. Fiorino, “Polychromatic wave-optics models for image-plane speckle. 1. Well-resolved objects,” *Appl. Opt.*, vol. 57, no. 15, pp. 4090–4102, 2018.

- [10] N. R. Van Zandt, M. F. Spencer, M. J. Steinbock, B. M. Anderson, M. W. Hyde IV, and S. T. Fiorino, “Polychromatic wave-optics models for image-plane speckle. 2. Unresolved objects,” *Appl. Opt.*, vol. 57, no. 15, pp. 4103–4110, 2018.
- [11] N. R. Van Zandt, M. F. Spencer, and S. T. Fiorino, “Speckle mitigation for wavefront sensing in the presence of weak turbulence,” *Appl. Opt.*, vol. 58, no. 9, pp. 2300–2310, 2019.
- [12] N. R. Van Zandt and M. F. Spencer, “Improved adaptive-optics performance using polychromatic speckle mitigation,” *Appl. Opt.*, vol. 59, no. 4, pp. 1071–1081, 2020.
- [13] M. T. Banet and M. F. Spencer, “Compensated-beacon adaptive optics using least-squares phase reconstruction,” *Opt. Exp.*, vol. 28, no. 24, pp. 36 902–36 914, 2020.
- [14] C. J. Pellizzari, R. Trahan, H. Zhou, S. Williams, S. E. Williams, B. Nemati, M. Shao, and C. A. Bouman, “Optically coherent image formation and denoising using a plug and play inversion framework,” *Appl. Opt.*, vol. 56, no. 16, pp. 4735–4744, 2017.
- [15] C. J. Pellizzari, R. Trahan, H. Zhou, S. Williams, S. E. Williams, B. Nemati, M. Shao, and C. A. Bouman, “Synthetic aperture ladar: A model-based approach,” *IEEE Trans. Comput. Imaging*, vol. 3, no. 4, pp. 901–916, 2017.
- [16] J. W. Goodman, *Speckle Phenomena in Optics: Theory and Applications*, 2nd ed. Bellingham, WA: SPIE Press, 2020.
- [17] J. W. Goodman, “Statistical properties of laser speckle patterns,” in *Laser Speckle and Related Phenomena*, J. Dainty, Ed. Berlin/Heidelberg, DE: Springer-Verlag, 1975, ch. 2, pp. 9–75.
- [18] A. C. Bovik, *The Essential Guide to Image Processing*. Cambridge, MA: Academic Press, 2009.
- [19] J. W. Goodman, “Some fundamental properties of speckle,” *J. Opt. Soc. Am.*, vol. 66, no. 11, pp. 1145–1150, 1976.
- [20] N. Bender, H. Yilmaz, Y. Bromberg, and H. Cao, “Customizing speckle intensity statistics,” *Optica*, vol. 5, no. 5, pp. 595–600, 2018.
- [21] H. F. Schouten and T. D. Visser, “The role of correlation functions in the theory of optical wave fields,” *Am. J. Phys.*, vol. 76, no. 9, pp. 867–871, 2008.

- [22] J. D. Rigden and E. I. Gordon, "The granularity of scattered maser light," in *Proc. IRE*, vol. 50, 1962, pp. 2267–2368.
- [23] B. Oliver, "Sparkling spots and random diffraction," in *Proc. IEEE*, vol. 51, 1963, pp. 220–221.
- [24] R. V. Langmuir, "Scattering of laser light," *Appl. Phys. Lett.*, vol. 2, no. 2, pp. 29–30, 1963.
- [25] L. Allen and D. G. C. Jones, "An analysis of the granularity of scattered optical maser light," *Phys. Lett.*, vol. 7, no. 5, pp. 321–323, 1963.
- [26] N. R. Isenor, "Object-image relationships in scattered laser light," *Appl. Opt.*, vol. 6, no. 1, pp. 163–163, 1967.
- [27] T. M. Sporton, "The scattering of coherent light from a rough surface," *J. Phys. D*, vol. 2, no. 7, p. 1027, 1969.
- [28] V. V. Anisimov, S. M. Kozel, and G. R. Lokshin, "Space-time statistical properties of coherent radiation scattered by a moving diffuse reflector," *Opt. Spectrosc.*, vol. 27, no. 3, pp. 483–491, 1969.
- [29] B. E. A. Saleh, "Speckle correlation measurement of the velocity of a small rotating rough object," *Appl. Opt.*, vol. 14, no. 10, pp. 2344–2346, 1975.
- [30] I. Yamaguchi, "Real-time measurement of in-plane translation and tilt by electronic speckle correlation," *Jpn. J. Appl. Phys.*, vol. 19, no. 3, pp. L133–L136, 1980.
- [31] W. H. Peters and W. F. Ranson, "Digital imaging techniques in experimental stress analysis," *Opt. Eng.*, vol. 21, no. 3, pp. 427–431, 1982.
- [32] T. Yoshimura, "Statistical properties of dynamic speckles," *J. Opt. Soc. Am. A*, vol. 3, no. 7, pp. 1032–1054, 1986.
- [33] T. Okamoto and T. Asakura, "The statistics of dynamic speckles," in *Progress in Optics*, E. Wolf, Ed. Amsterdam, NL: Elsevier, 1995, vol. XXXIV, ch. III, pp. 185–250.
- [34] P. Horváth, M. Hrabovsky, and P. Šmíd, "Application of speckle decorrelation method for small translation measurements," *Opt. Appl.*, vol. 34, no. 2, pp. 203–218, 2004.
- [35] M. Françon, "Information processing using speckle patterns," in *Laser Speckle and Related Phenomena*, J. Dainty, Ed. Berlin/Heidelberg, DE: Springer-Verlag, 1975, ch. 5, pp. 203–253.

- [36] M. Françon, *Laser Speckle and Applications in Optics*. Cambridge, MA: Academic Press, 1979.
- [37] D. C. Scott Miller, *Probability and Random Processes: with Applications to Signal Processing and Communications*, 2nd ed. Cambridge, MA: Academic Press, 2012.
- [38] I. Yamaguchi, “Fringe formation in speckle photography,” *J. Opt. Soc. Am. A*, vol. 1, no. 1, pp. 81–86, 2003.
- [39] J. W. Goodman, *Introduction to Fourier Optics*, 4th ed. New York, NY: W. H. Freeman, 2017.
- [40] J. W. Goodman, *Statistical Optics*, 2nd ed. Hoboken, NJ: Wiley, 2015.
- [41] J. D. Gaskill, *Linear Systems, Fourier Transforms, and Optics*, 1st ed. New York, NY: Wiley, 1978.
- [42] L. Leushacke and M. Kirchner, “Three-dimensional correlation coefficient of speckle intensity for rectangular and circular apertures,” *J. Opt. Soc. Am. A*, vol. 7, no. 5, pp. 827–832, 1990.
- [43] J. E. Ward, D. P. Kelly, and J. T. Sheridan, “Three-dimensional speckle size in generalized optical systems with limiting apertures,” *J. Opt. Soc. Am. A*, vol. 26, no. 8, pp. 1855–1864, 2009.
- [44] J. Marron and G. M. Morris, “Correlation measurements using clipped laser speckle,” *Appl. Opt.*, vol. 25, no. 5, pp. 789–793, 1986.
- [45] R. Henao, J. A. Pomarico, N. Russo, R. D. Torroba, and M. Trivi, “Multimode optical fiber core measurement by speckle correlation,” *Opt. Eng.*, vol. 35, no. 1, pp. 26–30, 1996.
- [46] Q. B. Li and F. P. Chiang, “Three-dimensional dimension of laser speckle,” *Appl. Opt.*, vol. 31, no. 29, pp. 6287–6291, 1992.
- [47] J. H. Churnside, “Speckle from a rotating diffuse object,” *J. Opt. Soc. Am.*, vol. 72, no. 11, pp. 1464–1469, 1982.
- [48] H. T. Yura, B. Rose, and S. G. Hanson, “Speckle dynamics from in-plane rotating diffuse objects in complex ABCD optical systems,” *J. Opt. Soc. Am.*, vol. 15, no. 5, pp. 1167–1173, 1998.
- [49] A. E. Ennos, “Speckle interferometry,” in *Laser Speckle and Related Phenomena*, J. Dainty, Ed. Berlin/Heidelberg, DE: Springer-Verlag, 1975, ch. 6, pp. 203–253.

- [50] M. J. Campbell and T. D. V. Swinscow, *Statistics at Square One*, 11th ed. London, GB: BMJ Books, 2009.
- [51] T. J. Brennan, P. H. Roberts, and D. C. Mann, “*WaveProp*: A wave optics simulation system for use with MATLAB [user’s guide],” Anaheim, CA, 2010.
- [52] J. D. Schmidt, *Numerical Simulation of Optical Wave Propagation with Examples in MATLAB*. Bellingham, WA: SPIE Press, 2010, vol. PM199.
- [53] A. E. Siegman, *Lasers*, revised ed. Sausalito, CA: University Science Books, 1986.
- [54] D. Voelz, *Computational Fourier Optics: A MATLAB[®] Tutorial*, ser. Tutorial Texts in Optical Engineering. Bellingham, WA: SPIE Press, 2011, vol. TT89.
- [55] M. W. Hyde IV and S. R. Bose-Pillai, “Fresnel spatial filtering of quasihomogeneous sources for wave optics simulations,” *Opt. Eng.*, vol. 56, no. 8, 2017.
- [56] D. Burrell, “Wave-optics simulation of correlated speckle fields,” M.S. thesis, Univ. Cent. Florida, Coll. Opt. & Photon., Orlando, FL, 2020.
- [57] D. J. Burrell, M. F. Spencer, N. R. Van Zandt, and R. G. Driggers, “Wave-optics simulation of dynamic speckle: II. In an image plane,” *Appl. Opt.*, vol. 60, no. 25, pp. G77–G90, 2021.
- [58] F. Zernike, “The concept of degree of coherence and its application to optical problems,” *Physica*, vol. 5, no. 8, pp. 785–795, 1938.
- [59] G. Cloud, *Optical Methods of Engineering Analysis*. Cambridge, GB: Cambridge University Press, 1995.
- [60] T. J. Skinner, “Surface texture effects in coherent imaging,” *J. Opt. Soc. Am.*, vol. 53, no. 11, p. 1350, 1963.
- [61] M. Owner-Petersen, “Decorrelation and fringe visibility: on the limiting behavior of various electronic speckle-pattern correlation interferometers,” *J. Opt. Soc. Am. A*, vol. 8, no. 7, pp. 1082–1089, 1991.
- [62] D. C. O’Shea, *Elements of Modern Optical Design*. Hoboken, NJ: Wiley-Interscience, 1985.
- [63] R. Kingslake, *Optics in Photography*. Bellingham, WA: SPIE Press, 2010, vol. PM06.
- [64] A. Rowlands, *Physics of Digital Photography*. Bristol, GB: IOP Publishing, 2017.

- [65] S. G. Lukishova, Y. V. Senatsky, N. E. Bykovsky, and A. S. Scheulin, “Beam shaping and suppression of self-focusing in high-peak-power Nd:glass laser systems,” in *Self-focusing: Past and Present*, R. W. Boyd, S. G. Lukishova, and Y. R. Shen, Eds. Springer, 2009, pp. 191–229.
- [66] D. Li, D. P. Kelly, R. Kirner, and J. T. Sheridan, “Speckle orientation in paraxial optical systems,” *Appl. Opt.*, vol. 51, no. 4, pp. A1–A10, 2012.
- [67] J. Marron and G. M. Morris, “Image-plane speckle from rotating, rough objects,” *J. Opt. Soc. Am. A*, vol. 2, no. 9, pp. 1395–1402, 1985.
- [68] D. W. Li and F. P. Chiang, “Decorrelation functions in laser speckle photography,” *J. Opt. Soc. Am. A*, vol. 3, no. 7, pp. 1023–1031, 1986.
- [69] R. L. Easton, Jr., *Fourier Methods in Imaging*. New York, NY: Wiley, 2010.
- [70] G. D. Boreman, *Modulation Transfer Function in Optical and Electro-Optical Systems*. Bellingham, WA: SPIE Press, 2001.
- [71] D. G. Smith, *Field Guide to Physical Optics*, J. S. Tyo, Ed. Bellingham, WA: SPIE Press, 2013, vol. FG17.
- [72] D. J. Burrell, M. F. Spencer, M. K. Beason, and R. G. Driggers, “Active-tracking scaling laws using the noise-equivalent angle due to speckle,” *J. Opt. Soc. Am. A*, vol. 40, no. 5, pp. 904–913, 2023.
- [73] G. A. Tyler and D. L. Fried, “Image-position error associated with a quadrant detector,” *J. Opt. Soc. Am.*, vol. 72, no. 6, pp. 804–808, 1982.
- [74] P. Merritt and M. Spencer, *Beam Control for Laser Systems*, 2nd ed. Albuquerque, NM: Directed Energy Professional Society, 2018.
- [75] D. Burrell, J. Garretson, J. Vorenberg, and R. Driggers, “Active vs. passive tracking: when to illuminate?” in *Infrared Imaging Systems: Design, Analysis, Modeling, and Testing XXXIII*, G. C. Holst and D. P. Haefner, Eds., vol. 12106, International Society for Optics and Photonics. SPIE, 2022, p. 121060F.
- [76] R. B. Holmes, “Scintillation-induced jitter of projected light with centroid trackers,” *J. Opt. Soc. Am. A*, vol. 26, no. 2, pp. 313–316, 2009.
- [77] D. L. Fried, “Speckle effects in target position measurement,” the Optical Sciences Company, Anaheim, CA, Tech. Rep. TR-452, 1982.
- [78] J. B. Shellan, “An analysis of the impact of speckle on the reconstructed phase for a Hartmann wavefront sensor,” the Optical Sciences Company, Anaheim, CA, Tech. Rep. TR-1645, 2004.

- [79] N. R. Van Zandt, J. E. McCrae, M. F. Spencer, M. J. Steinbock, M. W. Hyde IV, and S. T. Fiorino, “Polychromatic wave-optics models for image-plane speckle. 1. Well-resolved objects,” *Appl. Opt.*, vol. 57, no. 15, pp. 4090–4102, 2018.
- [80] N. R. Van Zandt, M. F. Spencer, M. J. Steinbock, B. M. Anderson, M. W. Hyde IV, and S. T. Fiorino, “Polychromatic wave-optics models for image-plane speckle. 2. Unresolved objects,” *Appl. Opt.*, vol. 57, no. 15, pp. 4103–4110, 2018.
- [81] N. R. V. Zandt, M. F. Spencer, and S. T. Fiorino, “Speckle mitigation for wavefront sensing in the presence of weak turbulence,” *Appl. Opt.*, vol. 58, no. 9, pp. 2300–2310, 2019.
- [82] N. R. V. Zandt and M. F. Spencer, “Improved adaptive-optics performance using polychromatic speckle mitigation,” *Appl. Opt.*, vol. 59, no. 4, pp. 1071–1081, 2020.
- [83] P. H. Merritt and J. R. Albertine, “Beam control for high-energy laser devices,” *Opt. Eng.*, vol. 52, no. 2, p. 021005, 2012.
- [84] R. Baribeau and M. Rioux, “Centroid fluctuations of speckled targets,” *Appl. Opt.*, vol. 30, no. 26, pp. 3752–3755, 1991.
- [85] G. W. Allan, R. Allured, J. Ashcom, L. Liu, and K. Cahoy, “Temporally averaged speckle noise in wavefront sensors for beam projection in weak turbulence,” *Appl. Opt.*, vol. 60, no. 16, pp. 4723–4731, 2021.
- [86] R. K. Tyson, *Principles of Adaptive Optics*, 3rd ed. Boca Raton, FL: CRC Press, 2010.
- [87] H. Helmers and J. Burke, “How knowledge about speckle intensity and phase gradients can improve electronic speckle pattern interferometry,” in *18th Congress of the International Commission for Optics*, A. J. Glass, J. W. Goodman, M. Chang, A. H. Guenther, and T. Asakura, Eds., vol. 3749, International Society for Optics and Photonics. SPIE, 1999, pp. 216 – 217.
- [88] J. L. Miller, E. J. Friedman, J. N. Sanders-Reed, K. Schwertz, and B. K. McComas, *Photonics Rules of Thumb*, 3rd ed. Bellingham, WA: SPIE Press, 2020.
- [89] M. F. Spencer, “Spatial heterodyne,” in *Encyclopedia of Modern Optics*, 2nd ed., B. D. Guenther and D. G. Steel, Eds. Oxford: Elsevier, 2018, pp. 369–400.

- [90] D. Burrell, J. Beck, M. Beason, and B. Berry, “Wave-optics sampling constraints in the presence of speckle and anisoplanatism,” in *Unconventional Imaging and Adaptive Optics 2021*, J. J. Dolne and M. F. Spencer, Eds., vol. 11836, International Society for Optics and Photonics. SPIE, 2021, p. 1183603.
- [91] J. Reolons, L. C. Andrews, and R. L. Phillips, “Analysis of beam wander effects for a horizontal-path propagating Gaussian-beam wave: focused beam case,” *Opt. Eng.*, vol. 46, no. 8, p. 086002, 2007.
- [92] R. Kizito, M. C. Roggemann, T. J. Schulz, and Y. Zhang, “Image sharpness metric-based deformable mirror control for beam projection systems operating in strong scintillation,” in *Free-Space Laser Communication and Active Laser Illumination III*, D. G. Voelz and J. C. Ricklin, Eds., vol. 5160. SPIE, 2004, pp. 406 – 416.
- [93] J. Rha, R. S. Jonnal, K. E. Thorn, J. Qu, Y. Zhang, and D. T. Miller, “Adaptive optics flood-illumination camera for high speed retinal imaging,” *Opt. Express*, vol. 14, no. 10, pp. 4552–4569, 2006.
- [94] T. Du, Y. Kong, X. Qian, W. Ding, and Z. Wang, “Suppression of speckle noise in digital holography with spatial and temporal domain depolarization,” *IEEE Access*, vol. 8, pp. 22 266–22 274, 2020.
- [95] D. J. Burrell, M. F. Spencer, N. R. Van Zandt, and R. G. Driggers, “Wave-optics simulation of dynamic speckle: I. In a pupil plane,” *Appl. Opt.*, vol. 60, no. 25, 2021.
- [96] S. V. Egge, U. Österberg, and A. Aksnes, “Speckle contrast of the sum of N partially correlated speckle patterns,” *J. Opt. Soc. Am. A*, vol. 29, no. 6, pp. 1188–1198, 2012.
- [97] A. Klenke, *Probability Theory: A Comprehensive Course*, 3rd ed. New York, NY: Springer, 2020.
- [98] S. Jukna, *Extremal Combinatorics With Applications in Computer Science*, 2nd ed., ser. Texts in Theoretical Computer Science. New York, NY: Springer, 2011.
- [99] D. J. Burrell, M. F. Spencer, N. R. Van Zandt, and R. G. Driggers, “Wave-optics simulation of dynamic speckle: II. In an image plane,” *Appl. Opt.*, vol. 60, no. 25, 2021.
- [100] V. I. Tatarski, *Wave Propagation in a Turbulent Medium*. New York, NY: McGraw-Hill, 1961.

- [101] D. L. Fried, “Branch point problem in adaptive optics,” *J. Opt. Soc. Am. A*, vol. 15, no. 10, pp. 2759–2768, 1998.
- [102] G. A. Tyler, “Reconstruction and assessment of the least-squares and slope discrepancy components of the phase,” *J. Opt. Soc. Am. A*, vol. 17, no. 10, pp. 1828–1839, 2000.
- [103] D. L. Fried, “Adaptive optics wave function reconstruction and phase unwrapping when branch points are present,” *Opt. Commun.*, vol. 200, no. 1, pp. 43–72, 2001.
- [104] M. J. Steinbock, M. W. Hyde, and J. D. Schmidt, “LSPV+7, a branch-point-tolerant reconstructor for strong turbulence adaptive optics,” *Appl. Opt.*, vol. 53, no. 18, pp. 3821–3831, 2014.
- [105] M. F. Spencer and T. J. Brennan, “Deep-turbulence phase compensation using tiled arrays,” *Opt. Express*, vol. 30, no. 19, pp. 33 739–33 755, 2022.
- [106] L. C. Andrews and R. L. Phillips, *Laser Beam Propagation through Random Media*. Bellingham, WA: SPIE Press, 2005, vol. PM152.
- [107] J. R. Beck, J. P. Bos, T. J. Brennan, and M. F. Spencer, “Wave-optics investigation of branch-point density,” *Optical Engineering*, vol. 61, no. 4, p. 044104, 2022.
- [108] D. L. Fried, “Statistics of a geometric representation of wavefront distortion,” *J. Opt. Soc. Am.*, vol. 55, no. 11, pp. 1427–1435, 1965.
- [109] D. L. Fried, “Optical resolution through a randomly inhomogeneous medium for very long and very short exposures,” *J. Opt. Soc. Am.*, vol. 56, no. 10, pp. 1372–1379, 1966.
- [110] R. K. Tyson, *Introduction to Adaptive Optics*, ser. Tutorial Texts in Optical Engineering. Bellingham, WA: SPIE Press, 2000, vol. TT41.
- [111] S. E. J. Shaw and E. M. Tomlinson, “Diffractive anisoplanatism and tracker bandwidth limitations,” MIT Lincoln Laboratory, Lexington, MA, Tech. Rep. 82-1010, 2018.
- [112] S. E. J. Shaw and E. M. Tomlinson, “Analytic propagation variances and power spectral densities from a wave-optics perspective,” *J. Opt. Soc. Am. A*, vol. 36, no. 7, pp. 1267–1278, 2019.
- [113] K. B. Doyle, V. L. Genberg, and G. J. Michels, *Integrated Optomechanical Analysis*, 2nd ed. Bellingham, WA: SPIE Press, 2012.

- [114] D. L. Fried, “Anisoplanatism in adaptive optics,” *J. Opt. Soc. Am.*, vol. 72, no. 1, pp. 52–61, 1982.
- [115] D. Burrell and M. Beason, “Fast statistical testing of scintillated, speckled irradiance,” in *Propagation Through and Characterization of Atmospheric and Oceanic Phenomena*. Optica Publishing Group, 2021, p. PW4F.5.
- [116] V. P. Aksenov, V. V. Dudorov, V. V. Kolosov, and V. Y. Venediktov, “Probability distribution of intensity fluctuations of vortex laser beams in the turbulent atmosphere,” *Opt. Express*, vol. 27, pp. 24 705–24 716, 2019.
- [117] D. Burrell, J. Beck, M. Beason, and B. Berry, “Wave-optics sampling constraints in the presence of speckle and anisoplanatism,” in *Unconventional Imaging and Adaptive Optics*, J. J. Dolne and M. F. Spencer, Eds., vol. 11836. SPIE, 2021, p. 1183603.
- [118] N. Takato, M. Iye, and I. Yamaguchi, “Wavefront reconstruction errors of Shack–Hartmann wavefront sensors,” *Publ. Astron. Soc. Pac.*, vol. 106, no. 696, pp. 182–188, 1994.
- [119] A. Dubra, “Wavefront sensor and wavefront corrector matching in adaptive optics,” *Opt. Express*, vol. 15, no. 6, pp. 2762–2769, 2007.
- [120] J. F. Holmes, M. H. Lee, and J. R. Kerr, “Effect of the log-amplitude covariance function on the statistics of speckle propagation through the turbulent atmosphere,” *J. Opt. Soc. Am.*, vol. 70, no. 4, pp. 355–360, 1980.
- [121] W. Ligu, G. Lei, L. Yaqing, Y. Zhiqiang, Y. Lihong, and L. Yao, “Spatiotemporal characteristics of dynamic speckle from a 3D target in atmospheric turbulence,” *Heliyon*, vol. 9, no. 2, 2023.
- [122] D. J. Burrell, N. R. V. Zandt, M. F. Spencer, and T. J. Brennan, “Wave-optics simulation of correlated speckle fields for use in closed-loop-phase-compensation studies,” in *Unconventional and Indirect Imaging, Image Reconstruction, and Wavefront Sensing 2018*, J. J. Dolne and P. J. Bones, Eds., vol. 10772. SPIE, 2018, p. 1077207.
- [123] N. R. Van Zandt, J. E. McCrae, and S. T. Fiorino, “Modeled and measured image-plane polychromatic speckle contrast,” *Opt. Eng.*, vol. 55, no. 2, p. 024106, 2016.
- [124] R. A. Raynor, M. F. Spencer, and T. D. Moore, “Modeling coherence propagation in a homogenizing light pipe for speckle mitigation,” in *Unconventional and Indirect Imaging, Image Reconstruction, and Wavefront Sensing 2017*, J. J. Dolne and R. P. Millane, Eds., vol. 10410. SPIE, 2017, p. 104100X.

- [125] M. W. Hyde IV, S. Basu, D. G. Voelz, and X. Xiao, “Experimentally generating any desired partially coherent Schell-model source using phase-only control,” *J. Appl. Phys.*, vol. 118, no. 9, p. 093102, 2015.
- [126] M. W. Hyde IV and M. F. Spencer, “Behavior of tiled-aperture arrays fed by vector partially coherent sources,” *Appl. Opt.*, vol. 57, no. 22, pp. 6403–6409, 2018.
- [127] Noah R. Van Zandt, M. F. Spencer, J. E. McCrae, and S. T. Fiorino, “Polychromatic speckle mitigation at surface discontinuities,” in *IEEE Aerospace Conference*, 2018, pp. 1–9.
- [128] E. Wolf, *Introduction to the Theory of Coherence and Polarization of Light*. Cambridge, GB: Cambridge University Press, 2007.
- [129] N. R. Van Zandt, M. W. Hyde, S. R. Bose-Pillai, D. G. Voelz, X. Xiao, and S. T. Fiorino, “Synthesizing time-evolving partially-coherent Schell-model sources,” *Opt. Commun.*, vol. 387, pp. 377–384, 2017.
- [130] N. R. Van Zandt, M. W. Hyde IV, S. R. Bose-Pillai, S. T. Fiorino, and M. F. Spencer, “Simulating time-evolving non-cross-spectrally pure Schell-model sources,” in *IEEE Aerospace Conference*, 2017, pp. 1–9.
- [131] R. E. Hufnagel, “Propagation through atmospheric turbulence,” in *The Infrared Handbook*, Revised ed., W. L. Wolfe and G. J. Zissis, Eds. Bellingham, WA: SPIE Press, 1985, vol. PM02, ch. 10.
- [132] G. C. Valley, “Isoplanatic degradation of tilt correction and short-term imaging systems,” *Appl. Opt.*, vol. 19, no. 4, pp. 574–577, 1980.
- [133] P. B. Ulrich, “Hufnagel–Valley profiles for specified values of the coherence length and isoplanatic angle,” W. J. Schafer Associates, Arlington, VA, Tech. Rep. MA-TN-88-01, 1099.
- [134] P. Hickson, “Atmospheric and adaptive optics,” *The Astronomy and Astrophysics Review*, vol. 22, no. 1, p. 76, 2014.
- [135] W. Schneider, Jr., “Defense Science Board Task Force on Directed Energy Weapons,” Office of the Under Secretary of Defense for Acquisition, Technology, and Logistics, Washington, DC, Tech. Rep., 2007.
- [136] H. T. Yura and M. T. Tavis, “Centroid anisoplanatism,” *J. Opt. Soc. Am. A*, vol. 2, no. 5, pp. 765–773, 1985.

- [137] C. J. Carrano, “Anisoplanatic performance of horizontal-path speckle imaging,” in *Advanced Wavefront Control: Methods, Devices, and Applications*, J. D. Gonglewski, M. A. Vorontsov, and M. T. Gruneisen, Eds., vol. 5162. SPIE, 2003, pp. 14 – 27.
- [138] D. P. Greenwood, “Bandwidth specification for adaptive optics systems,” *J. Opt. Soc. Am.*, vol. 67, no. 3, pp. 390–393, 1977.
- [139] J. R. Leigh, *Applied Digital Control: Theory, Design and Implementation*, 2nd ed. London, GB: Prentice Hall International, 1992.
- [140] G. F. Franklin, J. D. Powell, and M. L. Workman, *Digital Control of Dynamic Systems*, 3rd ed. Boston, MA: Addison-Wesley Longman, 1997.
- [141] R. K. Tyson and B. W. Frazier, *Field Guide to Adaptive Optics*, 2nd ed. Bellingham, WA: SPIE Press, 2012.
- [142] J. G. Proakis and D. G. Manolakis, *Digital Signal Processing: Principles, Algorithms, and Applications*, 5th ed. London, GB: Pearson, 2021.
- [143] J. C. Dainty, Ed., *Laser Speckle and Related Phenomena*, ser. Topics in Applied Physics. Berlin, DE: Springer-Verlag, 1975.
- [144] M. Born and E. Wolf, *Principles of Optics: Electromagnetic Theory of Propagation, Interference and Diffraction of Light*, 60th Anniversary ed. Cambridge, GB: Cambridge University Press, 2019.
- [145] T. S. Ross, “Limitations and applicability of the Maréchal approximation,” *Appl. Opt.*, vol. 48, no. 10, pp. 1812–1818, 2009.
- [146] R. J. Noll, “Zernike polynomials and atmospheric turbulence,” *J. Opt. Soc. Am.*, vol. 66, no. 3, pp. 207–211, 1976.
- [147] G. D. Boreman, *Modulation Transfer Function in Optical and Electro-Optical Systems*, 2nd ed. Bellingham, WA: SPIE Press, 2021.
- [148] J. F. Riker, G. A. Tyler, and J. L. Vaughn, “Speckle imaging from an array,” in *Unconventional Imaging and Wavefront Sensing XII*, J. J. Dolne, T. J. Karr, and D. C. Dayton, Eds., vol. 9982. SPIE, 2016, p. 99820J.
- [149] J. F. Riker, G. A. Tyler, and J. L. Vaughn, “Long-range speckle imaging theory, simulation, and brassboard results,” in *Unconventional and Indirect Imaging, Image Reconstruction, and Wavefront Sensing 2017*, J. J. Dolne and R. P. Millane, Eds., vol. 10410. SPIE, 2017, p. 104100Q.

- [150] J. L. Vaughn, “Estimating the achieved three-bar resolution for an image that does not contain a three-bar chart,” the Optical Sciences Company, Anaheim, CA, Tech. Rep. TR-935, 1988.
- [151] G. A. Tyler, “Analysis of three bar target resolution for coherently illuminated objects,” the Optical Sciences Company, Anaheim, CA, Tech. Rep. TR-1913, 2015.
- [152] L. C. Andrews, R. L. Phillips, and C. Y. Hopen, *Laser Beam Scintillation with Applications*. Bellingham, WA: SPIE Press, 2001, vol. PM99.
- [153] “Standard for characterization of image sensors and cameras,” European Machine Vision Association, Barcelona, ES, Standard 1288, 2020, release 4.0 Linear.
- [154] N. R. Van Zandt, M. F. Spencer, M. J. Steinbock, B. M. Anderson, M. W. Hyde IV, and S. T. Fiorino, “Comparison of polychromatic wave-optics models,” in *Unconventional Imaging and Wavefront Sensing XII*, vol. 9982, no. 2. SPIE, 2016, p. 024106.
- [155] L. C. Andrews, “Aperture-averaging factor for optical scintillations of plane and spherical waves in the atmosphere,” *J. Opt. Soc. Am. A*, vol. 9, no. 4, pp. 597–600, 1992.
- [156] R. L. Fante, “The effect of source temporal coherence on light scintillations in weak turbulence,” *J. Opt. Soc. Am.*, vol. 69, no. 1, pp. 71–73, 1979.
- [157] Y. Baykal, C. F. Ouyang, and M. A. Plonus, “Scintillation index for a temporally partially coherent, spherical wave light source in weak turbulence,” *Radio Sci.*, vol. 16, no. 3, pp. 343–345, 1981.
- [158] O. Korotkova, “Scintillation index of a stochastic electromagnetic beam propagating in random media,” *Opt. Commun.*, vol. 281, no. 9, pp. 2342–2348, 2008.
- [159] D. L. Fried, “Aperture averaging of scintillation,” *J. Opt. Soc. Am.*, vol. 57, no. 2, pp. 169–175, 1967.
- [160] J. Blitzstein and J. Hwang, *Introduction to Probability*, ser. Chapman & Hall/CRC Texts in Statistical Science. CRC Press, 2014.
- [161] V. S. Rao Gudimetla and J. F. Holmes, “Probability density function of the intensity for a laser-generated speckle field after propagation through the turbulent atmosphere,” *J. Opt. Soc. Am.*, vol. 72, no. 9, pp. 1213–1218, 1982.

- [162] C. M. McIntyre, M. H. Lee, and J. H. Churnside, “Statistics of irradiance scattered from a diffuse target containing multiple glints,” *J. Opt. Soc. Am.*, vol. 70, no. 9, pp. 1084–1095, 1980.
- [163] J. F. Holmes and V. S. Rao Gudimetla, “Variance of intensity for a discrete-spectrum, polychromatic speckle field after propagation through the turbulent atmosphere,” *J. Opt. Soc. Am.*, vol. 71, no. 10, pp. 1176–1179, 1981.
- [164] J. F. Holmes, J. R. Kerr, R. A. Elliott, M. H. Lee, P. A. Pincus, and M. E. Fossey, “Experimental pulsed laser remote crosswind measurement system – feasibility study and design (part V),” Oregon Graduate Center, Beaverton, OR, Tech. Rep. ARSCD-CR-79-007, 1978.
- [165] J. F. Holmes, “Speckle propagation through turbulence: its characteristics and effects,” in *Topical Meeting on Optical Remote Sensing of the Atmosphere*. Optica Publishing Group, 1985, p. TuB2.
- [166] J. L. Bufton, R. S. Iyer, and L. S. Taylor, “Scintillation statistics caused by atmospheric turbulence and speckle in satellite laser ranging,” *Appl. Opt.*, vol. 16, no. 9, pp. 2408–2413, 1977.
- [167] *Goldeye G/CL User Guide*, Allied Vision Technologies GmbH, Stadtroda, DE, 2008, v4.4.2.
- [168] D. Burrell and R. Driggers, “Target pose estimation from dual-plane speckle return,” in *IEEE Research and Applications of Photonics in Defense (RAPID)*, Miramar Beach, FL, 2022.
- [169] P. F. McManamon, *LiDAR Technologies and Systems*. Bellingham, WA: SPIE Press, 2019, vol. PM300.
- [170] D. Burrell, B. Berry, M. Spencer, and R. Driggers, “Laser speckle mitigation through substandard compressive sensing,” in *Computational Optical Sensing and Imaging*, Washington, DC, 2020, p. JW4D.5.
- [171] J. M. Cobb and P. Michaloski, “A laser speckle reduction system,” in *Illumination Optics II*, vol. 8170, Marseille, FR, 2011, p. 81700D.
- [172] H. Chunning, G. Huadong, and W. Changlin, “Edge preservation evaluation of digital speckle filters,” in *IEEE International Geoscience and Remote Sensing Symposium*, vol. 4, Toronto, ON, 2002, pp. 2471–2473.
- [173] T. Leportier and M.-C. Park, “Filter for speckle noise reduction based on compressive sensing,” *Opt. Eng.*, vol. 55, no. 12, p. 121724, 2016.

- [174] D. Burrell, M. Kemnetz, J. Beck, and M. Beason, “Efficiently calculating extended isoplanatic angles over horizontal paths,” in *Propagation Through and Characterization of Atmospheric and Oceanic Phenomena*, Vancouver, BC, 2022, p. PW4F.6.
- [175] M. A. van Dam *et al.*, “Angular anisoplanatism in laser guide star adaptive optics,” in *Advances in Adaptive Optics II*, B. L. Ellerbroek and D. B. Calia, Eds., vol. 6272. SPIE, 2006, pp. 987–995.
- [176] J. Stone, P. H. Hu, S. P. Mills, and S. Ma, “Anisoplanatic effects in finite-aperture optical systems,” *J. Opt. Soc. Am. A*, vol. 11, no. 1, pp. 347–357, 1994.
- [177] D. Burrell and M. Beason, “Fast statistical testing of scintillated, speckled irradiance,” in *Propagation Through and Characterization of Atmospheric and Oceanic Phenomena*, Washington, DC, 2021, p. PW4F.5.
- [178] G. W. Snedecor and W. G. Cochran, *Statistical Methods*, 8th ed. Hoboken, NJ: Wiley-Blackwell, 1989.
- [179] D. Burrell, J. Beck, M. Beason, and B. Berry, “Wave-optics sampling constraints in the presence of speckle and anisoplanatism,” in *Unconventional Imaging and Adaptive Optics*, San Diego, CA, 2021.
- [180] A. T. Young, “Seeing: its cause and cure,” *Astrophys. J.*, vol. 189, 1974.
- [181] D. A. Hope, S. M. Jefferies, M. Hart, and J. G. Nagy, “High-resolution speckle imaging through strong atmospheric turbulence,” *Opt. Express*, vol. 24, no. 11, 2016.
- [182] M. C. Roggemann and A. C. Koivunen, “Wave-front sensing and deformable-mirror control in strong scintillation,” *J. Opt. Soc. Am. A*, vol. 17, no. 5, 2000.
- [183] A. D. Wheelon, “Skewed distribution of irradiance predicted by the second-order Rytov approximation,” *J. Opt. Soc. Am. A*, vol. 18, no. 11, 2001.
- [184] J. M. Beckers, “Adaptive optics for astronomy: Principles, performance, and applications,” *Annu. Rev. Astron. Astrophys.*, vol. 31, no. 1, 1993.
- [185] M. F. Spencer, “Wave-optics investigation of turbulence thermal blooming interaction,” *Opt. Eng.*, vol. 59, no. 8, 2020.